DESIGN, DEVELOPMENT, AND STUDY OF REACTION-BASED LUMINESCENT AND MRI PROBES FOR SENSING AND IMAGING

MAK HO NAM

PhD

The Hong Kong Polytechnic University

2025

The Hong Kong Polytechnic University

Department of Applied Biology and Chemical Technology

Design, Development, and Study of Reaction-Based Luminescent and MRI Probes for Sensing and Imaging

Mak Ho Nam

A thesis submitted in partial fulfilment of the requirements for the degree of Doctor of Philosophy

August 2024

CERTIFICATE OF ORIGINALITY

I hereby declare that this thesis is my own work and that, to the best of my knowledge and belief, it reproduces no material previously published or written, nor material that has been accepted for the award of any other degree or diploma, except where due acknowledgement has been made in the text.

_____ (Signed)

_____Mak Ho Nam_____ (Name of student)

Abstract

With the emerging need of powerful tools for harmful species sensing and bioimaging, new molecules or sensing mechanisms are routinely developed to optimize the detection performance of chemical sensing probes. In this thesis, reaction-based luminescent and MRI probes are designed for sensing and bioimaging applications. In the presence of a target analyte, the probes undergo specific chemical reactions to provide responses in luminescence and MRI signals. The aim of this work is to develop innovative tools for real-time monitoring of toxic species in the environment, in commercial products, and for biomedical analysis.

Palladium-based catalysts are frequently used in pharmaceutical industry and palladium contamination in pharmaceutical products is a significant concern. Over the past decade, chemists have continuously developed new palladium sensors to improve their performance in detecting palladium ions. As Pd^0 and Pd^{2+} react with different scavengers, it is necessary to distinguish between different oxidation states of palladium and quantify them in pharmaceutical products. However, to the best of our knowledge, available palladium ion differentiators are rare. In Chapter 2, a novel porphyrin-coumarin conjugated fluorescent probe for distinguishing different oxidation states of palladium (Pd^0 and Pd^{2+}), PPIX-L2, is developed. PPIX-L2 can react with Pd^0 to show a 24-fold coumarin fluorescence enhancement (λex: 361 nm, λem: 440 nm). It can also interact with Pd^{2+} to quench 98% of the porphyrin emission (λex: 400 nm, λem: 630 nm). Both actions show high selectivity. Moreover, PPIX-L2 demonstrates improved sensitivity towards Pd^0 and Pd^{2+} with detection limits of 75 nM and 382 nM for Pd^0 and Pd^{2+}, respectively. This study provides a fluorescence differentiator, PPIX-L2, for the quantification of Pd^0 and Pd^{2+} with an improved detecting sensitivity.

Hydrogen sulfide (H_2S) is recognized as a reactive sulfur species (RSS) and is highly toxic. It can be produced endogenously and plays a vital role in cellular processes in the human body. However, to date, most sensing probes are single-modality design, which limits their sensitivity and utility. Chapter 3 mainly focuses on synthesis and application of reaction-based fluorescence/T_1-MRI dual-modality probe, NBD[Gd]-L2, for H_2S imaging. NBD[Gd]-L2 provides both fluorescence and MRI signal responses in the presence of H_2S. In the fluorescence response, it shows an 88.4% fluorescence quenching with a detection limit of 578 nM in 60 minutes. In biological experiments, NBD[Gd]-L2 demonstrates low cytotoxicity in a selected normal cell line (HK-2) and a cancer cell line (HeLa) and exhibits a "turn-off" property in confocal experiments when the cells are incubated with exogenous H_2S. In the MRI response, the T_1-weighted relaxivity (r_1) value demonstrates a 36.4% reduction because of the loss of molecular weight and changes in the residual water lifetime of the Gd^{3+} complex. Due to the reduction in r_1 value, NBD[Gd]-L2 in MR phantom experiments shows a "bright" image at the initial state and the image is "darkened" after the addition of H_2S. This study provides a lanthanide-based fluorescence/MRI dual probe for the detection of H_2S.

Hydrazine (N_2H_4) is well known as a highly reactive chemical compound and has been utilized in various scientific research and industrial fields. However, it is highly toxic to the human body and has the potential to pollute the environment through industrial processes. In Chapter 4, the focus is mainly on the design, development and study of a lanthanide-based hydrazine probe, Hz[Ln]-L1. When Tb^{3+} ions are coordinated, Hz[Tb]-L1 exhibits a luminescence response signal for hydrazine detection. In the presence of hydrazine, Hz[Tb]-L1 demonstrates a 129-fold enhancement of the Tb luminescence in three minutes with a detection limit of 256 nM. When

Gd^{3+} is inserted into the ligand, an obvious magnetic response is produced by Hz[Gd]-L1 in response to hydrazine. In detail, the T_1-weighted relaxivity value (r_1) shows a 2.7-fold enhancement, increasing from 1.5 $mM^{-1}s^{-1}$ to 4.0 $mM^{-1}s^{-1}$. Additionally, in the MRI phantom experiment, Hz[Gd]-L1 demonstrates a "dark" image in the initial state which turns "bright" after interacting with hydrazine. From the luminescence lifetime experiment and HRMS analysis, it is confirmed that the phthalimide group is removed in the presence of hydrazine, causing the hydration number of the complex to change from 0 to 1 and resulting in an r_1-enhancing property. This study provides a lanthanide-based probe for hydrazine, showing a 129-fold increase in Tb luminescence and a 2.7-fold enhancement in the T_1-weighted relaxivity with the coordination of Tb or Gd, respectively.

Formaldehyde is also well known as an environmental toxin and carcinogen. An overload of formaldehyde can damage the central nervous system. It is important to develop selective and sensitive fluorescent probes for formaldehyde imaging. Recently, an analyte regenerating strategy for formaldehyde has been developed. The key to this strategy is enabling formaldehyde detection with no or minimum perturbation to the homeostasis of formaldehyde in biological systems. However, extra care should be taken with formaldehyde regenerating fluorescent probes due to the risk of degradation of the probe. In Chapter 5, formaldehyde regenerate fluorescent probes, Cou-NSu is designed and studied. Although Cou-NSu shows a selective response toward formaldehyde, a self-enhancing emission peak appears upon storage in a 10 mM PBS buffer solution/ 1% DMSO which could adversely affect the accuracy and reproducibility of formaldehyde detection. From the LC-MS analysis, a hydrolysate of Cou-NSu is found, confirming that Cou-NSu undergoes hydrolysis in the presence of water at neutral pH. This limits the biological application of current

analyte regenerate strategy for formaldehyde detection. Of note, the hydrolysis of probe employing this strategy has not been previously observed and reported. This study provides a new formaldehyde probe designed following the analyte-regenerating strategy, pointing out the risk of hydrolysis which may negatively affect the quantification study of formaldehyde.

In conclusion, four chemical probes are designed for detecting heavy metals or small molecules, that are environmentally and physiologically toxic. It is hoped that the reaction-based chemical probes described here will inspire the design of powerful chemical tools for practical applications in environmental and biomedical fields in the future.

Acknowledgements

First and foremost, I would like to express my deepest gratitude to my chief supervisor, Prof. Wong for providing me this life-changing opportunity to work in his research group. Over the years of my PhD study, he gave me countless chances to learn and grow. Although my performance might not be as ideal as he expected, he still patiently motivates me to work hard and guides me to understand the areas for improvements. The inspiring feedback from Prof. Wong always provide a clear direction for me to conduct my research. This work would never have been possible without his constant support and guidance.

I am also grateful to my mentor, Dr. Lijun Jiang. She always shares her experiences with me on both research and personal aspects. Her numerous supports and encouragement help me to improve my research project.

A special thanks to all past and current group members from Prof. Wong's research group and Y1301 Lab, particularly Prof. Ka-leung Wong, Dr. Yanjuan Gu, Dr. Chi-tung Yeung, Dr. Wai-sum. Lo, Dr. Xueyang Fang, Dr. Shiying Li, Dr Kwok-ho Lui, Dr. King-him Yim, Dr Ting-hin Hui, Ms. Daisy Yuen-ting Wong, Mr. Xin Li, Ms. Helen Sin-man Ho, Mr. Hugo Lik-hang Tse, Ms. Xuehan Wang and Ms. Joyce Pui-yu Wong, for their experience shared and valuable friendship which have enriched my time here.

I would also like to thank all the staff in the Department of Applied Biology and Chemical Technology and University Research Facility in Life Science, especially Dr. P.-K. So, Dr. O.-C. Lau and Dr. C.-M. Chan, for their sincere help in my research work.

To my parents and my brother, your unconditional support, guidance and encouragement have meant the world to me. Thank you for your endless patience and for always believing this “unwise and stubborn kid”.

Lastly, I would like to thank Ms. Eva Ng, whose love and support have always been my motivating force, helping me to face all the difficulties and challenges. Without you, I would not have the strength to complete this study.

Thank you all for being a part of this PhD journey. I wish everyone mentioned a happy and healthy life.

Table of Contents

List of Abbreviations

a.u.	Arbitrary unit
Abs	Absorbance
br	Broad
$CDCl_3$	Deuterated chloroform
cyclen	1,4,7,10-tetraazacyclododecane
d	Doublet
dd	Doublet of doublets
DMEM	Dulbecco's Modified Eagle Medium
em	Emission
eq.	Equivalent
ESI-	Electrospray ionization with negative ion detection
ESI+	Electrospray ionization with positive ion detection
ex	Excitation
g	Gram
h	Hour
H_2O	Water
HeLa	Human cervical carcinoma
Hz	Hertz
K	Kelvin
Ln	Lanthanide
m	Multiplet
M	mol dm^{-3}

m/z	Mass-to-charge ratio
MALDI-TOF	Matrix-Assisted Laser Desorption/ Ionization Time-of-Flight
mM	Millimolar
mmol	Millimole
MRI	Magnetic resonance imaging
ms	Millisecond
MTT	3-(4,5-dimethylthiazol-2-yl)-2,5-tetrazolium bromide assay
nm	Namometer
NMR	Nuclear magnetic resonance
PBS	Phosphate buffer saline
q	Quartet
Rf	Radio frequency
RT	Room temperature
s	Singlet
t	Triplet
TLC	Thin layer chromatography
UV/vis	Ultraviolet/visible
μs	Microsecond
τ	Lifetime
°C	Degree Celsius

Chapter 1: General introduction

Molecular sensing and imaging is an interdisciplinary field which combines the knowledge from organic chemistry, analytical chemistry, biochemistry and physical chemistry and plays an important role in modern scientific research.[1, 2] The study of this field involves the design, development and application of the techniques to detect targets and monitor the conditions in environment, commercial products (such as cosmetics and pharmaceuticals products) and even in living organisms with minimal perturbation to their original systems.[3-5] In recent decades, scientists have developed many powerful and functional probes and contrast agents to detect specific substances such as metal ions,[6] metabolites[7] and toxic species[8, 9] with high sensitivity. Reaction-based chemical probe is one of the vital categories in sensor designing.[10, 11] In the presence of the target analyte, a reaction-based probe can undergo chemical reactions with the analyte and give responsive signals. The response of the signal can roughly be classified into “turn-on” and “turn-off” types. In the “turn-on” probes, they initially produce a low intensity of signal (“off” state). After interaction with the target, they demonstrate a high intensity of signal (“on” state). Conversely, “turn-off” probe starts with a high intensity of signal (“on” state) and decrease to low intensity when the target analyte is detected. With the use of advanced modalities such as optical imaging and magnetic resonance imaging (MRI), real-time spatiotemporal data can be obtained, providing scientists with information to observe and solve the ongoing problems in the system. As our world continues to evolve, designing new targets or functions for probes is still necessary to solve future challenges.[12, 13]

1.1 Fluorescent probe

Small molecule-based fluorescent sensors (fluorescent probes) have been frequently used in chemistry, biology, and human physiology.

1.1.1 Fluorescence

The term “luminescence” was first introduced by the German physicist Wiedemann using the German word “luminescenz” in 1888. Luminescence is a blanket term for light emission by energy excitation without heating. Luminescent materials are widely applied in our daily lives, such as displays, securities, counterfeits, lasers, sensing and bioimaging. Luminescence generally depends on the type of excited state and can be grouped into two categories: fluorescence and phosphorescence. [14, 15]

The fluorescence of organic molecules relates to delocalized electronic structure. The conjugated π system absorbs the energy from the photons of incoming UV/ visible light that match the potential energy difference between π and π* orbital. The HOMO (Highest Occupied Molecular Orbital) π electron is then excited to the LUMO (Lowest Unoccupied Molecular Orbital) π* orbital. This high energy excited state molecule has a thermodynamic driving force to bring antibonding π* electron back to fully bonded ground state (Figure 1.1). There are mainly three mechanisms involved in deexcitation of excited stated molecules, including internal conversion (IC), intersystem crossing (ISC) and fluorescence. IC is a non-radiative transition of electron in high energy orbital to low energy orbital. Similarly, ISC is a non-radiative transition process of electron between two orbitals, but ISC involves inverting the spinning of electron during transition. The

electron in singlet excited state can then be passed to triplet excited state. Fluorescence is the emission of light as a photon with the energy matching the transition from an excited state to the ground state where direct relaxation occurs (Figure 1.2). Fluorescence measurements rely on the difference between the maximum excitation and emission wavelength. With the separation of excitation and emission wavelength, the emission intensity can be detected with minimal impact from the excitation source. During the relaxation of the electron from excited state to ground state, the loss of vibrational energy occurs. From the equation $E = hc/\lambda$, energy is inversely proportional to the wavelength. The energy loss during the relaxation leads to a longer wavelength in emission. The difference between the excitation and emission wavelengths was discovered by Sir George G. Stokes and is called Stokes' shift.[15-17]

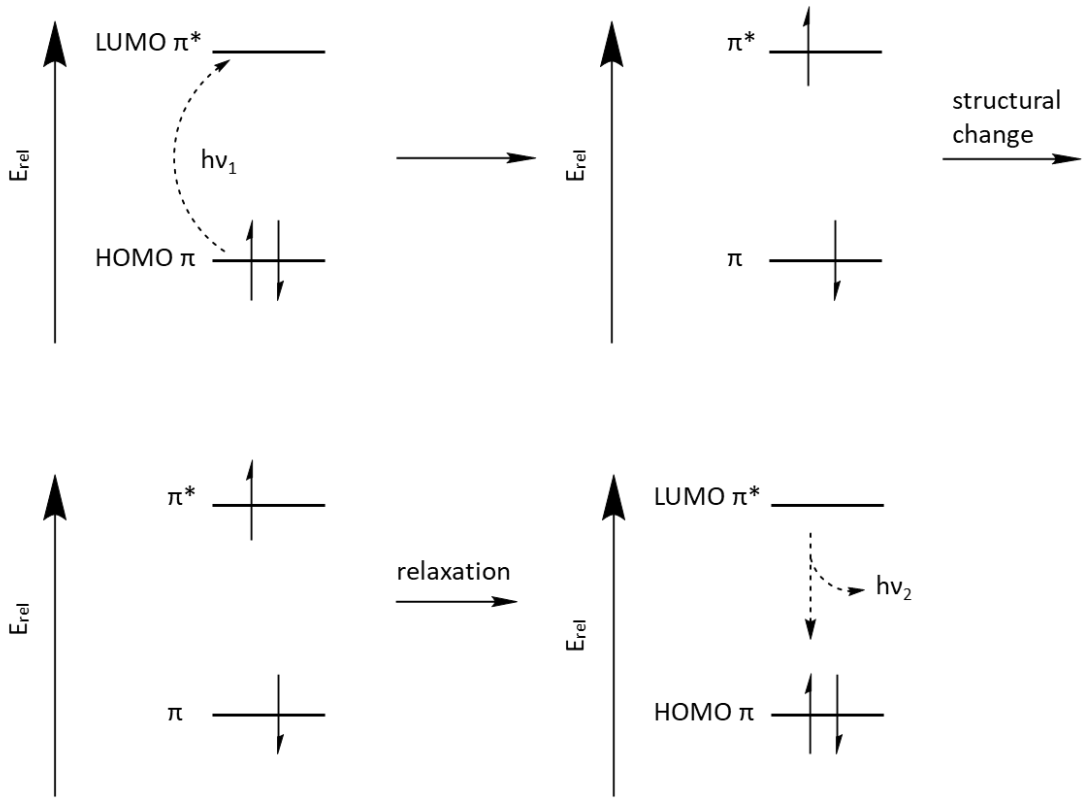

Figure 1.1: Simplified energy diagram of excitation (top) and emission (bottom) in π-conjugated system, where π* denotes the excited state, ν denotes frequency and hν denotes the radiation energy.

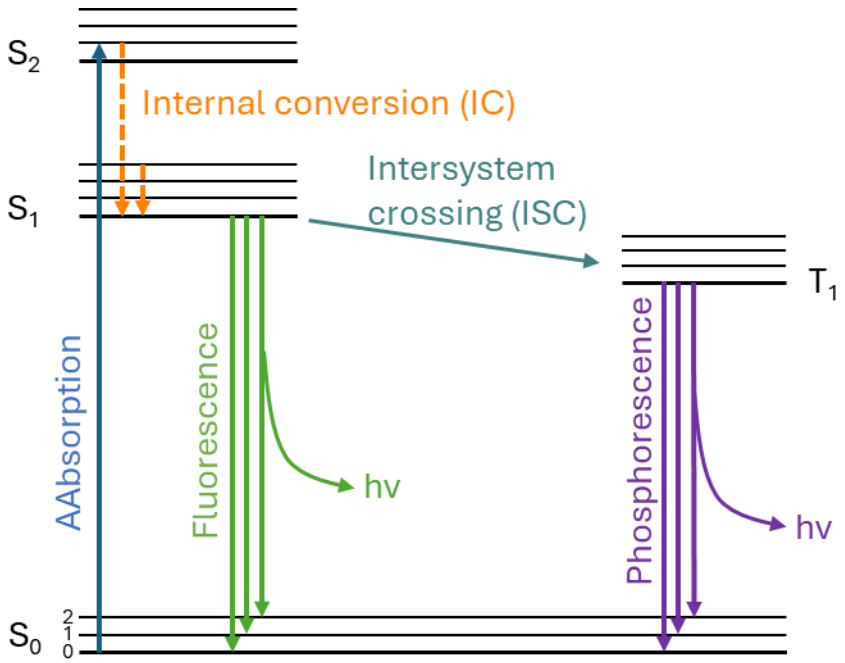

Figure 1.2: IC, ISC, fluorescence, and phosphorescence in the Jablonski diagram, where S_0, S_1 and S_2 denote the singlet ground, first and second electronic state, respectively, and T_1 denotes the first triplet state.

The fluorescence of these probes can be changed in response to environmental changes (pH, solvent, viscosity), substance binding (metal ions), and chemical reactions (metal ions, bioactive substances).[5, 6, 18-23] By developing different effective fluorescent probes sensing protocols, scientists can accurately identify various harmful species in human body, improving their understanding of human physiological processes and pathology pathways. For example, the highly sensitive fluorescence measurement of fluorescence microscopy allows us to obtain spatiotemporal resolution images in cellular imaging.[24] In sensing and imaging purposes, reaction-based fluorescent probes are frequently used to create signal responses (either “turn-on” or “turn-off”) for visualizing target analyte. To produce the signal intensity response of the

fluorescent probe, different fluorescence quenching mechanisms are used. When the probe undergoes reactions with target analyte, either activation or deactivation of the fluorescence quenching mechanism can help to give responsive signal, allowing scientists to understand the presence of analyte or even its quantity.

1.1.2 Fluorescence-based sensing mechanism

To perform fluorescence changes, fluorescent probes undergo either a chemical selective reaction or a receptor-analyte selective interaction. When the receptor and analyte undergo an irreversible chemical reaction, the fluorescent probe can be called chemidosimeter. When the receptor and analyte undergo a reversible non-covalent interaction, the fluorescent probe can be called chemosensor.[25] Over the years, several common fluorescence mechanisms have been frequently used to generate fluorescence responses, such as Photoinduced Electron Transfer (PET),[26, 27] Intramolecular Charge Transfer (ICT),[28-30] Förster Resonance Energy Transfer (FRET),[31, 32] Excited-State Intramolecular Proton Transfer (ESIPT)[33, 34] and Aggregation Induced Emission (AIE).[35, 36]

1.1.2.1 Photoinduced electron transfer

Photoinduced electron transfer (PET) is a widely used mechanism to quench the fluorescence of a fluorophore.[18] The mechanism of PET involves the interaction of an electron donor and a fluorophore. In a PET “turn-on” probe, the electron energy of the donor should lie between the HOMO and LUMO of fluorophore. When a fluorophore absorbs incoming UV or visible light, the HOMO π electron is excited to the LUMO π^* orbital. As the energy level of electron donor is

lower than the π* orbital, the donor preferentially transfers an electron to occupy the vacancy in fluorophore π orbital. Therefore, it blocks the relaxation of π*→π which leads to fluorescence (Figure 1.3, top). When the donor reacts, the electron energy of the donor becomes lower than the π orbital of fluorophore, blocking PET pathway and restoring the fluorescence (Figure 1.3, bottom).

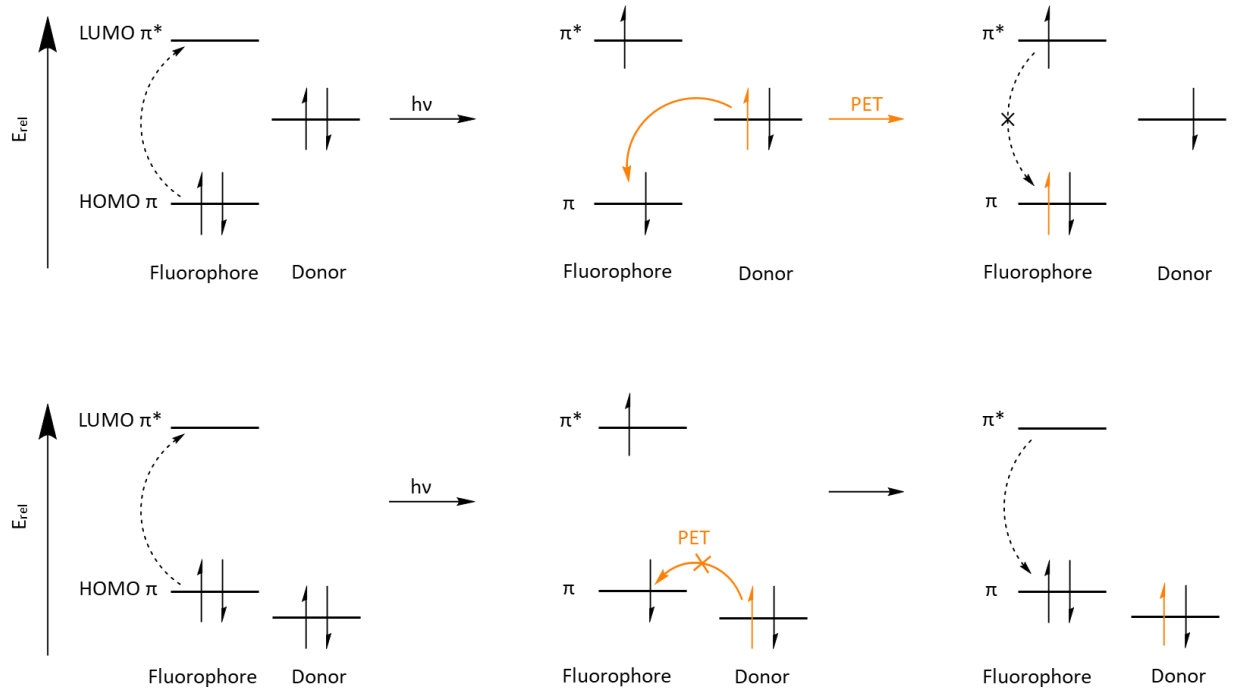

Figure 1.3: A schematic energy diagram of PET mechanism. (top) PET pathway is allowed. (bottom) PET pathway is blocked.

The nitrogen atom is considered a good donor for PET mechanism.[37, 38] Fluorescence can be quenched by the lone pair electrons of nitrogen atom through PET pathway.[27] When the lone pair turns into σ-bond electron pair, the energy of σ orbital becomes lower than that of π orbital. The electron from nitrogen atom can no longer preferentially transfer to the π orbital, blocking PET to restore the emission of fluorophore. In this example, in the presence of formaldehyde (FA),

a methylenehydrazine group is formed, blocking PET pathway (Figure 1.4, top). Another efficient PET donor is an electron-rich heterocycle. Similar to nitrogen atom, if the energy of π orbital of the heterocycle lies between π and π* orbital of fluorophore, it can also serve as a PET quencher.[39] To recover the fluorescence, covalent modification by the analyte would lower the electron density of donor system. In the example, the ring reacts when presence of hypochlorous acid, the pyrrole is oxidized to keto form and block PET pathway (Figure 1.4, bottom). However, the covalent modification is irreversible. This heterocycle PET quenching mechanism cannot be used in cumulative analyte measurement.

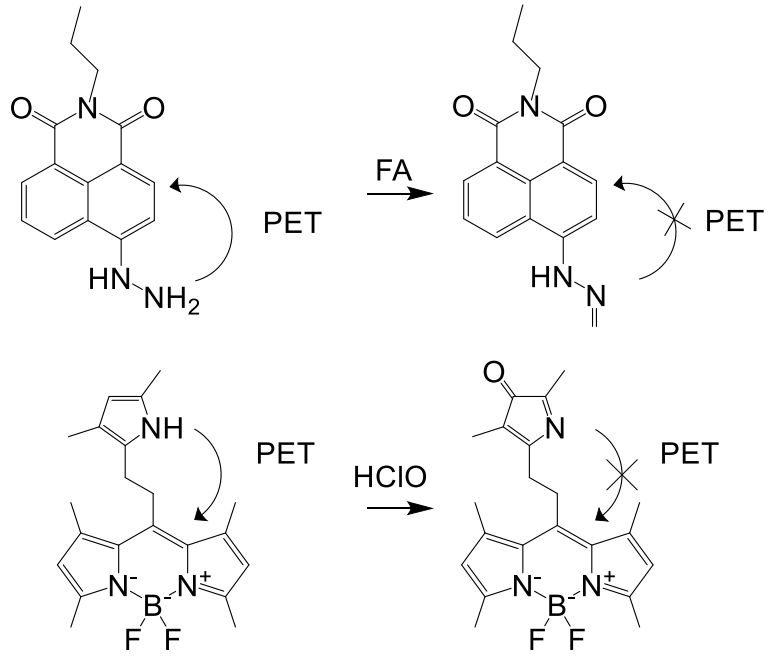

Figure 1.4: PET quenching by N atom (top) and electron-rich heterocycle (bottom).

1.1.2.2 Intramolecular charge transfer

Intramolecular charge transfer (ICT) is another frequently used fluorescence quenching mechanism.[40] In ICT mechanism, the probe consists of an electron donor and electron acceptor

located at two ends of the fluorophore. The fluorophores sometimes act as either donor or acceptor. For ICT system, excited state has a stronger dipole moment compared to the ground state (Figure 1.5).[41] During the polarization change, the original optimal solvation for ground state is no longer optimal for excited state. The excited state maintains for a short period of time to allow the solvation shell rearrangement to achieve the optimal solvation, and this process reduces the excited state energy. However, the fluorescence from the excited state is much faster than the solvation optimization for the ground state. The solvation for ground state is in a sub-optimal state due to not having enough time for shell rearrangement. This results a higher ground state energy than the original ground state energy. With the combined effect of ground and excited state, the energy difference between the π and π* orbital becomes smaller. In the equation $E = hc/\lambda$, the reduction in energy gap results in a longer emission wavelength (Figure 1.6). In the case of fluorescent probe, the polarization of the probe can be altered to shift the emission wavelength in the presence of analyte, such as metal ions and bioactive analytes. The covalent reaction and metal coordination can either increase or decrease the difference in energy levels between ground and excited states. The emission wavelength is shorter when ICT is reduced; while the emission wavelength becomes longer when the ICT is strengthened. For example, the fluorescence of a polarized probe is quenched by ICT pathway (Figure 1.7).[42] When calcium ions binds with fura-2 group, the electron donation from nitrogen atom is reduced. Hence, the ICT pathway of the probe is reduced, and fluorescence shifts to a shorter wavelength.

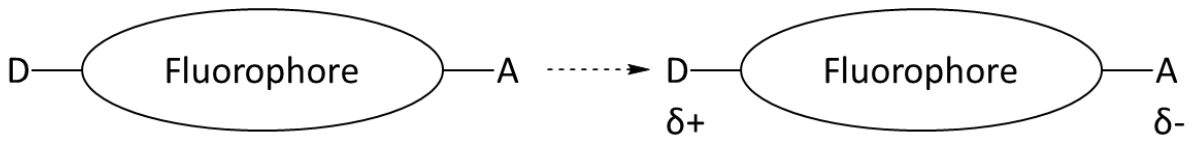

Figure 1.5: Dipole moment increases when excitation of ICT systems.

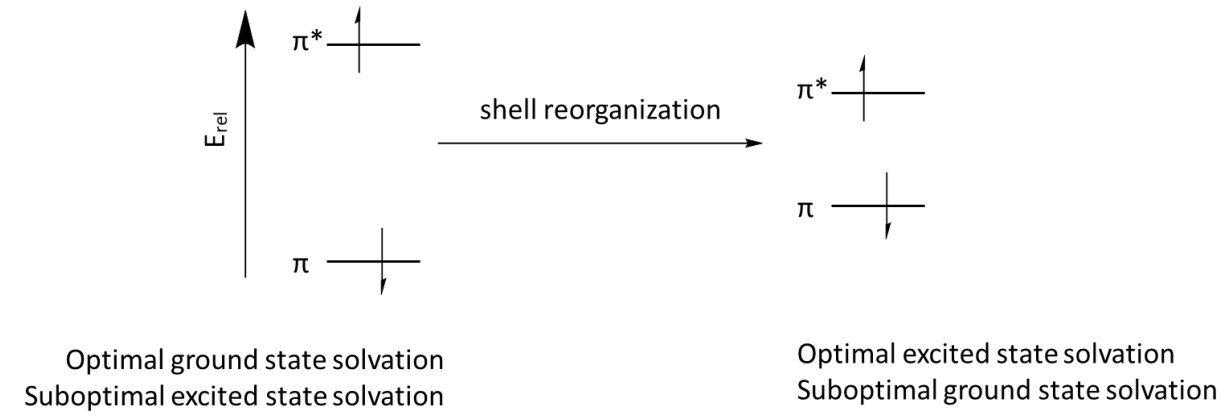

Figure 1.6: A schematic energy diagram of ICT systems with solvation effect in polar solvent.

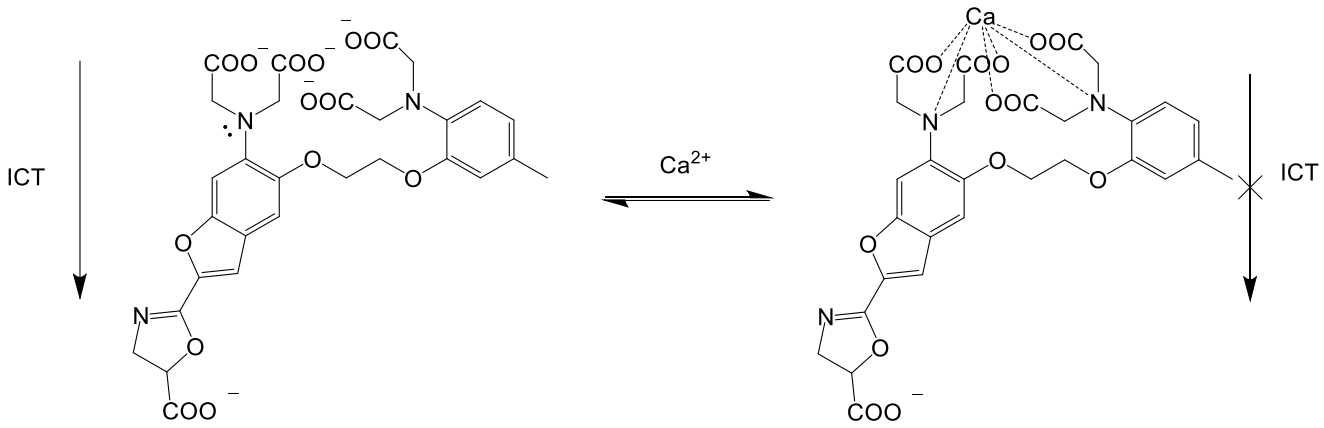

Figure 1.7: An ICT-based probe for Ca^{2+} detection.

1.1.2.3 Förster resonance energy transfer

Förster resonance energy transfer (FRET) is based on the communication between two fluorophores. If the singlet excited state of two fluorophores match, the energy from the singlet excited state (S_1) of the donor fluorophore is transferred to the lower energy singlet excited state (S_1) of the acceptor fluorophore. The energy transfer in this mechanism is a non-radiative process, i.e., non-photon emission.[43] When the acceptor excited state receives the energy, a rapid relaxation occurs from the acceptor excited state (S_1) to the acceptor ground state (S_0). As the

acceptor ground state has higher energy than the donor ground state (S_0), the energy difference between the acceptor S_0 and S_1 orbitals is smaller than that of the donor S_0 and S_1 orbitals. The system emits a longer emission wavelength as the energy is reduced in the whole system (Figure 1.8). The efficiency of FRET is influenced by the distance between the two fluorophores and the overlap in their excitation and emission spectra. The efficiency of FRET is directly proportional to $1/r^6$, where r denotes the intermolecular average spatial separation. The extent of spectral overlap between the donor emission and the acceptor excitation controls the degree of FRET. The greater the overlap, the higher efficiency can be observed, thus greater signal intensity (Figure 1.9).[31] In this example, coumarin and merocyanines act as a FRET pair with coumarin as the donor to transfer excited state energy to the acceptor merocyanines (Figure 1.10).[44] In the presence of H_2S, FRET is eliminated and emission of merocyanines is reduced. Only a shorter wavelength emission from coumarin is observed which provides easy discrimination from merocyanine emission.

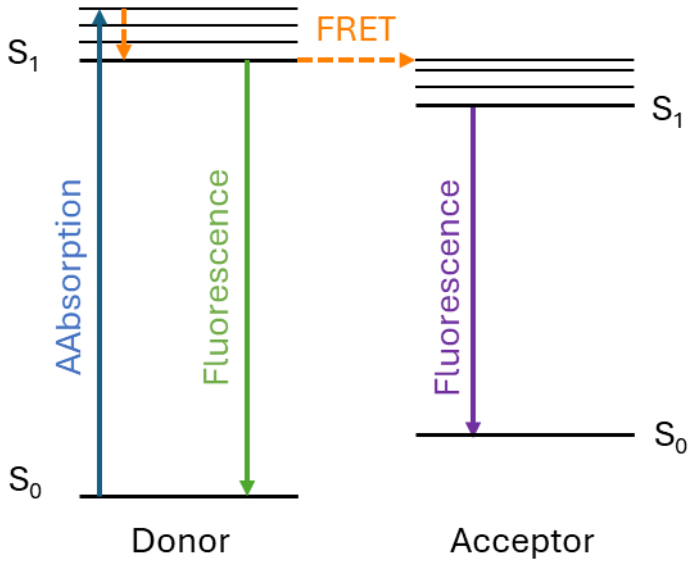

Figure 1.8: Jablonski diagram of FRET system.

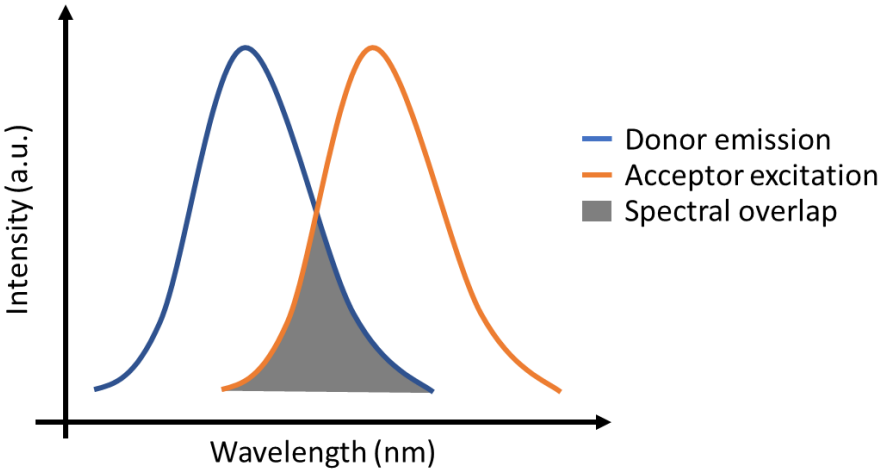

Figure 1.9: Spectral overlap between the donor emission and acceptor excitation in FRET system.

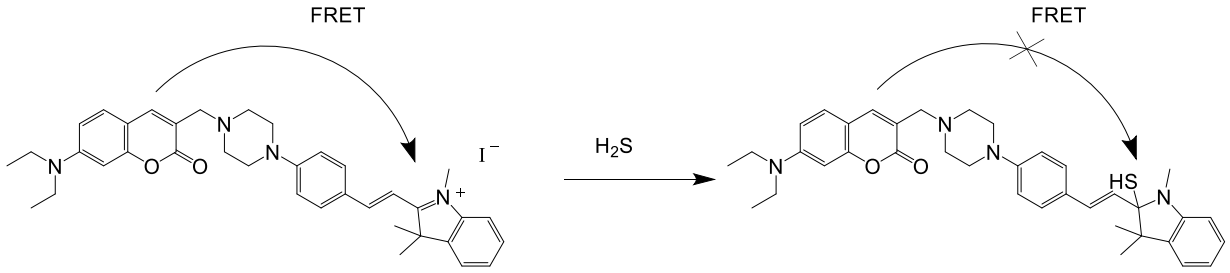

Figure 1.10: Coumarin-merocyanine FRET-based fluorescence probe.

1.1.2.4 Excited-state intramolecular proton transfer

Excited-state intramolecular proton transfer (ESIPT) involves an intramolecular hydrogen bond between a hydrogen bond donor, such as OH, NH_2, and a hydrogen bond acceptor, such as =N, and C=O.[40, 45-47] ESIPT is a four-level excitation and emission process. In the enol (E) form, an electron from the fluorophore ground state is excited to excited enol form (E*). During the excitation, a redistribution of electron charge occurs. This leads to an increase basicity of hydrogen

bond acceptor and an increase acidity of hydrogen bond donor. A rapid process, phototautomerization ($k_{ESIPT,} > 10^{12}\ s^{-1}$), occurs to convert E* form to excited keto form (K*). After the keto emission and return to the ground state keto form (K), reverse proton transfer occurs, and the molecule returns to initial E form (Figure 1.11). Due to the four-level excitation and emission process, ESIPT fluorophores exhibit a large Stokes' shift when during fluorescence measurements. However, the ESIPT emission is highly sensitive to the fluorescence measurement environment. For example, polar or hydrogen bond donating solvents may block the keto emission and inhibit the ESIPT process. Most of ESIPT fluorescence probes are ratiometric probes due to the dual-emission property from enol emission and keto emission. This property allows for direct quantification of analytes in biological or environmental system without calibration.[21] In the example, 2-(2-Hydroxyphenyl)benzothiazole (HBT) is used for ESIPT fluorescent probe development (Figure 1.12).[48] In the presence of formaldehyde, the probe undergoes a 2-aza-cope rearrangement and β-elimination to regenerate hydroxyl group. The excited enol form (E*) can convert to excited keto form (K*) by phototautomerization. As the energy difference between the ground and excited state of keto form is smaller than that of enol form, there is a significant increase in the maximum emission wavelength, creating a large Stokes' shift.

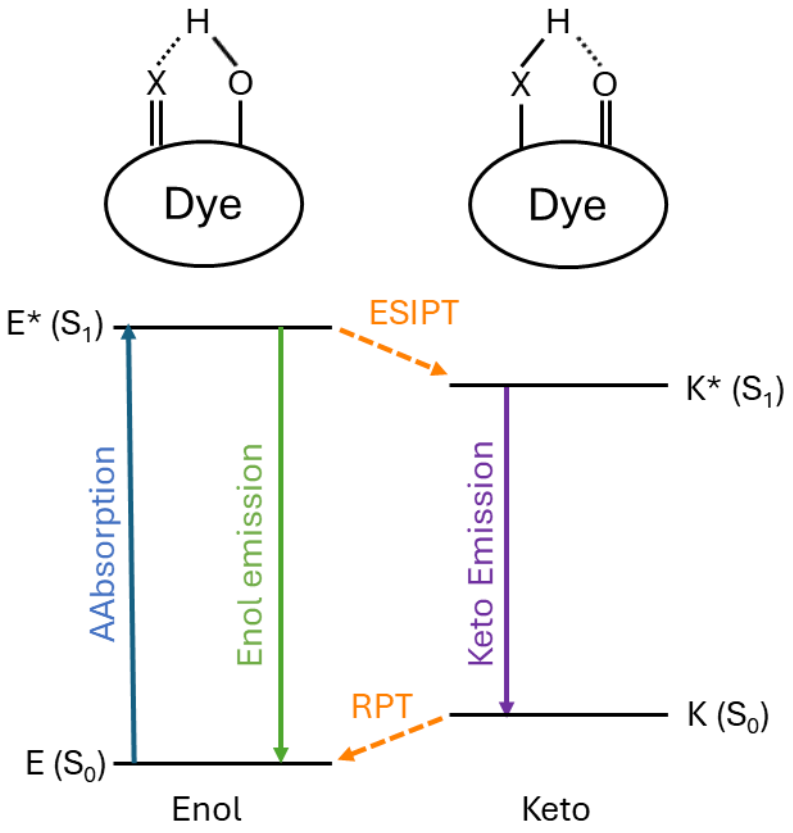

Figure 1.11: A schematic energy diagram correlating the reaction mechanism of the fluorescent probe, where S_0 and S_1 denote singlet ground and excited state, respectively, and RPT denotes reverse proton transfer.

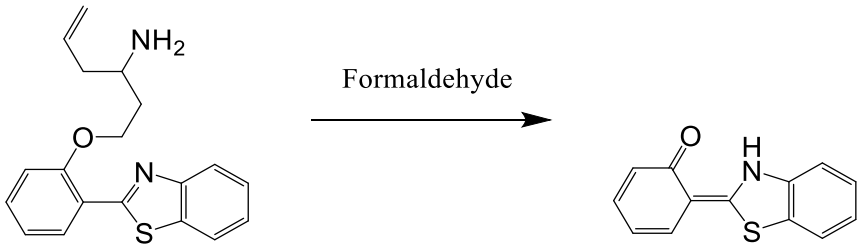

Figure 1.12: ESIPT-based-fluorescent probe for formaldehyde detection.

1.1.2.5 Aggregation-induced emission

Aggregation-induced emission (AIE) is a relatively new mechanism that causes an emission response.[49] For most traditional organic dye, there is a strong intermolecular π-π stacking property. When the dyes stack together and form aggregates, the emission of the dye is quenched , a phenomenon known as aggregation-caused quenching (ACQ).[50] Unlike ACQ, AIE luminogens (AIEgens) originally show little or no emission in dilute solution and demonstrate strong emission in aggregate form or in solid state.[51] The intramolecular motion of AIEgens, such as vibration and rotation, in dilute solution leads to a high non-radiative decay rate of AIEgens (k_{nr}) that causes the quenching of AIEgens emission. Once AIEgens form aggregates or are present in solid form, the intramolecular motion is reduced and increasing the π-π stacking effect. This results in the suppression of k_{nr} by up to four orders of magnitude. The radiative decay rate (k_r) shows only a little change in aggregate or in solid state.[52, 53] In dilute and low viscosity solutions, the excited state energy is reduced. However, the ground state energy rises, resulting in a decrease of energy gap between ground and excited state.[54] From the potential energy surface curve (PEC) of S_1, there is not much of an energy barrier to reach conical intersection (CI) (Figure 1.13, left).[55] It illustrates that relaxation to CI is easy. This causes the rapid non-radiative decay and results in a much larger k_{nr} value (10^{11} s^{-1}), which is larger than k_r (10^7 - 10^8 s^{-1}), leading to the emission quenching of the fluorophore. In aggregate or in solid state, PEC of S_1 becomes steeper. The steric hindrance from the nearby molecules leads to the rise of S_1 energy (Figure 1.13, right). The intramolecular motion of the fluorophore is also reduced due to increased energy barrier. The k_{nr} of the aggregate or solid is suppressed and able to compete with k_r. Therefore, the fluorescence is restored. In the example, the probe demonstrates an emission response to environmental viscosity change (Figure 1.14).[56] The authors propose that the probe can aggregate and form

multiple binding sites with ATP. This creates a more viscous environment and restricts the intramolecular rotation of the probe. The non-radiative decay is then blocked creating a new radiative pathway for fluorescence enhancement.

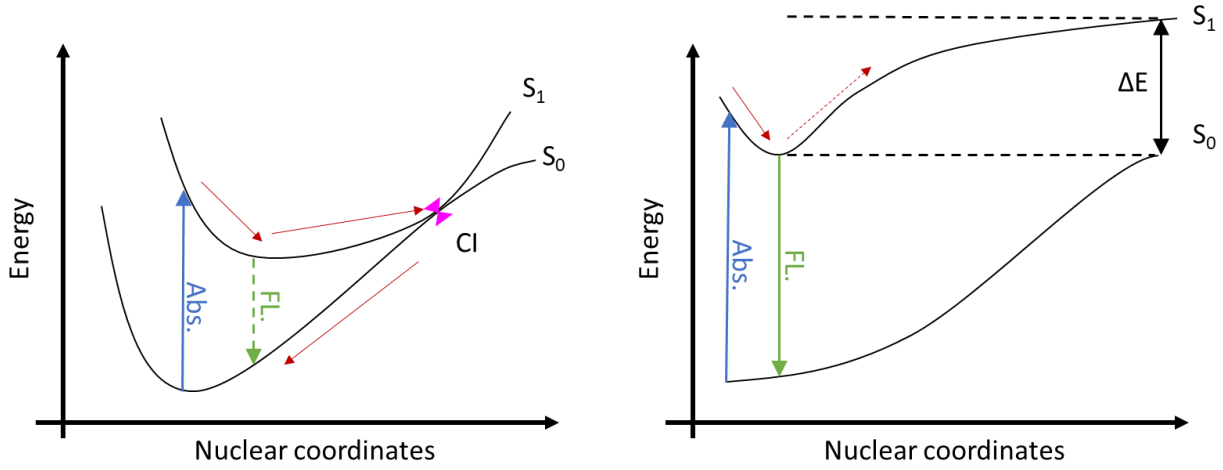

Figure 1.13: Potential energy curves with the proposed energy decay pathways of ACQ (left) and AIE fluorophores (right), where Abs. denotes absorption, FL. denotes fluorescence and CI denotes conical intersection.

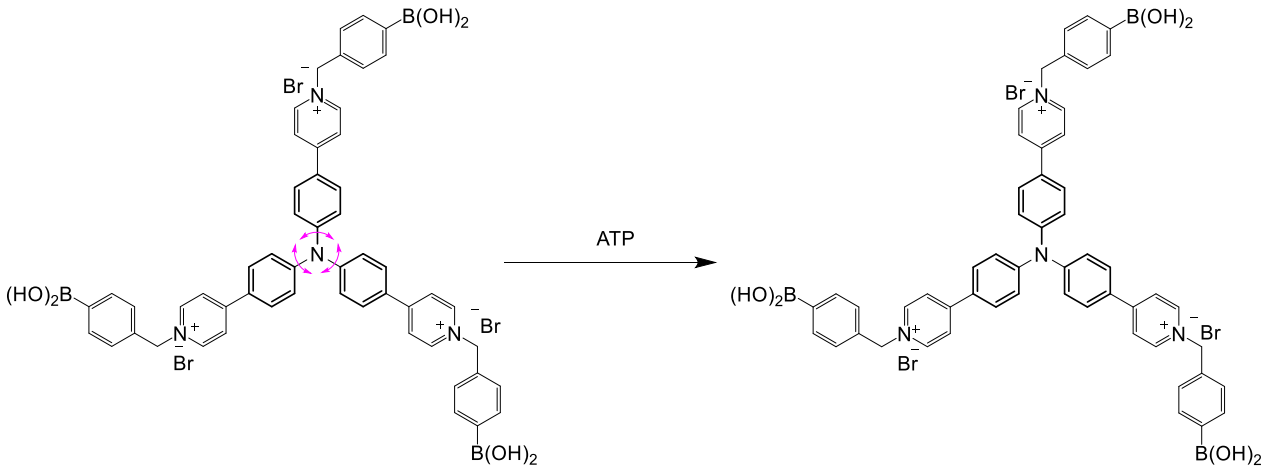

Figure 1.14: AIE-based fluorescent probe for ATP detection.

1.2 Lanthanide-based probe

Lanthanides are a series of chemical elements from lanthanum to lutetium (Z = 57 – 71). The trivalent lanthanide ions, Ln^{3+}, have a ground state electronic configuration of $[Xe]4f^n$ (n = 0 – 14). According to the Russell-Saunders spin-orbital coupling scheme, the energy levels are well-defined due to the shielding of the 4f orbital by the xenon core (54 electrons) especially because of the larger radial expansion of the $5s^2$ and $5p^6$ subshells. The 4f orbital then becomes the "inner orbital", providing the unique chemical and spectroscopic properties for the lanthanide metal ions. For example, in the visible and near-infrared (NIR) range, the inner 4f-4f transitions are sharp and easily recognized because these transitions are formally parity forbidden. This also helps with the long excited state lifetimes and allows the lanthanide ions to be used in the time-resolved imaging and luminescence microscopy.[57, 58]

Due to the parity forbidden nature of f-f transition in Ln^{3+} ions, the molar absorption extinction coefficient (ε) is low. To address this shortcoming, Weissman demonstrated the antenna effect for lanthanide complex luminescence in 1947. When the organic receptor (the antenna) of the lanthanide complex absorbs energy, the organic receptor is first excited to its singlet electronically excited state (S_1). Then, it undergoes intersystem crossing (ISC) from S_1 to a lower lying triplet excited state (T_1) (Figure 1.15). This intersystem crossing is a spin-forbidden process due to $\Delta S \neq 0$ which causes a very long-lived radiation relaxation. Although it is a spin-forbidden process, several mechanisms help to partially relax the selection rules such as coupling the vibration modes, *J*-state mixing and overlap with 5d orbital and charge transfer states. To transfer the energy from the antenna to the Ln^{3+} ions, a double-electron exchange mechanism (Dexter) and electrostatic multipolar mechanism (Förster) are proposed. The efficiency of the two mechanisms depends on

the distance between the donor and acceptor. The Dexter mechanism operates strictly at a short distance (30 – 50pm) which the orbital overlap significantly. The Förster mechanism operates at a longer distance (up to 1000 pm).[59-61]

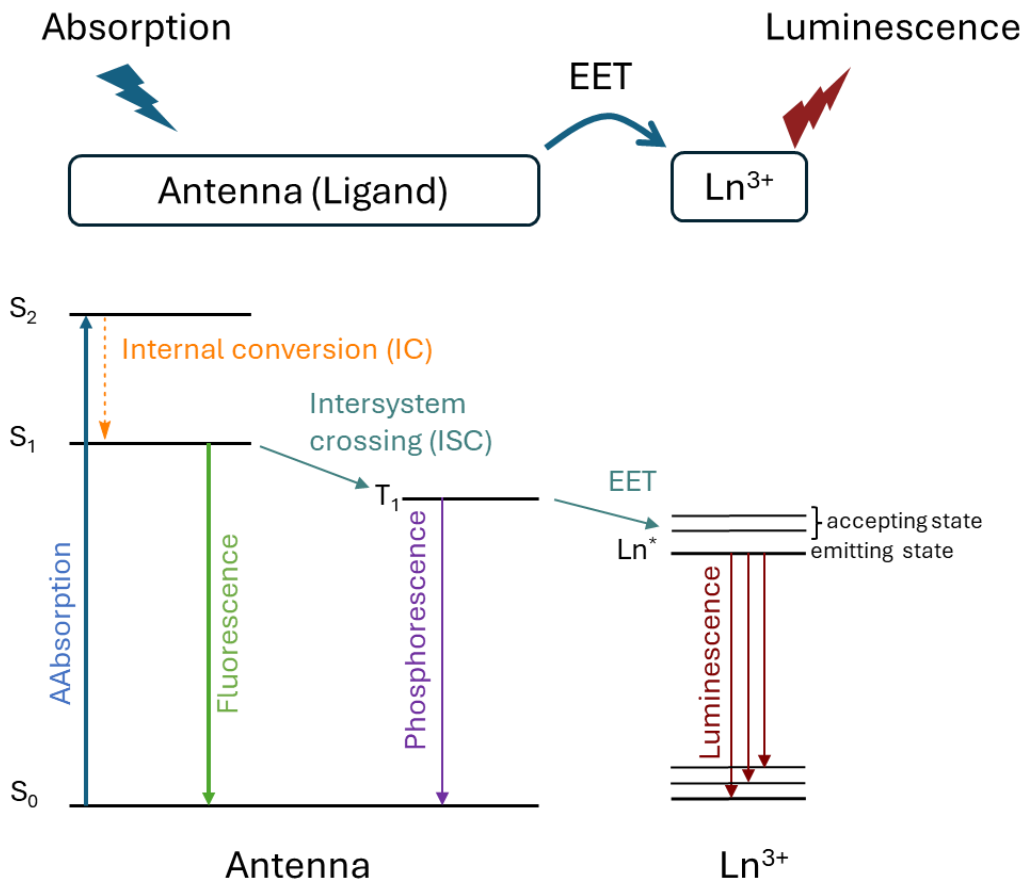

Figure 1.15: Jablonski diagram of energy transfer in the lanthanide complex luminescence system.

1.2.1 Lanthanide coordinating chemistry

When designing a lanthanide-based small-molecule probe for biomedical imaging purposes, a suitable lanthanide chelator is a key parameter. It is well known that free Ln^{3+} ions are highly toxic to the human body. However, forming a lanthanide complex can largely reduce the toxicity.

Therefore, a proper lanthanide chelator that effectively holds Ln^{3+} ions is crucial in the design of a lanthanide-based probe. Lanthanides are hard Lewis acids and preferentially coordinate with hard Lewis bases (carboxylates) and high electronegative atoms such as N and O. Interaction of the Ln^{3+} with water is also commonly found in the lanthanide complexes. Depending on the steric factors of the ligand, the coordination number of the lanthanide complex usually ranges from 6 to 12. Commonly, the lanthanide coordination numbers are 8 and 9.[62, 63]

In general, stable Ln^{3+} ion chelators are classified as linear polydentate ligands and macrocyclic compounds. Linear polydentate ligands, such as ethylenediaminetetraacetic acid (EDTA) and diethylenetriamine pentaacetate (DTPA), have acyclic structures that allow the denticity reduction of the complex. Macrocyclic compounds, such as 1,4,7,10-Tetraazacyclododecane-1,4,7,10-tetraacetic acid (DOTA) and 1,4,7-Triazacyclononane-1,4,7-triacetic acid (NOTA), with different pendant arms like carboxylates and amides, have macrocycle structures that provide excellent chelating abilities to Ln^{3+} (Figure 1.16). The antenna itself can sometimes be the pendant arms to chelate Ln^{3+} ions. Compared with linear polydentate ligands, macrocyclic ligands with pendant groups are more straightforward to synthesize. Cyclen is the most frequently used starting material for macrocyclic ligand. By the simple chemical modification of the amine groups of the cyclen such as protection, deprotection and alkylation, scientists can rationally design different ligands for different purposes.[64]

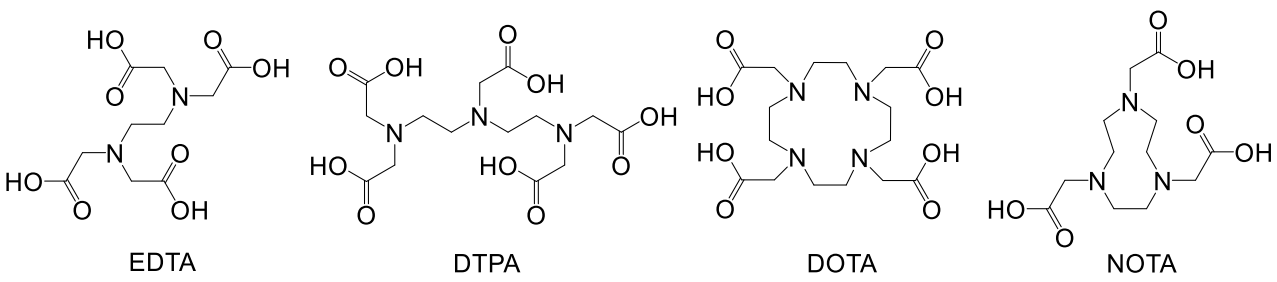

Figure 1.16: Example of lanthanide ions chelators.

1.2.2 Hydration number

The hydration number of the lanthanide is also an important consideration in the design and development of bio-inorganic imaging agents. The hydration number is defined as the number of water molecules (q) interacting in the inner coordination sphere of the Ln^{3+} complex. Lanthanide luminescence can be quenched by the high-energy vibrations. The quenching phenomenon is less likely to occur when the energy gap requires more phonons to bridge it. The solution of the complex in water $\tilde{\nu}(\mathrm{O-H})$ and deuterated water $\tilde{\nu}(\mathrm{O-D})$ are determined to be 3600 cm^{-1} and 2200 cm^{-1}, respectively. Therefore, the number of phonons is larger in deuterated water and O-D oscillators contribute little to luminescence deactivation. Hence, the luminescence lifetime of the complex in deuterated water is longer than that in water assuming all other deactivation paths are the same. In magnetic resonance imaging (MRI), the number of water molecules (q) coordinated to the lanthanide metal centre is highly related to the nuclear relaxation time. A larger hydration number would result in a faster nuclear relaxation time.[65, 66]

In determining the hydration number of the lanthanide complex, the luminescence lifetime method is a frequently used approach. The optical lifetime of the lanthanide complex in water and deuterated water is measured. The relative quenching effect of O-H and O-D oscillators allows for the calculation of the hydration number. The general form of the relationship is:

$$q = A \times (\Delta k_{obs} - B) - C \qquad \text{Equation 1.1}$$

$$\Delta k_{obs} = k_{H_2O} - k_{D_2O} = \frac{1}{\tau_{H_2O}} - \frac{1}{\tau_{H_2O}} \qquad \text{Equation 1.2}$$

where A is the inner-sphere contribution to the quenching, B is the corrective factor, C is the outer-sphere contribution of the closely diffusing solvent molecules, k is the decay rate and τ is the lifetime. For Gd^{3+} complex, it is common to replace the Gd^{3+} ion with Eu^{3+} or Tb^{3+} ions to form the corresponding complex and measure the lifetime of the complex in H_2O and D_2O to estimate the hydration number of Gd^{3+} complex.[59, 67, 68]

1.2.3 Lanthanide-based luminescence probes

Lanthanide-complex-based luminescent sensors (lanthanide luminescent probes) are also among the most widely used molecular sensors for sensing and imaging. The probes typically consist of three parts, namely the antenna (the chromophore), the lanthanide metal chelator and the lanthanide metal ions (Ln^{3+}). Within the probe, the antenna absorbs the excitation light and transfers energy to the Ln^{3+} ions for emission. The lanthanide ions demonstrate characteristic absorption and emission spectra in near-UV (Gd^{3+}), visible (Tb^{3+}, Eu^{3+}, Sm^{3+}, Dy^{3+}) and near-infrared range (Nd^{3+}, Yb^{3+}). Especially for Tb^{3+} and Eu^{3+} which display strong luminescence in

the visible range, they have been frequently used in developing luminescent probes for analyte sensing and imaging. Lanthanide luminescent probes have unique luminescence properties such as sharp emission peaks, large Stokes' shift, long luminescent lifetime (up to milliseconds) and resistance to photobleaching. With the advantage of long luminescent lifetimes, lanthanide luminescent probes are particularly useful in biological systems because the luminescence can be easily separated from the short-lived fluorescence (nanosecond range) emitted from the fluorophore in biological systems. To design a reaction-based lanthanide luminescent probe, similar to the reaction-based fluorescent probe, different fluorescence quenching transfer mechanisms, such as PET, ICT, and FRET, can be applied to the chromophore to create either "turn-on" or "turn-off" luminescent probes. By controlling the intensity signal of the chromophore, the amount of energy transferred to the Ln^{3+} ions and the Ln^{3+} luminescence can also be controlled, allowing the development probes with different functions.[69-71]

1.2.4 Lanthanide-based magnetic resonance imaging probe

Magnetic resonance imaging (MRI) is one of the most widely employed methods for imaging. Its operation is fundamentally based on the proton nuclear magnetic resonance (^{1}H NMR). MRI mainly measures the relaxation times of the hydrogen nuclei and intensity of the water proton signal in the body. Longitudinal relaxation time (T_1) and transverse relaxation time (T_2) are two important parameters in this imaging technique. T_1 is the time of magnetization (M) recovery to its initial maximum value (M_0) along the longitudinal axis, parallel to B_0, after the excitation by the radio frequency (RF) pulse (Figure 1.17 left). T_2 is the time of the magnetization (M_{xy}) decay along the transverse axis after the excitation by RF (Figure 1.17 right). From the curve of magnetization versus time plot, T_1 and T_2 can be calculated by the following equation:

$$M = M_0(1 - e^{\frac{-t}{T_1}})$$ Equation 1.3

$$M_{xy} = M_0 e^{\frac{-t}{T_2}}$$ Equation 1.4

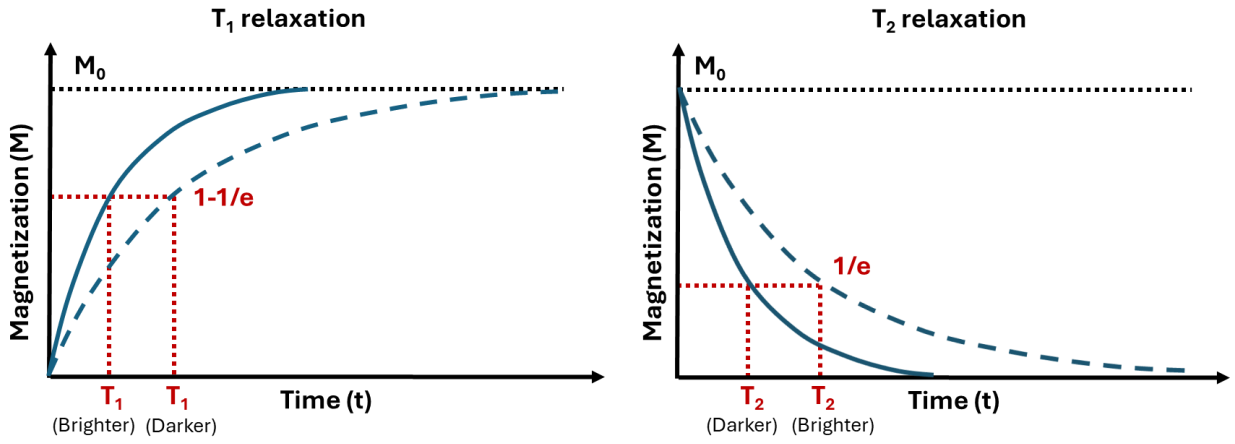

Figure 1.17: Plot of T_1 (left) and T_2 (right) relaxation in magnetization against time.

However, since over 60% of the human body is composed of fat and water, it is challenging to rely solely on the amount of water at the given location or on changes in proton density in the human body to show a clear signal difference in tissue. Paramagnetic contrast agents are commonly used chemical contrast agents to amplify the contrast by changing the magnetic relaxation time of T_1 and T_2. These contrast agents can produce a time-varying magnetic field that promote the T_1 and T_2 relaxation of the water molecules. A higher number of unpaired electrons in paramagnetic material can enhance rotational motion of the contrast agent and the electron spin flips. further enhancing the time-varying magnetic field. Gd^{3+} agents are frequently used as clinical

paramagnetic contrast agents due to the Gd^{3+} ion having the highest number of seven unpaired electrons in the 4f-orbital among the periodic table.[72, 73]

1.2.4.1 Relaxivity

The relaxivity of the paramagnetic agent demonstrates the change in relaxation rate in the solution as a function of concentration. It can be expressed by the following equations:

$$\frac{1}{\Delta T_1} = r_1 \cdot [C] \qquad \text{Equation 1.5}$$

$$\frac{1}{\Delta T_2} = r_2 \cdot [C] \qquad \text{Equation 1.6}$$

where r_1 and r_2 represent the longitudinal relaxivity and transverse relaxivity, respectively, T_1 and T_2 are longitudinal relaxation time and transverse relaxation times, respectively and C is the concentration of the solution.

In these equations, the relaxation time is the inverse of the relaxation rate. By measuring the relaxation rate of the contrast agent at different concentrations, a graph of relaxation rate ($1/\Delta T_1$ and $1/\Delta T_2$) against contrast concentration can be plotted. The slope of the change of relaxation rate against concentration curve allows for the determination of the corresponding relaxivity (r_1 and r_2) (Figure 1.18). [74, 75]

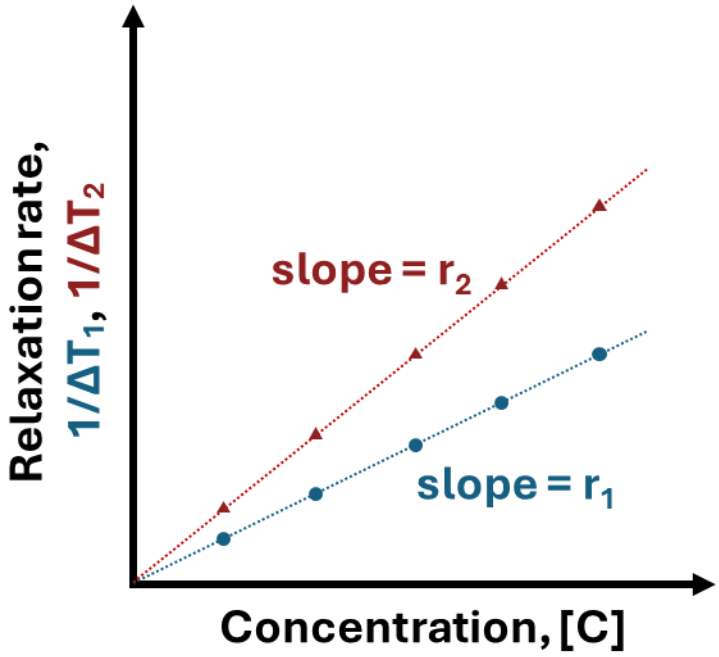

Figure 1.18: The plot of relaxation rate against concentration of contrast agent to determine the relaxivity (r_1 and r_2) of an MR contrast agent.

1.2.4.2 Strategies to design analyte-responsive lanthanide-based MRI probe

In the past few decades, various imaging techniques such as magnetic resonance imaging (MRI), positron emission tomography (PET), fluorescence imaging (FI) and single-photon emission computed tomography (SPECT) have been well-established and frequently used in bioimaging. Among these imaging techniques, MRI is the only non-invasive imaging method that allows high spatial resolution (10 µm – 1 mm) and three-dimensional images of the deep tissue in human body. Therefore, MRI is widely used for biomedical imaging and diagnosis.

T_1 contrast agent and T_2 contrast agents are two frequently used MRI contrast agents. With the help of the contrast agents, higher spatial resolution images can be obtained. The traditional MRI contrast agents provide a "always on" function which allows scientists to do imaging only. With the development of reaction-based MRI contrast agents, scientists can detect target analytes alongside the imaging function. Similar to luminescent probes, MRI probes can interact with the specific analyte to produce a response in the signal intensity.[76, 77]

To date, there are three mechanisms used in designing analyte-responsive MRI probes. Changing the number of water molecules (q) coordinated to the metal centre is the most frequently used mechanism. In Gd(III) complex, low hydration number ($q = 0$) will give a low relaxivity which produces a "darker" image. While the chemical reaction occurs in the probe, some lanthanide-coordinated moieties will be displaced by aqua ions, increasing the hydration number of the complex. A higher hydration number ($q \geq 1$) can increase the relaxivity of the probe and give a "brighter" image. Modifying the rotational tumbling times (τ_R) is also an important mechanism to alter the relaxivity of the probe. This approach is particularly useful when the probe is designed to bind with a specific enzyme. Upon binding with an enzyme, the molecular weight of the resultant substance will be very high. A larger substance will reduce the rotational tumbling times (τ_R) in water and allow water molecules to interact with the paramagnetic metal centre more easily and hence the relaxivity will be dramatically increased to provide a much "brighter" image. The mean residence lifetime (τ_M) of Gd(III)-bound water molecules is the parameter that is often overlooked. However, it is one of the key parameters to describe the rate of water exchange ($k_{ex} = 1/\tau_M$) between the inner-sphere coordination position and the bulk solvent. The paramagnetic agents should have an optimal value of τ_M to reach the maximal relaxivity. If the τ_M is too short, the relaxivity will be

limited due to insufficient time for the water molecules to bind to the paramagnetic centre to become fully relaxed. Conversely, if the τ_M is too long, relaxivity value will also be limited because fewer water molecules can reach the inner-coordinate sphere of the paramagnetic metal, affecting the T_1 of the bulk water. Although the ability to fine-tune the water change rate is still limited, understanding the optimal value of τ_M is considered to be an important parameter of developing next generation of responsive MRI probes (Figure 1.19). [76, 78-80]

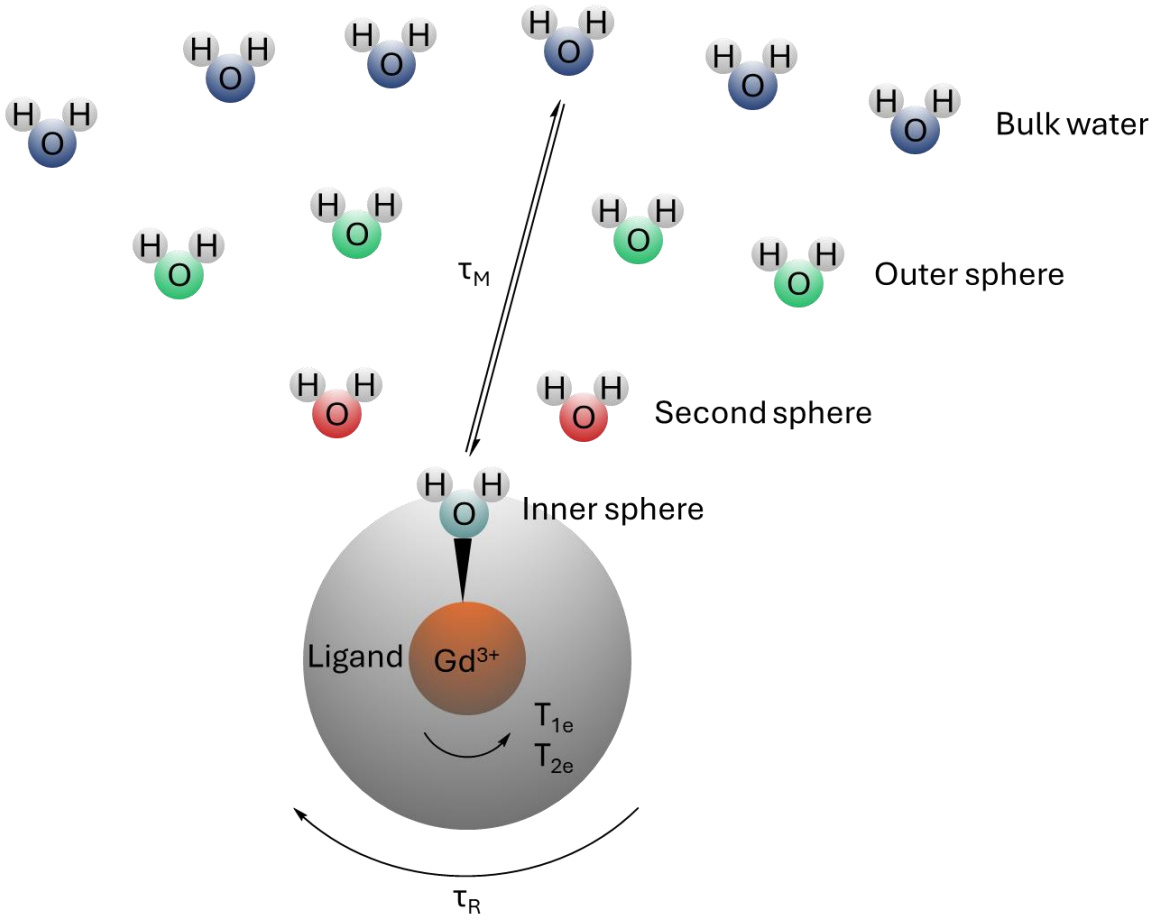

Figure 1.19: The important physical parameters that impact T_1 and T_2 of the MR contrast agent.

1.4 Reference

[1] G.-L. Law and W.-T. Wong, "An Introduction to Molecular Imaging," in *The Chemistry of Molecular Imaging*, N. Long and W.-T. Wong Eds.: John Wiley & Sons, Inc, 2014, pp. 1-24.

[2] M. A. Pysz, S. S. Gambhir, and J. K. Willmann, "Molecular imaging: current status and emerging strategies," *Clinical Radiology,* vol. 65, no. 7, pp. 500-516, 2010, doi: 10.1016/j.crad.2010.03.011.

[3] C.-W. Huang, C. Lin, M. K. Nguyen, A. Hussain, X.-T. Bui, and H. H. Ngo, "A review of biosensor for environmental monitoring: principle, application, and corresponding achievement of sustainable development goals," *Bioengineered,* vol. 14, no. 1, pp. 58-80, 2023, doi: 10.1080/21655979.2022.2095089.

[4] A. Othman, L. Norton, A. S. Finny, and S. Andreescu, "Easy-to-use and inexpensive sensors for assessing the quality and traceability of cosmetic antioxidants," *Talanta,* vol. 208, p. 120473, 2020, doi: 10.1016/j.talanta.2019.120473.

[5] D. Wu, A. C. Sedgwick, T. Gunnlaugsson, E. U. Akkaya, J. Yoon, and T. D. James, "Fluorescent chemosensors: the past, present and future," *Chemical Society Reviews,* vol. 46, no. 23, pp. 7105-7123, Dec 7 2017, doi: 10.1039/c7cs00240h.

[6] M. Formica, V. Fusi, L. Giorgi, and M. Micheloni, "New fluorescent chemosensors for metal ions in solution," *Coordination Chemistry Reviews,* vol. 256, no. 1-2, pp. 170-192, 2012, doi: 10.1016/j.ccr.2011.09.010.

[7] J. Krämer, R. Kang, L. M. Grimm, L. De Cola, P. Picchetti, and F. Biedermann, "Molecular Probes, Chemosensors, and Nanosensors for Optical Detection of Biorelevant Molecules

and Ions in Aqueous Media and Biofluids," *Chemical Reviews,* vol. 122, no. 3, pp. 3459-3636, 2022, doi: 10.1021/acs.chemrev.1c00746.

[8] N. Kwon, Y. Hu, and J. Yoon, "Fluorescent Chemosensors for Various Analytes Including Reactive Oxygen Species, Biothiol, Metal Ions, and Toxic Gases," *ACS Omega,* vol. 3, no. 10, pp. 13731-13751, 2018, doi: 10.1021/acsomega.8b01717.

[9] L. D. Rosales-Vázquez, A. Dorazco-González, and V. Sánchez-Mendieta, "Efficient chemosensors for toxic pollutants based on photoluminescent Zn(II) and Cd(II) metal–organic networks," *Dalton Transactions,* vol. 50, no. 13, pp. 4470-4485, 2021, doi: 10.1039/d0dt04403b.

[10] L. Wu, A. C. Sedgwick, X. Sun, S. D. Bull, X.-P. He, and T. D. James, "Reaction-Based Fluorescent Probes for the Detection and Imaging of Reactive Oxygen, Nitrogen, and Sulfur Species," *Accounts of Chemical Research,* vol. 52, no. 9, pp. 2582-2597, 2019, doi: 10.1021/acs.accounts.9b00302.

[11] J. Chan, S. C. Dodani, and C. J. Chang, "Reaction-based small-molecule fluorescent probes for chemoselective bioimaging," *Nature Chemistry,* vol. 4, no. 12, pp. 973-984, 2012, doi: 10.1038/nchem.1500.

[12] J. Zhao, J. Chen, S. Ma, Q. Liu, L. Huang, X. Chen, K. Lou, and W. Wang, "Recent developments in multimodality fluorescence imaging probes," *Acta Pharmaceutica Sinica B,* vol. 8, no. 3, pp. 320-338, May 2018, doi: 10.1016/j.apsb.2018.03.010.

[13] K. J. Bruemmer, S. W. M. Crossley, and C. J. Chang, "Activity-Based Sensing: A Synthetic Methods Approach for Selective Molecular Imaging and Beyond," *Angewandte Chemie International Edition,* vol. 59, no. 33, pp. 13734-13762, 2020, doi: 10.1002/anie.201909690.

[14] X. Cao, D. Huang, and Y. S. Zhang, "Bionanomaterials as Imaging Contrast Agents," in *Theranostic Bionanomaterials*, W. Cui and X. Zhao Eds.: Elsevier, 2019, pp. 401-421.

[15] J. R. Lakowicz, "Principles of fluorescence spectroscopy," 2006, doi: 10.1007/978-0-387-46312-4.

[16] M. Kasha, "Characterization of electronic transitions in complex molecules," *Discussions of the Faraday Society,* vol. 9, no. 0, pp. 14-19, 1950, doi: 10.1039/DF9500900014.

[17] M. Montalti, A. Credi, L. Prodi, and M. T. Gandolfi, "Handbook of Photochemistry," *Handbook of Photochemistry,* 2006, doi: 10.1201/9781420015195.

[18] B. Daly, J. Ling, and A. P. de Silva, "Current developments in fluorescent PET (photoinduced electron transfer) sensors and switches," *Chemical Society Reviews,* vol. 44, no. 13, pp. 4203-11, Jul 7 2015, doi: 10.1039/c4cs00334a.

[19] J. Wu, B. Kwon, W. Liu, E. V. Anslyn, P. Wang, and J. S. Kim, "Chromogenic/Fluorogenic Ensemble Chemosensing Systems," *Chemical Reviews,* vol. 115, no. 15, pp. 7893-943, Aug 12 2015, doi: 10.1021/cr500553d.

[20] L. You, D. Zha, and E. V. Anslyn, "Recent Advances in Supramolecular Analytical Chemistry Using Optical Sensing," *Chemical Reviews,* vol. 115, no. 15, pp. 7840-92, Aug 12 2015, doi: 10.1021/cr5005524.

[21] M. H. Lee, J. S. Kim, and J. L. Sessler, "Small molecule-based ratiometric fluorescence probes for cations, anions, and biomolecules," *Chemical Society Reviews,* vol. 44, no. 13, pp. 4185-91, Jul 7 2015, doi: 10.1039/c4cs00280f.

[22] X. Li, X. Gao, W. Shi, and H. Ma, "Design strategies for water-soluble small molecular chromogenic and fluorogenic probes," *Chemical Reviews,* vol. 114, no. 1, pp. 590-659, Jan 8 2014, doi: 10.1021/cr300508p.

[23] D. G. Cho and J. L. Sessler, "Modern reaction-based indicator systems," *Chemical Society Reviews,* vol. 38, no. 6, pp. 1647-62, Jun 2009, doi: 10.1039/b804436h.

[24] B. Huang, M. Bates, and X. Zhuang, "Super-resolution fluorescence microscopy," *Annual Review of Biochemistry* vol. 78, pp. 993-1016, 2009, doi: 10.1146/annurev.biochem.77.061906.092014.

[25] A. C. Sedgwick, H. H. Han, J. E. Gardiner, S. D. Bull, X. P. He, and T. D. James, "The development of a novel AND logic based fluorescence probe for the detection of peroxynitrite and GSH," *Chemical Science,* vol. 9, no. 15, pp. 3672-3676, Apr 21 2018, doi: 10.1039/c8sc00733k.

[26] S. Dadashi-Silab, S. Doran, and Y. Yagci, "Photoinduced Electron Transfer Reactions for Macromolecular Syntheses," *Chemical Reviews,* vol. 116, no. 17, pp. 10212-10275, 2016, doi: 10.1021/acs.chemrev.5b00586.

[27] Y. Tang, X. Kong, A. Xu, B. Dong, and W. Lin, "Development of a Two-Photon Fluorescent Probe for Imaging of Endogenous Formaldehyde in Living Tissues," *Angew. Chem., Int. Ed.,* vol. 55, no. 10, pp. 3356-9, Mar 1 2016, doi: 10.1002/anie.201510373.

[28] S. Sharma and K. S. Ghosh, "Overview on recently reported fluorometric sensors for the detection of copper ion based on internal charge transfer (ICT), paramagnetic effect and aggregation induced emission (AIE) mechanisms," *Journal of Molecular Structure,* vol. 1237, p. 130324, 2021, doi: 10.1016/j.molstruc.2021.130324.

[29] L. Jiang, R. Lan, T. Huang, C.-F. Chan, H. Li, S. Lear, J. Zong, W.-Y. Wong, M. Muk-Lan Lee, B. Dow Chan, W.-L. Chan, W.-S. Lo, N.-K. Mak, M. Li Lung, H. Lok Lung, S. Wah Tsao, G. S. Taylor, Z.-X. Bian, W. C. S. Tai, G.-L. Law, W.-T. Wong, S. L. Cobb, and K.-L. Wong, "EBNA1-targeted probe for the imaging and growth inhibition of tumours

associated with the Epstein–Barr virus," *Nature Biomedical Engineering,* vol. 1, no. 4, 2017, doi: 10.1038/s41551-017-0042.

[30] L. Jiang, H. L. Lung, T. Huang, R. Lan, S. Zha, L. S. Chan, W. Thor, T.-H. Tsoi, H.-F. Chau, C. Boreström, S. L. Cobb, S. W. Tsao, Z.-X. Bian, G.-L. Law, W.-T. Wong, W. C.-S. Tai, W. Y. Chau, Y. Du, L. H. X. Tang, A. K. S. Chiang, J. M. Middeldorp, K.-W. Lo, N. K. Mak, N. J. Long, and K.-L. Wong, "Reactivation of Epstein–Barr virus by a dual-responsive fluorescent EBNA1-targeting agent with Zn^{2+}-chelating function," *Proceedings of the National Academy of Sciences,* vol. 116, no. 52, pp. 26614-26624, 2019, doi: 10.1073/pnas.1915372116.

[31] L. Wu, C. Huang, B. P. Emery, A. C. Sedgwick, S. D. Bull, X. P. He, H. Tian, J. Yoon, J. L. Sessler, and T. D. James, "Forster resonance energy transfer (FRET)-based small-molecule sensors and imaging agents," *Chemical Society Reviews,* vol. 49, no. 15, pp. 5110-5139, Aug 7 2020, doi: 10.1039/c9cs00318e.

[32] X. Jia, Q. Chen, Y. Yang, Y. Tang, R. Wang, Y. Xu, W. Zhu, and X. Qian, "FRET-Based Mito-Specific Fluorescent Probe for Ratiometric Detection and Imaging of Endogenous Peroxynitrite: Dyad of Cy3 and Cy5," *Journal of the American Chemical Society,* vol. 138, no. 34, pp. 10778-10781, 2016, doi: 10.1021/jacs.6b06398.

[33] H. Gu, W. Wang, W. Wu, M. Wang, Y. Liu, Y. Jiao, F. Wang, F. Wang, and X. Chen, "Excited-state intramolecular proton transfer (ESIPT)-based fluorescent probes for biomarker detection: design, mechanism, and application," *Chemical Communications,* vol. 59, no. 15, pp. 2056-2071, 2023, doi: 10.1039/d2cc06556h.

[34] A. C. Sedgwick, W.-T. Dou, J.-B. Jiao, L. Wu, G. T. Williams, A. T. A. Jenkins, S. D. Bull, J. L. Sessler, X.-P. He, and T. D. James, "An ESIPT Probe for the Ratiometric Imaging of

Peroxynitrite Facilitated by Binding to Aβ-Aggregates," *Journal of the American Chemical Society,* vol. 140, no. 43, pp. 14267-14271, 2018, doi: 10.1021/jacs.8b08457.

[35] W. He, Z. Zhang, Y. Luo, R. T. K. Kwok, Z. Zhao, and B. Z. Tang, "Recent advances of aggregation-induced emission materials for fluorescence image-guided surgery," *Biomaterials,* vol. 288, p. 121709, 2022, doi: 10.1016/j.biomaterials.2022.121709.

[36] W. Fu, C. Yan, Z. Guo, J. Zhang, H. Zhang, H. Tian, and W.-H. Zhu, "Rational Design of Near-Infrared Aggregation-Induced-Emission-Active Probes: In Situ Mapping of Amyloid-β Plaques with Ultrasensitivity and High-Fidelity," *Journal of the American Chemical Society,* vol. 141, no. 7, pp. 3171-3177, 2019, doi: 10.1021/jacs.8b12820.

[37] A. Roth, H. Li, C. Anorma, and J. Chan, "A Reaction-Based Fluorescent Probe for Imaging of Formaldehyde in Living Cells," *J. Am. Chem. Soc.,* vol. 137, no. 34, pp. 10890-3, Sep 2 2015, doi: 10.1021/jacs.5b05339.

[38] T. F. Brewer and C. J. Chang, "An Aza-Cope Reactivity-Based Fluorescent Probe for Imaging Formaldehyde in Living Cells," *J. Am. Chem. Soc.,* vol. 137, no. 34, pp. 10886-9, Sep 2 2015, doi: 10.1021/jacs.5b05340.

[39] H. Zhu, J. Fan, J. Wang, H. Mu, and X. Peng, "An “Enhanced PET”-Based Fluorescent Probe with Ultrasensitivity for Imaging Basal and Elesclomol-Induced HClO in Cancer Cells," *Journal of the American Chemical Society,* vol. 136, no. 37, pp. 12820-12823, 2014, doi: 10.1021/ja505988g.

[40] J. Wu, W. Liu, J. Ge, H. Zhang, and P. Wang, "New sensing mechanisms for design of fluorescent chemosensors emerging in recent years," *Chemical Society Reviews,* vol. 40, no. 7, pp. 3483-95, Jul 2011, doi: 10.1039/c0cs00224k.

[41] C. Zhang, Z. Han, M. Wang, Z. Yang, X. Ran, and W. He, "A new BODIPY-derived ratiometric senor with internal charge transfer (ICT) effect: colorimetric/fluorometric sensing of Ag^{+}," *Dalton Transactions,* vol. 47, no. 7, pp. 2285-2291, Feb 13 2018, doi: 10.1039/c7dt04345g.

[42] G. Grynkiewicz, M. Poenie, and R. Y. Tsien, "A new generation of Ca^{2+} indicators with greatly improved fluorescence properties," *Journal of Biological Chemistry,* vol. 260, no. 6, pp. 3440-3450, 1985, doi: 10.1016/s0021-9258(19)83641-4.

[43] P. Taya, B. Maiti, V. Kumar, P. De, and S. Satapathi, "Design of a novel FRET based fluorescent chemosensor and their application for highly sensitive detection of nitroaromatics," *Sensors and Actuators B: Chemical,* vol. 255, pp. 2628-2634, 2018, doi: 10.1016/j.snb.2017.09.073.

[44] X. Feng, T. Zhang, J.-T. Liu, J.-Y. Miao, and B.-X. Zhao, "A new ratiometric fluorescent probe for rapid, sensitive and selective detection of endogenous hydrogen sulfide in mitochondria," *Chemical Communications,* vol. 52, no. 15, pp. 3131-3134, 2016, doi: 10.1039/c5cc09267a.

[45] J. Zhao, S. Ji, Y. Chen, H. Guo, and P. Yang, "Excited state intramolecular proton transfer (ESIPT): from principal photophysics to the development of new chromophores and applications in fluorescent molecular probes and luminescent materials," *Physical Chemistry Chemical Physics,* vol. 14, no. 25, pp. 8803-17, Jul 7 2012, doi: 10.1039/c2cp23144a.

[46] V. S. Padalkar and S. Seki, "Excited-state intramolecular proton-transfer (ESIPT)-inspired solid state emitters," *Chemical Society Reviews,* vol. 45, no. 1, pp. 169-202, Jan 7 2016, doi: 10.1039/c5cs00543d.

[47] J. E. Kwon and S. Y. Park, "Advanced organic optoelectronic materials: harnessing excited-state intramolecular proton transfer (ESIPT) process," *Advanced Materials,* vol. 23, no. 32, pp. 3615-42, Aug 23 2011, doi: 10.1002/adma.201102046.

[48] T. Quan, Z. Liang, H. Pang, G. Zeng, and T. Chen, "A ratiometric ESIPT probe based on 2-aza-Cope rearrangement for rapid and selective detection of formaldehyde in living cells," *The Analyst,* vol. 147, no. 2, pp. 252-261, 2022, doi: 10.1039/d1an01722e.

[49] Y. Chen, J. W. Y. Lam, R. T. K. Kwok, B. Liu, and B. Z. Tang, "Aggregation-induced emission: fundamental understanding and future developments," *Materials Horizons,* vol. 6, no. 3, pp. 428-433, 2019, doi: 10.1039/c8mh01331d.

[50] K. Zhang, J. Liu, Y. Zhang, J. Fan, C.-K. Wang, and L. Lin, "Theoretical Study of the Mechanism of Aggregation-Caused Quenching in Near-Infrared Thermally Activated Delayed Fluorescence Molecules: Hydrogen-Bond Effect," *The Journal of Physical Chemistry C,* vol. 123, no. 40, pp. 24705-24713, 2019, doi: 10.1021/acs.jpcc.9b06388.

[51] J. Luo, Z. Xie, J. W. Lam, L. Cheng, H. Chen, C. Qiu, H. S. Kwok, X. Zhan, Y. Liu, D. Zhu, and B. Z. Tang, "Aggregation-induced emission of 1-methyl-1,2,3,4,5-pentaphenylsilole," *Chemical Communications,* no. 18, pp. 1740-1, Sep 21 2001, doi: 10.1039/b105159h.

[52] T. Zhang, Y. Jiang, Y. Niu, D. Wang, Q. Peng, and Z. Shuai, "Aggregation effects on the optical emission of 1,1,2,3,4,5-hexaphenylsilole (HPS): a QM/MM study," *The Journal of Physical Chemistry A,* vol. 118, no. 39, pp. 9094-104, Oct 2 2014, doi: 10.1021/jp5021017.

[53] Q. Peng, Y. Yi, Z. Shuai, and J. Shao, "Toward quantitative prediction of molecular fluorescence quantum efficiency: Role of Duschinsky rotation," *Journal of the American Chemical Society,* vol. 129, no. 30, pp. 9333-9339, 2007, doi: 10.1021/JA067946E.

[54] Y. J. Gao, X. P. Chang, X. Y. Liu, Q. S. Li, G. Cui, and W. Thiel, "Excited-State Decay Paths in Tetraphenylethene Derivatives," *The Journal of Physical Chemistry A,* vol. 121, no. 13, pp. 2572-2579, Apr 6 2017, doi: 10.1021/acs.jpca.7b00197.

[55] S. Sasaki, S. Suzuki, W. M. C. Sameera, K. Igawa, K. Morokuma, and G.-I. Konishi, "Highly Twisted *N*,*N*-Dialkylamines as a Design Strategy to Tune Simple Aromatic Hydrocarbons as Steric Environment-Sensitive Fluorophores," *Journal of the American Chemical Society,* vol. 138, no. 26, pp. 8194-8206, 2016, doi: 10.1021/jacs.6b03749.

[56] H. Ma, M. Yang, C. Zhang, Y. Ma, Y. Qin, Z. Lei, L. Chang, L. Lei, T. Wang, and Y. Yang, "Aggregation-induced emission (AIE)-active fluorescent probes with multiple binding sites toward ATP sensing and live cell imaging," *Journal of Materials Chemistry B,* vol. 5, no. 43, pp. 8525-8531, 2017, doi: 10.1039/c7tb02399e.

[57] J.-C. G. Bünzli and S. V. Eliseeva, "Basics of Lanthanide Photophysics," in *Lanthanide Luminescence*, (Springer Series on Fluorescence, 2010, ch. Chapter 3, pp. 1-45.

[58] J.-C. G. Bünzli, "Lanthanide Luminescence for Biomedical Analyses and Imaging," *Chemical Reviews,* vol. 110, no. 5, pp. 2729-2755, 2010, doi: 10.1021/cr900362e.

[59] M. Hasegawa, H. Ohmagari, H. Tanaka, and K. Machida, "Luminescence of lanthanide complexes: From fundamental to prospective approaches related to water- and molecular-stimuli," *Journal of Photochemistry and Photobiology C: Photochemistry Reviews,* vol. 50, 2022, doi: 10.1016/j.jphotochemrev.2022.100484.

[60] E. G. Moore, A. P. S. Samuel, and K. N. Raymond, "From Antenna to Assay: Lessons Learned in Lanthanide Luminescence," *Accounts of Chemical Research,* vol. 42, no. 4, pp. 542-552, 2009, doi: 10.1021/ar800211j.

[61] B. Alpha, R. Ballardini, V. Balzani, J. M. Lehn, S. Perathoner, and N. Sabbatini, "ANTENNA EFFECT IN LUMINESCENT LANTHANIDE CRYPTATES: A PHOTOPHYSICAL STUDY," *Photochemistry and Photobiology,* vol. 52, no. 2, pp. 299-306, 1990, doi: 10.1111/j.1751-1097.1990.tb04185.x.

[62] N. C. Martinez-Gomez, H. N. Vu, and E. Skovran, "Lanthanide Chemistry: From Coordination in Chemical Complexes Shaping Our Technology to Coordination in Enzymes Shaping Bacterial Metabolism," *Inorganic Chemistry,* vol. 55, no. 20, pp. 10083-10089, 2016, doi: 10.1021/acs.inorgchem.6b00919.

[63] S. A. Cotton, "Establishing coordination numbers for the lanthanides in simple complexes," *Comptes Rendus. Chimie,* vol. 8, no. 2, pp. 129-145, 2005, doi: 10.1016/j.crci.2004.07.002.

[64] T. J. Clough, L. Jiang, K. L. Wong, and N. J. Long, "Ligand design strategies to increase stability of gadolinium-based magnetic resonance imaging contrast agents," *Nature Communications,* vol. 10, no. 1, p. 1420, Mar 29 2019, doi: 10.1038/s41467-019-09342-3.

[65] J. Ciupka, X. Cao-Dolg, J. Wiebke, and M. Dolg, "Computational study of lanthanide(iii) hydration," *Physical Chemistry Chemical Physics,* vol. 12, no. 40, p. 13215, 2010, doi: 10.1039/c0cp00639d.

[66] W. W. Rudolph and G. Irmer, "On the Hydration of the Rare Earth Ions in Aqueous Solution," *Journal of Solution Chemistry,* vol. 49, no. 3, pp. 316-331, 2020, doi: 10.1007/s10953-020-00960-w.

[67] R. M. Supkowski and W. D. Horrocks, "On the determination of the number of water molecules, q, coordinated to europium(III) ions in solution from luminescence decay lifetimes," *Inorganica Chimica Acta,* vol. 340, pp. 44-48, 2002, doi: 10.1016/s0020-1693(02)01022-8.

[68] A. Beeby, I. M. Clarkson, R. S. Dickins, S. Faulkner, D. Parker, L. Royle, A. S. De Sousa, J. A. G. Williams, and M. Woods, "Non-radiative deactivation of the excited states of europium, terbium and ytterbium complexes by proximate energy-matched OH, NH and CH oscillators: an improved luminescence method for establishing solution hydration states," *Journal of the Chemical Society, Perkin Transactions 2,* no. 3, pp. 493-504, 1999, doi: 10.1039/a808692c.

[69] E. Pershagen and K. E. Borbas, "Designing reactivity-based responsive lanthanide probes for multicolor detection in biological systems," *Coordination Chemistry Reviews,* vol. 273-274, pp. 30-46, 2014, doi: 10.1016/j.ccr.2013.10.012.

[70] X. Wang, H. Chang, J. Xie, B. Zhao, B. Liu, S. Xu, W. Pei, N. Ren, L. Huang, and W. Huang, "Recent developments in lanthanide-based luminescent probes," *Coordination Chemistry Reviews,* vol. 273-274, pp. 201-212, 2014, doi: 10.1016/j.ccr.2014.02.001.

[71] A. R. Lippert, T. Gschneidtner, and C. J. Chang, "Lanthanide-based luminescent probes for selective time-gated detection of hydrogen peroxide in water and in living cells," *Chemical Communications,* vol. 46, no. 40, p. 7510, 2010, doi: 10.1039/c0cc01560a.

[72] V. P. B. Grover, J. M. Tognarelli, M. M. E. Crossey, I. J. Cox, S. D. Taylor-Robinson, and M. J. W. McPhail, "Magnetic Resonance Imaging: Principles and Techniques: Lessons for Clinicians," *Journal of Clinical and Experimental Hepatology,* vol. 5, no. 3, pp. 246-255, 2015, doi: 10.1016/j.jceh.2015.08.001.

[73] S. Faulkner and O. A. Blackburn, "The Chemistry of Lanthanide MRI Contrast Agents," in *The Chemistry of Molecular Imaging*, N. J. Long and W. T. Wong Eds.: John Wiley & Sons, Inc, 2014, ch. 8, pp. 179-197.

[74] É. Tóth, L. Helm, and A. E. Merbach, "Relaxivity of MRI Contrast Agents," Springer Berlin Heidelberg, 2002, pp. 61-101.

[75] K. N. Raymond and V. C. Pierre, "Next Generation, High Relaxivity Gadolinium MRI Agents," *Bioconjugate Chemistry,* vol. 16, no. 1, pp. 3-8, 2005, doi: 10.1021/bc049817y.

[76] Q. Meng, M. Wu, Z. Shang, Z. Zhang, and R. Zhang, "Responsive gadolinium(III) complex-based small molecule magnetic resonance imaging probes: Design, mechanism and application," *Coordination Chemistry Reviews,* vol. 457, 2022, doi: 10.1016/j.ccr.2021.214398.

[77] J. Lux and A. D. Sherry, "Advances in gadolinium-based MRI contrast agent designs for monitoring biological processes in vivo," *Current Opinion in Chemical Biology,* vol. 45, pp. 121-130, 2018, doi: 10.1016/j.cbpa.2018.04.006.

[78] P. Caravan, C. T. Farrar, L. Frullano, and R. Uppal, "Influence of molecular parameters and increasing magnetic field strength on relaxivity of gadolinium- and manganese-based T1 contrast agents," *Contrast Media Mol Imaging,* vol. 4, no. 2, pp. 89-100, Mar-Apr 2009, doi: 10.1002/cmmi.267.

[79] A. D. Sherry and Y. Wu, "The importance of water exchange rates in the design of responsive agents for MRI," *Current Opinion in Chemical Biology,* vol. 17, no. 2, pp. 167-174, 2013, doi: 10.1016/j.cbpa.2012.12.012.

[80] P. Caravan, D. Esteban-Gómez, A. Rodríguez-Rodríguez, and C. Platas-Iglesias, "Water exchange in lanthanide complexes for MRI applications. Lessons learned over the last 25 years," *Dalton Transactions,* vol. 48, no. 30, pp. 11161-11180, 2019, doi: 10.1039/c9dt01948k.

Chapter 2: Fluorescent probe for discrimination of oxidation states of palladium

2.1 Introduction

Palladium is one of the rare transition metals that have often been used in chemistry. Palladium-catalysed reactions are crucial in the field of organic synthesis.[1, 2] Palladium-based catalysts can provide a much shorter route towards the desired product. The high activity of the catalyst enables the reaction of less reactive groups or triggers the reaction at lower temperatures.[3, 4] With a shorter synthetic route, fewer side products are formed, and manufacturing cost can be reduced. Therefore, some well-known Pd-catalysed cross-coupling reactions, such as Heck reaction, Suzuki reaction, Sonogashira coupling, Fukuyama coupling, Stille reaction, Hiyama coupling and Buchwald-Hartwig amination, are commonly utilized by pharmaceutical companies to perform drug synthesis.[2, 5-8] However, the metal contamination problem must be considered when using these palladium-catalysed reactions. Palladium residue in human body is highly toxic. Palladium complexes may form with biomacromolecules such as amino acids (e.g. L-methionine and L-cysteine), proteins (e.g., casein, silk fibroin), DNA, RNA and other macromolecules (e.g. vitamin B6).[9-12] The palladium content in pharmaceutical products is regulated at 5-10 ppm and the suggested dietary intake of palladium should not exceed 1.5-15 μg per person per day.[13, 14] It is important to detect and quantify palladium ion levels in pharmaceutical products.

The current palladium sensing methods include atomic absorption spectroscopy (AAS), X-ray fluorescence, and plasma emission methods (ICP-MS and ICP-AES). All of them are extremely sensitive to the matrix of the sample and susceptible to spectral interference. Other disadvantages

include large and costly of instruments required, highly trained personnel needed to operate these instruments, instruments can be easily cross-contaminated and serious sample preparation steps that are needed.[15] A fluorescent method is more desirable because the measurement requires spectrofluorometer which is significantly less expensive instrument. Fluorescent probe sensing methods have several advantages such as low operational costs and simple sample preparation steps. Also, these methods are not easily cross-contaminated because disposable cuvettes will be used to test the samples (~1 USD/ cuvette; 340-800 nm).[16] Moreover, small-molecule based fluorescent probes are often used as metal sensor.[17-19] Although many novel structures with improved properties sensors have been developed, it is still a highly active research field in recent years.

For the reaction-based fluorescent probes for palladium ion detection, there are mainly five detection mechanisms for palladium sensing, including deallylation, depropargylation, hydrolysis, Claisen rearrangement, and oxidative cyclization, which share common feature.[20] In detail, an electron-withdrawing group is bonded to the donor receptor of the probe in the initial state. During the sensing reaction, the electron-withdrawing group reacts, allowing charge transfer to the fluorophore to give fluorescence.

The first type of reaction-based probe is deallylation probes. In this mechanism, palladium is first attached to allyl sensing group and undergoes a palladium-catalysed allyl ether cleavage reaction to cleave the electron withdrawing group. After the deallylation, the charge restores to the dye resulting in a fluorescence enhancement (Figure 2.1).[21]

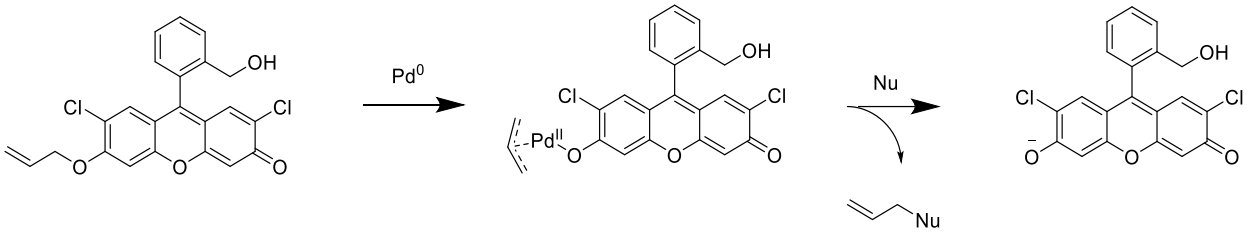

Figure 2.1: Example and sensing mechanism of deallylation-based fluorescent probe.

The second type of reaction-based sensor probe for palladium detection is depropargylation-based probe. A propargyl group is used in the terminal position of this type of probe. The propargyl group reacts with palladium ions in four ways to produce a highly fluorescent compound, including hydration of propargyl ether to form internal or terminal carbonyl compounds,[22] 5-oxazolecarbaldehyde formation by intramolecular Pd^{2+}-catalysed cyclisation of propargylamine,[23] formation of propane by hydrogenation of propyne in the presence of Pd on TiO_2 support[24] and formation of alcohol or amine by C-X bond cleavage and nucleophilic attack of allylpalladium intermediate.[25] For example, in hydration of propargyl ether mechanism, similar to deallylation reaction, Pd^{2+} ions are first attached to the propargyl group. After the hydration process to form a carbonyl group, the sensing group undergoes a palladium-catalysed cleavage reaction to restore the charge to the dye and give fluorescence enhancement (Figure 2.2).

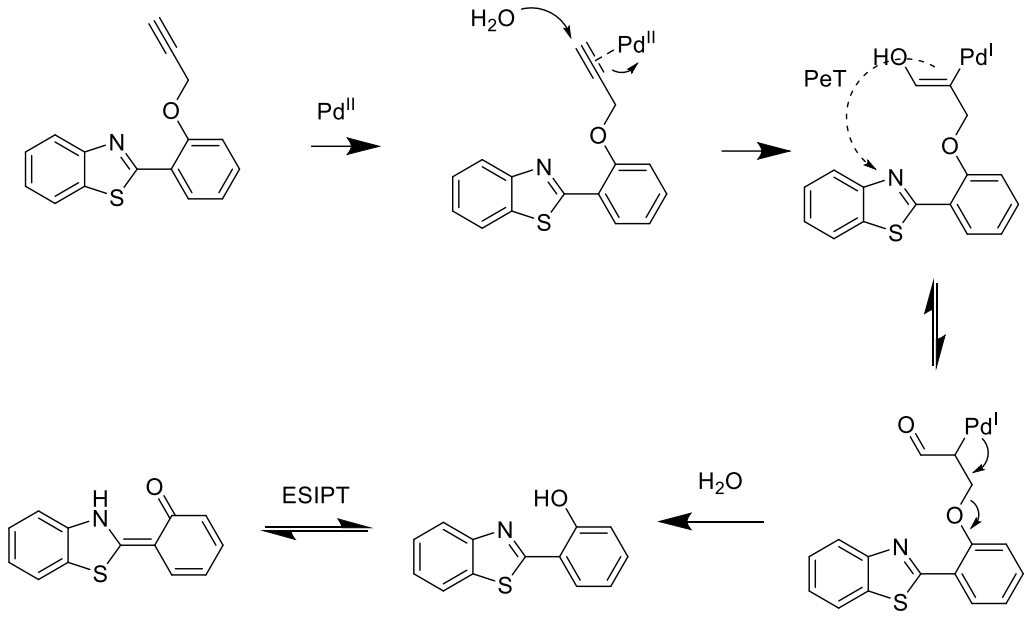

Figure 2.2: Example and sensing mechanism of depropargylation-based fluorescent probe.

The third type of reaction-based sensor is the hydrolysis-based fluorescent probe. In this type of sensing probe, the probe is coordinated with Pd^{2+} ion, then reacts with water and undergoes hydrolysis.[26] This process helps open the spirolactam ring to produce high fluorescence. With the properties of spiro-lactam framework and good photochemical ability, the probes demonstrate a fast response time and a good limit of detection (Figure 2.3).

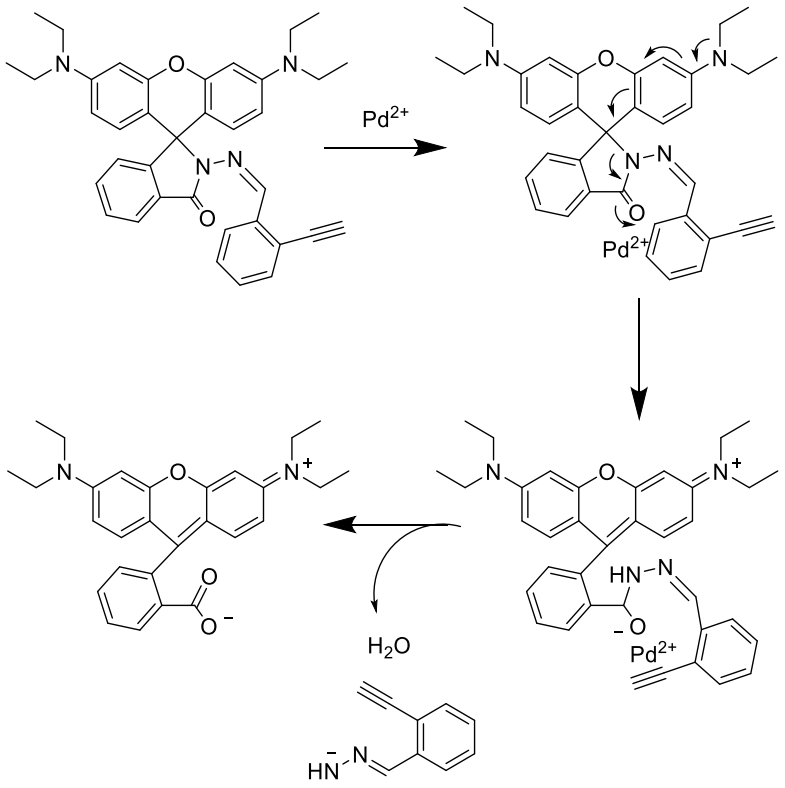

Figure 2.3: Example and sensing mechanism of hydrolysis-based fluorescent probe.

The fourth type of reaction-based sensor utilizes Claisen rearrangement. The probes undergo Claisen rearrangement in the presence of Pd^{2+} and Pd^{4+} to obtain fluorescence enhancement (Figure 2.4).[27] However, these types of probes have a major disadvantage that a high pH (pH 10) and high temperature (50 °C) are needed in the reaction. Therefore, there are limited bio-application with this probe.

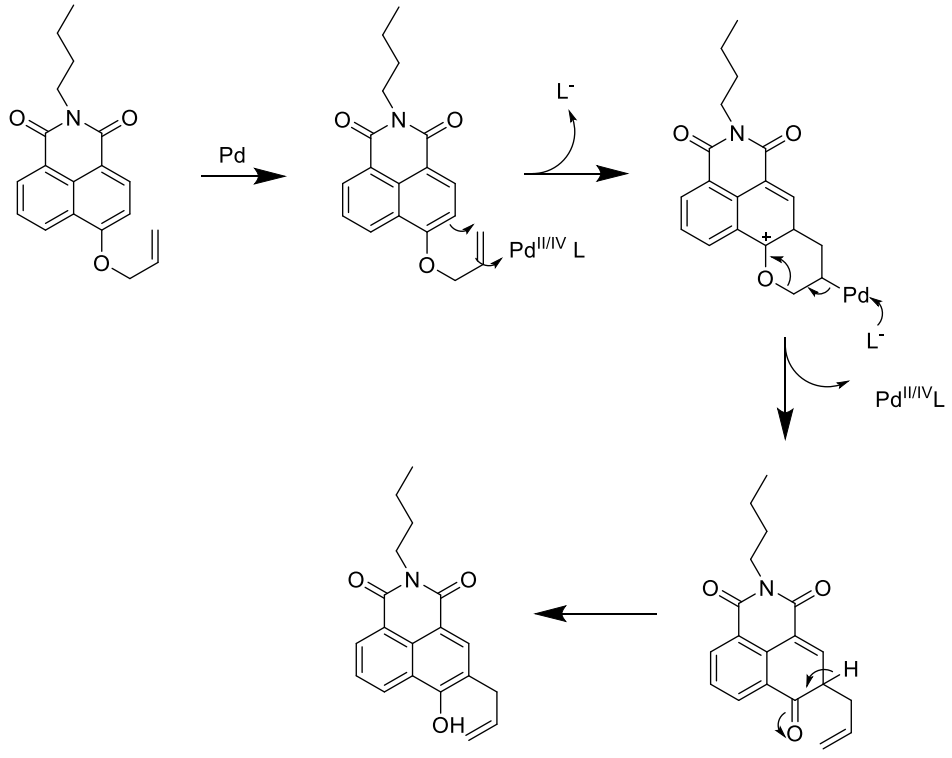

Figure 2.4: Example and sensing mechanism of Claisen rearrangement-based fluorescent probe.

The fifth type of reaction is the oxidative cyclization reaction-based probe. This type of probe utilizes the oxidative insertion of Pd^0 to form a Pd intermediate. [28] The iodophenylspirolactam derivative of rhodamine B then undergoes a Pd-catalysed ring-opening to produce high fluorescence (Figure 2.5).

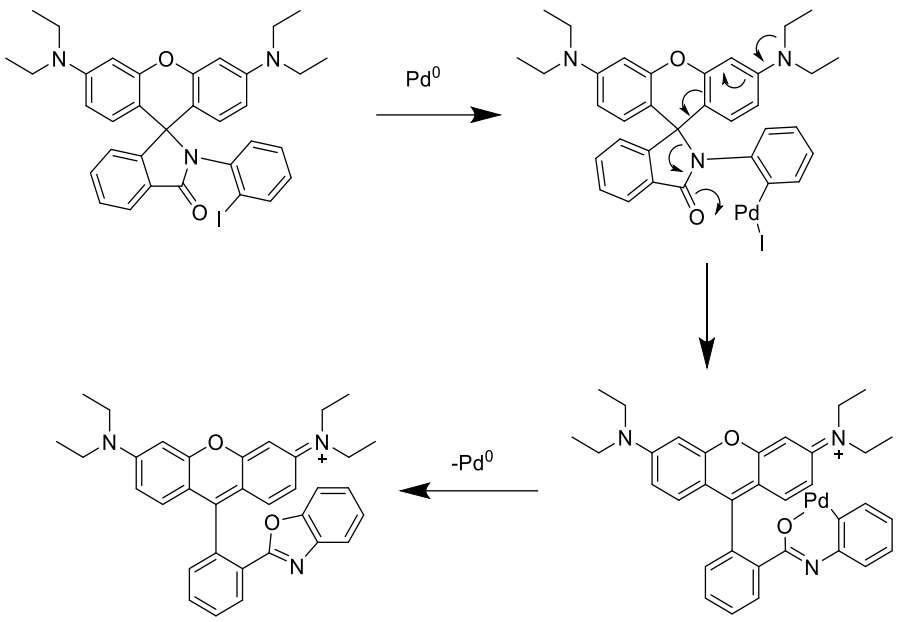

Figure 2.5: Example and sensing mechanism of oxidative cyclization reaction-based fluorescent probe.

2.2 Scope of study

To the best of our knowledge, most of the reported palladium ion sensing probes cannot discriminate between different oxidation states of palladium (i.e., Pd^0, Pd^{2+}), and both oxidation forms of palladium could remain and cause palladium contamination in pharmaceutical drugs. Since the purification methods for removing Pd^0 and Pd^{2+} are different, it is necessary to identify the correct oxidation state of Pd in order to select the appropriate purification method. Therefore, in this chapter, we design a novel fluorescent probe (PPIX-L2) for discriminating Pd^0 and Pd^{2+}. The probe is mainly constructed from two parts: coumarin and PPIX moieties. The coumarin moiety utilizes the deallylation mechanism for Pd^0 sensing, while the PPIX moiety utilizes the heavy metal quenching property for Pd^{2+} sensing. The photophysical studies are conducted to investigate the discriminating ability for Pd^0 and Pd^{2+} (Figure 2.6).

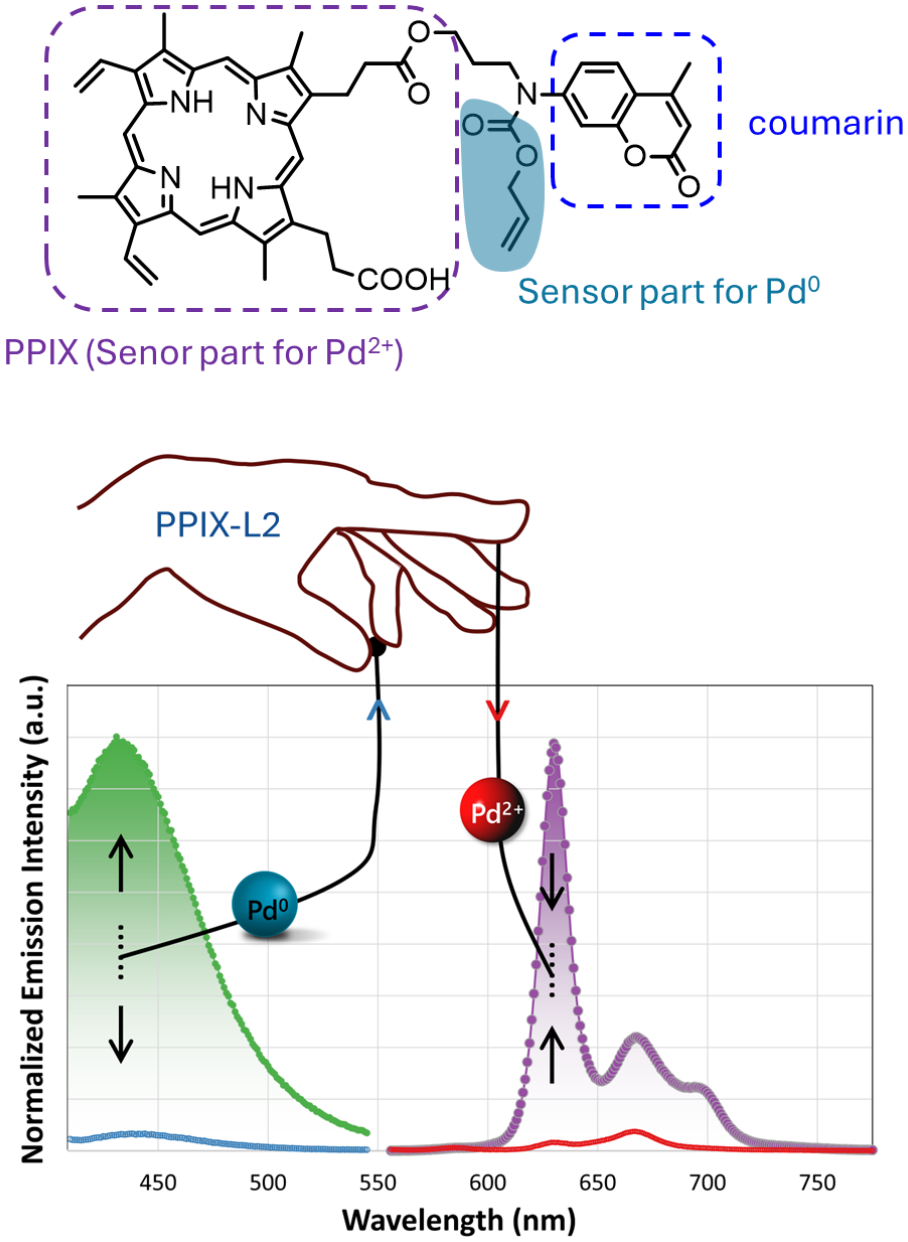

Figure 2.6: Design of PPIX-L2.[29]

2.3 Results and discussion

2.3.1 Synthetic work (Route 1)

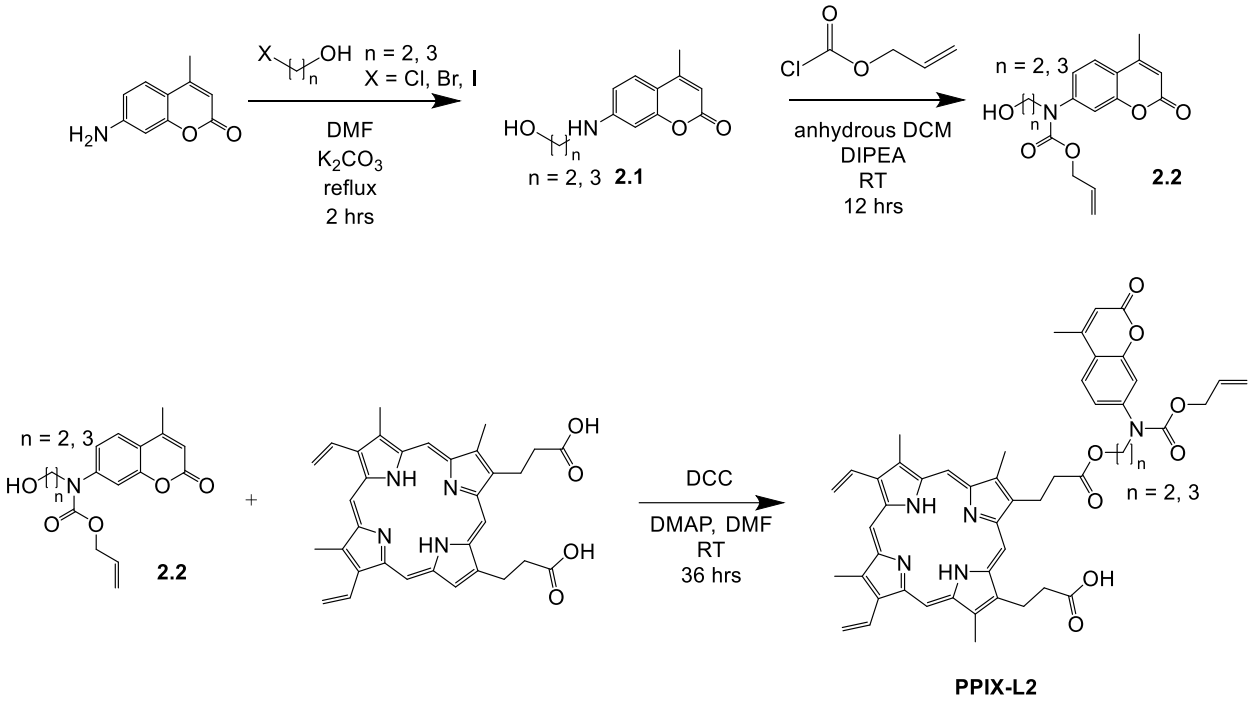

Scheme 2.1: Synthetic route 1 for PPIX-L2.

The porphyrin-coumarin fluorescent probe (PPIX-L2) was designed to be synthesized through two routes. Route 1 was a more straightforward synthetic route without using any protecting groups on the hydroxyl group. (Scheme 2.1) It was initially planned to have an alkylation on the amine part of the 7-amino-4-methylcoumarin with an alcohol halide. In the first step, alcohol halide such as 2-chloroethanol, 2-bromoethanol, 2-iodoethanol and 3-bromo-1-propanol were chosen as the candidates for alkylation (Figure 2.7). By using the chosen alcohol halide, the halogen reactivity and length of carbon chain were tested to optimize the production yield of intermediate 2.1. It was shown that bromide had better reactivity than chloride and had similar reactivity with iodide. Also,

a three-carbon chain alcohol had a better reactivity than two-carbon chain due to the decreased electron donating effect from the hydroxyl group. The amine group of 7-amino-4-methylcoumarin can perform nucleophilic attack on α-carbon atom more readily as the α-carbon atom was less electron-rich in three-carbon chain alcohol. (Table 2.1)

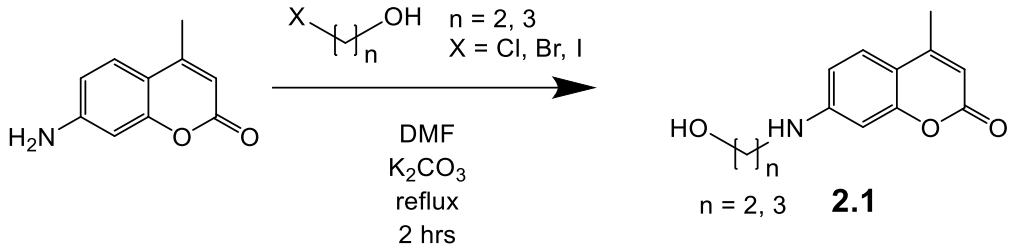

Figure 2.7: Reaction conditions for synthesis of compound 2.1.

Table 2.1: Entries of different alcohol halides in the first step of synthetic route.

Entry	Alcohol Halide	Yield %
1	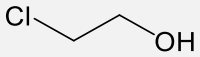	13%
2	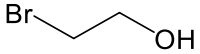	15%
3	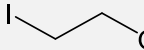	15%
4	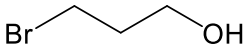	19%

In the second step, the amine group of compound 2.1a was planned to react with allyl chloroformate to afford compound 2.2a. However, the hydroxyl group of compound 2.1a preferentially performed nucleophilic attack on allyl chloroformate to produce compound 2.2b (Figure 2.8). This result may be due to the steric hindrance occurring around the secondary amine

group of compound 2.2b. From the NMR spectra of compound 2.2b (Figure 2.9, bottom), the 2H on benzene ring (δ 6.55 - 6.46) did not shift much compared to compound 2.1a (Figure 2.9, top). If compound 2.2a had been synthesized successfully, the two phenyl H peaks should have moved to downfield slightly due to the reduced electron density caused by the carbonyl group. Therefore, route 1 for synthesizing PPIX-L2 was unsuccessful. A protecting group for hydroxyl group was needed before the reaction with allyl chloroformate to avoid production of compound 2.2b.

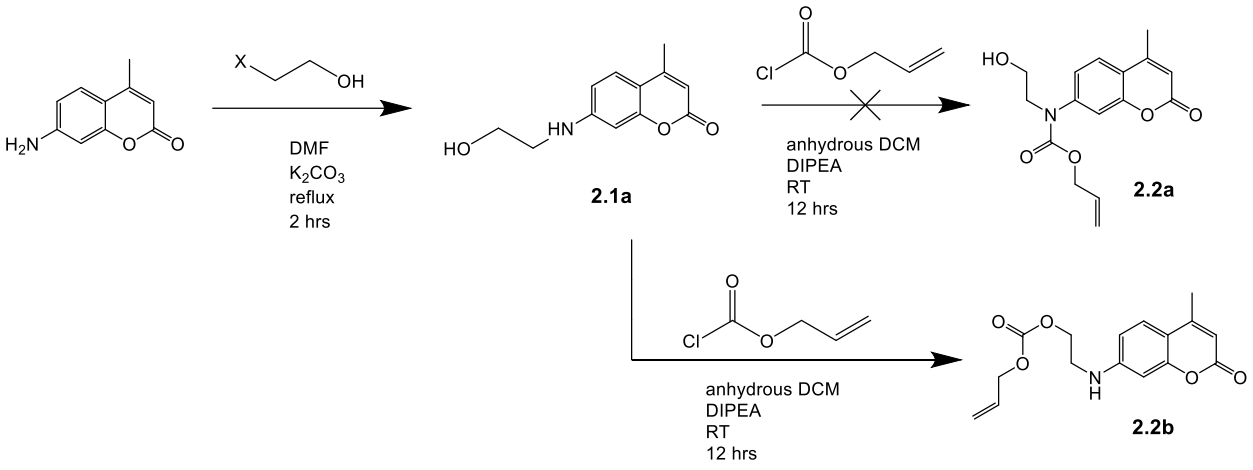

Figure 2.8: Side product compound 1.2b formed in the second step.

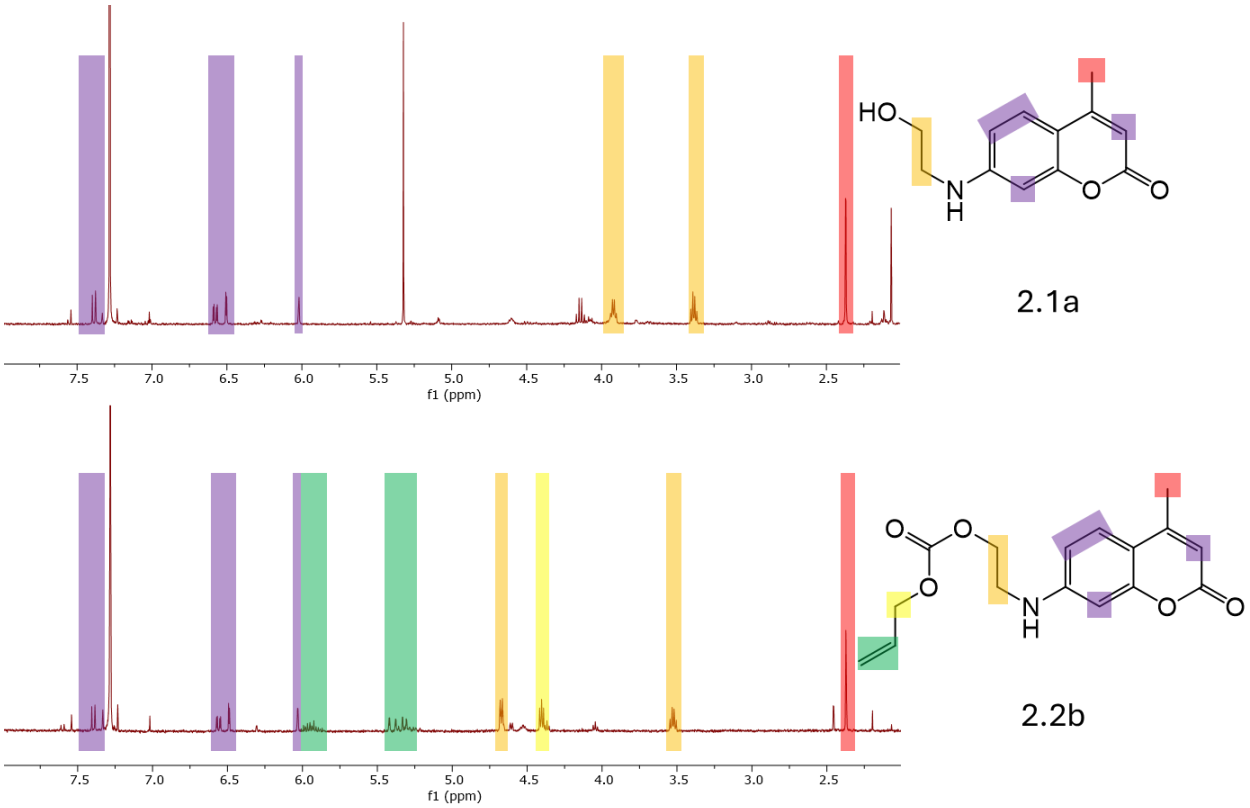

Figure 2.9: (top) Chemical structure and NMR spectra of compound 2.1a. (bottom) Chemical structure and NMR spectra of compound 2.2b. Colour bars represent the ^{1}H NMR peak assignment of the compounds.

2.3.2 Synthetic work (Route 2)

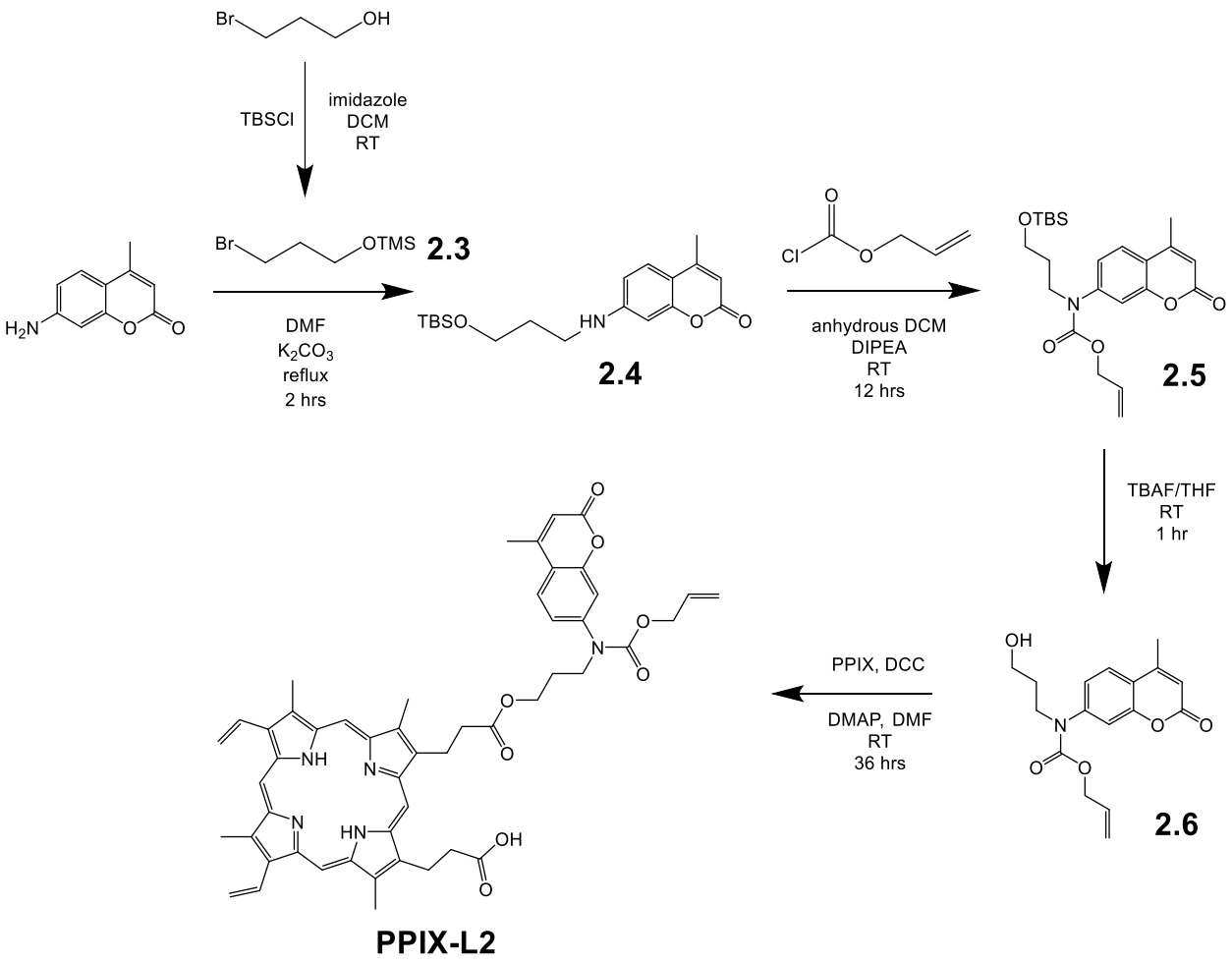

Scheme 2.2: Synthetic route 2 for PPIX-L2.

Due to the production of a side product in Route 1 step 2, it is necessary to protect the reactive hydroxyl group before the reaction with allyl chloroformate. In Route 2, tert-butyldimethylsilyl (TBS) group was considered to mask the hydroxyl group prior to the alkylation reaction of the amine group in 7-amino-4-methylcoumarin. In the choice of alcohol halide, 3-bromo-1-propanol was shown to be the better candidate in the test from Route 1 step 1. Therefore 3-bromo-1-propanol was chosen to be the starting material in Route 2. In step 1, the hydroxyl group of 3-bromo-1-

propanol was protected by tert-butyldimethylsilyl (TBS) group by reacting with tert-butyldimethylsilyl chloride to form (3-bromopropoxy)(tert-butyl)dimethylsilane (compound 2.3). Then, compound 2.3 was used to perform alkylation reaction with 7-amino-4- methylcoumarin to produce compound 2.4. After compound 2.4 reacted with allyl chloroformate, the starting material (compound 2.3) was completely converted, yielding a non-fluorescent compound 2.5 successfully without any observed side products. The TBS group on compound 2.5 was removed by tetra-n-butylammonium fluoride (TBAF) to form compound 2.6. In the last step, the carboxylic acid of protoporphyrin IX (PPIX) was first activated by a mild coupling agent and catalyst, N,N'-Dicyclohexylcarbodiimide (DCC) and 4-dimethylaminopyridine (DMAP), respectively, and underwent esterification with compound 2.6 to yield the final product, PPIX-L2. (Scheme 2.2)

2.3.3 Photophysical measurements and fluorescence titration experiment

Fluorescence response of PPIX-L2 to Pd^0 and Pd^{2+}:

To study the fluorescence response of PPIX-L2 towards Pd^0, $Pd(PPh_3)_4$ was used as the Pd^0 source for fluorescence titration with PPIX-L2. Nitrogen bubbling was applied to the solution throughout the titration to avoid the oxidation of Pd^0 during the measurement. PPIX-L2 was first dissolved in MeOH. After the addition of Pd^0 to the solution, PPIX-L2 underwent Pd^0-catalyzed Tsuji–Trost reaction. The coumarin fluorescence signal centred at 440 nm and the absorbance signal centre at 353 nm gradually increased (Figure 2.10 – 2.12). From the bar chart, PPIX-L2 displayed a time-dependent response and had a quick response to Pd^0. There was a 1.5-fold fluorescence increase in emission intensity right after the addition of Pd^0. Then, the fluorescence signal demonstrated a significant growth over three hours and slight rise in the fourth hour. The signal reached saturation

with a total of 24-fold increase in fluorescence intensity after four hours (Figure 2.13). To verify the Pd^0-catalyzed Tsuji–Trost reaction between Pd^0 and PPIX-L2 (Figure 2.14 top), a MALDI-TOF mass analysis was performed after the reaction was completed. The mass spectrum showed the expected mass of PPIX-L0 (calculated $[M+H]^+$ = 778.36, found $[M+H]^+$ = 778.443) which confirmed the Pd^0-catalyzed Tsuji–Trost reaction mechanism (Figure 2.14 bottom). Metal selectivity experiment was done by titrating other metal ions with PPIX-L2. There were no obvious changes in fluorescence signal after four hours of titration (Figure 2.15).

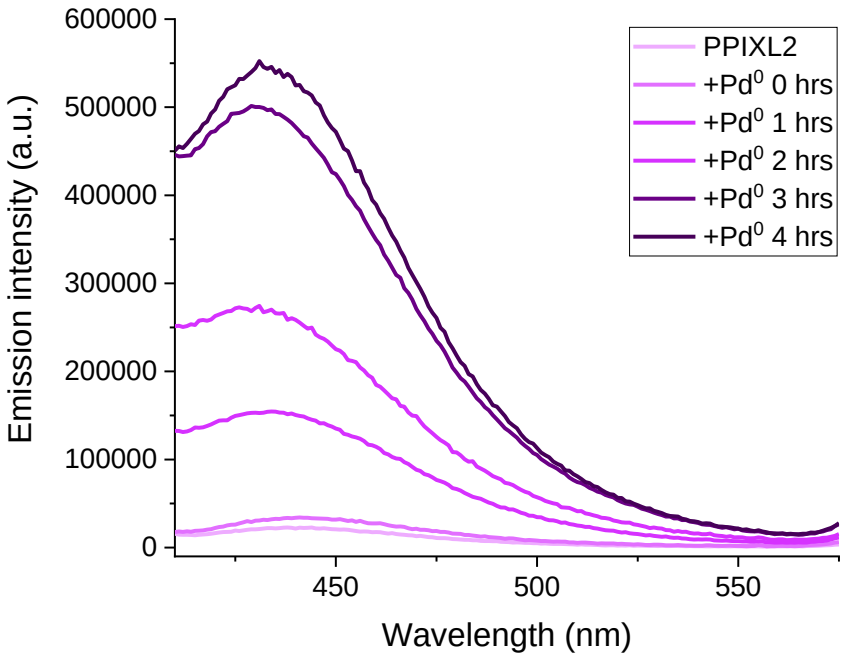

Figure 2.10: Time-dependent fluorescence titration of 2 μM PPIX-L2 in MeOH to 10 μM of Pd^0. λex: 361 nm, slit: 5-5 nm.

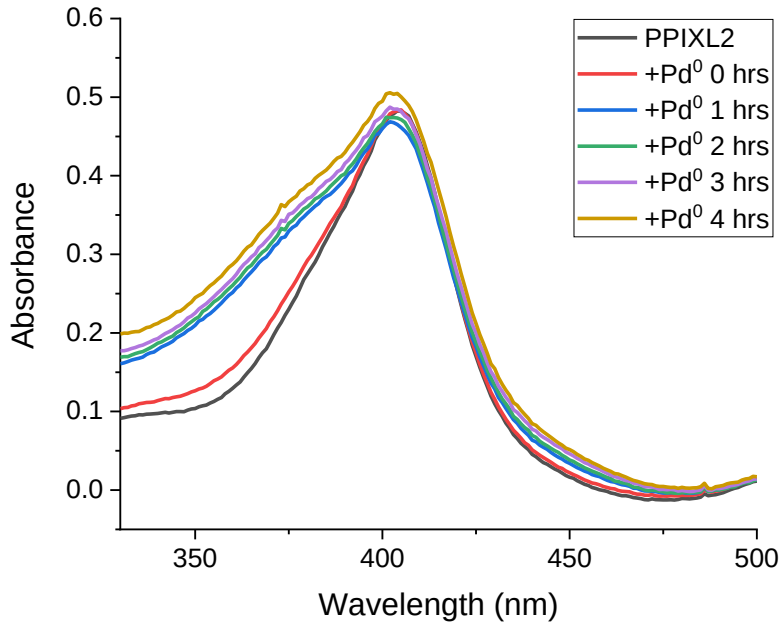

Figure 2.11: Time-dependent absorption titration of 5 μM PPIX-L2 in MeOH to 10 μM of Pd^0.

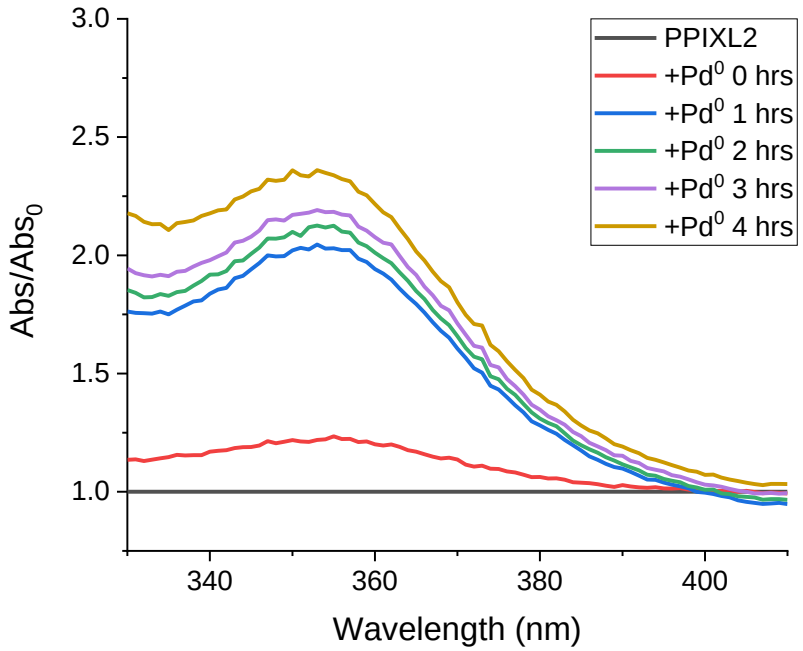

Figure 2.12: Abs/Abs_0 vs wavelength spectra of 5 μM PPIX-L2 in MeOH to 10 μM of Pd^0. Time points represent 0, 1, 2, 3, and 4 hours after the addition of Pd^0.

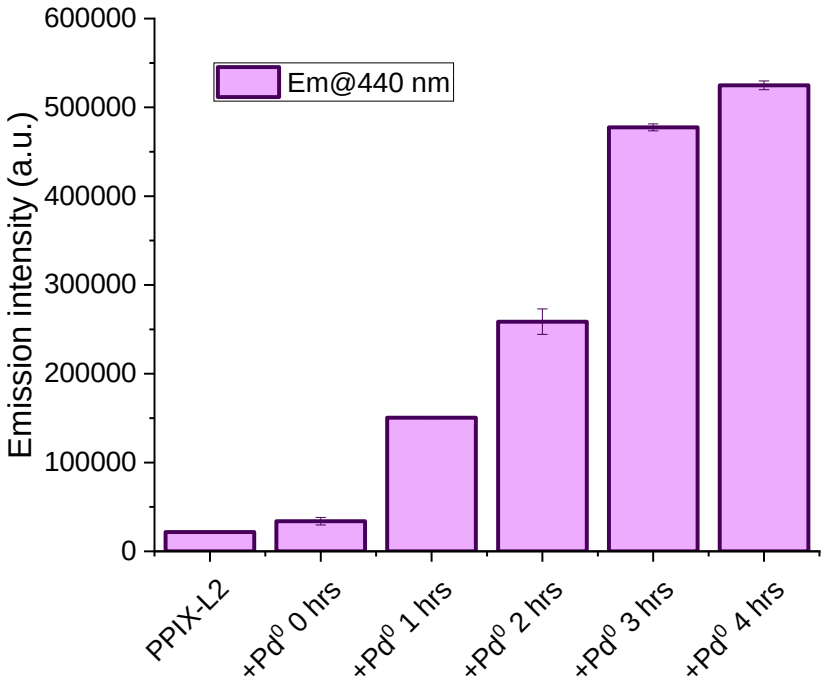

Figure 2.13: Time-dependent fluorescence intensity of coumarin at 440 nm for 2 μM PPIX-L2 in MeOH to 10 μM of Pd^0. λex: 361 nm, slit: 5-5 nm.

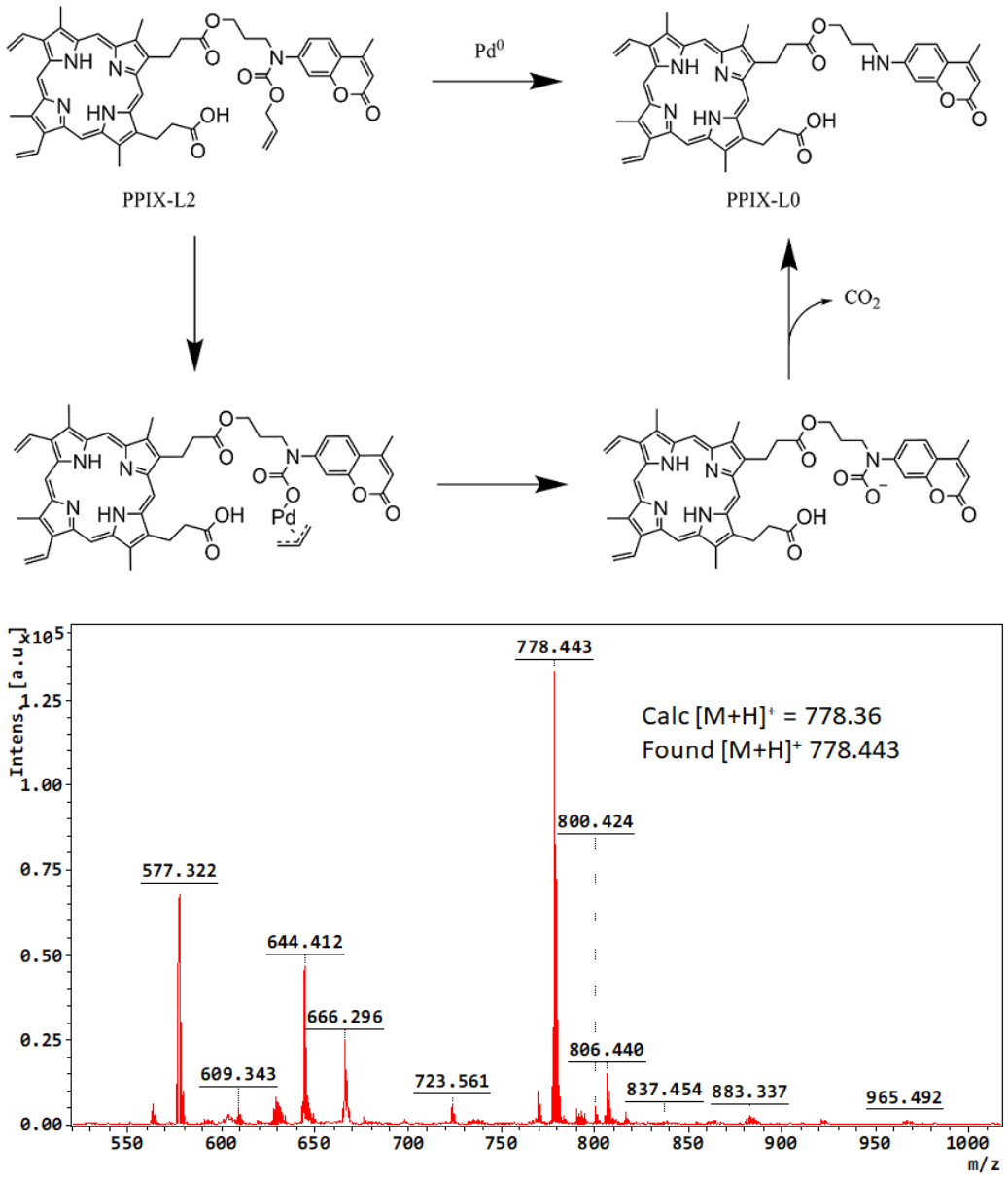

Figure 2.14: (top) A proposed Tsuji-Trost reaction mechanism for Pd^0 detection by PPIX-L2. (bottom) MALDI-TOF mass spectrum of 5 equivalents of Pd^0 added to 2 μM PPIX-L2 in MeOH to form PPIX-L0.

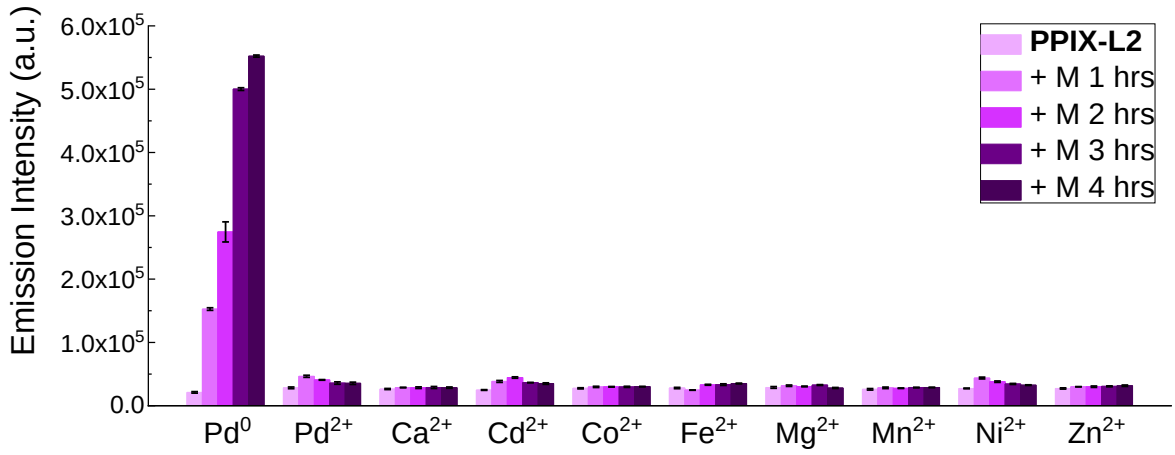

Figure 2.15: Fluorescence metal selectivity experiment of 2 μM PPIX-L2 in MeOH to 10 μM of different metals (M). The y-axis represents the coumarin fluorescence intensity of PPIX-L2 at 440 nm. λex: 361 nm, slit: 5-5 nm.

To study the fluorescence response of PPIX-L2 towards Pd^{2+}, $PdCl_2$ was used as the Pd^{2+} source for fluorescence titration experiment. After the addition of Pd^{2+} to the solution of PPIX-L2, the fluorescence intensity of porphyrin plunged while there was no effect on the coumarin emission (Figure 2.16). From the bar chart, the decrease in fluorescence was determined to be time-dependent (Figure 2.17). Porphyrin fluorescence was reduced by 81% right after addition of Pd^{2+} and reached complete at the time point of one hour with almost all porphyrin emission being quenched. To further investigate the fast fluorescence response of porphyrin in the first hour, an additional fluorescence titration experiment was performed. Most porphyrin fluorescence was quenched in first 10 minutes, confirming the fast and efficient detection of Pd^{2+} ion using PPIX-L2 (Figure 2.18). In the metal selectivity experiment, the coordination interaction of porphyrin toward Pd^{2+} was compared with other divalent metal cation and Pd^{0} ions. It was found that other tested metal ions produced much smaller or even no quenching effect towards porphyrin

fluorescence (Figure 2.19). As the porphyrin core may act as cavity of other metal ions, metal competition experiment was conducted. PPIX-L2 was first treated with other metal ions followed by addition of Pd^{2+} ions. It was found that there was a fast and significance decrease of porphyrin emission which demonstrate Pd^{2+} could displace other metals from the porphyrin cavity (Figure 2.20).

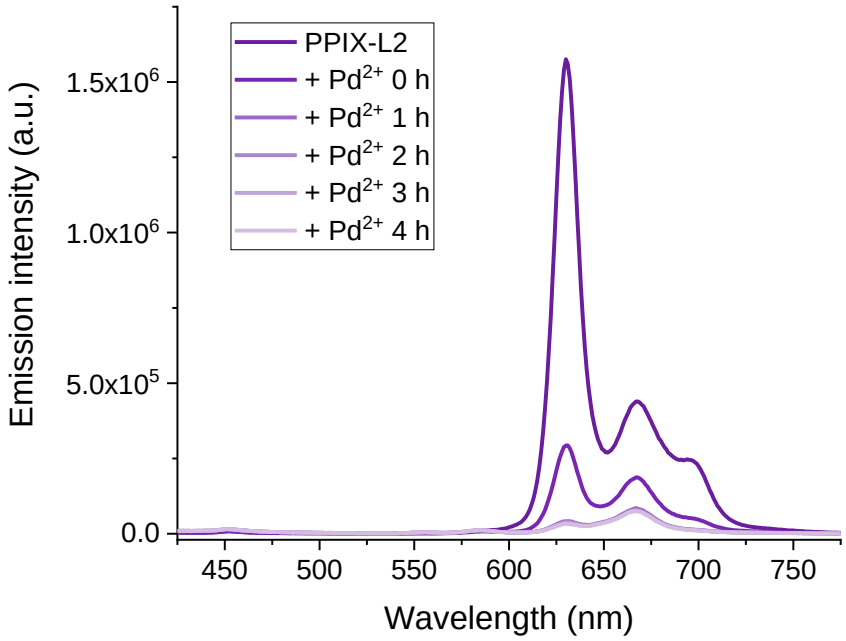

Figure 2.16: Time-dependent fluorescence titration of 2 μM PPIX-L2 in MeOH to 10 μM of Pd^{2+}. λex: 400 nm, slit: 5-5 nm.

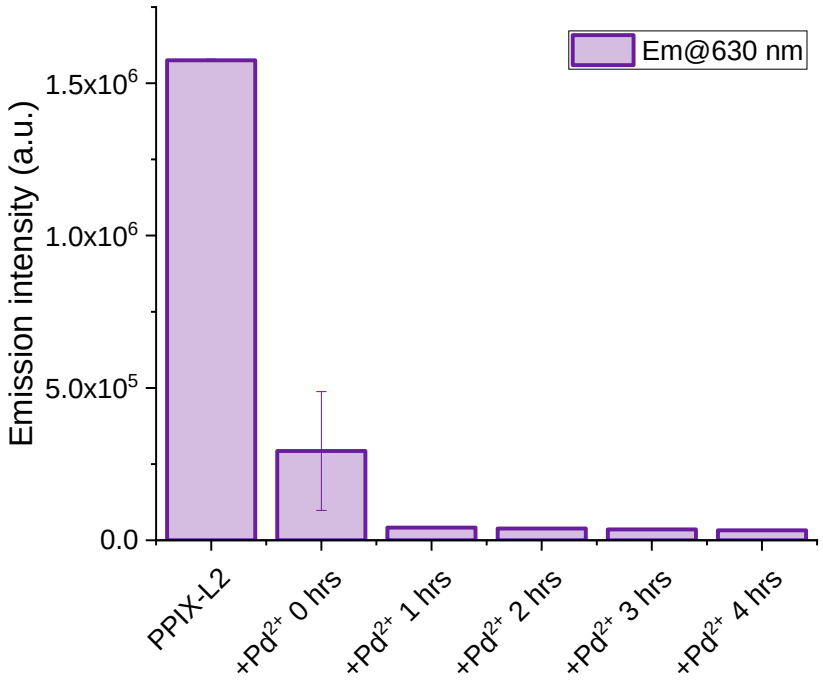

Figure 2.17: Time-dependent fluorescence intensity of porphyrin at 630 nm for 2 μM PPIX-L2 in MeOH to 10 μM of Pd^{2+}. λex: 400 nm, slit: 5-5 nm.

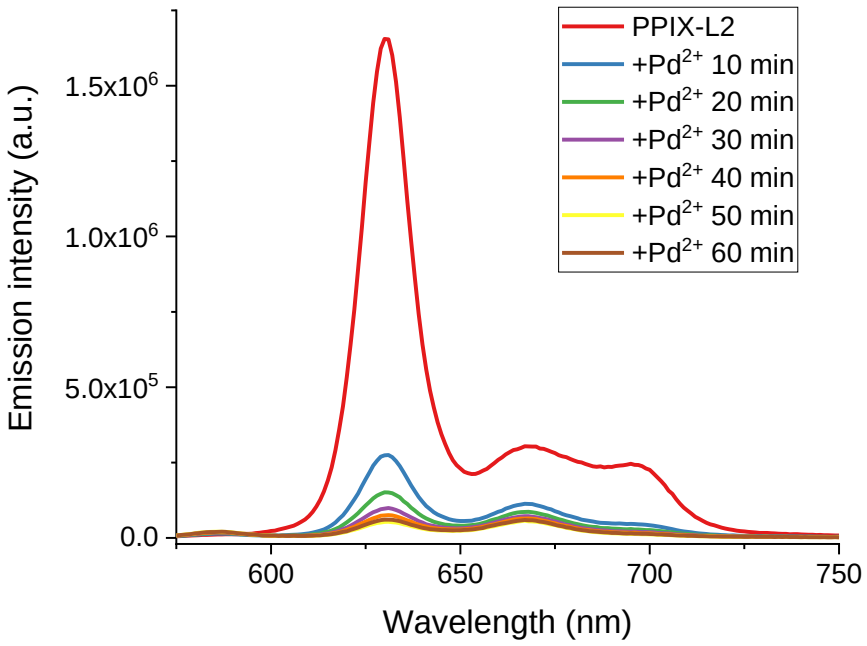

Figure 2.18: Time-dependent porphyrin fluorescence spectra of 2 μM PPIX-L2 in MeOH to 10 μM of Pd^{2+} within the first hour. λex: 400 nm, slit: 5-5 nm.

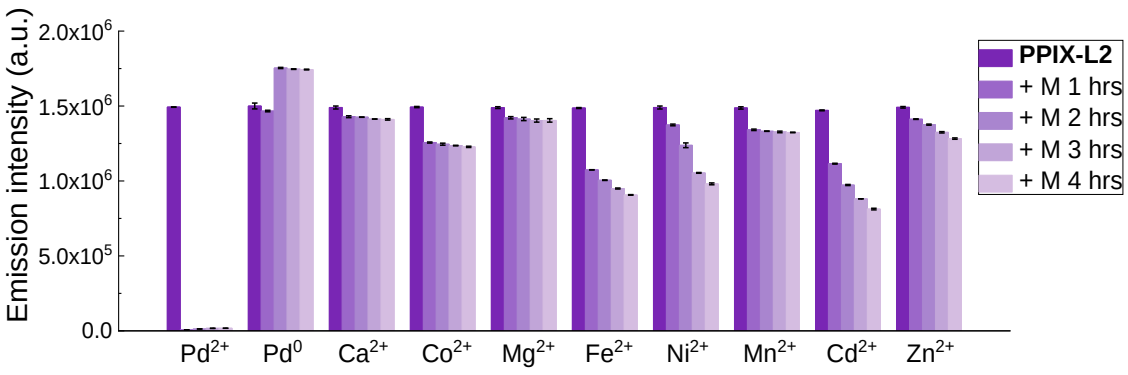

Figure 2.19: Fluorescence metal selectivity experiment of 2 µM PPIX-L2 in MeOH to 10 µM of different metal (M). The y-axis represents the porphyrin fluorescence intensity of PPIX-L2 at 630 nm. λex: 400 nm, slit: 5-5 nm.

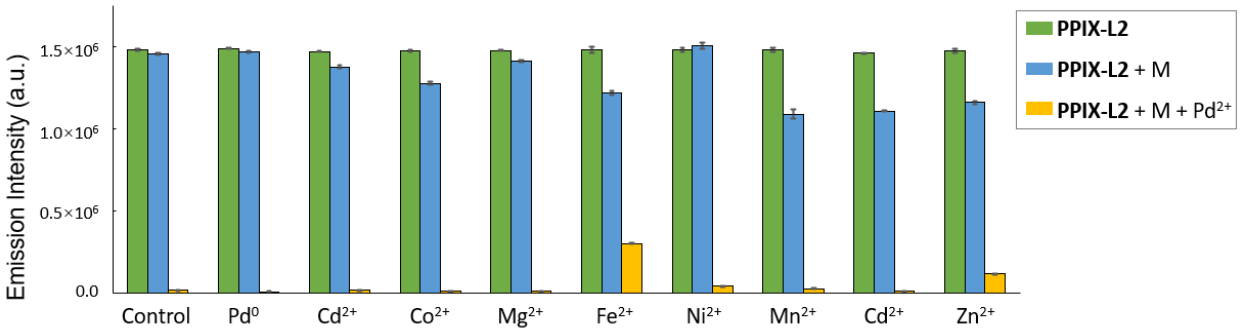

Figure 2.20: Fluorescence metal competition experiment of 2 µM PPIX-L2 in MeOH to 10 µM of Pd^{2+} and different metal (M). The y-axis represents the porphyrin fluorescence intensity of PPIX-L2 at 630 nm and measured at 1 hour after addition of Pd^{2+} and M. λex: 400 nm, slit: 5-5 nm.

Further studies were conducted on the binding mechanism of PPIX-L2 and Pd^{2+} ions. Different concentrations of Pd^{2+} (i.e., 0.1, 0.2, 0.5, 1, 2, 5 and 10 µM) were added to the 5 µM solution of PPIX-L2 and were treated for 8 hours in order to have a complete interaction (Figure 2.21). The

fluorescence quenching property of Pd^{2+} was mathematically analysed using Stern-Volmer equation (Equation 2.1) and the binding constant between PPIX-L2 and Pd^{2+} was determined by double logarithmic equation (Equation 2.2).[30]

$$\frac{F_0}{F} = 1 + K_{sv}[C] \qquad \text{Equation 2.1}$$

where F_0 refers to the initial fluorescence intensity of fluorophore, F refers to the fluorescence intensity of fluorophore in the presence of quencher, [C] refers to the varying concentration of the quencher and K_{sv} is the Stern-Volmer constant.

$$log\frac{F_0 - F}{F} = log\, K_b + n\, log[C] \qquad \text{Equation 2.2}$$

where F_0 refers to the initial fluorescence intensity of fluorophore, F refers to the fluorescence intensity of fluorophore in the presence of quencher, [C] refers to the varying concentration of the quencher, n refers to the number of binding sites and K_b is the binding constant of the quencher-fluorophore complex.

The linear relationship between the relative emission intensity of PPIX-L2 and the concentration of Pd^{2+} ions provided an easy graphical way to determine Stern-Volmer constant (Figure 2.22). The slope of Stern-Volmer plot gave the Stern-Volmer constant, which is 1.1 x 10^6 M^{-1}. The large Stern-Volmer constant demonstrated that Pd^{2+} was a good quencher of PPIX-L2. Using Equation 2.2 and the double logarithmic plot (Figure 2.23), the binding constant of Pd^{2+} and PPIX-L2 can be calculated. [C] and $\frac{F_0 - F}{F}$ refers to x, y values of any point on the calibration curve of double

logarithmic plot and the slope of the plot gave the number of binding sites. The binding constant K_b was calculated as 1.43 x 10^7 M^{-1}, which illustrated the strong binding between Pd^{2+} and PPIX-L2 with a 1:1 binding stoichiometry.

An absorption titration experiment was conducted to confirm the coordination of Pd^{2+} ion with the four pyrrolic nitrogen atoms in the nitrogen cavity. It is known that metal-chelated porphyrin is more symmetrical than the porphyrin free base. This situation will simplify the Q band pattern and form two Q bands.[31] For the case of Pd^{2+}-chelated porphyrin, the two Q bands of porphyrin appeared at around 525 and 560 nm.[32-34] In the absorption spectra (Figure 2.24), it was shown that the four Q bands of PPIX-L2 diminished and two Q band at around 519 and 555 nm appeared after 60 minutes which matched the results from the previous literature. Furthermore, MALDI-TOF analysis was conducted to confirm that Pd^{2+} bound to the cavity of PPIX-L2 to form Pd-PPIX-L2 with expected mass (Figure 2.25). The results verified the formation of Pd-PPIX-L2 complex. It is suggested that the fluorescence quenching of PPIX-L2 by Pd^{2+} is the result from heavy metal effect which causes the phosphorescence emission.[35]

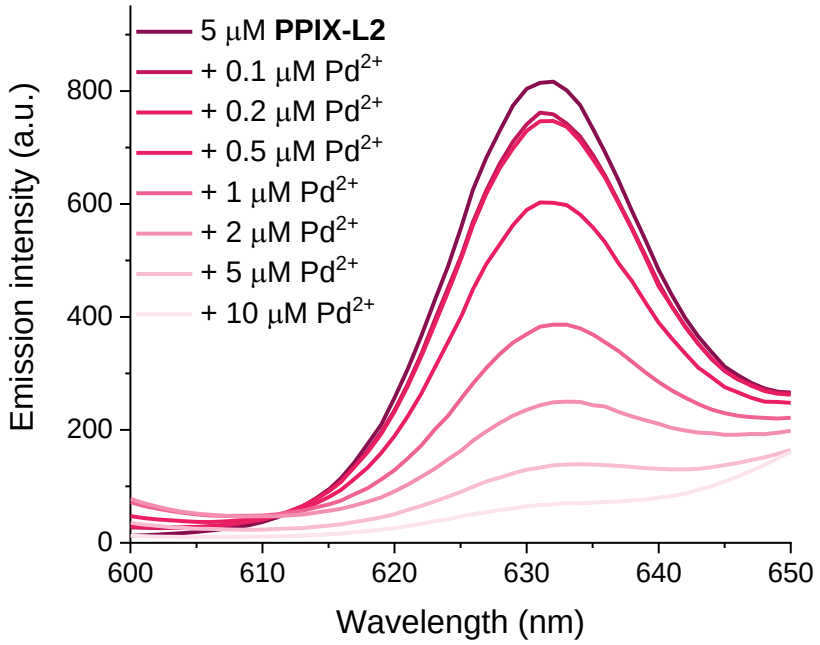

Figure 2.21: Dose-dependent fluorescence titration of 5 μM PPIX-L2 in MeOH to 0.1 – 10 μM Pd^{2+} at the timepoint of 8 hours. λex: 400 nm, slit: 5-5 nm.

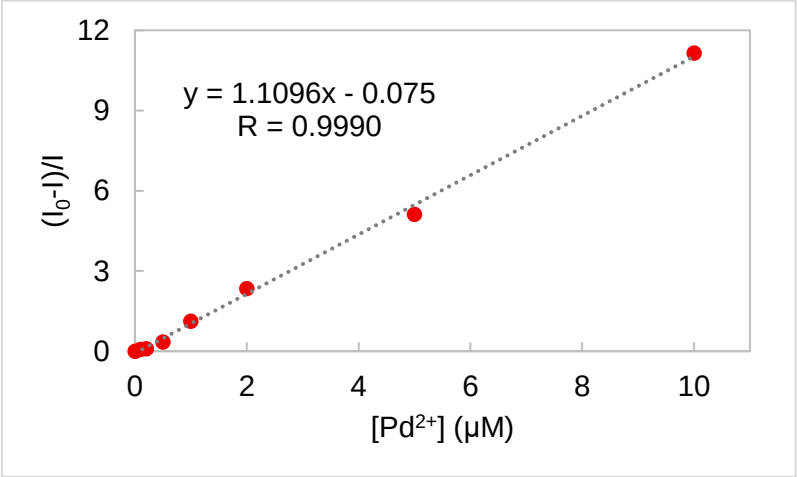

Figure 2.22: Stern–Volmer analysis of 5 μM PPIX-L2 in MeOH with various concentration of Pd^{2+}. I_0: initial fluorescence intensity, I: final fluorescence intensity.

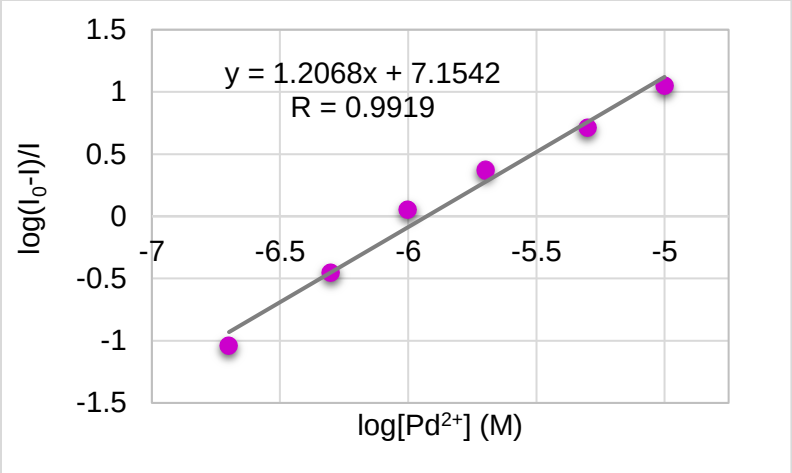

Figure 2.23: Double logarithmic plot of the Stern–Volmer analysis of Stern–Volmer analysis of 5 μM PPIX-L2 in MeOH to various concentration of Pd^{2+}. I_0: initial fluorescence intensity, I: final fluorescence intensity.

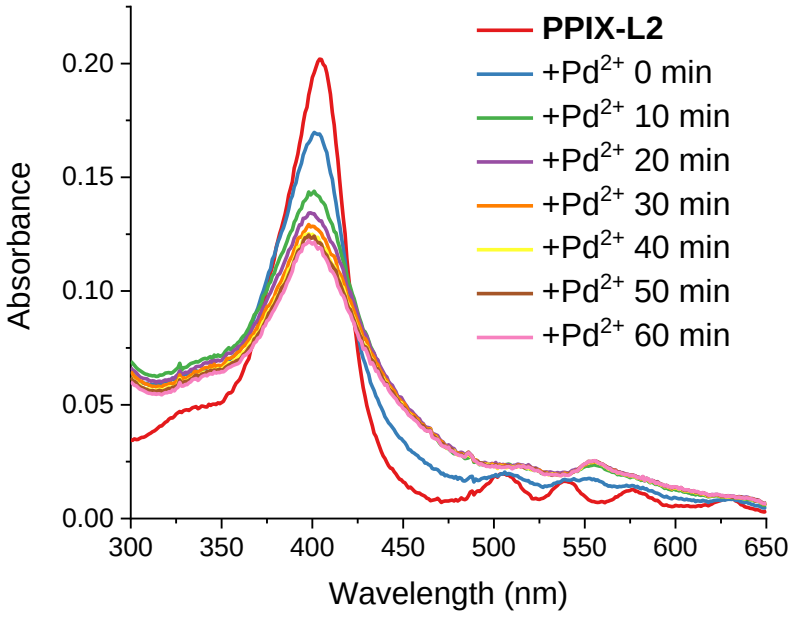

Figure 2.24: Time-dependent absorption titration of 2 μM PPIX-L2 in MeOH to 10 μM Pd^{2+}.

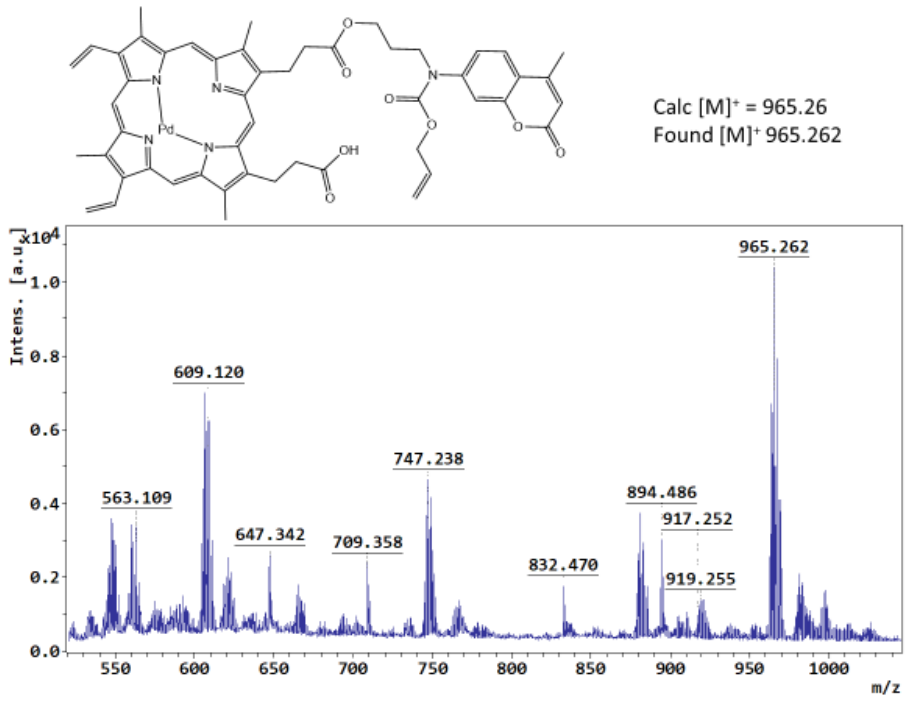

Figure 2.25: MALDI-TOF spectrum of the reaction between 2 μM PPIX-L2 in MeOH to 10 μM Pd^{2+} and form Pd-PPIX-L2.

After fluorescence response study and detection mechanism study for Pd^0 and Pd^{2+}, the detection limit of PPIX-L2 was then investigated towards two palladium species. Various concentrations of Pd^0 and Pd^{2+} were added to PPIX-L2. The relationship between the concentration of metal ions and the fluorescence intensity of PPIX-L2 was studied. A linear relationship was found in the concentration range of 0 - 1 μM at 2 hours after addition of Pd^0 and 0 - 4 μM at 1 hour after addition of Pd^{2+} (Figure 2.26). The detection limit was calculated according to the method from the previously reported literature.[36] 3σ method was used to calculate the detection limit of PPIX-L2 with the following equation:

$$Detection\ limit = \frac{3\sigma}{k}$$ Equation 2.3

where σ is the standard deviation of blank measurements, k is the slope of the fluorescence intensity versus analyte concentrations.

The limit of detection for Pd^0 was calculated as 75 nM while that for Pd^{2+} was 382 nM. To further investigate the metal sensing ability of PPIX-L2, the concentration of Pd^0 and Pd^{2+} was quantified in one mixed sample with known concentration of Pd^0 and Pd^{2+} ($[Pd^0]$ = 0.25 μM, $[Pd^{2+}]$ = 2 μM). The fluorescence intensity of PPIX-L2 with the mixed sample was recorded and substituted into the calibration curve. The calculated concentrations were 0.23 μM and 2.17 μM for Pd^0 and Pd^{2+} respectively with around 8% error compared to the actual concentration (Table 2.2). Furthermore, an additional detection limit measurement was done using the mixed sample (Figure 2.27). The detection limit of Pd^0 in presence of 0.5 μM Pd^{2+} was calculated as 97 nM while the detection limit of Pd^{2+} in presence of 0.25 μM Pd^0 was calculated as 390 nM. Although detection limit in mixed sample was higher than that in pure sample, it is still far lower than the previous reported palladium ions differentiators.

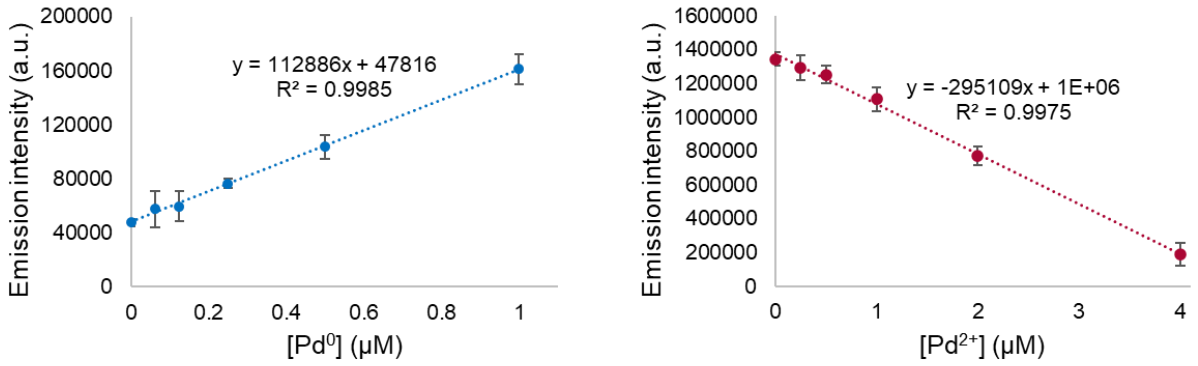

Figure 2.26: Dose-dependent fluorescence titration of 2 μM PPIX-L2 to 0 – 1 μM of Pd^0 and 0 – 4 μM Pd^{2+} in MeOH for the calculation of detection limits. (left) The linear relationship between the coumarin fluorescence intensity of 2 μM PPIX-L2 and the concentration of Pd^0. Fluorescence intensity was measured after addition of Pd^0 and incubation for two hours. (λex = 361 nm, λem = 440 nm, slit: 5-5 nm) (right) The linear relationship between the porphyrin fluorescence intensity of 2 μM PPIX-L2 and the concentration of Pd^{2+}. Fluorescence intensity was measured after the addition of Pd^{2+} and incubated for one hour. (λex = 400 nm, λem = 630 nm, slit: 5-5 nm)

Table 2.2: Quantification of Pd^0 and Pd^{2+} by PPIX-L2 in a sample mixture. Fluorescence measurements were conducted three times. The mean values were taken for calculation.

	Intensity measured (a.u.)	Calculated concentration (μM)	Actual concentration (μM)	%Error
Pd^0	73617.16 ± 545.12	0.23 ± 0.0034	0.25	-8.58
Pd^{2+}	735794.35 ± 4219.9	2.17 ± 0.017	2	8.36

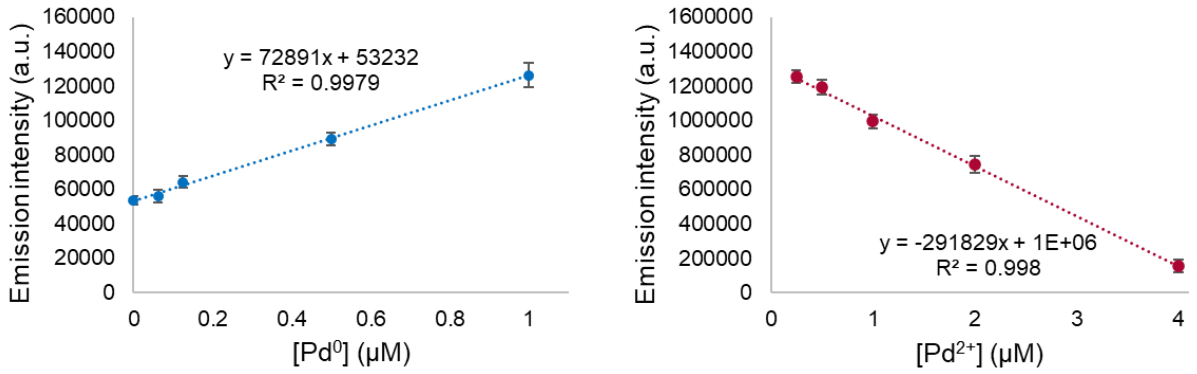

Figure 2.27: Dose-dependent fluorescence titration of 2 µM PPIX-L2 to 0 – 1 µM of Pd^0 and 0 – 4 µM Pd^{2+} in MeOH for the calculation of detection limits in the mixed sample solution. (left) The linear relationship between the coumarin fluorescence intensity of 2 µM PPIX-L2 and the concentration of Pd^0. Fluorescence intensity was measured after addition of various concentrations of Pd^0 and 0.5 µM Pd^{2+} and incubation for two hours. (λex = 361 nm, λem = 440 nm, slit: 5-5 nm) (right) The linear relationship between the porphyrin fluorescence intensity of 2 µM PPIX-L2 and the concentration of Pd^{2+}. Fluorescence intensity was measured after addition of various concentrations of Pd^{2+} and 0.25 µM Pd^0 and incubation for two hours. (λex = 400 nm, λem = 630 nm, slit: 5-5 nm)

2.4 Conclusion and future works

To conclude, a coumarin-porphyrin conjugated fluorescence probe, PPIX-L2, was synthesized. The probe can be used to discriminate between different palladium metal ions with different oxidation states (i.e., Pd^0 and Pd^{2+}). The fluorescence response towards Pd^0 and Pd^{2+} was confirmed with high selectivity. The detection mechanism of Pd^0 PPIX-L2 was Tsuji-Trost reaction, while that of Pd^+ was binding to the cavity of porphyrin. The sensing mechanism of Pd^{2+} was confirmed by Stern-Volmer analysis which suggested a strong binding property of Pd^{2+} to porphyrin. Absorption titration experiments and MALDI-TOF analysis demonstrated the Pd^{2+} coordination with four pyrrolic nitrogen, forming a palladium-porphyrin complex. The probe, PPIX-L2, achieved a lower detection limit (75 nM for Pd^0 and 382 nM for Pd^{2+}) compared to previously reported palladium ions differentiators. The detection limit of PPIX-L2 towards Pd^0 meets the requirements for palladium contamination set by European Agency.

As the detection limit of PPIX-L2 towards Pd^0 meets the requirements for palladium contamination set by European Agency, PPIX-L2 can be applied to pharmaceutical drugs, including the new chemical entities developed in pharmaceutical industry, to determine palladium ion contamination. The detection limit towards Pd^{2+} can be further improved, thus future work is suggested to focus on the improvement of detection sensitivity towards Pd^{2+}.

2.5 Experimental Section

Chemicals ands and Materials:

All moisture-sensitive reactions were conducted under a nitrogen atmosphere. Anhydrous solvents were distilled and stored over 3 Å molecular sieves. Deuterated solvents were purchased from Cambridge Isotope Laboratories. All other solvents and reagents were of reagent grade and purchased from either Sigma-Aldrich Chemical Co. or Dieckmann and used without further purification. Thin-layer chromatography (TLC) was performed using pre-coated silica gel 60, F254 plates with a thickness of 0.2 mm. Column chromatography was conducted using silica gel and laboratory grade solvents or on a Biotage flash purification system Isolera^{TM} Prime. Fluorescence spectra were recorded on Horiba FluoroMax 4 Spectrofluorometer in a 1 cm quartz cuvette.

Nuclear magnetic resonance:

NMR spectra were recorded on Bruker Avance III 400 MHz spectrometers (1H NMR on 400 MHz, 13C NMR on 101 MHz) at 298 K. Chemical shifts δ were reported in parts per million (ppm) and referenced to corresponding solvent peak (2.50 for DMSO-d6 and 7.26 for $CDCl_3$). Coupling constants *J* were reported in Hertz (Hz) and multiplicities were abbreviated as: s = singlet, d = doublet, t = triplet, dd = doublets of doublets, td = triplets of doublets and m = multiplet.

Mass spectrometry:

High-resolution mass spectra, reported as m/z, were conducted by University Research Facility in Life Science, Hong Kong Polytechnic University using Agilent 6540 liquid chromatography – electrospray ionization quadrupole-TOF mass spectrometer or Bruker UltrafleXtreme MALDI-TOF-TOF mass spectrometer. Low-resolution mass spectra were conducted using Waters Acquity H-Class UPLC with QDa mass detector for monitoring reactions and determining the correct fraction during purification of product.

Synthesis of compound 2.3:

A 2 mL solution of tert-butyldimethylsilyl chloride (TBSCl) (3.78 mmol) in dichloromethane (DCM) was added dropwise over one minute to a stirred mixture containing 3-bromo-1-propanol (3.60 mmol) and imidazole (7.20 mmol) dissolved in 2 mL DCM at room temperature. The reaction mixture was stirred for one hour at room temperature. Once the reaction was confirmed complete by TLC, 5 mL of water was added to the reaction mixture. The aqueous layer was extracted three times with 5 mL of DCM. The combined organic layers were dried over anhydrous magnesium sulfate ($MgSO_4$). The inorganic salt was removed by filtration to collect the organic filtrate. The filtrate was concentrated under reduced pressure to give (3-bromopropoxy)-tert-butyldimethylsilane as a pale-yellow oil (Yield: 90%).^{1}H-NMR (400 MHz, $CDCl_3$) δ_H (ppm): 3.74 (2H, t, J = 5.8 Hz), 3.52 (2H, t, J = 6.6 Hz), 2.03 (2H, m), 0.81 (9H, s), 0.07 (6H, s). ^{13}C-NMR (101 MHz, $CDCl_3$) δ 60.52, 35.67, 30.71, 26.01, 18.40, -5.27.

Synthesis of compound 2.4 and 2.5:

A stirred solution of 7-amino-4-methylcoumarin (0.57 mmol) in 3 mL of dimethylformamide (DMF) at room temperature was treated with (3-bromopropoxy)-tert-butyldimethylsilane (1.14 mmol) and K_2CO_3 (2.85 mmol). The reaction mixture was heated to reflux for two hours. Once the reaction was confirmed complete by TLC, the reaction mixture was allowed to cool and concentrated under reduced pressure. The residue was purified by silica gel chromatography using hexane (HEX) and ethyl acetate (EA) as eluents to give compound 2.3 as pale-yellow solid with a yield of 31%. Compound 2.3 (0.14 mmol) and N,N-diisopropylethylamine (DIPEA) (0.71 mmol) were dissolved in 10 mL of anhydrous DCM under a nitrogen atmosphere. Allyl chloroformate was added to the reaction mixture which was stirred at room temperature for 12 hours. Once the reaction was confirmed complete by TLC, the reaction mixture was washed three times with 5 mL water. The organic phase was dried over anhydrous $MgSO_4$, filtered and concentrated under reduced pressure. The residue was purified by silica gel chromatography using hexane (HEX) and ethyl acetate (EA) as eluents to give compound 2.4 as pale-yellow oil with a yield of 80%. ^{1}H-NMR (400 MHz, $CDCl_3$) δ_H (ppm): 7.56 (1H, dd, J_1 = 7.2 Hz, J_2 = 2.0 Hz), 7.27 - 7.24 (2H, m), 6.26 (1H, d, J = 1.2 Hz), 5.96 – 5.86 (1H, m), 5.28 – 5.19 (2H, m), 4.64 (2H, td, J_1 = 5.6 Hz, J_2 = 1.2 Hz), 3.86 (2H, t, J = 7.2 Hz), 3.63 (2H, t, J = 6.0 Hz), 2.43 (3H, d, J = 1.2 Hz), 1.83 (2H, m), 0.84 (9H, s), 0.00 (6H, s). ^{13}C-NMR (101 MHz, $CDCl_3$) δ 160.73, 154.63, 153.78, 152.03, 145.43, 132.30, 124.77, 122.33, 117.95, 117.73, 114.46, 66.59, 60.22, 47.54, 31.60, 25.82, 18.59, 18.17, -5.46. HRMS (TOF ES$^+$): m/z calcd. for $C_{23}H_{34}NO_5Si$ $[M+H]^+$ 432.2206, found 432.2221.

Synthesis of compound 2.6:

Tetra-n-butylammonium fluoride (TBAF) (0.12 mmol) was added to a solution of compound 2.5 (0.11 mmol) dissolved in 5 mL tetrahydrofuran (THF). The mixture was allowed to stir for one hour at room temperature. Once the reaction was confirmed complete by TLC, reaction mixture was concentrated under reduced pressure. The residue was dissolved in 10 mL of DCM and washed three times with 5 mL of water. The organic layer was dried over anhydrous $MgSO_4$, filtered and concentrated under reduced pressure. The crude product was purified on Biotage using HEX and EA as the eluents to give compound 2.6 as a pale-yellow solid with a yield of 78%.^{1}H-NMR (400 MHz, $CDCl_3$) δ_H (ppm): 7.59 (1H, d, J = 8.4 Hz), 7.26 (1H), 7.21 (1H, t, J = 2.0 Hz), 6.29 (1H, d, J = 1.2 Hz), 5.92 – 5.83 (1H, m), 5.25 – 5.18 (2H, m), 4.63 (2H, td, J_1 = 5.6 Hz, J_2 = 1.6 Hz), 3.91 (2H, t, J = 6.4 Hz), 3.69 (2H, t, J = 6.0 Hz), 2.44 (3H, d, J = 1.2 Hz), 1.76 (2H, m). ^{13}C-NMR (101 MHz, $CDCl_3$) δ 160.60, 155.29, 153.72, 152.06, 144.71, 132.07, 125.02, 122.72, 118.12, 118.05, 114.77, 114.60, 66.75, 58.95, 46.99, 30.94, 18.56. HRMS (TOF ES$^+$): m/z calcd. for $C_{17}H_{20}NO_5$ $[M+H]^+$ 318.1341, found 318.1329.

Synthesis of PPIX-L2:

Protoporphyrin IX (PPIX) (0.0467 mmol), N,N'-dicyclohexylcarbodiimide (DCC) (0.0467 mmol) and 4-dimethylaminopyridine (DMAP) (0.0187 mmol) were dissolved in 2 mL of anhydrous DMF. The mixture was stirred at 0 °C using an ice bath under a nitrogen atmosphere. After 15 minutes, compound 2.6 (0.561 mmol) was added to the reaction mixture, which was allowed to stir under a nitrogen atmosphere in the dark at room temperature for 36 hours. Once the reaction was confirmed complete by TLC, the reaction mixture was concentrated under reduced pressure. The residue was purified by silica gel chromatography using DCM and MeOH as eluents to give PPIX-L2 as a

black solid with a yield of 51%. 1H NMR (400 MHz, $CDCl_3$) δ 10.09 – 9.90 (m, 4H), 8.32 – 8.17 (m, 2H), 6.44 – 6.16 (m, 6H), 5.95 (s, 2H), 5.74 – 5.63 (m, 1H), 5.10 – 4.99 (m, 2H), 4.35 (d, *J* = 7.9 Hz, 6H), 3.99 (d, *J* = 5.4 Hz, 2H), 3.71 – 3.53 (m, 14H), 3.29 (t, *J* = 7.4 Hz, 4H), 1.51 (s, 3H), 0.92 – 0.78 (m, 2H) , -4.07 (s, 2H). ^{13}C-NMR (101 MHz, $CDCl_3$) δ 176.23, 173.81, 160.57, 153.94, 153.72, 152.80, 151.57, 151.55, 143.46, 143.42, 137.79, 136.03, 132.00, 131.98, 130.12, 130.03, 129.94, 123.67, 120.12, 120.01, 117.80, 117.79, 113.79, 97.01, 96.52, 96.28, 95.71, 77.48, 77.36, 77.16, 76.84, 66.49, 66.46, 62.02, 46.35, 37.07, 36.81, 26.76, 17.75, 17.71, 12.49, 12.40, 11.48, 11.39. HRMS (TOF ES^+): m/z calcd. for $C_{51}H_{52}N_5O_8$ $[M+H]^+$ 862.3816, found 862.3801.

2.6 Reference

[1] G. Zeni and R. C. Larock, "Synthesis of Heterocycles via Palladium π-Olefin and π-Alkyne Chemistry," *Chemical Reviews,* vol. 104, no. 5, pp. 2285-2310, 2004, doi: 10.1021/cr020085h.

[2] A. Biffis, P. Centomo, A. Del Zotto, and M. Zecca, "Pd Metal Catalysts for Cross-Couplings and Related Reactions in the 21st Century: A Critical Review," *Chemical Reviews,* vol. 118, no. 4, pp. 2249-2295, 2018, doi: 10.1021/acs.chemrev.7b00443.

[3] A. C. Frisch and M. Beller, "Catalysts for Cross-Coupling Reactions with Non-activated Alkyl Halides," *Angewandte Chemie International Edition,* vol. 44, no. 5, pp. 674-688, 2005, doi: 10.1002/anie.200461432.

[4] Q. Xiao, S. Sarina, A. Bo, J. Jia, H. Liu, D. P. Arnold, Y. Huang, H. Wu, and H. Zhu, "Visible Light-Driven Cross-Coupling Reactions at Lower Temperatures Using a Photocatalyst of Palladium and Gold Alloy Nanoparticles," *ACS Catalysis,* vol. 4, no. 6, pp. 1725-1734, 2014, doi: 10.1021/cs5000284.

[5] Z. Zhou, D.-G. Chen, M. L. Saha, H. Wang, X. Li, P.-T. Chou, and P. J. Stang, "Designed Conformation and Fluorescence Properties of Self-Assembled Phenazine-Cored Platinum(II) Metallacycles," *Journal of the American Chemical Society,* vol. 141, no. 13, pp. 5535-5543, 2019, doi: 10.1021/jacs.9b01368.

[6] D. Wang, A. B. Weinstein, P. B. White, and S. S. Stahl, "Ligand-Promoted Palladium-Catalyzed Aerobic Oxidation Reactions," *Chemical Reviews,* vol. 118, no. 5, pp. 2636-2679, 2018, doi: 10.1021/acs.chemrev.7b00334.

[7] P. Ruiz-Castillo and S. L. Buchwald, "Applications of Palladium-Catalyzed C–N Cross-Coupling Reactions," *Chemical Reviews,* vol. 116, no. 19, pp. 12564-12649, 2016, doi: 10.1021/acs.chemrev.6b00512.

[8] R. Jana, T. P. Pathak, and M. S. Sigman, "Advances in Transition Metal (Pd,Ni,Fe)-Catalyzed Cross-Coupling Reactions Using Alkyl-organometallics as Reaction Partners," *Chemical Reviews,* vol. 111, no. 3, pp. 1417-1492, 2011, doi: 10.1021/cr100327p.

[9] T. Z. Liu, S. D. Lee, and R. S. Bhatnagar, "Toxicity of palladium," *Toxicology Letters,* vol. 4, no. 6, pp. 469-473, 1979, doi: 10.1016/0378-4274(79)90113-9.

[10] C. Melber and I. Mangelsdorf, "Palladium Toxicity in Animals and in in vitro Test Systems — An Overview," Springer-Verlag, pp. 575-596.

[11] R. M. Yusop, A. Unciti-Broceta, E. M. V. Johansson, R. M. Sánchez-Martín, and M. Bradley, "Palladium-mediated intracellular chemistry," *Nature Chemistry,* vol. 3, no. 3, pp. 239-243, 2011, doi: 10.1038/nchem.981.

[12] X. Wang, Z. Guo, S. Zhu, H. Tian, and W. Zhu, "A naked-eye and ratiometric near-infrared probe for palladium via modulation of a pi-conjugated system of cyanines," *Chemical Communications,* vol. 50, no. 88, pp. 13525-8, Nov 14 2014, doi: 10.1039/c4cc05871b.

[13] J. S. Carey, D. Laffan, C. Thomson, and M. T. Williams, "Analysis of the reactions used for the preparation of drug candidate molecules," *Organic & Biomolecular Chemistry,* vol. 4, no. 12, p. 2337, 2006, doi: 10.1039/b602413k.

[14] C. E. Garrett and K. Prasad, "The Art of Meeting Palladium Specifications in Active Pharmaceutical Ingredients Produced by Pd-Catalyzed Reactions," *Advanced Synthesis & Catalysis,* vol. 346, no. 8, pp. 889-900, 2004, doi: 10.1002/adsc.200404071.

[15] N. Jakubowski, I. Feldmann, and D. Stuewer, "Grimm-type Glow Discharge Ion Source for Operation With a High Resolution Inductively Coupled Plasma Mass Spectrometry Instrument," *Journal of Analytical Atomic Spectrometry,* vol. 12, no. 2, pp. 151-157, 1997, doi: 10.1039/a604136a.

[16] A. L. Garner and K. Koide, "Studies of a fluorogenic probe for palladium and platinum leading to a palladium-specific detection method," *Chemical Communications,* no. 1, pp. 86-88, 2009, doi: 10.1039/b814197e.

[17] G. J. Stasiuk, F. Minuzzi, M. Sae-Heng, C. Rivas, H.-P. Juretschke, L. Piemonti, P. R. Allegrini, D. Laurent, A. R. Duckworth, A. Beeby, G. A. Rutter, and N. J. Long, "Dual-Modal Magnetic Resonance/Fluorescent Zinc Probes for Pancreatic β-Cell Mass Imaging," *Chemistry - A European Journal,* vol. 21, no. 13, pp. 5023-5033, 2015, doi: 10.1002/chem.201406008.

[18] E. R. H. Walter, J. A. G. Williams, and D. Parker, "APTRA-Based Luminescent Lanthanide Complexes Displaying Enhanced Selectivity for Mg^{2+}," *Chemistry - A European Journal,* vol. 24, no. 30, pp. 7724-7733, May 28 2018, doi: 10.1002/chem.201800745.

[19] T. Hirayama, M. Inden, H. Tsuboi, M. Niwa, Y. Uchida, Y. Naka, I. Hozumi, and H. Nagasawa, "A Golgi-targeting fluorescent probe for labile Fe(ii) to reveal an abnormal cellular iron distribution induced by dysfunction of VPS35," *Chemical Science,* vol. 10, no. 5, pp. 1514-1521, Feb 7 2019, doi: 10.1039/c8sc04386h.

[20] R. Balamurugan, J.-H. Liu, and B.-T. Liu, "A review of recent developments in fluorescent sensors for the selective detection of palladium ions," *Coordination Chemistry Reviews,* vol. 376, pp. 196-224, 2018, doi: 10.1016/j.ccr.2018.07.017.

[21] A. L. Garner and K. Koide, "Oxidation State-Specific Fluorescent Method for Palladium(II) and Platinum(IV) Based on the Catalyzed Aromatic Claisen Rearrangement," *Journal of the American Chemical Society,* vol. 130, no. 49, pp. 16472-16473, 2008, doi: 10.1021/ja8065539.

[22] M. Santra, S.-K. Ko, I. Shin, and K. H. Ahn, "Fluorescent detection of palladium species with an O-propargylated fluorescein," *Chemical Communications,* vol. 46, no. 22, p. 3964, 2010, doi: 10.1039/c001922d.

[23] E. M. Beccalli, E. Borsini, G. Broggini, G. Palmisano, and S. Sottocornola, "Intramolecular Pd (II) -Catalyzed Cyclization of Propargylamides : Straightforward Synthesis of 5-Oxazolecarbaldehydes Direct synthesis of 2-substituted 5-oxazolecarbaldehydes was performed by intramolecular reaction of propargylamides through treatment," *The Journal of Organic Chemistry,* vol. 73, no. 12, pp. 4746-4749, 2008, doi: 10.1021/jo800621n.

[24] K. V. Kovtunov, I. E. Beck, V. V. Zhivonitko, D. A. Barskiy, V. I. Bukhtiyarov, and I. V. Koptyug, "Heterogeneous addition of H2 to double and triple bonds over supported Pd catalysts: a parahydrogen-induced polarization technique study," *Physical Chemistry Chemical Physics,* vol. 14, no. 31, p. 11008, 2012, doi: 10.1039/c2cp40690j.

[25] M. Pal, K. Parasuraman, and K. R. Yeleswarapu, "Palladium-Catalyzed Cleavage of O/N-Propargyl Protecting Groups in Aqueous Media under a Copper-Free Condition," *Organic Letters,* vol. 5, no. 3, pp. 349-352, 2003, doi: 10.1021/ol027382t.

[26] F. Liu, J. Du, M. Xu, and G. Sun, "A Highly Sensitive Fluorescent Sensor for Palladium and Direct Imaging of Its Ecotoxicity in Living Model Organisms," *Chemistry: An Asian Journal,* vol. 11, no. 1, pp. 43-8, Jan 2016, doi: 10.1002/asia.201500767.

[27] X. Li, H. Huang, Y. Zhu, H. Zhao, and Z. Wang, "Highly selective fluorescence detection of $Pd^{2+/4+}$ species based on a catalyzed aromatic Claisen rearrangement," *RSC Advances,* vol. 5, no. 128, pp. 105810-105813, 2015, doi: 10.1039/c5ra17831b.

[28] M. E. Jun and K. H. Ahn, "Fluorogenic and Chromogenic Detection of Palladium Species through a Catalytic Conversion of a Rhodamine B Derivative," *Organic Letters,* vol. 12, no. 12, pp. 2790-2793, 2010, doi: 10.1021/ol100905g.

[29] L. Jiang, H.-N. Mak, E. R. H. Walter, W.-T. Wong, K.-L. Wong, and N. J. Long, "A fluorescent probe for the discrimination of oxidation states of palladium," *Chemical Science,* vol. 12, no. 29, pp. 9977-9982, 2021, doi: 10.1039/d1sc01616d.

[30] R. Waseem, A. Shamsi, T. Khan, M. I. Hassan, S. N. Kazim, M. Shahid, and A. Islam, "Unraveling the Binding Mechanism of Alzheimer's Drugs with Irisin: Spectroscopic, Calorimetric, and Computational Approaches," *International Journal of Molecular Sciences,* vol. 23, no. 11, p. 5965, 2022, doi: 10.3390/ijms23115965.

[31] R. Giovannetti, "The Use of Spectrophotometry UV-Vis for the Study of Porphyrins," *Macro To Nano Spectroscopy,* 2012, doi: 10.5772/38797.

[32] Z. Valicsek and O. Horváth, "Application of the electronic spectra of porphyrins for analytical purposes: The effects of metal ions and structural distortions," *Microchemical Journal,* vol. 107, pp. 47-62, 2013, doi: 10.1016/j.microc.2012.07.002.

[33] S. Drouet, C. O. Paul-Roth, V. Fattori, M. Cocchi, and J. A. G. Williams, "Platinum and palladium complexes of fluorenyl porphyrins as red phosphors for light-emitting devices," *New Journal of Chemistry,* vol. 35, no. 2, pp. 438-444, 2011, doi: 10.1039/c0nj00561d.

[34] Q.-X. Wan and Y. Liu, "The Ionic Palladium Porphyrin as a Highly Efficient and Recyclable Catalyst for Heck Reaction in Ionic Liquid Solution Under Aerobic

Conditions," *Catalysis Letters,* vol. 128, no. 3-4, pp. 487-492, 2008, doi: 10.1007/s10562-008-9780-2.

[35] L. Zang, H. Zhao, J. Hua, W. Cao, F. Qin, J. Yao, Y. Tian, Y. Zheng, and Z. Zhang, "Comparison study on the influence of the central metal ions in palladium(ii)- and gadolinium(iii)-porphyrins for phosphorescence-based oxygen sensing," *Journal of Materials Chemistry C,* vol. 4, no. 40, pp. 9581-9587, 2016, doi: 10.1039/c6tc01762b.

[36] X.-B. Wang, H.-J. Li, C. Liu, Y.-X. Hu, M.-C. Li, and Y.-C. Wu, "Simple Turn-On Fluorescent Sensor for Discriminating Cys/Hcy and GSH from Different Fluorescent Signals," *Analytical Chemistry,* vol. 93, no. 4, pp. 2244-2253, 2021, doi: 10.1021/acs.analchem.0c04100.

2.7 Appendix

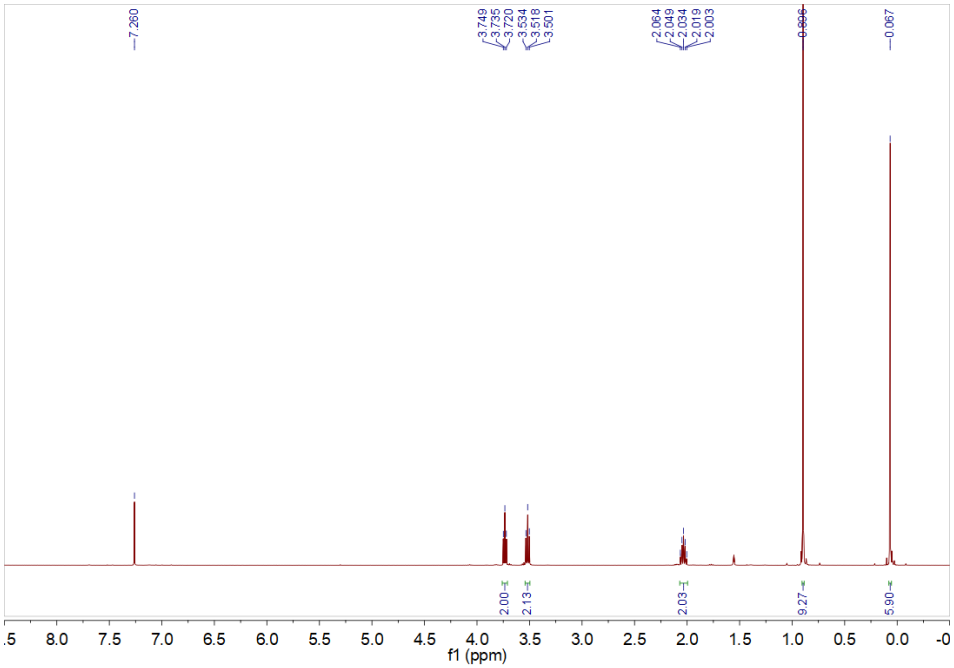

Figure 2.28: ^{1}H NMR spectrum of (3-bromopropoxy)-tert-butyldimethylsilane (400 MHz, $CDCl_3$).

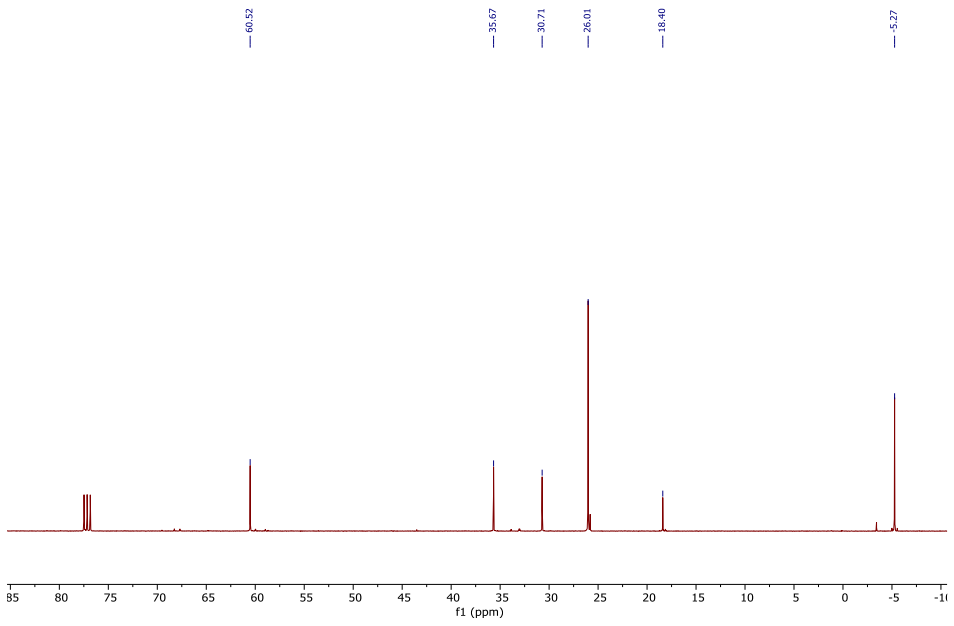

Figure 2.29: ^{13}C NMR spectrum of (3-bromopropoxy)-tert-butyldimethylsilane (101 MHz, $CDCl_3$).

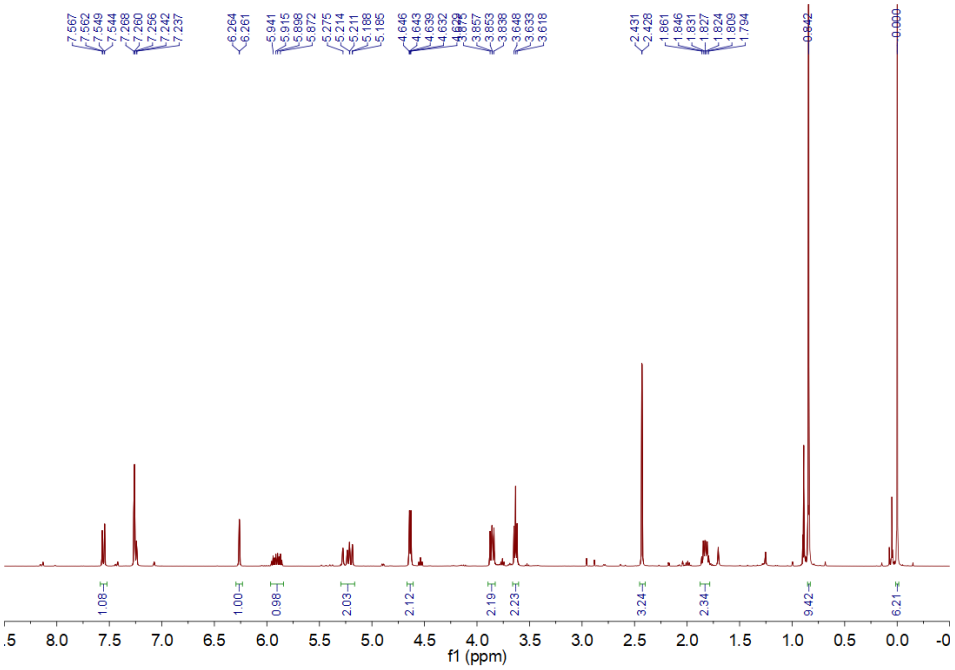

Figure 2.30: ^{1}H NMR spectrum of compound 3 (400 MHz, $CDCl_3$).

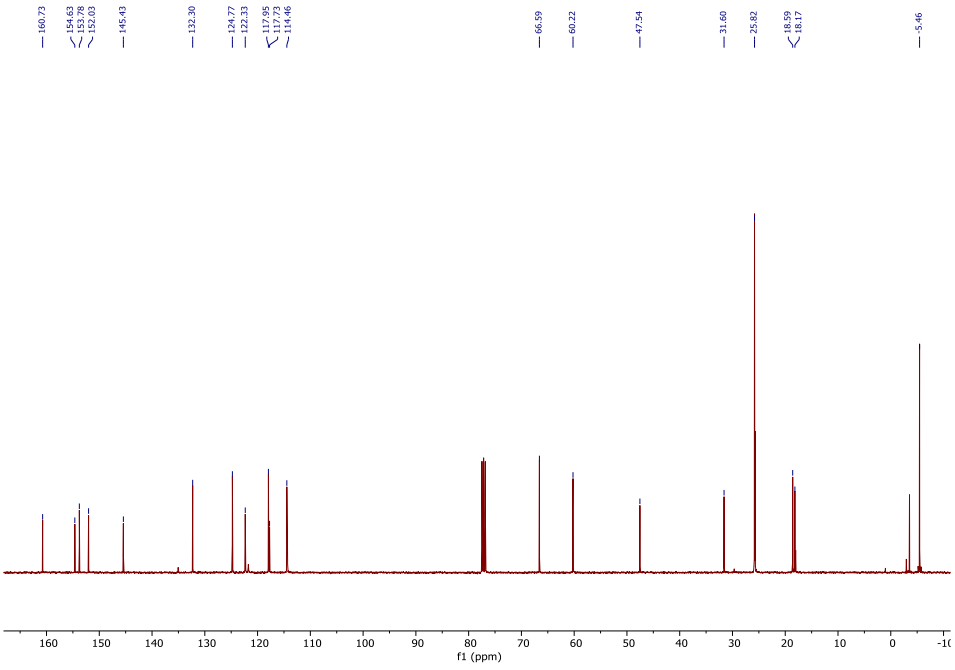

Figure 2.31: ^{13}C NMR spectrum of compound 3 (101 MHz, $CDCl_3$).

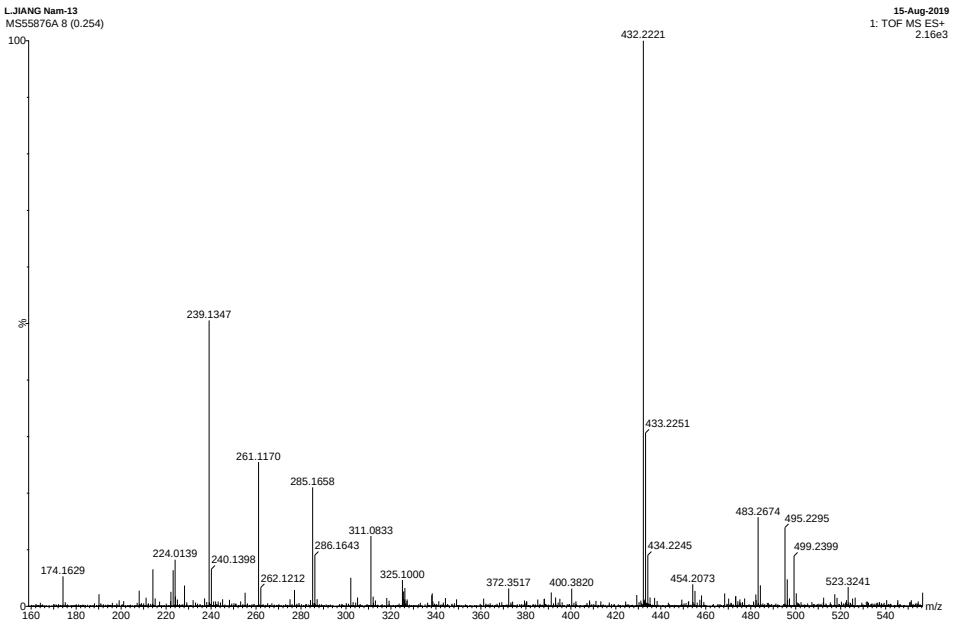

Figure 2.32: High-resolution mass spectrum of compound 3.

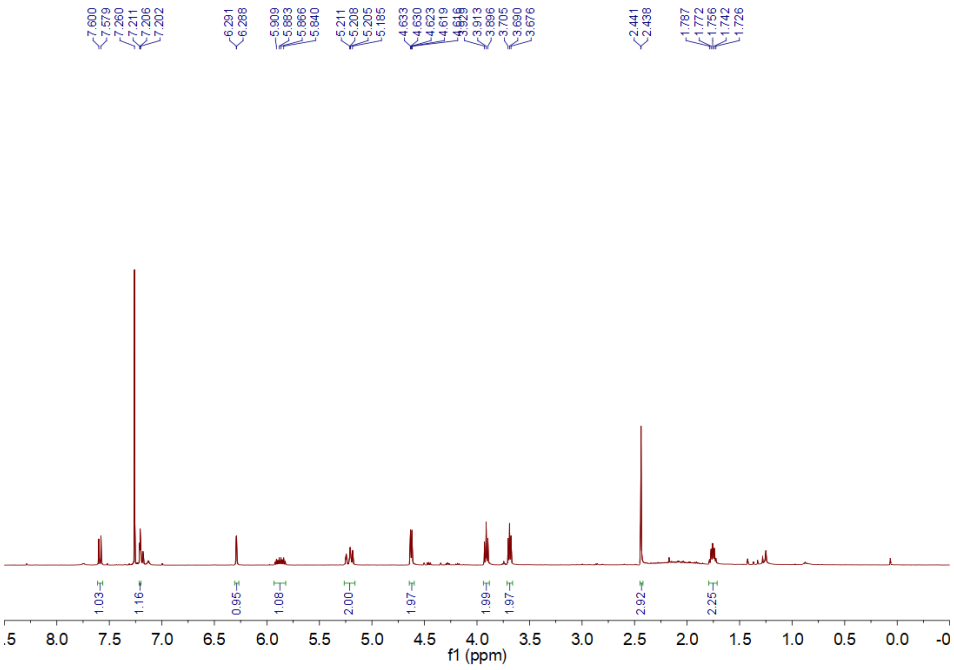

Figure 2.33: ^{1}H NMR spectrum of compound 4 (400 MHz, $CDCl_3$).

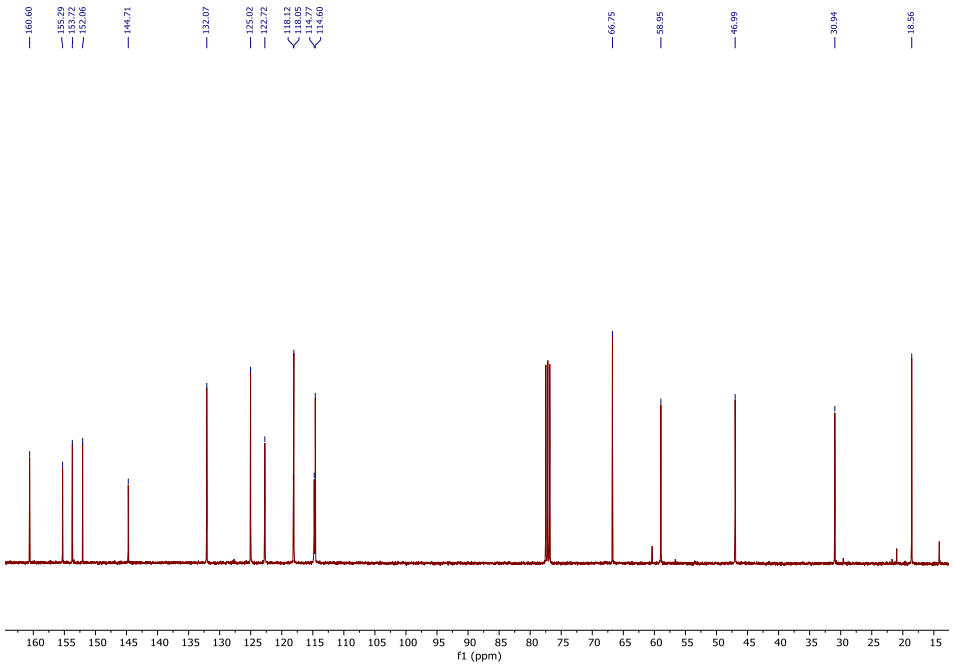

Figure 2.34: ^{13}C NMR spectrum of compound 4 (101 MHz, $CDCl_3$).

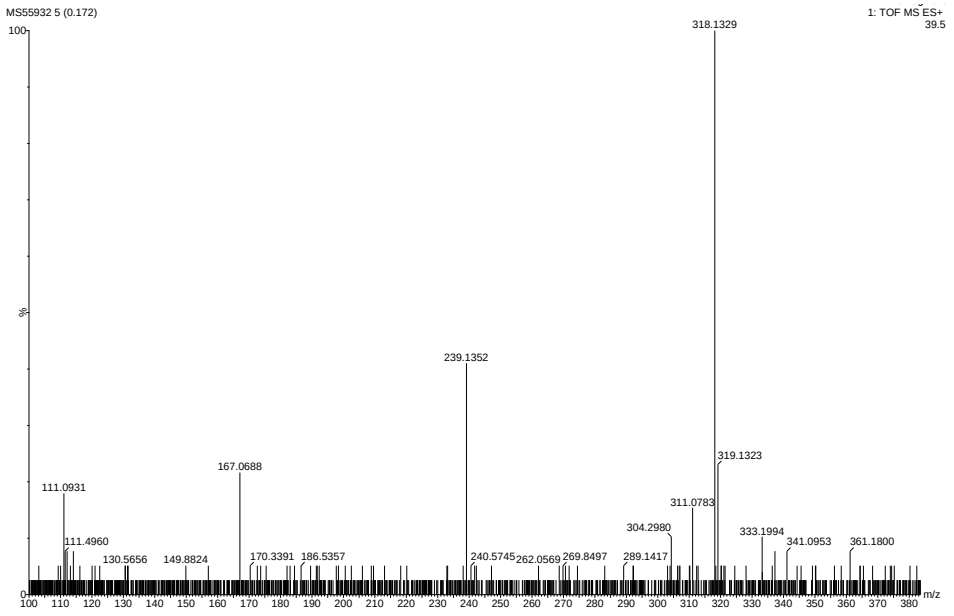

Figure 2.35: High-resolution mass spectrum of compound 4.

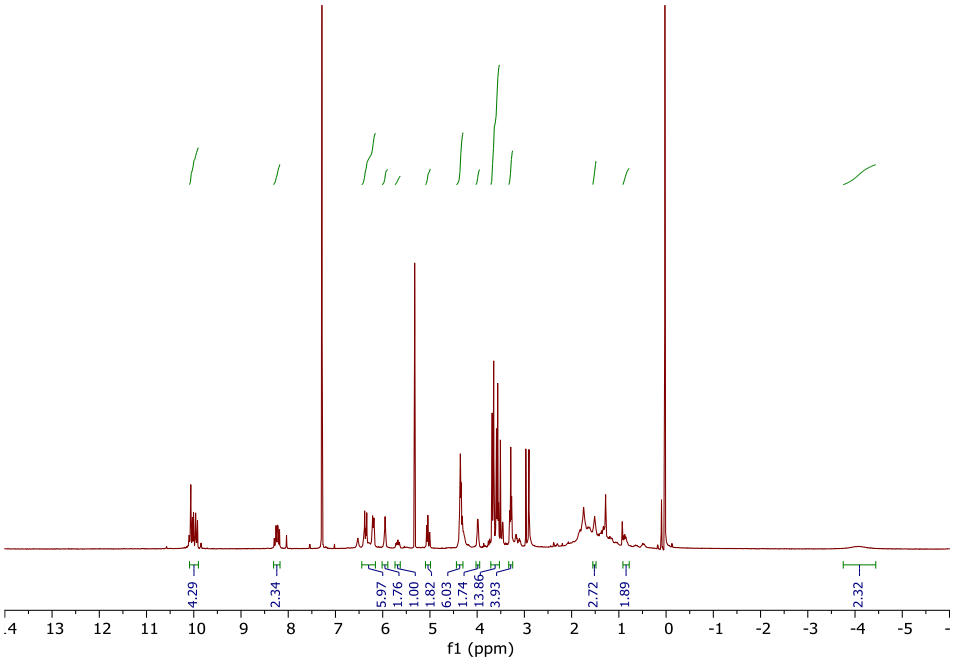

Figure 2.36: ^{1}H NMR spectrum of PPIX-L2 (400 MHz, $CDCl_3$).

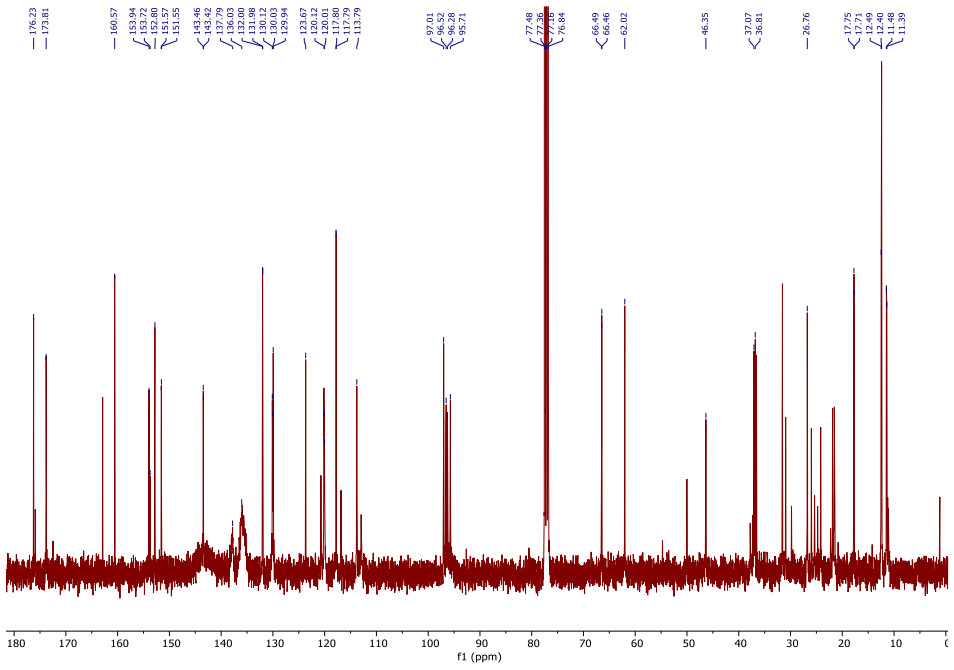

Figure 2.37: ^{13}C NMR spectrum of PPIX-L2 (101 MHz, $CDCl_3$).

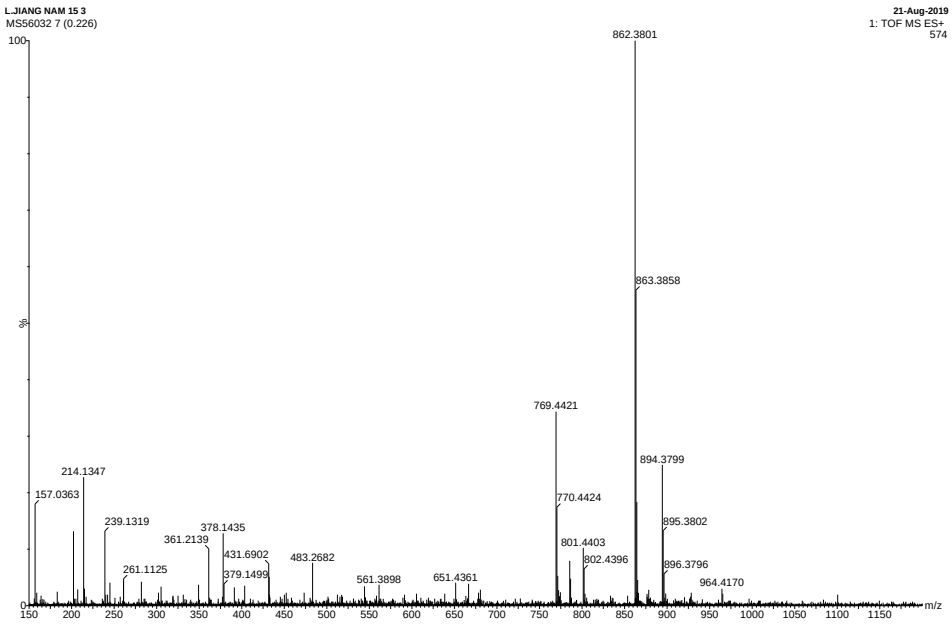

Figure 2.38: High-resolution mass spectrum of PPIX-L2.

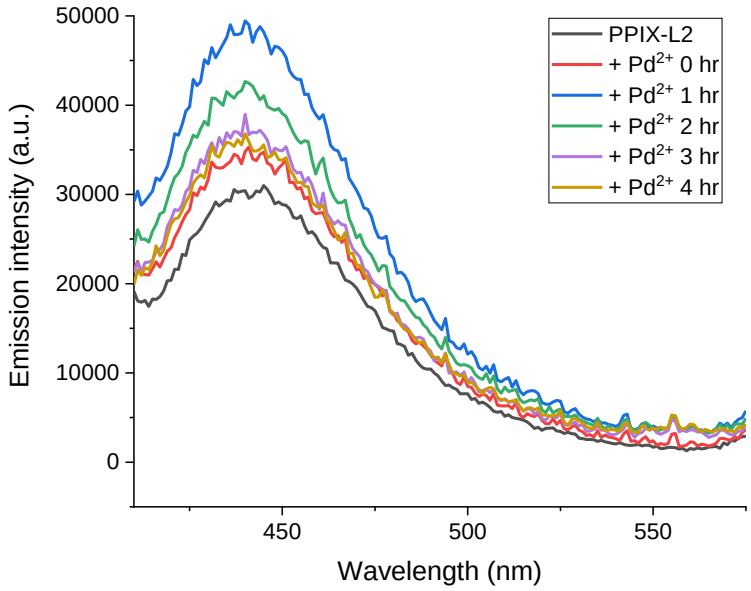

Figure 2.39: Fluorescence metal selectivity experiment of 2 μM PPIX-L2 in MeOH to 10 μM Pd^{2+} after four hours of incubation. λex: 361 nm, slit: 5-5 nm.

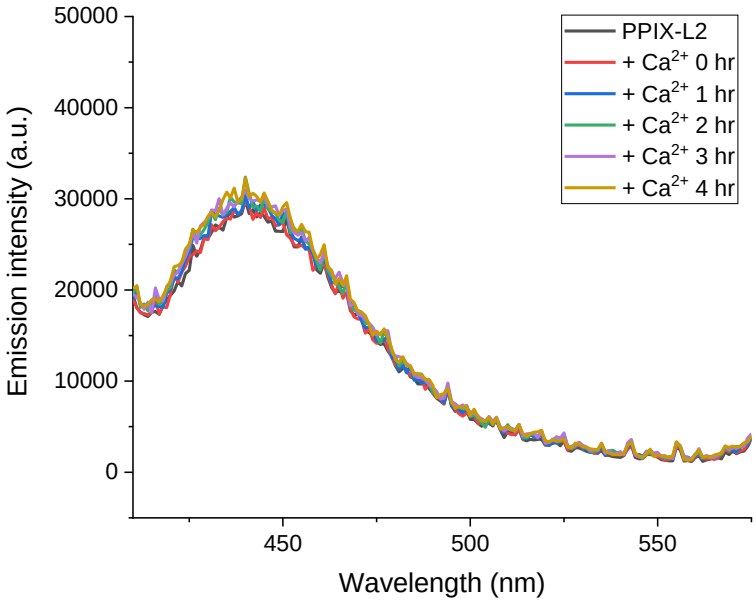

Figure 2.40: Fluorescence metal selectivity experiment of 2 μM PPIX-L2 in MeOH to 10 μM Ca^{2+} after four hours of incubation. λex: 361 nm, slit: 5-5 nm.

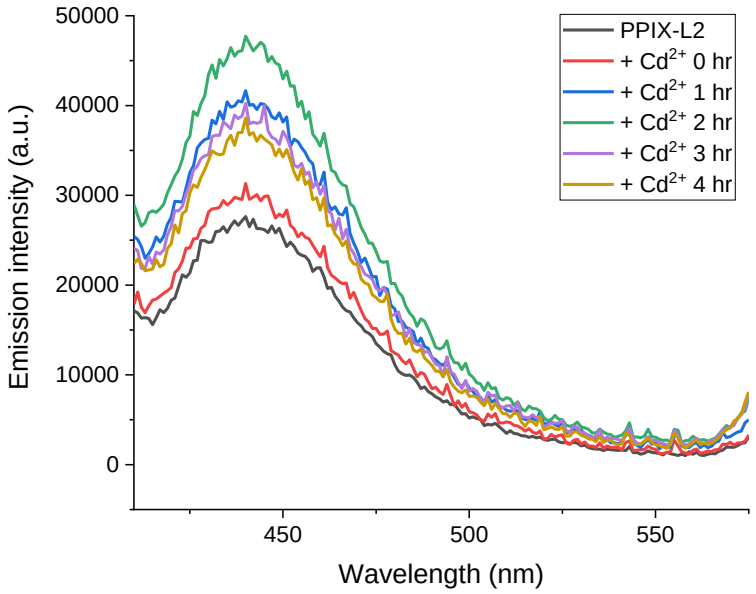

Figure 2.41: Fluorescence metal selectivity experiment of 2 μM PPIX-L2 in MeOH to 10 μM Cd^{2+} after four hours of incubation. λex: 361 nm, slit: 5-5 nm.

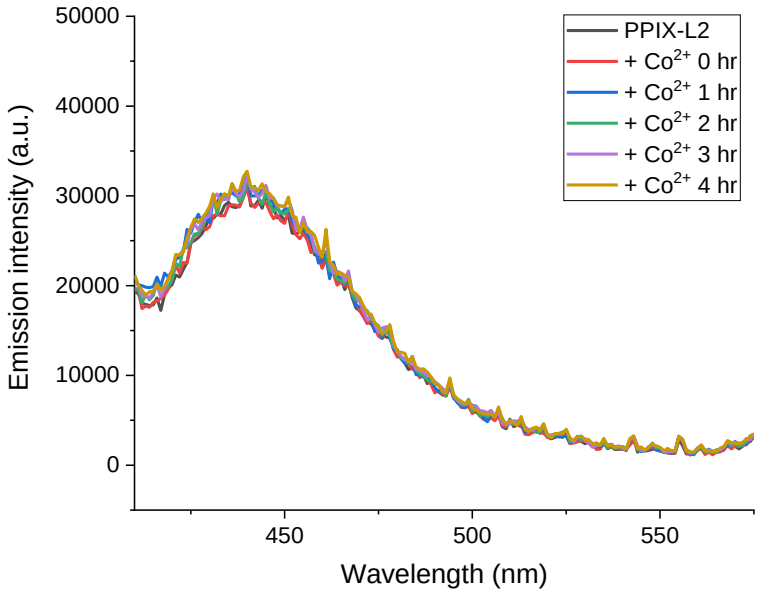

Figure 2.42: Fluorescence metal selectivity experiment of 2 μM PPIX-L2 in MeOH to 10 μM Co^{2+} after four hours of incubation. λex: 361 nm, slit: 5-5 nm.

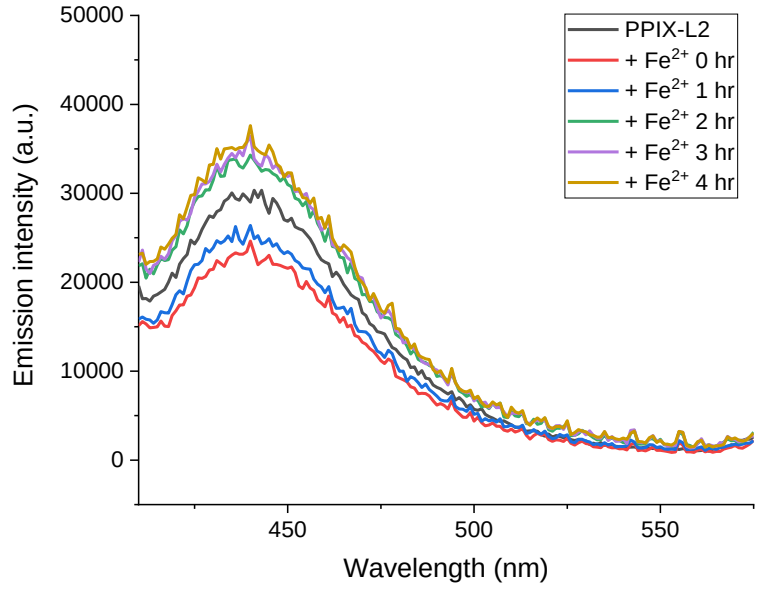

Figure 2.43: Fluorescence metal selectivity experiment of 2 μM PPIX-L2 in MeOH to 10 μM Fe^{2+} after four hours of incubation. λex: 361 nm, slit: 5-5 nm.

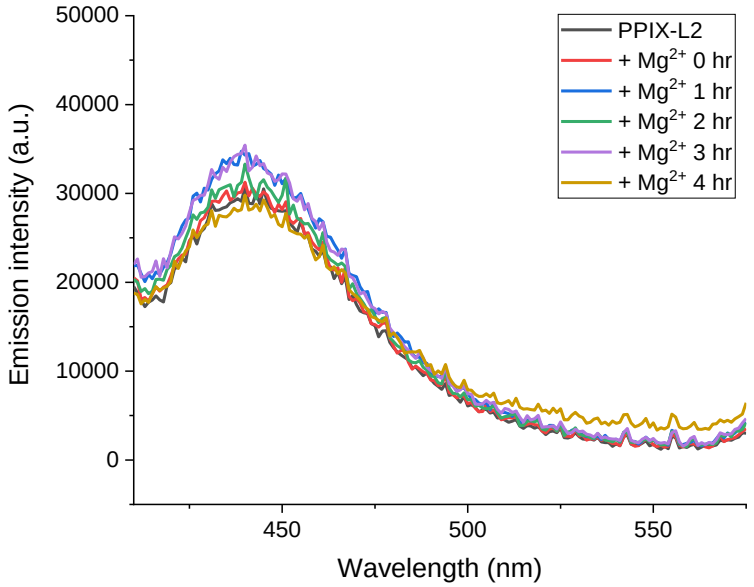

Figure 2.44: Fluorescence metal selectivity experiment of 2 µM PPIX-L2 in MeOH to 10 µM Mg^{2+} after four hours of incubation. λex: 361 nm, slit: 5-5 nm.

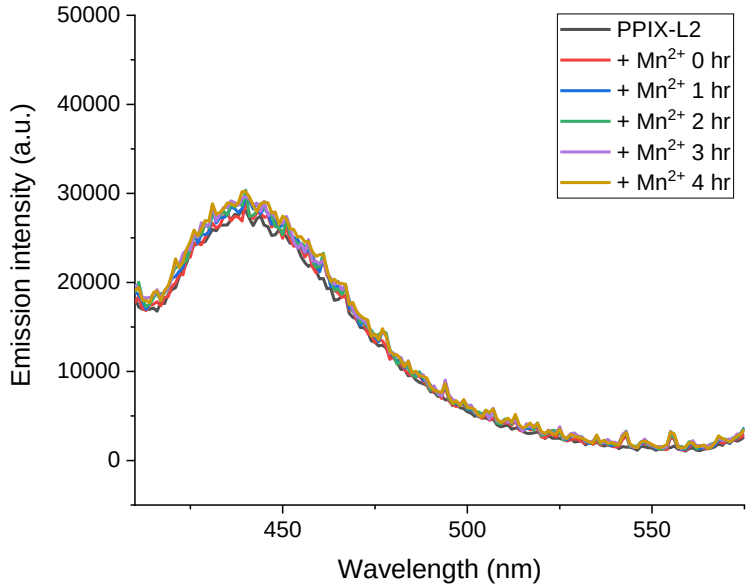

Figure 2.45: Fluorescence metal selectivity experiment of 2 µM PPIX-L2 in MeOH to 10 µM Mn^{2+} after four hours of incubation. λex: 361 nm, slit: 5-5 nm.

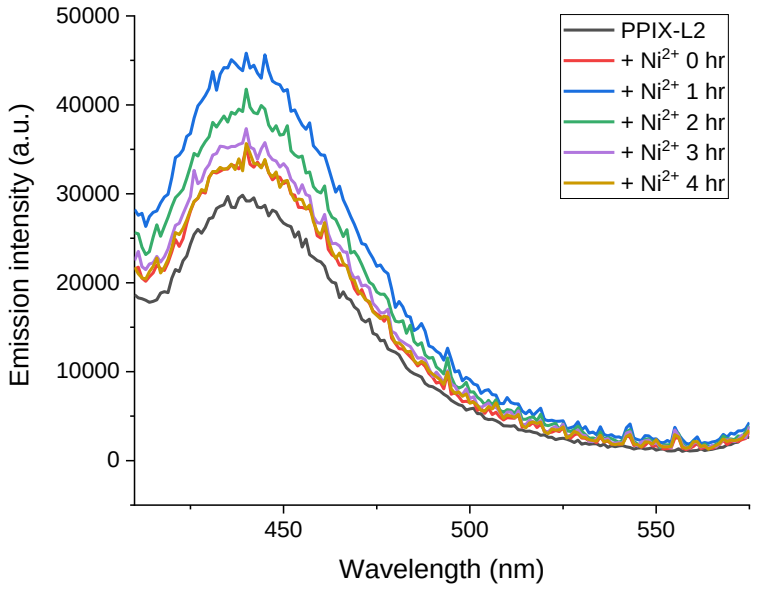

Figure 2.46: Fluorescence metal selectivity experiment of 2 µM PPIX-L2 in MeOH to 10 µM Ni^{2+} after four hours of incubation. λex: 361 nm, slit: 5-5 nm.

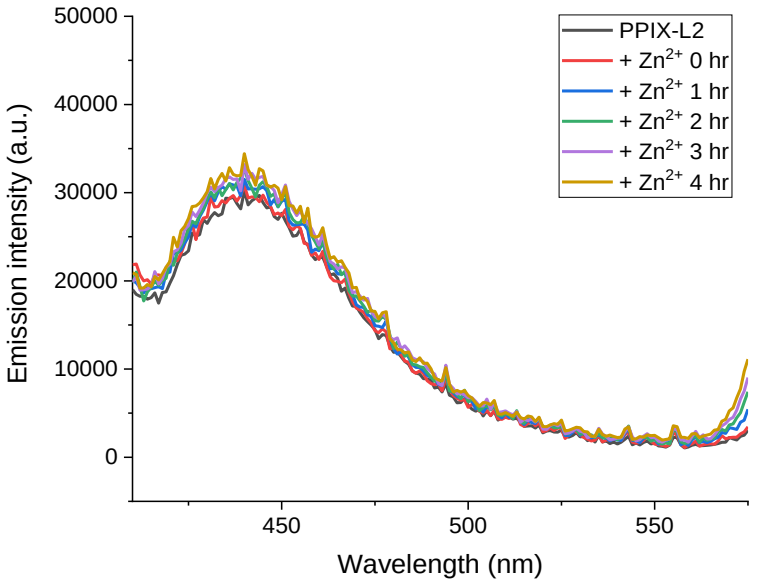

Figure 2.47: Fluorescence metal selectivity experiment of 2 µM PPIX-L2 in MeOH to 10 µM Zn^{2+} after four hours of incubation. λex: 361 nm, slit: 5-5 nm.

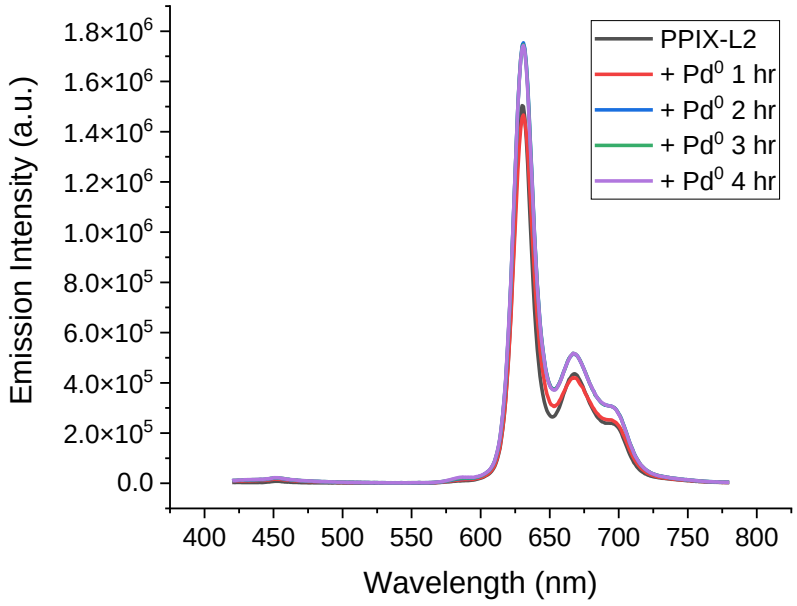

Figure 2.48: Fluorescence metal selectivity experiment of 2 μM PPIX-L2 in MeOH to 10 μM Pd^0 after four hours of incubation. λex: 400 nm, slit: 5-5 nm.

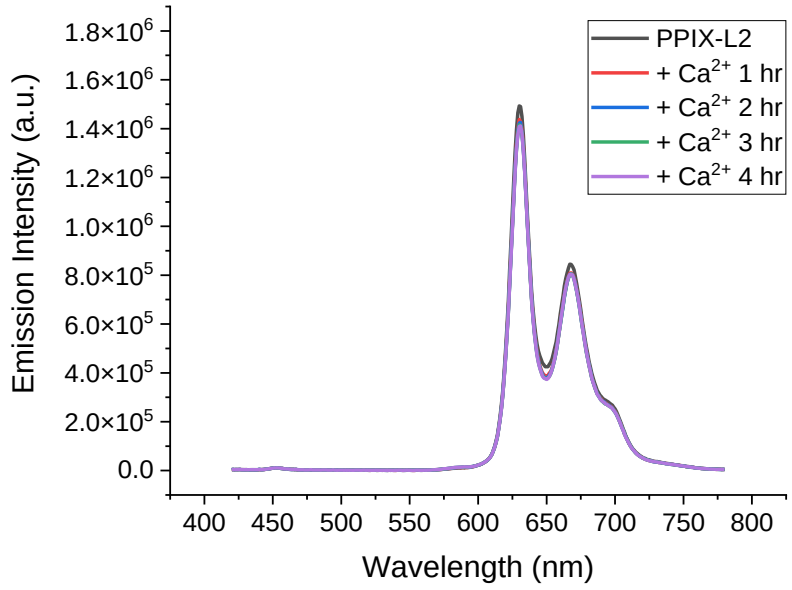

Figure 2.49: Fluorescence metal selectivity experiment of 2 μM PPIX-L2 in MeOH to 10 μM Ca^{2+} after four hours of incubation. λex: 400 nm, slit: 5-5 nm.

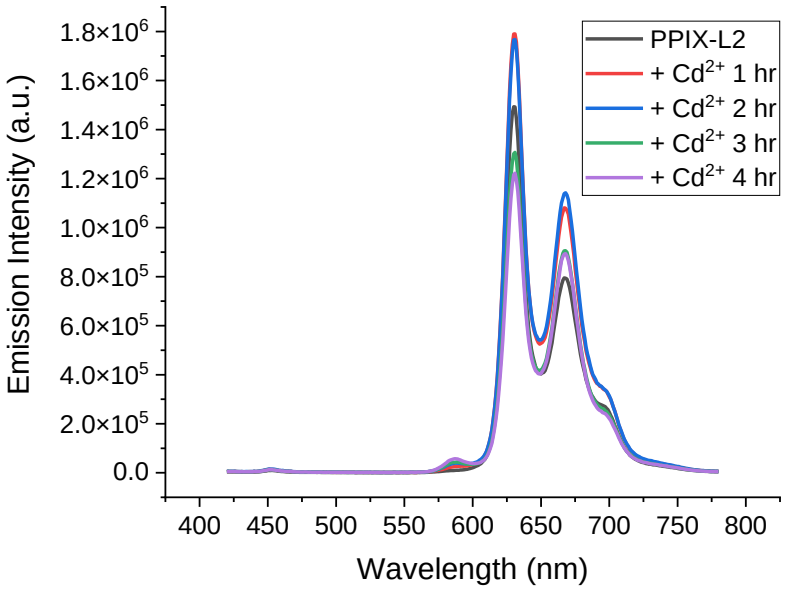

Figure 2.50: Fluorescence metal selectivity experiment of 2 μM PPIX-L2 in MeOH to 10 μM Cd^{2+} after four hours of incubation. λex: 400 nm, slit: 5-5 nm.

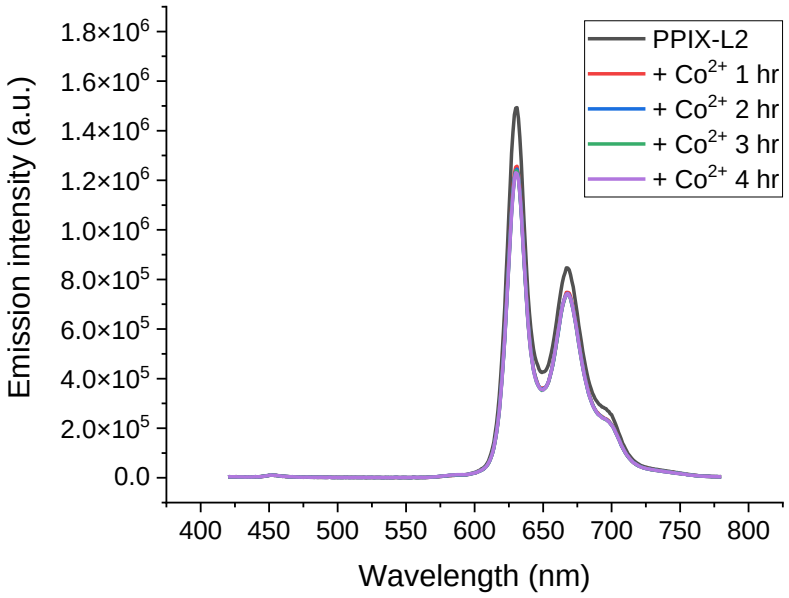

Figure 2.51: Fluorescence metal selectivity experiment of 2 μM PPIX-L2 in MeOH to 10 μM Co^{2+} after four hours of incubation. λex: 400 nm, slit: 5-5 nm.

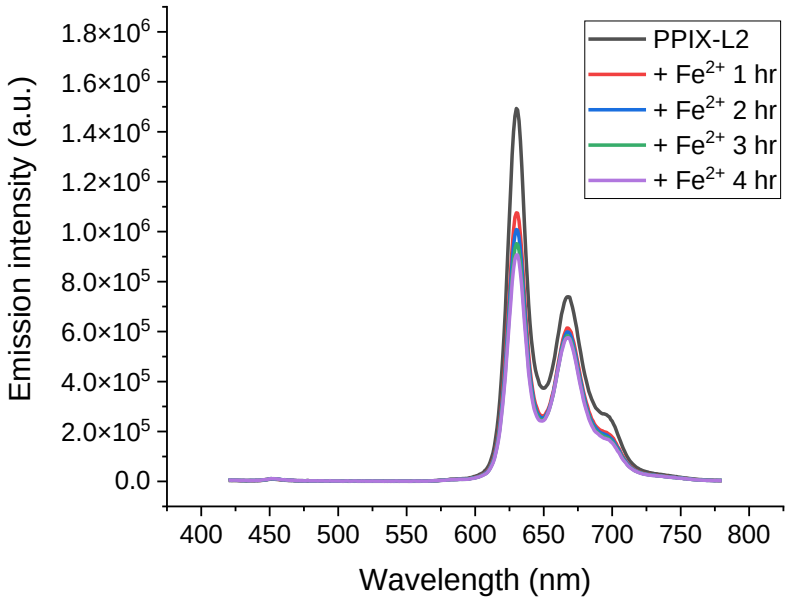

Figure 2.52: Fluorescence metal selectivity experiment of 2 μM PPIX-L2 in MeOH to 10 μM Fe^{2+} after four hours of incubation. λex: 400 nm, slit: 5-5 nm.

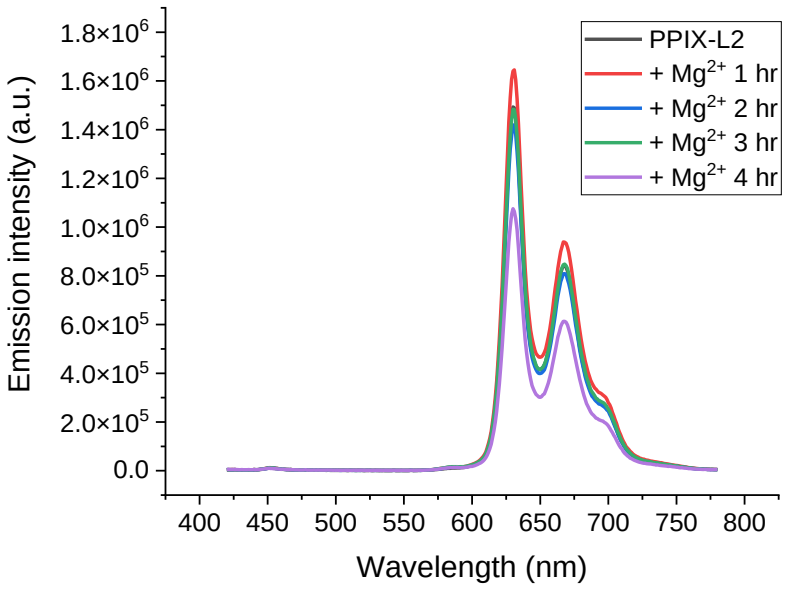

Figure 2.53: Fluorescence metal selectivity experiment of 2 μM PPIX-L2 in MeOH to 10 μM Mg^{2+} after four hours of incubation. λex: 400 nm, slit: 5-5 nm.

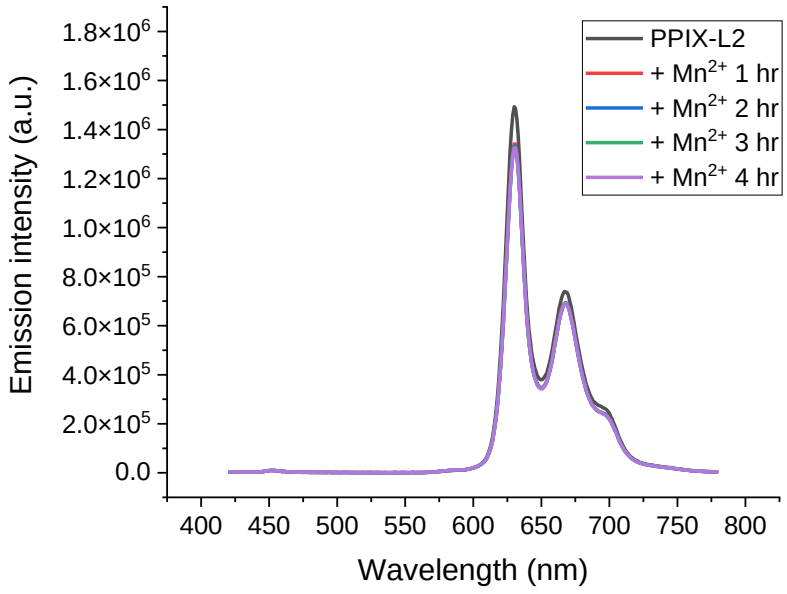

Figure 2.54: Fluorescence metal selectivity experiment of 2 μM PPIX-L2 in MeOH to 10 μM Mn^{2+} after four hours of incubation. λex: 400 nm, slit: 5-5 nm.

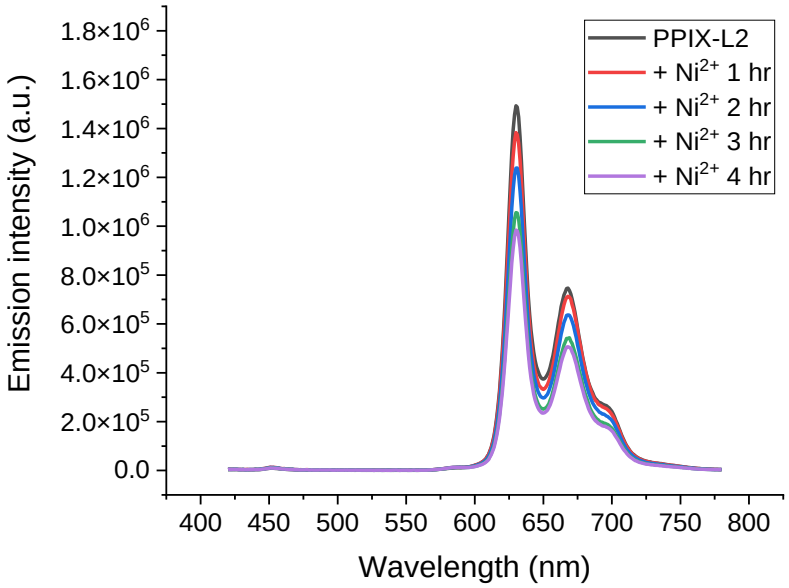

Figure 2.55: Fluorescence metal selectivity experiment of 2 μM PPIX-L2 in MeOH to 10 μM Ni^{2+} after four hours of incubation. λex: 400 nm, slit: 5-5 nm.

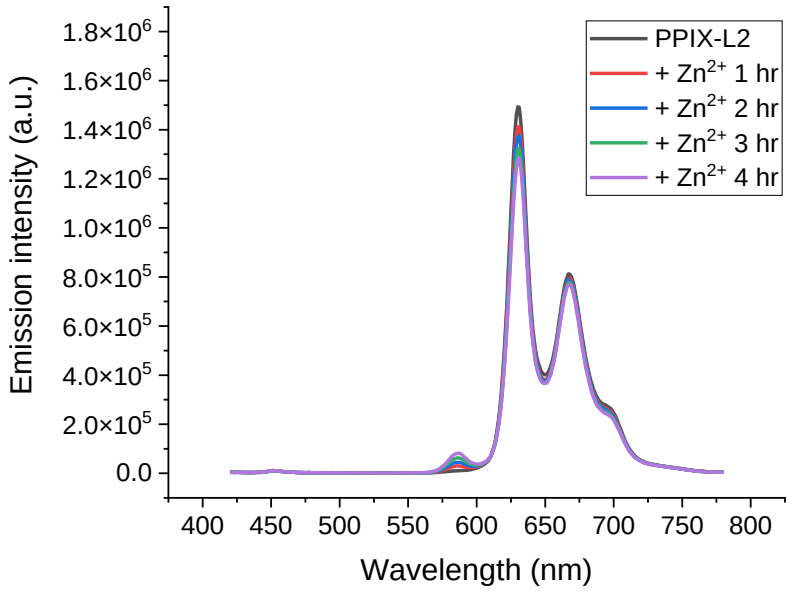

Figure 2.56: Fluorescence metal selectivity experiment of 2 μM PPIX-L2 in MeOH to 10 μM Zn^{2+} after four hours of incubation. λex: 400 nm, slit: 5-5 nm.

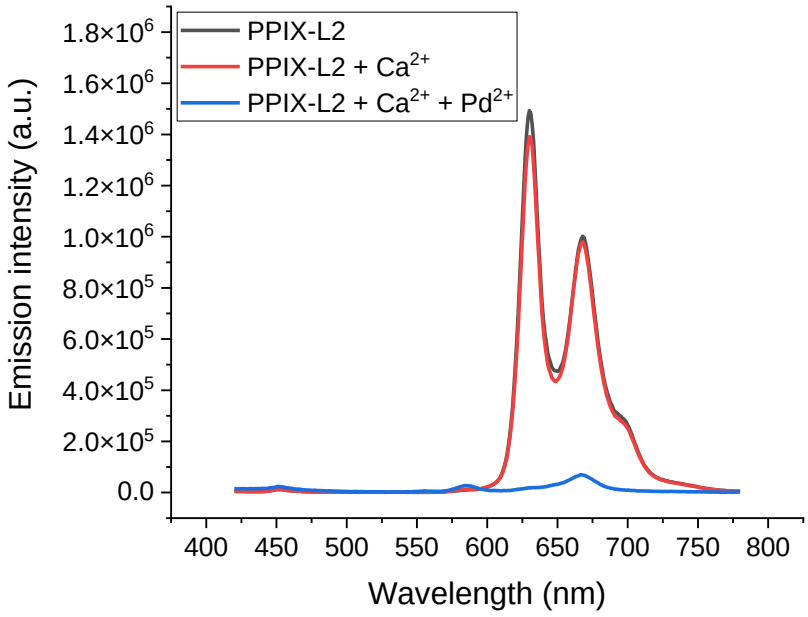

Figure 2.57: Fluorescence metal competition experiment of 2 μM PPIX-L2 in MeOH to 10 μM Ca^{2+} after four hours of incubation. λex: 400 nm, slit: 5-5 nm.

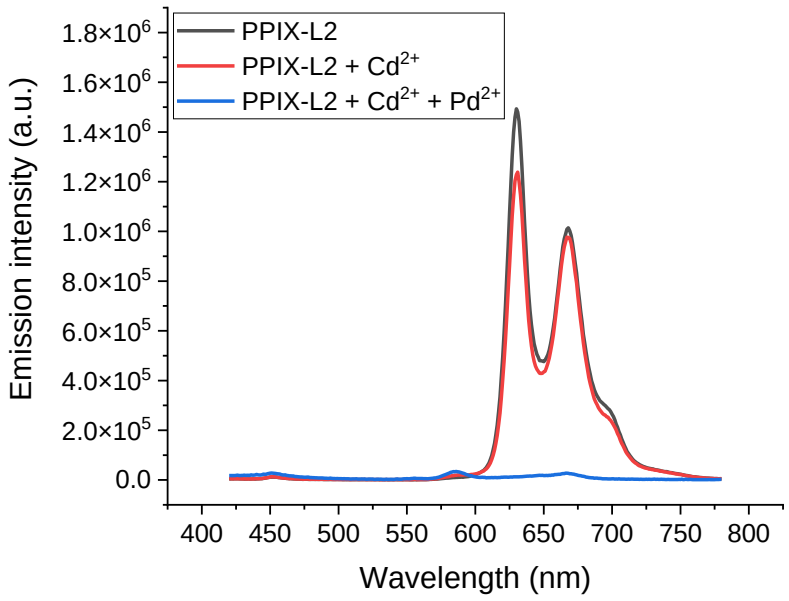

Figure 2.58: Fluorescence metal competition experiment of 2 µM PPIX-L2 in MeOH to 10 µM Cd^{2+} after four hours of incubation. λex: 400 nm, slit: 5-5 nm.

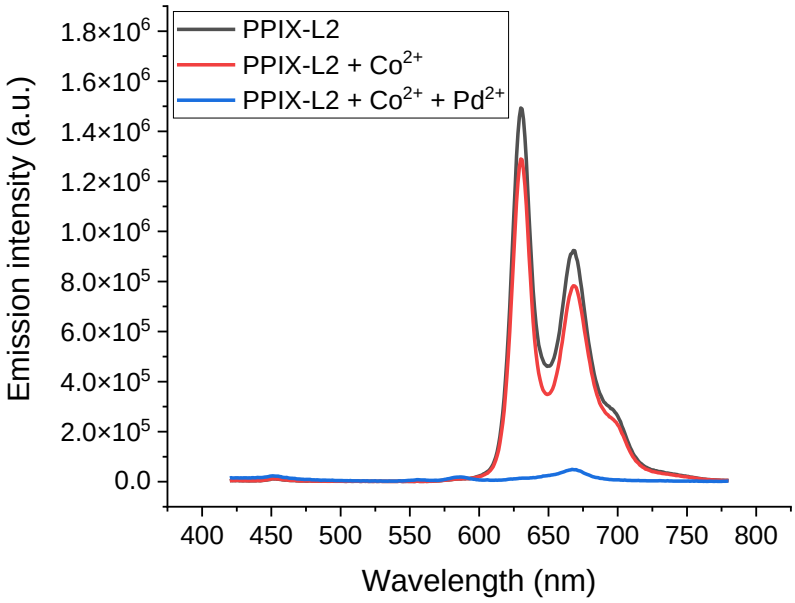

Figure 2.59: Fluorescence metal competition experiment of 2 µM PPIX-L2 in MeOH to 10 µM Co^{2+} after four hours of incubation. λex: 400 nm, slit: 5-5 nm.

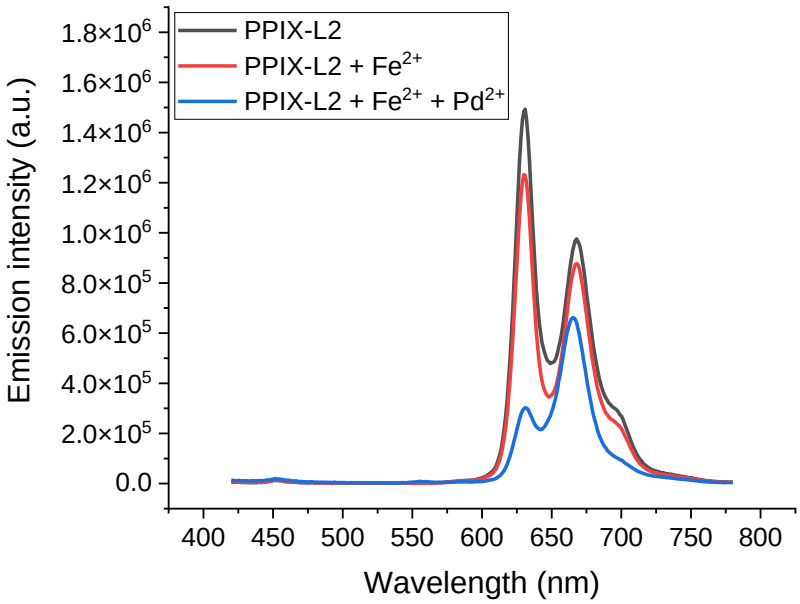

Figure 2.60: Fluorescence metal competition experiment of 2 µM PPIX-L2 in MeOH to 10 µM Fe^{2+} after four hours of incubation. λex: 400 nm, slit: 5-5 nm.

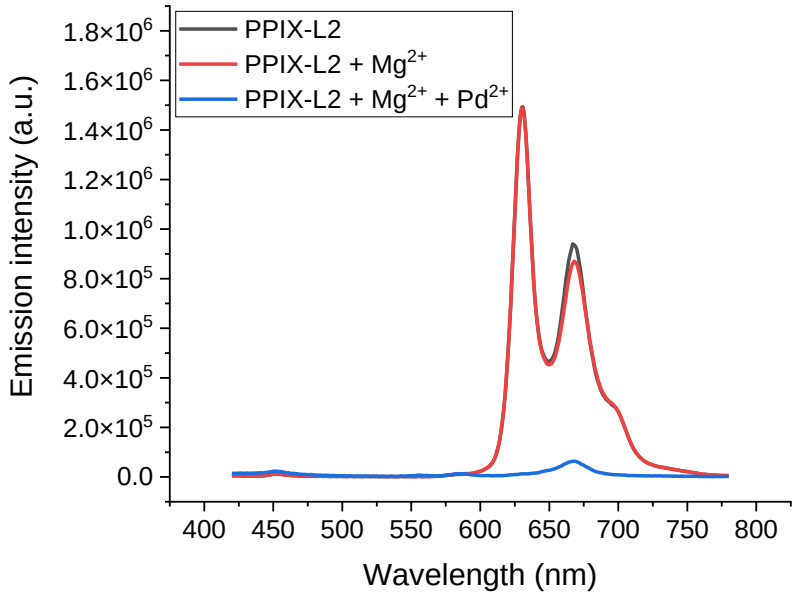

Figure 2.61: Fluorescence metal competition experiment of 2 µM PPIX-L2 in MeOH to 10 µM Mg^{2+} after four hours of incubation. λex: 400 nm, slit: 5-5 nm.

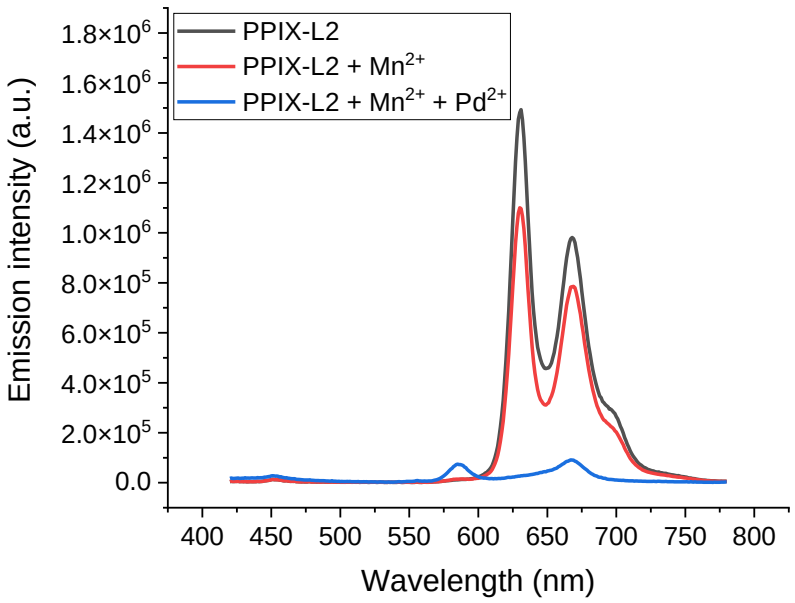

Figure 2.62: Fluorescence metal competition experiment of 2 µM PPIX-L2 in MeOH to 10 µM Mn^{2+} after four hours of incubation. λex: 400 nm, slit: 5-5 nm.

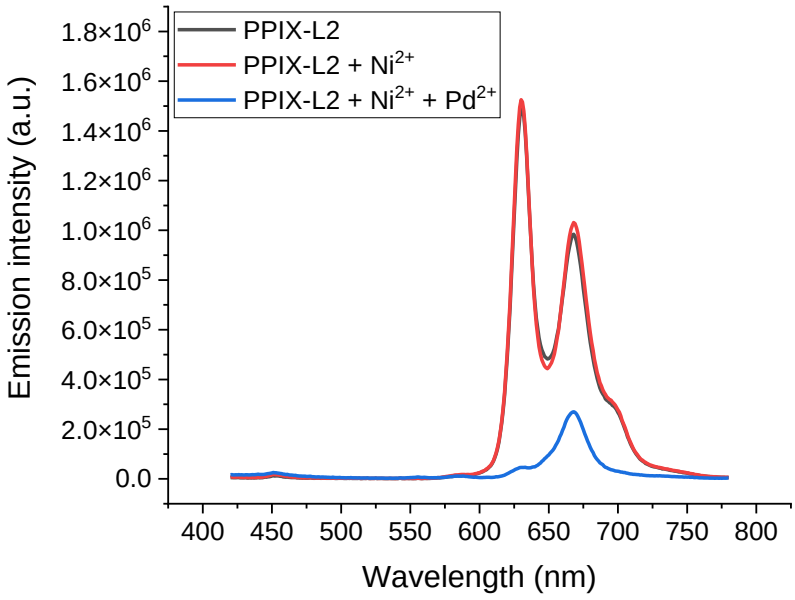

Figure 2.63: Fluorescence metal competition experiment of 2 µM PPIX-L2 in MeOH to 10 µM Ni^{2+} after four hours of incubation. λex: 400 nm, slit: 5-5 nm.

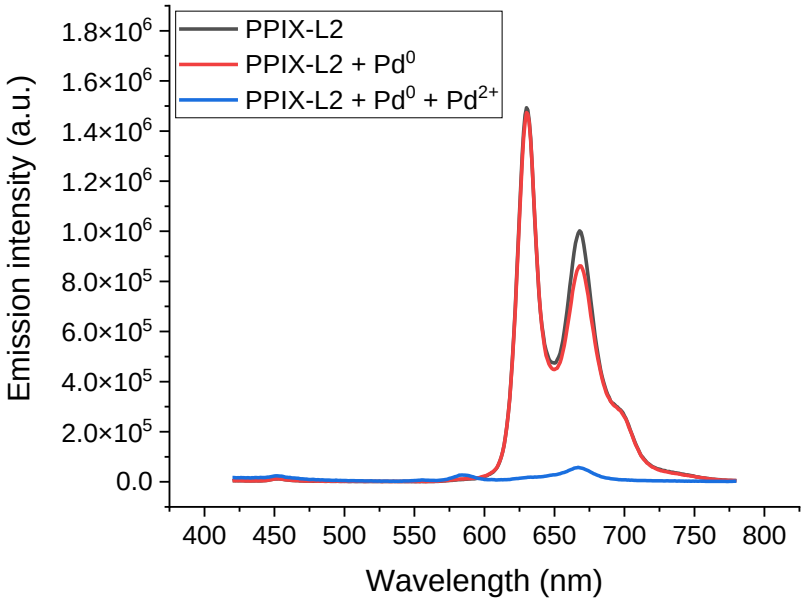

Figure 2.64: Fluorescence metal competition experiment of 2 µM PPIX-L2 in MeOH to 10 µM Pd^0 after four hours of incubation. λex: 400 nm, slit: 5-5 nm.

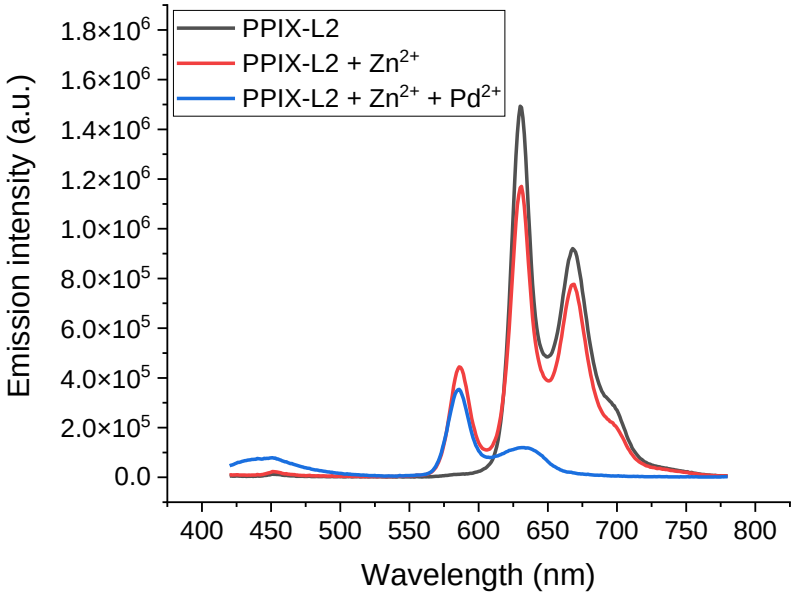

Figure 2.65: Fluorescence metal competition experiment of 2 µM PPIX-L2 in MeOH to 10 µM Zn^{2+} after four hours of incubation. λex: 400 nm, slit: 5-5 nm.

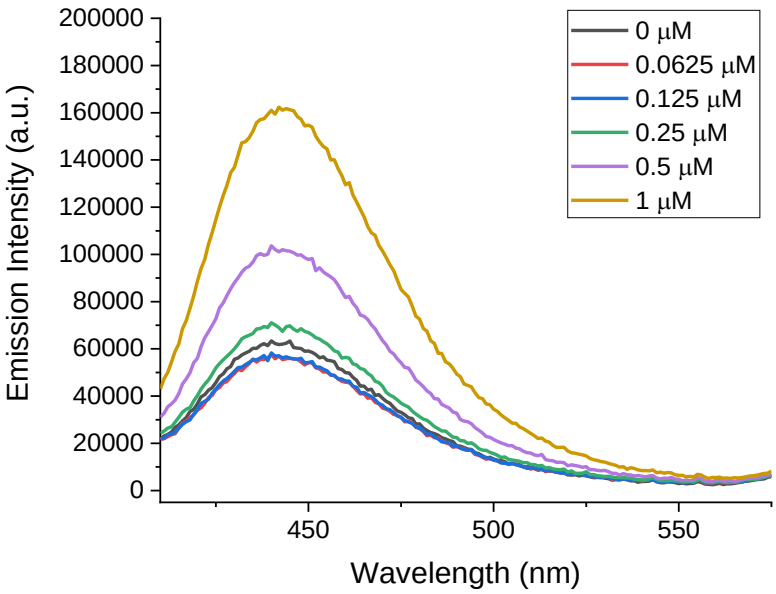

Figure 2.66: Detection limit fluorescence titration of 2 µM PPIX-L2 in MeOH to 0 - 1 µM Pd^0 after two hours of incubation. λex: 361 nm, slit: 5-5 nm.

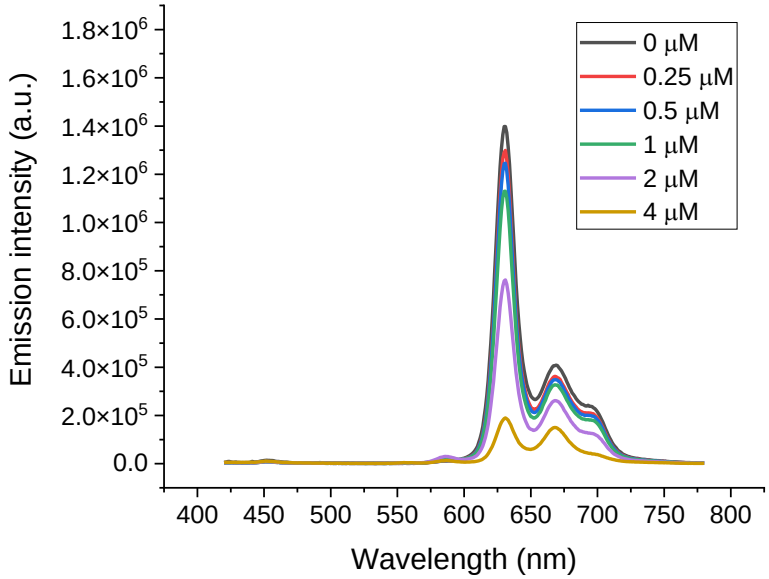

Figure 2.67: Detection limit fluorescence titration of 2 µM PPIX-L2 in MeOH to 0 - 4 µM Pd^{2+} after one hour of incubation. λex: 400 nm, slit: 5-5 nm.

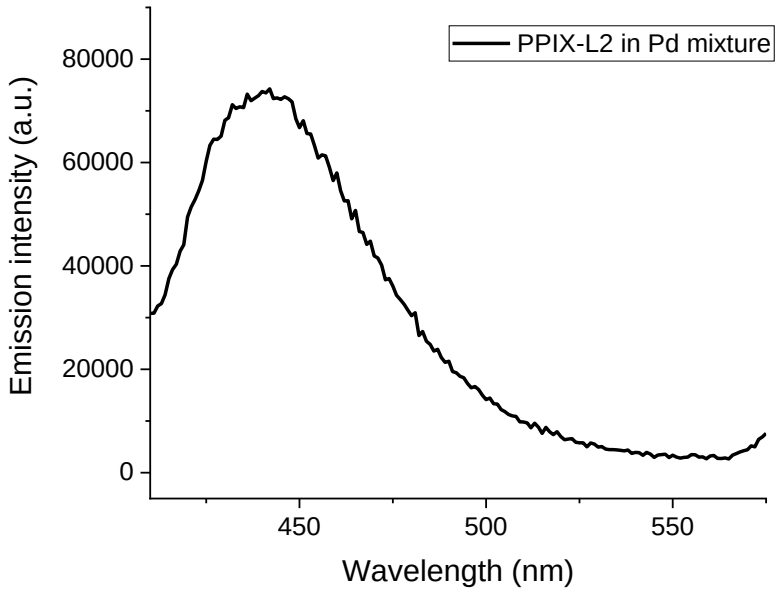

Figure 2.68: Quantification of Pd^0 in a sample mixture by 2 μM PPIX-L2 in MeOH after two hours of incubation. λex: 361 nm, slit: 5-5 nm.

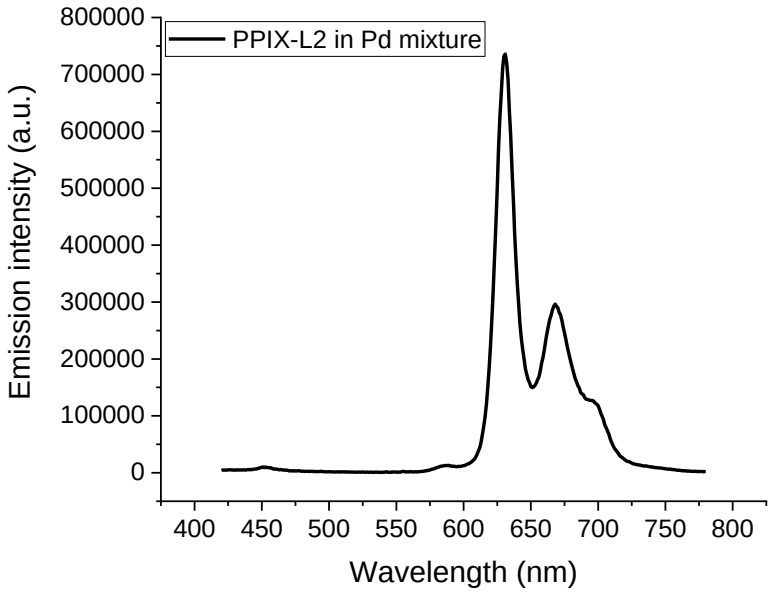

Figure 2.69: Quantification of Pd^{2+} in a sample mixture by 2 μM PPIX-L2 in MeOH after one hour of incubation. λex: 400 nm, slit: 5-5 nm.

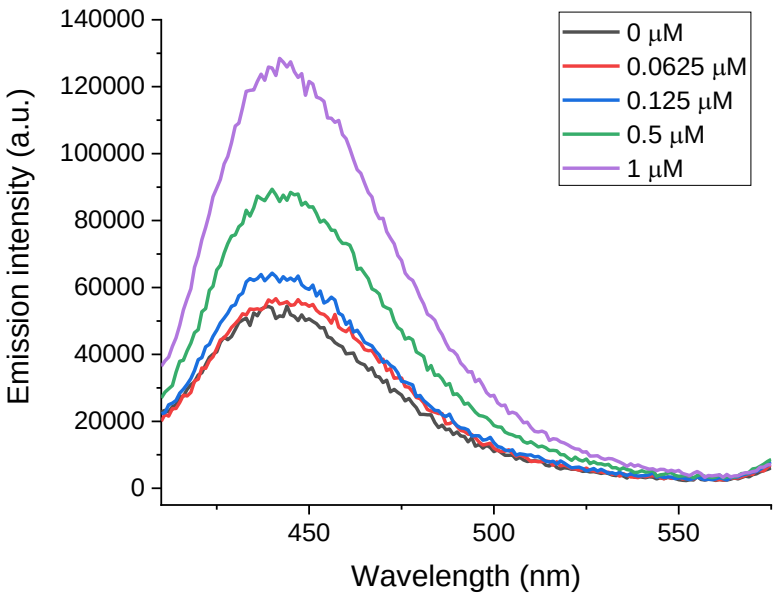

Figure 2.70: Detection limit fluorescence titration of 2 µM PPIX-L2 in MeOH to 0 - 1 µM Pd^0 after two hours of incubation in presence of 2 µM Pd^{2+}. λex: 361 nm, slit: 5-5 nm.

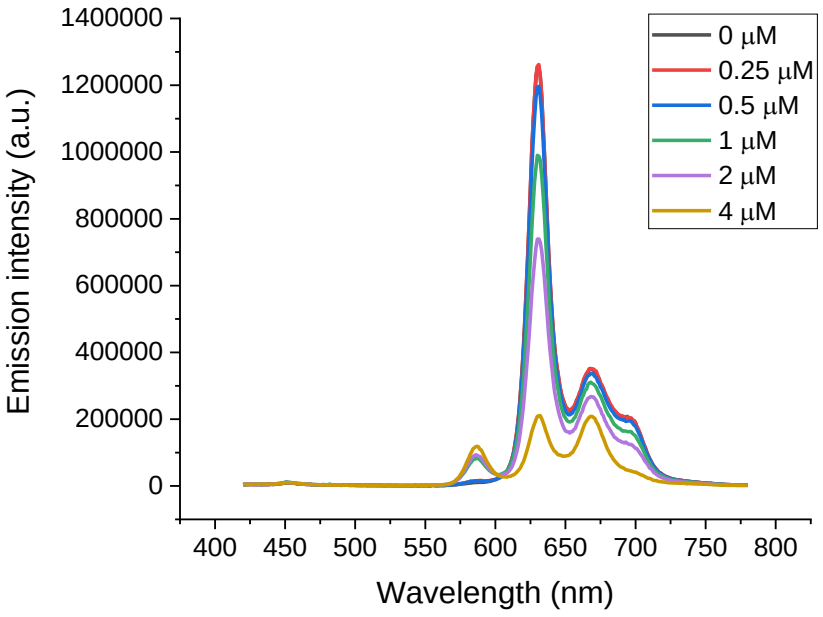

Figure 2.71: Detection limit fluorescence titration of 2 µM PPIX-L2 in MeOH to 0 - 1 µM Pd^0 after two hours of incubation in presence of 0.25 µM Pd^0. λex: 400 nm, slit: 5-5 nm.

Chapter 3: Luminescence/T_1-MRI dual-modality probe for H_2S imaging

3.1 Introduction

Hydrogen sulfide (H_2S) is one of the reactive sulfur species (RSS) and is considered a highly toxic substance to human body.[1-3] H_2S, along with carbon monoxide and nitric oxide, is an important gasotransmitter in the human body.[4] Over the past decades, emerging chemical biology research has put more focus on these gaseous molecules because they can be produced endogenously.[5] H_2S is produced through transsulfuration pathway by the enzymes such as cystathionine β-synthase (CBS) and cystathionine γ-lyase (CSE) in mammal system.[6] Within the transsulfuration pathway, the biothiols including cysteine, homocysteine and glutathione are consumed to produce H_2S.[7] H_2S participates in various cellular activities such as vasodilation regulation,[8] new blood vessel formation,[9] inflammation reduction[10] and oxidative stress regulation.[11] It is also reported that H_2S has been linked to various diseases, including Alzheimer's disease, Parkinson's disease[12, 13] and colon cancer. [14, 15]

In recent years, the development of new H_2S detection strategies has become highly necessary to support the surge in studies of H_2S in health science. Optical imaging is one of the most frequently used imaging techniques because it offers a real-time and high-sensitivity analysis of H_2S at the cellular level.[16, 17] Magnetic resonance imaging (MRI) is another commonly used clinical technique due to its non-invasive properties. It offers the advantages such as high spatial resolution, no tissue penetration limitations and no ionizing radiation.[18-20] However, no single imaging technique is perfect. It is difficult to rely solely on one method to obtain detailed and

comprehensive data. Therefore, combining the advantages of optical imaging and magnetic resonance imaging can not only improve the accuracy and specificity of the imaging results, but also reduce the disadvantages of both techniques.[21, 22]

To date, reaction-based small organic molecules[23, 24] and nanostructure-based materials[25, 26] have been employed for fluorescence and magnetic resonance dual-modal imaging. For the reaction-based fluorescent probe, three main strategies are used for H_2S detection.[27] The first one is the copper sulfide precipitation method. In this strategy, fluorescence of the probes is quenched by the pronounced quenching effect of the Cu^{2+} ion. In the presence of H_2S, the Cu^{2+} ion is allowed to react with H_2S, causing a precipitation reaction to form CuS. When the Cu^{2+} ion is released in the form of CuS, the quenching effect no longer exists, and the fluorescence of the probe is restored (Figure 3.1). [28]

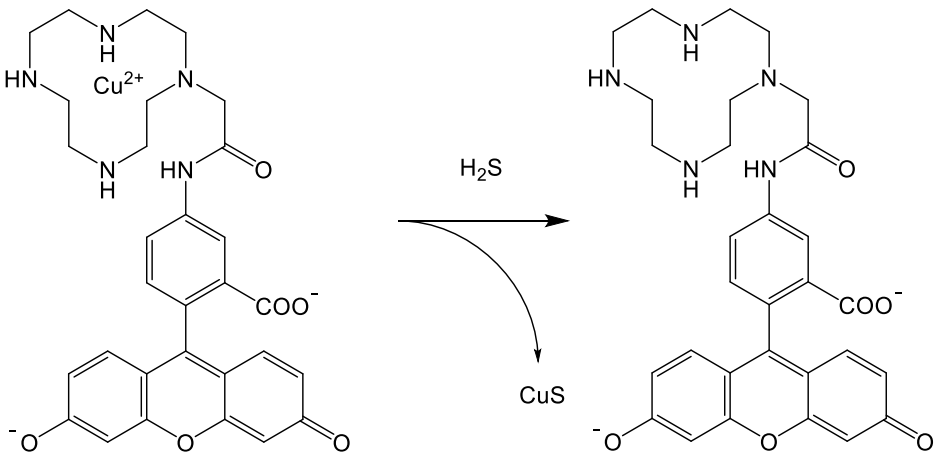

Figure 3.1: Example and sensing mechanism of copper sulfide precipitation-based fluorescent probe.

The second mechanism involves a reduction reaction of the probe, as H_2S is a reducing agent that can reduce the functional groups such as azide and nitro groups. In these types of probes, the electron-withdrawing property of azide and nitro group can effectively "pull" the electrons from the fluorophore to the electron-withdrawing groups. The fluorescence is then quenched by the ICT mechanism. In the presence of H_2S, the azide or nitro group is reduced to an electron-donating amine group, restoring the fluorescence of the probe (Figure 3.2).[29]

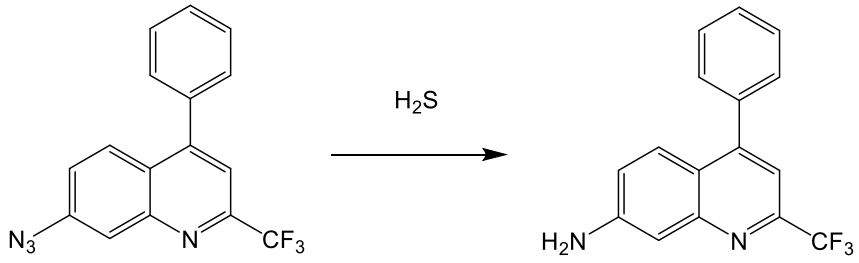

Figure 3.2: Example and sensing mechanism of reduction reaction-based fluorescent probe.

The third sensing mechanism of H_2S is the HS^- based thiolysis. In this reaction, the HS^- undergoes nucleophilic reaction to cleave the functional groups such as 2,4-dinitrophenyl (DNP), 2,4-dinitrobenzenesulfonyl (DBS), nitrobenzoxadiazole (NBD), disulfide linkage and diselenide linkage. After the thiolysis reaction, the fluorescence-quenching moiety is cleaved, releasing the fluorescence of the probe (Figure 3.3). [30]

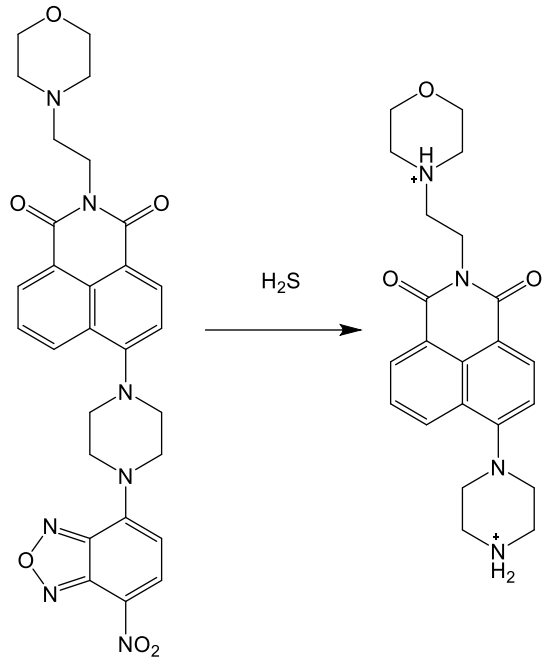

Figure 3.3: Example and sensing mechanism of nitrobenzoxadiazole thiolysis-based fluorescent probe.

For the reaction-based MRI probe, most of examples are nanostructure-based materials which still carry unknown risks due to their particle size and prolonged secretion time.[31] Small molecule-based MRI probes are very rare and often suffer from the problems such as single-modality detection and poor solubility in water. The development of lanthanide complexes successfully combines the diverse strengths of organic molecules and inorganic nanomaterials, offering high probe solubility in water, multimodal detection, low cytotoxicity and real-time sensitive analyte detection.

3.2 Scope of study

Although two optical/MRI nanoprobes have been developed for H_2S sensing,[32, 33] the safety concerns of nanomaterials in vivo are still unknown.[31] In this chapter, the dual-modality lanthanide-based molecular probe, NBD[Gd]-L2, is developed for H_2S detection. In the presence of H_2S, the C-N bond of NBD-piperazine is proposed to undergo thiolysis[34], forming NBD-SH and pz[Gd].[35] After the cleavage of the C-N bond, changes in the fluorescence signal and the relaxivity value will be studied. The fluorescence signal is expected to be quenched due to the formation of NBD-SH, and the MR signal is expected to change due to the loss of the NBD moiety, in response to H_2S (Figure 3.4).

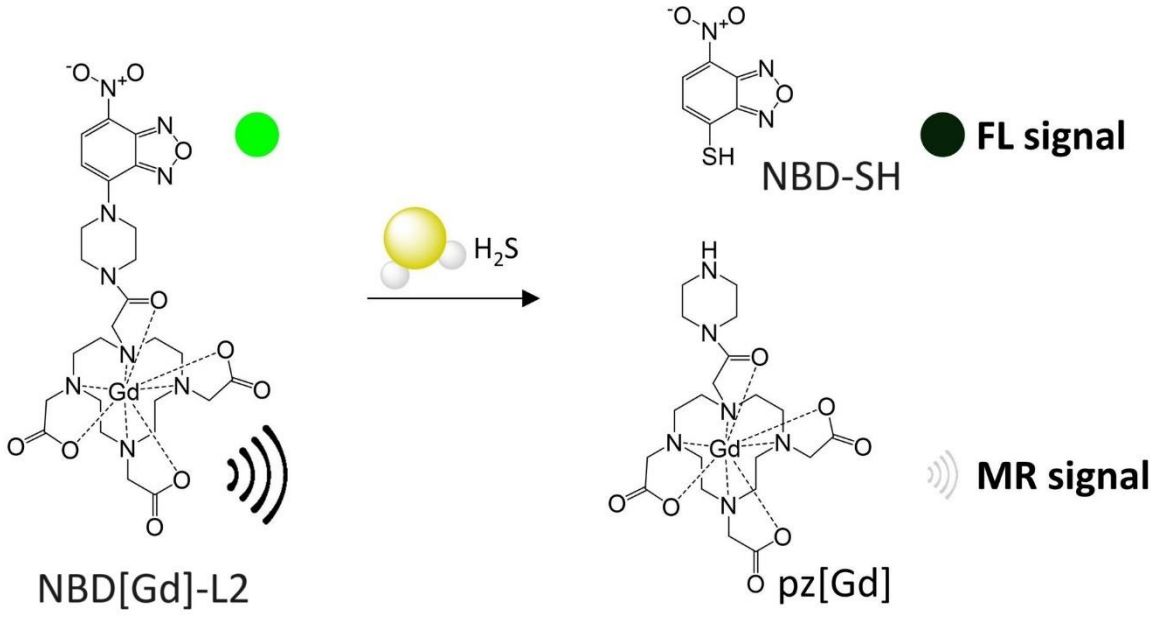

Figure 3.4: Design of the NBD[Gd]-L2.[36]

3.3 Result and discussion

Due to the excellent H_2S-triggered thiolysis property of nitrobenzoxadiazole (NBD) amine, NBD amine has attracted much attention and has been frequently utilized in H_2S detection and bioimaging over the past decade.[27, 35] H_2S can rapidly cleave the C-N bond of NBD amine by a nucleophilic aromatic substitution reaction under physiological conditions (neutral pH, 37°C and aquatic environment). However, most of the published small molecule-based H_2S probes have poor water solubility and require organic solvents such as dimethyl sulfoxide, ethanol and acetonitrile as co-solvent to dissolve the probes.[16] To meet the requirements of biological applications, improving the water solubility of the sensing probe is a top priority.

In the designed probes, NBD[Gd]-L1 and NBD[Gd]-L2, we chose the commercially available 4-chloro-7-nitro-2,1,3-benzoxadiazole (NBD-Cl) and 1,4,7,10-tetraazacyclododecane-1,4,7-tris(t-butyl acetate) (DO3A-tBu) as the starting materials to construct the dual-modality H_2S-sensing probe.

3.3.1 Design and synthesis of NBD[Gd]-L1

In the first attempt at a fluorescence/T_1-MRI dual-modality probe, NBD[Gd]-L1 was designed to link the NBD moiety directly to the lanthanide chelator, DO3A-tBu. After deprotection of tert-butyl group with TFA, gadolinium ions were expected to form lanthanide complexes with the organic ligand accordingly under methanol and water mixture (2:1) with pH adjusted to 6-7 using aqueous sodium hydroxide solution. In the design of NBD[Gd]-L1, the nine coordination sites of lanthanide can be completely occupied by the DO3A moiety (8 coordination sites) and NBD

moiety (1 coordination site). In the absence of H_2S, NBD[Gd]-L1 was expected to have a zero hydration number (q = 0) due to the full occupation of coordination site. In the presence of H_2S, thiolysis was expected to occur, cleaving the NBD moiety. This would reduce the number of occupied coordination sites of lanthanide, and the hydration number (q) would change from 0 to 1. The increase in hydration number would enhance the relaxation rate and produce a turn-on effect in MR imaging. In the fluorescence part, NBD[Gd]-L1 was expected to have strong fluorescence signal upon coupling with DO3A. After the thiolysis by H_2S, NBD moiety would be cleaved in the form of NBD-SH, resulting in a weak fluorescence signal and demonstrate a turn-off property in fluorescence imaging (Figure 3.5).

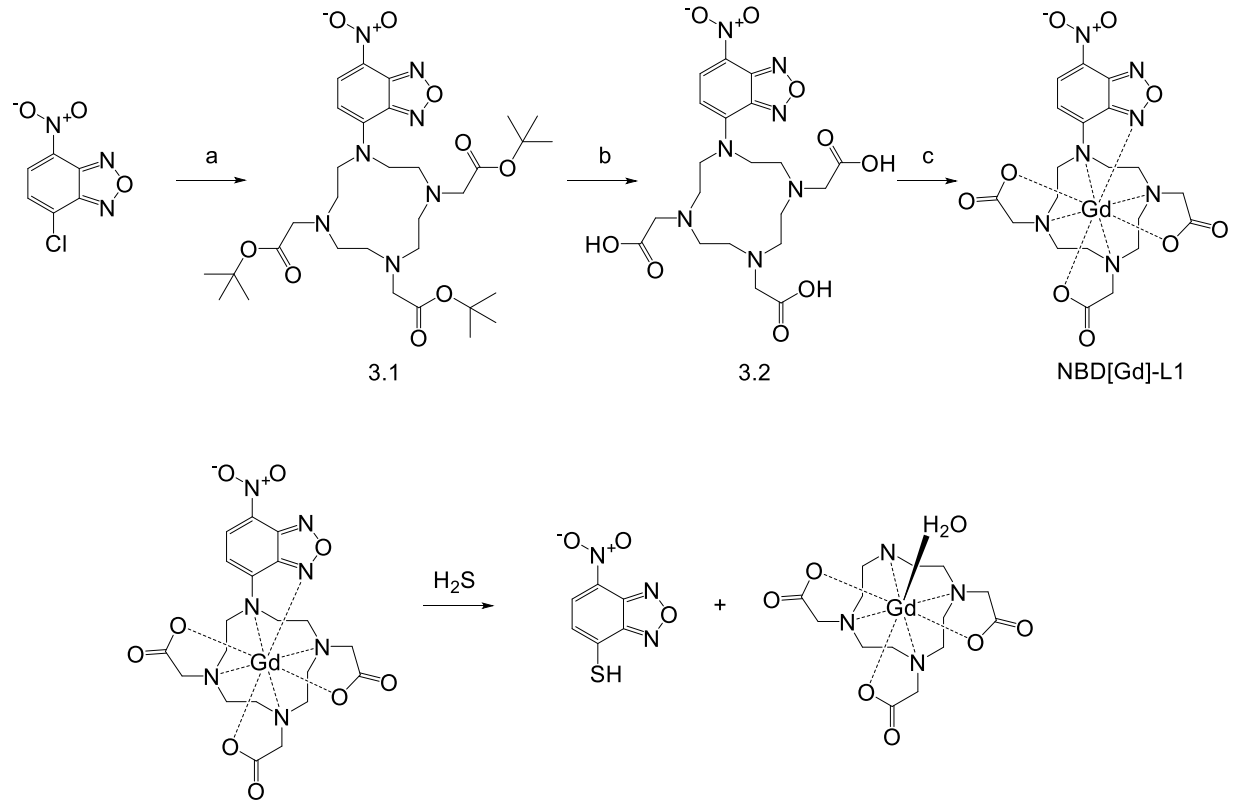

Figure 3.5: Synthetic route of NBD[Gd]-L1. Reagents and conditions: a. TEA, RT, 12 hours; b. TFA, RT, 12 hours; c. $GdCl_3 \cdot 6H_2O$/ $Gd(CF_3SO_3)_3$/ $Gd(CH_3COO)_3$, H_2O/MeOH, pH 5-6, RT - reflux, 24 h.

However, after the deprotection of the carboxyl group on compound 3.2, the organic ligand failed to form a lanthanide complex with lanthanide salt. In testing the complexation property of the organic ligand, three different gadolinium salts such as gadolinium(III) chloride hexahydrate, gadolinium(III) trifluoromethanesulfonate and gadolinium(III) acetate were used. The three gadolinium salts, each with a different counter ion, were added to conduct complexation reaction in methanol and water mixture (2:1) with pH 6-7 adjusted by aqueous sodium hydroxide solution and the reaction temperature was varied from room temperature to 50 °C, 80 °C and reflux, and the reaction proceeded for 24 hours. After 24 hours, high resolution mass spectrometer was used to check the complexation condition of the ligand (Table 3.1). From the LCMS data, only one peak corresponding to the mass of the ligand was displayed and the mass of the lanthanide metal complex could not be detected (Figure 3.6). The failure of the complexation may be due to the rigidity of the ligand. The rigid ligand backbone significantly hinders its ability to form lanthanide complex. In the ^{1}H NMR spectrum of compound 3.1, the spectrum demonstrated the rigidity of cyclen, causing the sharp and narrow peaks due to the lack of conformational changes or motions in compound 3.1 (Figure 3.7).

Table 3.1: Entries for NBD[Gd]-L1 complexation.

Entry	Lanthanide salt	Solvent	Temperature	Yield% (MS)
1	$GdCl_3 \cdot 6H_2O$	MeOH/H_2O (2:1), pH 6-7 (aq. NaOH)	RT	N.D.
2	$GdCl_3 \cdot 6H_2O$		50°C	N.D.
3	$GdCl_3 \cdot 6H_2O$		80 °C	N.D.
4	$GdCl_3 \cdot 6H_2O$		reflux	N.D.
5	$Gd(CF_3SO_3)_3$		RT	N.D.

6	$Gd(CF_3SO_3)_3$		50°C	N.D.
7	$Gd(CF_3SO_3)_3$		80 °C	N.D.
8	$Gd(CF_3SO_3)_3$		reflux	N.D.
9	$Gd(CH_3COO)_3$		RT	N.D.
10	$Gd(CH_3COO)_3$		50°C	N.D.
11	$Gd(CH_3COO)_3$		80 °C	N.D.
12	$Gd(CH_3COO)_3$		reflux	N.D.

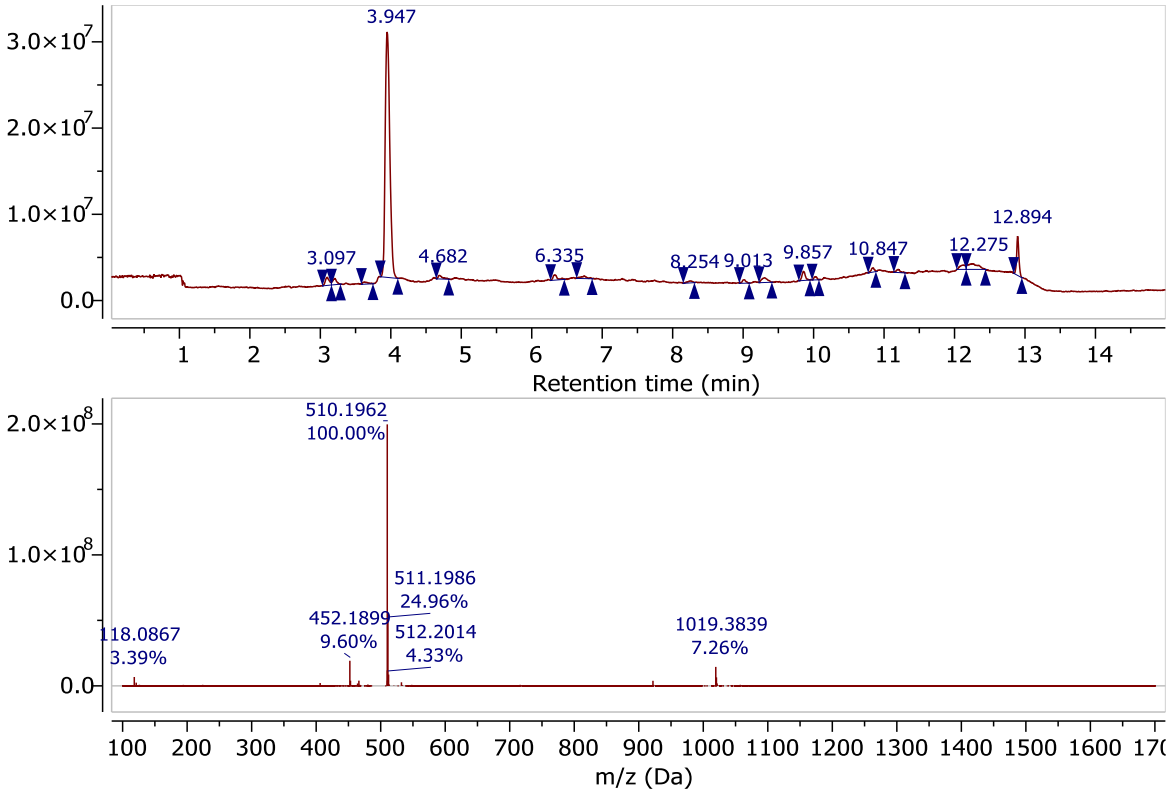

Figure 3.6: (top) UPLC chromatogram of compound 3.2. (bottom) Mass spectrum of compound 3.2.

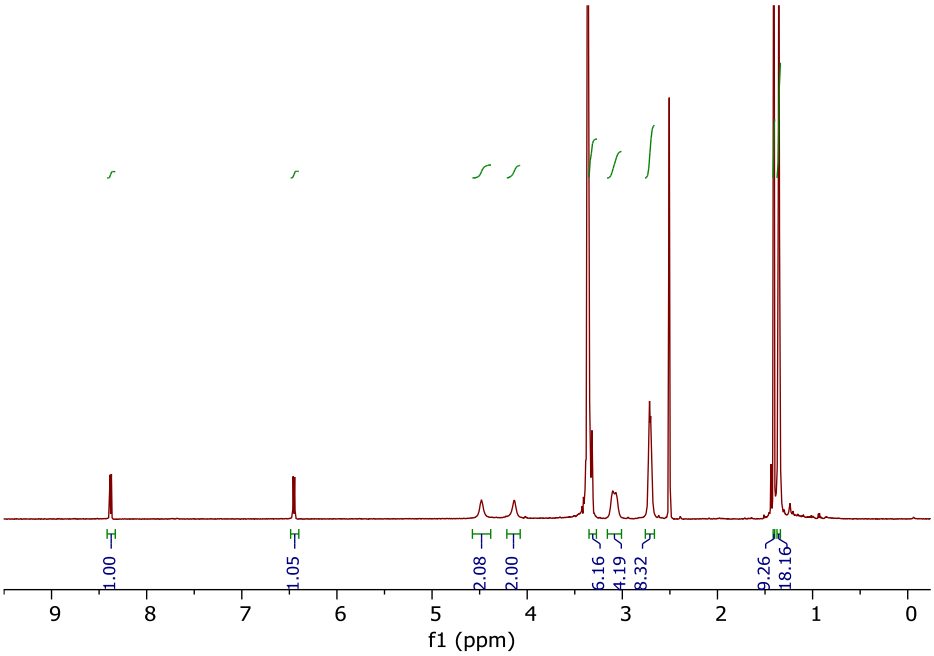

Figure 3.7: ^{1}H NMR spectrum of compound 3.1.

3.3.2 Design and synthesis of NBD[Gd]-L2

Due to the failure of lanthanide complexation in NBD[Gd]-L1, structural modification was performed on the linker between NBD and cyclen moiety. In the design of NBD[Gd]-L2, a piperazine carboxylate group was added between NBD and cyclen to reduce the rigidity of the molecule. NBD[Gd]-L2 was synthesized in five concise and high yielding steps (Figure 3.8). To improve the efficiency of synthesizing the compound 3.3, the first two steps were carried out in a one-pot synthesis. NBD-Cl was first allowed to react with the excess piperazine to yield NBD-piperazine. The reaction was monitored by low-resolution mass spectrometry (LRMS) and nuclear magnetic resonance spectroscopy (NMR) with less than 10% of over-reacted by-product observed. Then, triethylamine and chloroacetyl chloride were directly added to the solution mixture to react with the second amine group on piperazine, yielding compound 3.3. After purification of

compound 3.3, it was then reacted with another starting material, DO3A-tBu, to produce compound 3.4. In NBD[Gd]-L2, the DO3A moiety serves two purposes: it acted as a thermodynamically stable lanthanide chelator to avoid demetallation or further toxicity issues[37, 38] and it improved the solubility of the probe in water. After the deprotection of three tert-butyl ester groups in compound 3.4 using trifluoroacetic acid (TFA), TFA was removed under reduced pressure. Lanthanide complexation was done by adding gadolinium(III) chloride hexahydrate to the reaction mixture and the pH of reaction solution was maintained at pH 6 - 7 to yield the final product NBD[Gd]-L2.

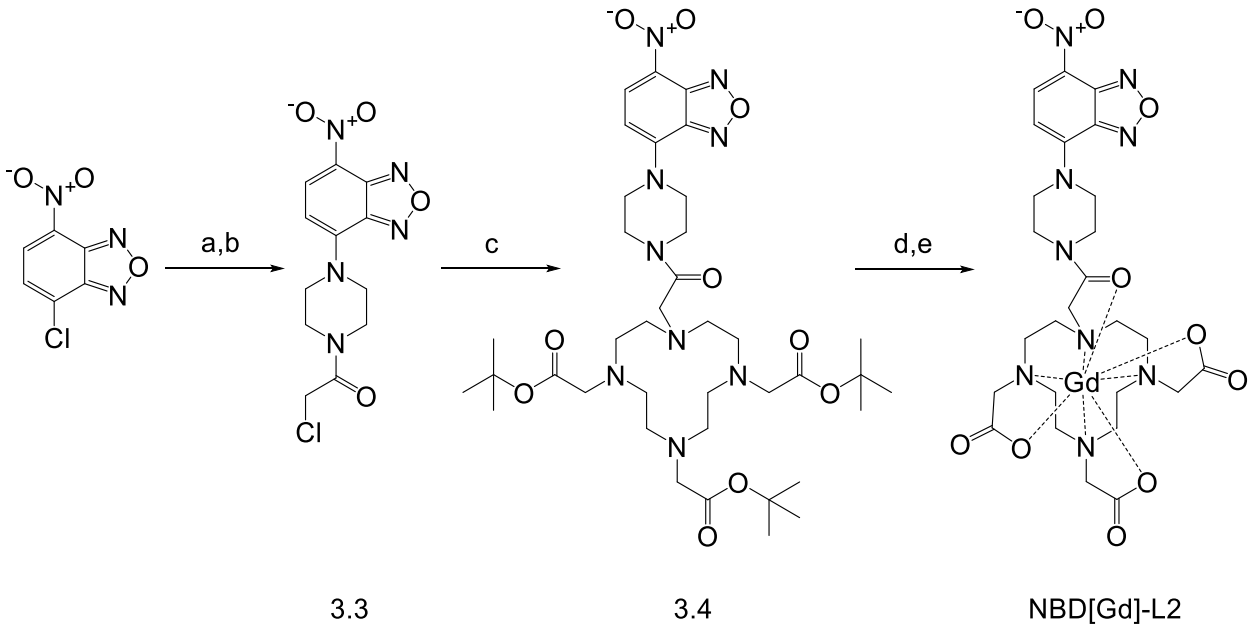

Figure 3.8: Synthetic route of NBD[Gd]-L2. Reagent and conditions: a. piperazine, THF, 0°C, 2 h; b. chloroacetyl chloride, triethylamine, THF, 0°C, 2 h; c. DO3A-tBu, K_2CO_3, ACN, N_2, 50°C, 12 h; d. TFA, RT, 12 h; e. $GdCl_3 \cdot 6H_2O$, H_2O/MeOH, pH 6-7, RT, 24 h.

3.3.3 Spectral measurements and response of NBD[Gd]-L2 towards H_2S

To test the thiolysis effect on NBD[Gd]-L2, time-dependent UV-visible absorption and fluorescence measurements were conducted to examine the optical signal response in the presence of H_2S. In UV-vis absorption measurements, 10 μM of NBD[Gd]-L2 was dissolved in 10 mM PBS buffer solution (pH 7.4) and displayed a strong absorption peak centred at 490 nm. After addition of 10 equivalents of H_2S to the system, the peak at 490 nm gradually vanished and red-shifted to 528 nm over 60 minutes. The significant 35 nm red shift caused the colour to change from light yellow to pink, which could be observed with naked eye (Figure 3.9). The pink colour was attributed to the cleavage of NBD-piperazine and formation of NBD-SH in the system. From the overlaid absorption spectra, a clear isosbestic point was found at 512 nm, demonstrating a clean set of overall transformation from NBD-piperazine to NBD-SH.[39] Furthermore, mass analysis was conducted to verify the reaction between NBD[Gd]-L2 and H_2S. The expected mass of NBD-SH and pz[Gd] was discovered in the mass spectrum, confirming the H_2S-triggered thiolytic reaction mechanism (Figure 3.10).

In the time-dependent fluorescence measurements, NBD[Gd]-L2 was studied under the same conditions as UV-vis absorption measurements. After adding 10 equivalents of H_2S for 60 minutes, the emission intensity at 545 nm was reduced by 88.4% compared to the initial value. From the emission intensity against time plot, the curve of emission change was fitted with a single exponential function with good correlation ($R^2 = 0.9985$) and the half-life of the reaction was 14.9 minutes (Figure 3.11). A dose-dependent absorption and emission response experiment was then conducted. In the absorption and emission titrations with H_2S, varying concentrations of H_2S were added to the NBD[Gd] and incubated for 60 minutes. A linear relationship was observed when

treating NBD[Gd]-L2 with 0 – 15 μM of H_2S in both titrations (Figure 3.12 and 3.13). The emission titration data were then used to examine the detection limit of the probe. Limit of detection (LOD) of NBD[Gd]-L2 was calculated to be 0.578 μM using the three-sigma method: LOD = 3σ/k.[40] In the selectivity experiment of NBD[Gd]-L2 towards H_2S, we chose different substances, including biothiols, amino acids and reactive anions. The emission intensity was recorded after adding 100 μM of these substances for 60 minutes. Most of the tested species did not show significant changes in emission intensity, especially the biothiols (Cys, GSH and Hcy). However, due to the strong oxidative property of ClO^-, there was a slight quenching effect on the probe. Nevertheless, the fluorescence quenching ability of ClO^- was much weaker than that of H_2S. These results show that NBD[Gd]-L2 has a good selectivity property towards H_2S (Figure 3.14).

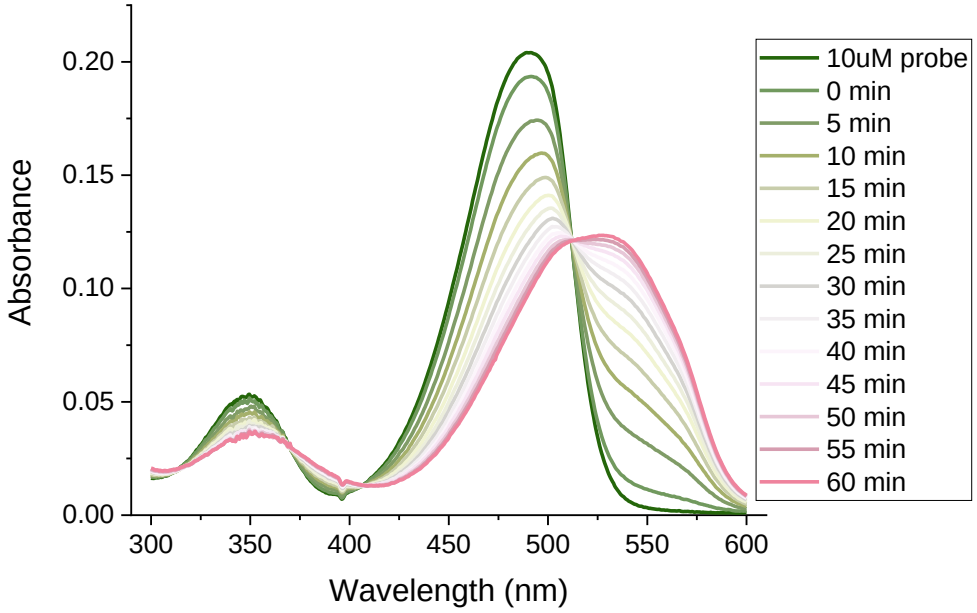

Figure 3.9: Time-dependent absorption titration of 10 μM NBD[Gd]-L2 in PBS to 100 μM of H_2S.

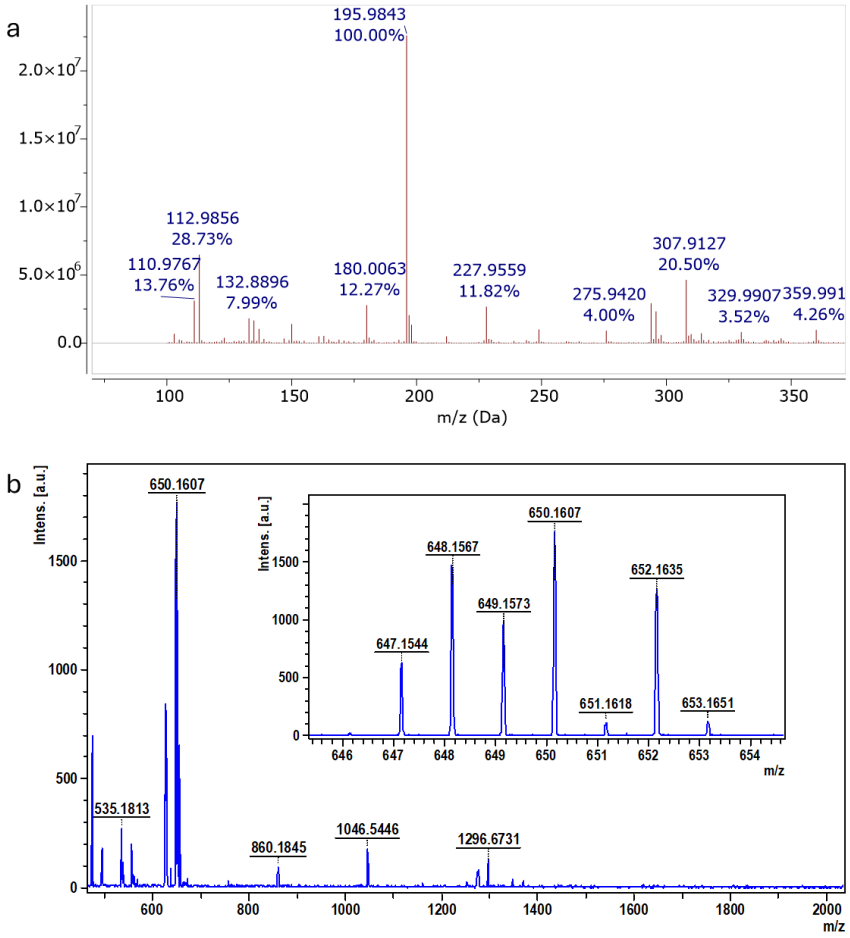

Figure 3.10: a) Mass spectrum of NBD-SH (calc $[M-H]^-$ = 197.9978) b) Mass spectrum of pz[Gd] (calc $[M+Na]^+$ = 650.1549). Inlet graph shows the focused mass spectrum ranging from m/z 645 to 655.

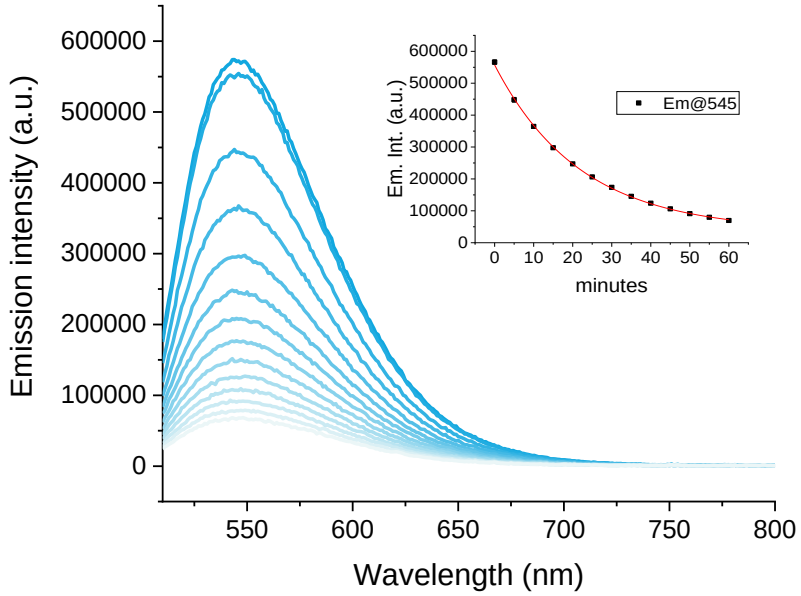

Figure 3.11: Time-dependent fluorescence titration of 10 µM NBD[Gd]-L2 in PBS to 100 µM of H_2S. Inlet graph shows the emission at 545 nm over 60 min. λex: 490 nm, slit: 5-5 nm.

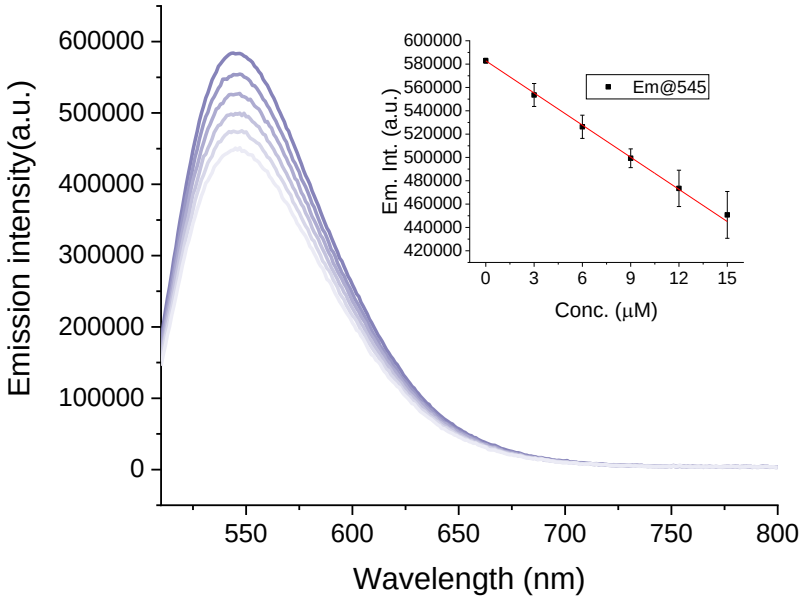

Figure 3.12: Dose-dependent fluorescence titration of 10 µM NBD[Gd]-L2 in PBS to 0 – 15 µM of H_2S. Inlet graph shows the emission at 545 nm at 60 min timepoint. λex: 490 nm, slit: 5-5 nm.

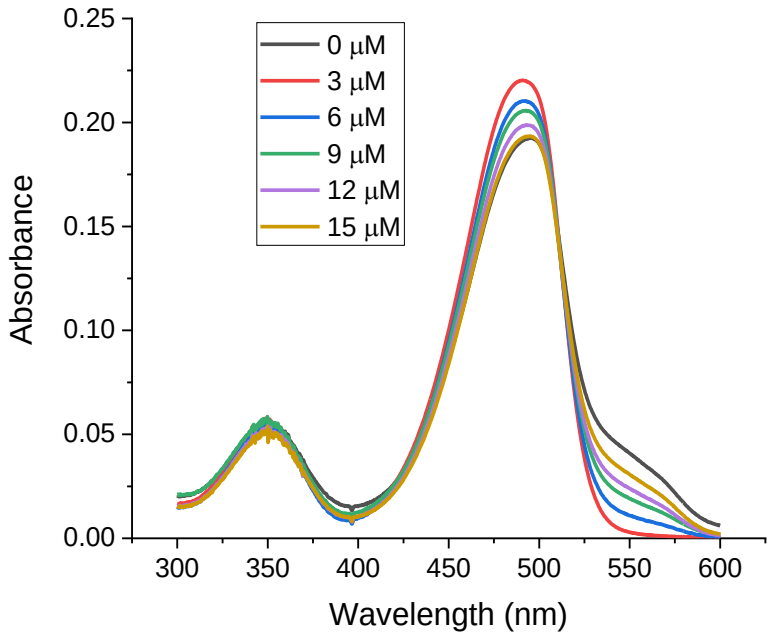

Figure 3.13: Dose-dependent absorption titration of 10 μM NBD[Gd] in PBS to 0 – 15 μM of H_2S.

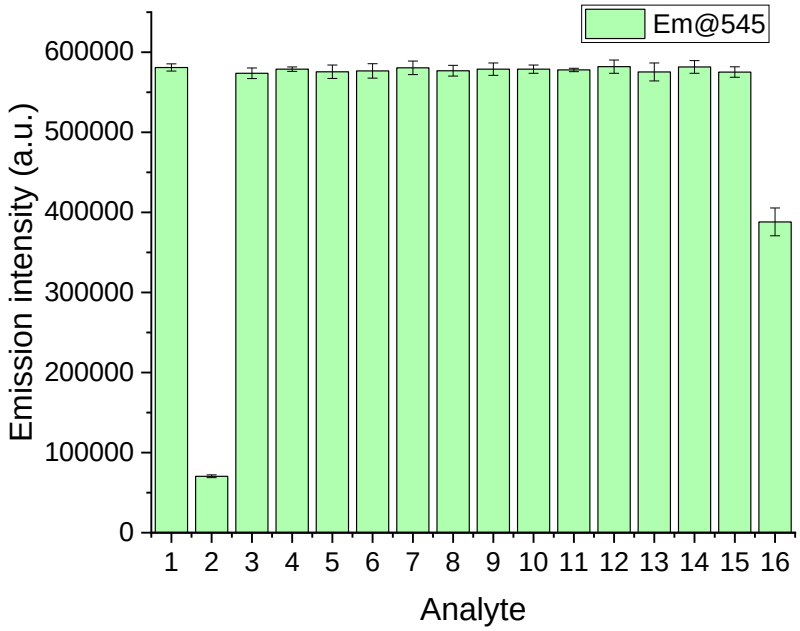

Figure 3.14: Fluorescence selectivity experiment of 10 μM NBD[Gd]-L2 in PBS to 100 μM analyte after one hour of incubation. 1: Control, 2: H_2S, 3: Cys, 4: GSH, 5: Hcy, 6: Arg, 7: Asn, 8: Asp, 9: Glu, 10: His, 11: Lys, 12: Met, 13: Pro, 14: Thr, 15: Br^-, 16: ClO^-. λex: 490 nm, λem: 545 nm, slit: 5-5 nm.

3.3.4 Cytotoxicity and fluorescence imaging in cells

After confirming the interaction between NBD[Gd]-L2 and H_2S, we investigated the potential application of NBD[Gd]-L2 in intracellular imaging. To examine the cell cytotoxicity, MTT assays were conducted on living normal human kidney cells (HK-2), cervical cancer cells (HeLa) and murine colorectal carcinoma cells (CT26). The experiment showed that the cell viability of HK-2 and HeLa cells was higher than 80% even when the concentration of probe rose to 500 μM and it only slightly reduced to around 70% in HeLa cells at 1000 μM of probe. In the normal HK-2 cells, cell viability remained over 90% at the probe concentration up to 1000 μM, demonstrating a low cytotoxic effect of probe on the normal living cells. Interestingly, when incubating CT26 cells with various concentrations of NBD[Gd]-L2, the cell viability dropped with increasing amounts of probe added, reaching 24% when 1000 μM of NBD[Gd]-L2 was added to the cellular environment. The cytotoxic effect of NBD[Gd]-L2 on CT26 cells may be due to the consumption of endogenous H_2S by NBD[Gd]-L2. As H_2S plays a vital role in the progression of CT26 and promotes the cancer cell proliferation, the reduction of H_2S concentration inhibits the growth of CT26 cells. When high levels of NBD[Gd]-L2 are incubated with living cells, NBD[Gd]-L2 may significantly consume the endogenous H_2S, leading to a potential cytotoxic effect on live CT26 cells (Figure 3.15). [41, 42]

Confocal imaging experiments were conducted to investigate intracellular imaging in living cells. In all experiments, the blue-fluorescent DNA stain 4',6-diamidino-2-phenylindole (DAPI) was used to label the cell nucleus. To test exogenous H_2S imaging ability, HeLa cells with exogenous H_2S were employed in the imaging experiment. 10 μM of NBD[Gd]-L2 was first added to the living cells and incubated for four hours. Then, 500 μM of H_2S was added to the cellular

environment and further incubated for 30 minutes. After incubation, the green fluorescence produced by NBD[Gd]-L2 in the HeLa cells was significantly quenched (Figure 3.16). Furthermore, to compare the imaging ability of H_2S in normal living cells and cancer cells with endogenous H_2S, confocal imaging experiments on HK-2 and CT26 living cells were conducted. In the experiment, 10 μM of NBD[Gd]-L2 was incubated with the cells for four hours. The green fluorescence in CT26 cells was almost completely quenched while the fluorescence in HK-2 cells remained. These results demonstrate the good imaging ability of NBD[Gd]-L2 in living cells for both exogenous and endogenous H_2S (Figure 3.17).

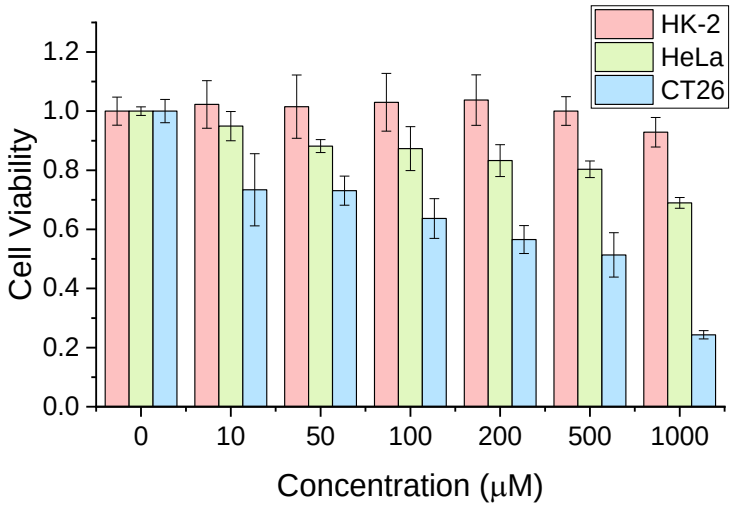

Figure 3.15: Cell viabilities of NBD[Gd]-L2 at concentrations 0 - 1000 μM for HK-2, HeLa and CT26 cells after 24 hours of incubation.

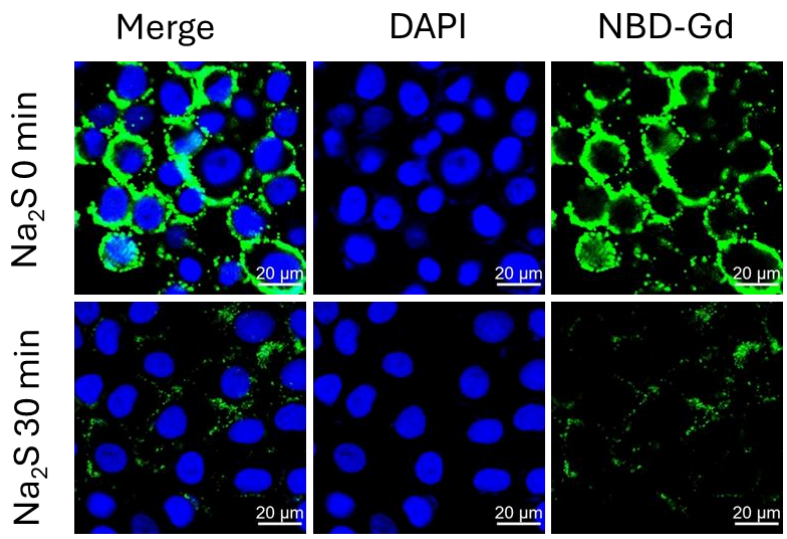

Figure 3.16: Confocal fluorescence imaging for exogenous H_2S sensing in HeLa cells. Cells were treated with 10 μM NBD[Gd]-L2 and incubated with 500 μM H_2S for 30 minutes.

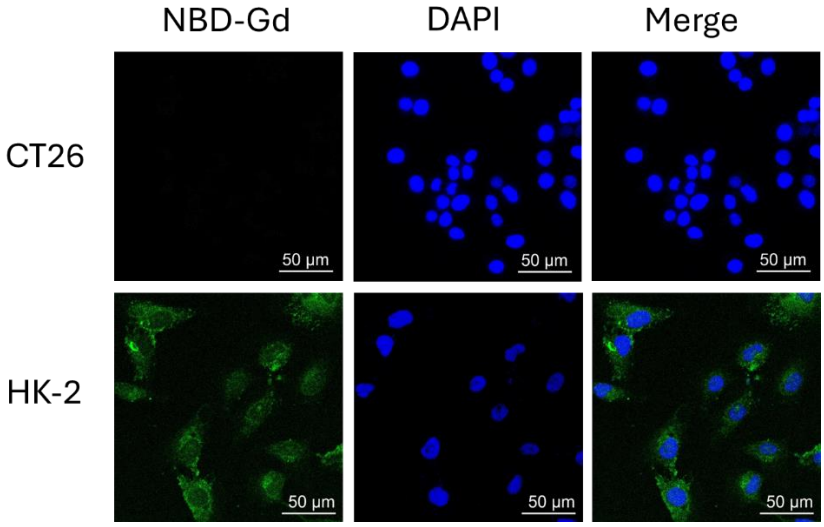

Figure 3.17: Confocal fluorescence imaging for endogenous H_2S sensing in CT26 and HK-2 cells. Cells were treated with 10 μM NBD[Gd]-L2 and incubated for four hours.

3.3.5 Magnetic resonance imaging (MRI) signal response of NBD[Gd]-L2 to H_2S

Next, we investigated the potential application of NBD[Gd]-L2 as an MRI contrast agent. MRI signal response of NBD[Gd]-L2 to H_2S was examined. Before measuring the magnetic relaxivity of NBD[Gd]-L2, the value of the clinical contrast agent Gadoteric acid (GdDOTA) was first measured as a reference. According to the equation $1/\Delta T_1 = r_1 \cdot [Gd]$, the longitudinal relaxivity (r_1) can be calculated as the slope from the $1/\Delta T_1$ vs [Gd] plot.[43] Relaxivity measurements were conducted on a series of concentrations (0 – 1 mM) of GdDOTA in 10 mM PBS buffer solution (pH 7.4) and the corresponding r_1 value was determined as 3.9 $mM^{-1}s^{-1}$ (1.4 T, 20°C). Since H_2S and H_2O have similar chemical properties, excess H_2S may affect the accuracy of r_1 value determination. Therefore, it is necessary to investigate whether the addition of H_2S affects the r_1 value. By adding 5 equivalents of H_2S solution to 0 – 1 mM GdDOTA, the r_1 value of GdDOTA + H_2S was determined to be 3.8 $mM^{-1}s^{-1}$ (1.4 T, 20°C). This result demonstrated that the addition of H_2S has a minor influence on the r_1 value of Gd complex (Figure 3.18 and Table 3.2).

To evaluate the changes in magnetic relaxivity, two sets of samples, NBD[Gd]-L2 and NBD[Gd]-L2 + H_2S, were prepared with the same set of concentrations as GdDOTA. For the preparation of the sample set of NBD[Gd]-L2 + H_2S, NBD[Gd]-L2 was first dissolved in PBS buffer solution. Then, 5 equivalents of H_2S solution were added to NBD[Gd]-L2 solution to obtain a 1 mM NBD[Gd]-L2 + H_2S solution. After four hours of stirring at room temperature, the sample solutions of NBD[Gd]-L2 were prepared by serial dilution method. The r_1 values for NBD[Gd]-L2 and NBD[Gd]-L2 + H_2S were measured as 4.4 $mM^{-1}s^{-1}$ and 2.8 $mM^{-1}s^{-1}$ respectively (Table 3.2). The 36.4% reduction in r_1 value was attributed to the change in the molecular weight of NBD[Gd]-L2 (Figure 3.18). Due to the H_2S-triggered thiolytic cleavage reaction, NBD-piperazine moiety was

cleaved and released as NBD-SH. This reaction caused a molecular weight loss to gadolinium complex. The reduced molecular weight increased the tumbling rate and decreased the r_1 value.[44] In the MR phantom experiments, GdDOTA, GdDOTA + H_2S and NBD[Gd]-L2 showed a "brighter" image and higher signal intensity than NBD[Gd]-L2 + H_2S which matched the results in relaxivity measurements that r_1 values of GdDOTA, GdDOTA + H_2S and NBD[Gd]-L2 were similar and higher than that of NBD[Gd]-L2 + H_2S (Figure 3.19 and 3.20).

Equation	y = a + b*x			
Plot	GdDOTA	GdDOTA+H2S	NBD[Gd]-L2	NBD[Gd]-L2 + H
Weight	Instrumental			
Intercept	0.32268 ± 1.56557E-	0.33266 ± 0.0019	0.34804 ± 0.0013	0.29661 ± 0.019
Slope	3.93489 ± 0.00486	3.78446 ± 0.0167	4.35323 ± 0.0095	2.7954 ± 0.1954
Residual Sum of Square	1.90744	5.60413	7.52188	40.22091
Pearson's r	1	0.99996	0.99999	0.99037
R-Square (COD)	0.99999	0.99992	0.99998	0.98083
Adj. R-Square	0.99999	0.9999	0.99998	0.97603

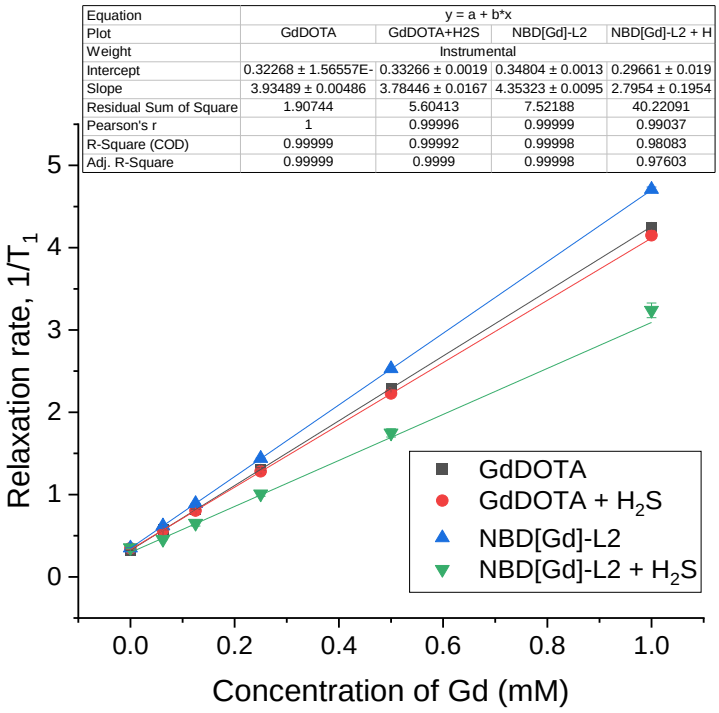

Figure 3.18: The T_1-weighted relaxivity (r_1) of GdDOTA, GdDOTA + H_2S, NBD[Gd]-L2 and NBD[Gd]-L2 + H_2S, measured at 1.4 T and 20°C.

Table 3.2: T_1-weighted relaxivity (r_1) values of GdDOTA, GdDOTA + H_2S, NBD[Gd]-L2 and NBD[Gd]-L2 + H_2S.

At 1.4T, 25°C in PBS:	**r_1, $mM^{-1}s^{-1}$**
GdDOTA (reference)	3.9 ± 0.0049
GdDOTA + H_2S	3.8 ± 0.017
NBD[Gd]-L2	4.4 ± 0.0095
NBD[Gd]-L2 + H_2S	2.8 ± 0.20

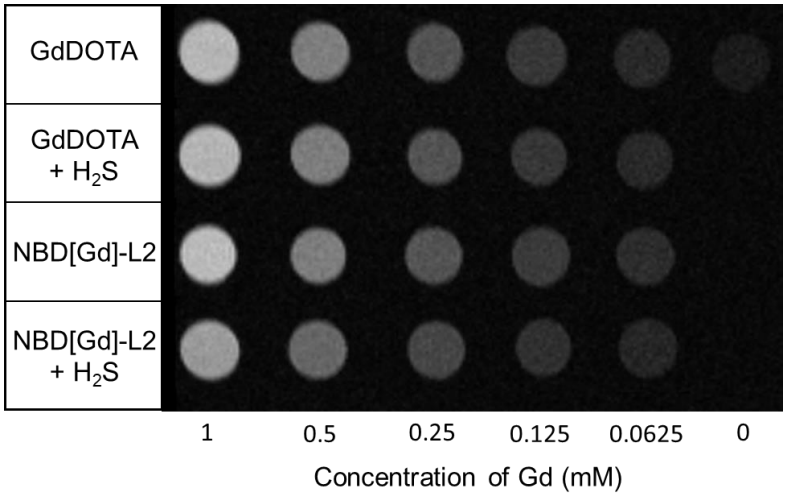

Figure 3.19: T_1-weighted MR phantom image of 0 - 1 mM GdDOTA, 0 - 1 mM GdDOTA + H_2S, 0 - 1 mM NBD[Gd]-L2 and 0 - 1 mM NBD[Gd]-L2 + 5 eq. H_2S in PBS, acquired at 7 T and 25°C.

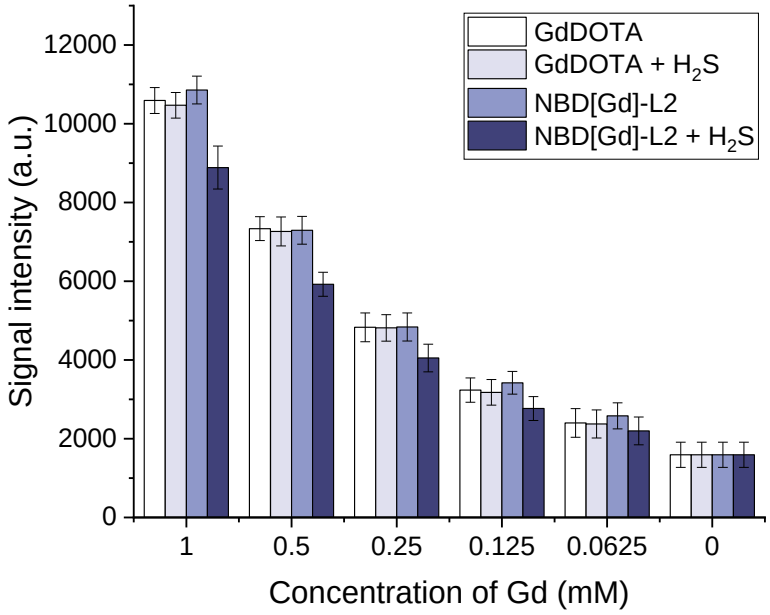

Figure 3.20: Signal intensity of the T_1-weighted MR phantom image of 0 - 1 mM GdDOTA, 0 – 1 mM GdDOTA + 5 eq. H_2S, 0 - 1 mM NBD[Gd]-L2 and 0 - 1 mM NBD[Gd]-L2 + 5 eq. H_2S in PBS, acquired at 7 T and 25°C.

To further investigate the change in relaxivity, the water exchange rate of the complexes was determined. A variable temperature ^{17}O T_2 measurement was performed to analyse the water exchange rate.[45] By measuring the transverse ^{17}O relaxation rate as a function of temperature on the aqueous solution of NBD[Gd]-L2 and NBD[Gd]-L2 + H_2S at 1 mM, the data were fitted to a four-parameter model to estimate the water exchange rate of the complexes. In the Gd^{3+} complex, the paramagnetic shift of $H_2{}^{17}O$ is small, so the reduced transverse relaxation rate ($1/T_{2r}$) of the bulk $H_2{}^{17}O$ can be determined by the following equation:

$$\frac{1}{T_{2r}} = \left(\frac{1}{T_2} - \frac{1}{T_{2A}}\right)\left(\frac{[H_2O]}{q[Gd]}\right) = \frac{1}{T_{2m} + \tau_m} \qquad \text{Equation 3.1}$$

where $1/T_{2A}$ refers to the relaxation rate of the diamagnetic reference, q refers to the hydration number of the Gd^{3+} complex. $1/T_{2m}$ refers to the relaxation rate of the coordinated water oxygen. In the high temperature (fast exchange condition), $1/T_{2r} = 1/T_{2m}$; while in low temperature (slow exchange condition), $1/T_{2r} \approx 1/\tau_m = k_{ex}$ (water exchange rate).

In the relaxation mechanism of $1/T_{2m}$, the scalar contribution is the most important parameter. It is a function of the spin quantum number of Gd^{3+} (S = 7/2), electronic relaxation time of Gd^{3+} ($T_{1e,}$ which is also written as T_{1e}^{HF} in the "high field" condition), the mean residence lifetime (τ_M) and the hyperfine coupling constant between Gd^{3+} ions and the oxygen nucleus of the water molecule ($A/\hbar$). In this set of equations, some assumptions have been made. The water exchange rate ($1/\tau_m = k_{ex}$) is assumed using Eyring equations (Equation 3.2) where $\Delta S^{\ddagger}$ and $\Delta H^{\ddagger}$ refer to the activation entropy and enthalpy for the water exchange process respectively. The term k_{ex}^{298} refers the water exchange process at a temperature of 298.15 K. In this equation, R refers to the gas constant while, k_b and h refer to the Boltzmann constant and Planck constant respectively. For the hyperfine coupling constant, it was previously reported that the $A/\hbar$ value for coordination of lanthanide and oxygen (Ln-O) is in a narrow range. It is then assumed that the $A/\hbar$ for the water molecule coordinated to Gd^{3+} ion is -3.8 x 10^6 rad/s.[45] Furthermore, the water exchange rate (k_{ex}) and electronic relaxation rate ($1/T_{1e}$) are also assumed to have exponential temperature dependence. To analyse the variable temperature data, they were then fitted into a well-developed four parameters model: the water exchange rate at 298.15 K (k_{ex}^{298}), activation enthalpy for water exchange process ($\Delta H^{\ddagger}$), electronic relaxation rate at 298.15 K ($1/T_{1e}^{298}$) and $1/T_{1e}$ activation energy ($\Delta E_{T_{1e}}$). (Equation 3.1 – 3.4) From the fitted curves, the four relaxation parameters were estimated (Figure 3.21 and 3.22) and summarized in the Table 3.3. As the residual water lifetime

is the inverse of the water exchange rate constant ($1/k_{ex}$), the residual water lifetime of NBD[Gd]-L2 and NBD[Gd]-L2 + H_2S at 298.15 K was then calculated to be 1.54 μs and 0.323 μs respectively. Compared to NBD[Gd]-L2 + H_2S, the extended residual water lifetime of NBD[Gd]-L2 allowed enough time for bulk water to reach the inner sphere of NBD[Gd]-L2 and become fully relaxed. Therefore, the relaxivity of NBD[Gd]-L2 was higher than that of NBD[Gd]-L2 + H_2S.[46, 47]

$$\frac{1}{T_{2m}} \approx \frac{1}{T_2^{sclar}} = \frac{S(S+1)}{3}\left(\frac{A}{\hbar}\right)^2 \tau_{sc}; \frac{1}{\tau_{sc}} = \frac{1}{T_{1e}} + \frac{1}{\tau_m} \qquad \text{Equation 3.2}$$

$$\frac{1}{\tau_m} = k_{ex} = \frac{k_B T}{h} \exp\left[\frac{\Delta S^{\ddagger}}{R} - \frac{\Delta H^{\ddagger}}{RT}\right] = \frac{k_{ex}^{298} T}{298.15} \exp\left[\frac{\Delta H^{\ddagger}}{R}\left(\frac{1}{298.15} - \frac{1}{T}\right)\right] \qquad \text{Equation 3.3}$$

$$\frac{1}{T_{1e}^{HF}} = \frac{1}{T_{1e}^{298}} \exp\left[\frac{\Delta E_{T_{1e}}}{R}\left(\frac{1}{T} - \frac{1}{298.15}\right)\right] \qquad \text{Equation 3.4}$$

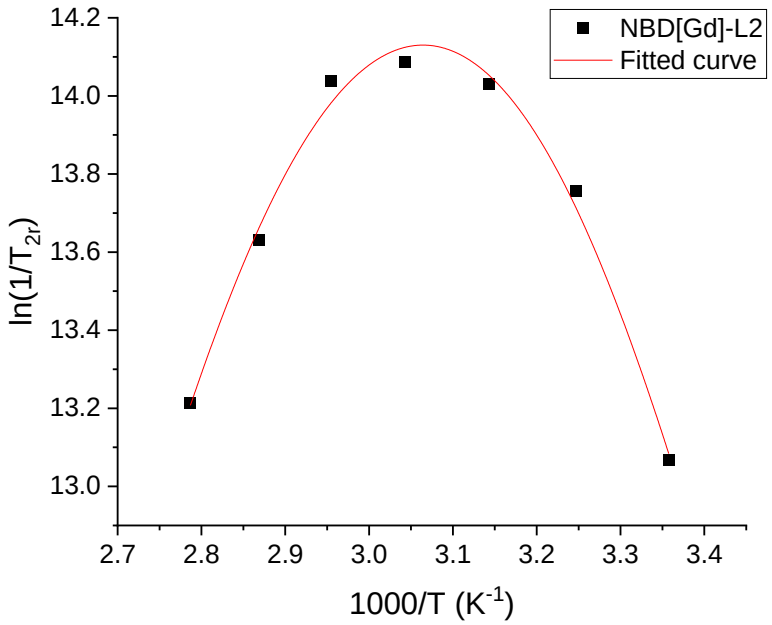

Figure 3.21: Variable temperature transverse relaxation in $H_2{}^{17}O$ of NBD[Gd]-L2.

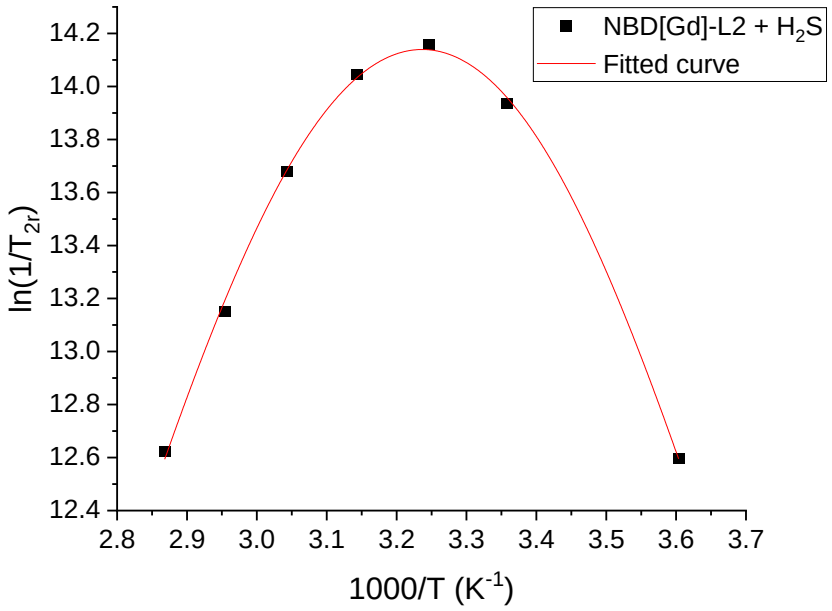

Figure 3.22: Variable temperature transverse relaxation in $H_2{}^{17}O$ of NBD[Gd]-L2 + H_2S.

Table 3.3: Water exchange parameters for NBD[Gd]-L2 and NBD[Gd]-L2 + H_2S in PBS (14.1 T).

	NBD[Gd]-L2	**NBD[Gd]-L2 + H_2S**
k_{ex}^{298} ($x10^6$ s^{-1})	0.649 ± 0.0879	3.059 ± 1.581
$\Delta H^{\ddagger}$ (kJ mol^{-1})	70.994 ± 1.563	70.368 ± 0.638
$1/T_{1e}^{298}$ ($x10^7$ s^{-1})	3.652 ± 1.114	3.712 ± 0.259
$\Delta E_{T_{1e}}$ (kJ mol^{-1})	-1.084 ± 8.541	-0.564 ± 4.106

3.4 Conclusion and future works

In this work, we presented a gadolinium complex-based fluorescence/ MRI dual-responsive probe, NBD[Gd]-L2, for H_2S detection in a physiological environment. NBD[Gd]-L2 can completely dissolve in PBS buffer solution, addressing the common water solubility problem of small organic molecule-based fluorescent probes that often require organic solvent such as DMSO, ethanol, and ACN as co-solvent to dissolve the probe. NBD[Gd]-L2 highly responded to H_2S, showing 88.4% fluorescence quenching with a detection limit of 578 nM within 60 minutes. Furthermore, NBD[Gd]-L2 displayed a magnetic relaxivity changing property in the presence of H_2S. With the assistance of H_2S-triggered thiolytic cleavage reaction, NBD-piperazine was cleaved, resulting in a molecular weight loss in gadolinium complex. This increase in the tumbling rate of the complex, led to a 36.4% reduction in the T_1-weighted relaxivity (r_1) value. Furthermore, in the variable temperature T_2 $H_2{}^{17}O$ study, the residual water lifetime of NBD[Gd]-L2 was one order of magnitude longer than that of NBD[Gd]-L2 + H_2S. This allowed enough time for bulk water to reach Gd^{3+} and become fully relaxed, contributing to a higher relaxivity (r_1) in NBD[Gd]-L2. In biological experiments, NBD[Gd]-L2 demonstrated low cytotoxicity in the investigated HK-2 and HeLa cells. In confocal imaging and MR phantom experiment, NBD[Gd]-L2 showed significant signal changes, demonstrating its the potential in bioimaging.

For future work, the sensing properties of the probe should be improved as the fluorescence and magnetic response of NBD[Gd]-L2 both show a “turn-off” property. In probe development, a “turn-on” mechanism is still a more preferred option because it is easier to measure the response signal with higher contrast against the background noise. This can also help increase the sensitivity of the probe. In terms of optical response properties, a new chromophore could be applied to probe.

As NBD moiety can act as a FRET quencher for H_2S sensing probe, a new chromophore could be used to give responsive fluorescence signal directly or even be an antenna to transfer energy to a luminescent lanthanide ion such as Tb^{3+}, Eu^{3+}, producing a long luminescence lifetime signal. This would further increase the signal-to-noise ratio and improve the sensitivity of the probe. In terms of magnetic response properties, further development can apply a self-immolative linker to the probe. As the self-immolative linkers contain carbamate functional group, the carbamate functional group could be one of the coordinators to the lanthanide metal centre. By removing the self-immolative linker, the hydration number of the lanthanide could be increased, providing a relaxivity enhancement property to the probe.

3.5 Experimental Section

General information

Deuterated solvents were purchased from Cambridge Isotope Laboratories. All other solvents and reagents were reagent grade and purchased from either Sigma-Aldrich Chemical Co. or Dieckmann and used without further purification. Thin-layer chromatography (TLC) was performed using pre-coated silica gel 60, F254 plates with a thickness of 0.2 mm. Column chromatography was conducted using silica gel and laboratory grade solvents. NMR spectra were recorded on Bruker Avance III 600 MHz spectrometers (^{1}H NMR on 600 MHz, ^{13}C NMR on 151 MHz) at 298 K. Chemical shifts δ were reported in parts per million (ppm) and referenced to corresponding solvent peak (2.50 for DMSO-d6 and 7.26 for $CDCl_3$). Coupling constants *J* were reported in Hertz (Hz) and multiplicities were abbreviated as: s = singlet, d = doublet, t = triplet, dd = doublets of doublets, td = triplets of doublets and m = multiplet. High-resolution mass spectra, reported as m/z, were conducted by University Research Facility in Life Science, Hong Kong Polytechnic University from Agilent 6540 liquid chromatography – electrospray ionisation quadrupole-TOF mass spectrometer or Bruker UltrafleXtreme MALDI-TOF-TOF mass spectrometer. Low-resolution mass spectra were conducted by Waters Acquity H-Class UPLC with QDa mass detector for monitoring reactions and determining correct fraction during purification of product. Fluorescence spectra were recorded on Horiba FluoroMax 4 Spectrofluorometer in a 1 cm quartz cuvette.

HPLC methods

Analytical HPLC was carried out using Agilent 1260 Infinity II LC system equipped with a 1260 Infinity II Quaternary Pump and an inline diode array UV-Vis detector. Semi-preparative HPLC was carried out with Waters semi-preparative HPLC system equipped with 2535 Quaternary Gradient Solvent Pump, 2707 Autosampler, Fraction Collector III and 2998 Photodiode Array Detector. Absorbance at 254 and 490 nm was monitored. The column used for analytical HPLC was an Atlantis T3 Column, 5 μm, 4.6 x 250 mm C18 reverse phase column. The column used for semi-preparative HPLC was Atlantis T3 OBD Prep Column, 5 μm, 19 x 250 mm, C18 reverse phase column.

Cell culture and Cytotoxicity Test

HK-2, HeLa and CT26 cells were grown in Dulbecco's Modified Eagle Medium (DMEM). The medium was supplemented with 10% fetal bovine serum and 1% penicillin and streptomycin. The cell lines were incubated at 37°C in a humidified atmosphere containing 5% CO2. Cell viability was measured by the MTT assay. The cells were placed in a 96-well plate and incubated for twelve hours for adherence. The various concentrations of NBD[Gd]-L2 (0, 10, 50, 100, 200, 500, 1000 μM) in phosphate-buffered saline (PBS) were added and incubated for 24 hours. After discarding media from cell cultures, 50 μL of serum-free media and 50 μL of MTT solution were added to each well and the plate was incubated at 37°C for 3 hours. When the incubation finished 150 μL of MTT solvent was added into each well. The plate was wrapped in foil and shaken on an orbital shaker for 15 minutes. Optical absorbance was measured at 590 nm on a BioTek Synergy 2 plate reader. Relative cell viability was determined by the equation RV = (Ae – A0)/(Ac – A0) x 100%,

where Ae is the absorbance of the experimental test; Ac is the absorbance of the control test (DMSO only); A0 is the absorbance of the blank test (no cells).

In vitro fluorescence imaging

HK-2, HeLa and CT26 cells were seeded on a 35 mm glass bottom petri dish. The cells were incubated with NBD[Gd]-L2 (10 μM) and co-stained with 4',6-diamidino-2-phenylindole (DAPI) for four hours. The cells were then washed twice with phosphate buffered saline (PBS) and the fresh medium was added before imaging. Images were acquired using 405 and 488 nm laser excitation of ZEISS LSM 980 with Airyscan 2 confocal laser scanning microscope.

Relaxometry at 1.41 T

T_1-weighed relaxation times were measured on a Magritek Benchtop NMR Spinsolve 60 MHz equipped with MestReNova software. T_1 relaxation times were measured with the following parameters: Scans: 2, Acquisition time: 6.4 s, Repetition time: 30 s, Maximum inversion time: 2, 5, 10, 15 s, Dummy Scans: 2, Number of steps: 11.

MR imaging of solution phantom at 7 T

Relaxivity measurements at 7 Tesla were performed on Bruker Biospec 70/20 USR Magnetic Resonance Imaging System with a 20 cm bore running on a ParaVision® 360 software. Samples were prepared and placed in glass capillary tube with approximate diameter of 1 mm. The capillary tube was then secured to a 50 ml centrifuge tube which was placed in a volume radiofrequency

coil with 40 mm inner diameter and centred in the magnet bore. T1 relaxation time was measured using variable repetition time accelerated spin echo sequence (RARE-VTR) with the parameters: TR = 300 ms; TE = 11ms, field of view = 40mm x 40 mm, matrix size = 384 x 384, number of axial slices = 5, slice thickness = 1 mm.

Synthesis work and characterization:

Synthesis of compound 3.3:

To a stirred solution of 4-Chloro-7-nitro-2,1,3-benzoxadiazole (0.5 mmol) in 5 mL of THF at 0°C, piperazine (0.75 mmol) was added. The resulting mixture was stirred for two hours, and the progress of the reaction was monitored by TLC. After the starting material, 4-Chloro-7-nitro-2,1,3-benzoxadiazole, was consumed, chloroacetyl chloride and triethylamine were dropwise added to the reaction mixture which was allowed to warm to room temperature for two hours. Then, the reaction mixture was evaporated to dryness under reduced pressure. The residue was purified by flash column chromatography (dichloromethane/methanol = 100:1 v/v) on silica gel to give yellow solid compound 3.3 with a yield of 84%. ^{1}H NMR (600 MHz, DMSO-d_6) δ 8.53 (dd, J = 9.1, 1.1 Hz, 1H), 6.64 (d, J = 9.1 Hz, 1H), 4.49 (s, 2H), 4.22 (d, J = 26.5 Hz, 4H), 3.79 (dt, J = 24.2, 5.4 Hz, 4H). ^{13}C NMR (151 MHz, DMSO) δ 165.55, 145.93, 145.29, 145.24, 136.82, 121.76, 103.78, 49.25, 48.79, 44.25, 42.53, 41.53. HRMS (ESI-TOF): m/z calcd. $[M+Na]^+$ = 348.0476, found 348.0475.

Synthesis of compound 3.4:

Compound 3.3 (0.418 mmol), DO3A-tBu (0.4598 mmol) and K_2CO_3 (1.254 mmol) were suspended in anhydrous ACN under a nitrogen atmosphere and the suspension was stirred for 12 hours at 50°C. When the reaction was complete, the reaction mixture was allowed to return to room temperature and the inorganic salts were filtered off. The mixture was then evaporated to dryness under reduced pressure. The residue was purified by flash column chromatography (dichloromethane/methanol = 15:1 v/v) on silica gel to give yellow solid compound 3.4 with a yield of 56%. ^{1}H NMR (600 MHz, DMSO-d_6) δ 8.54 (d, J = 9.1 Hz, 1H), 6.65 (d, J = 9.2 Hz, 1H), 4.38 – 3.97 (m, 4H), 3.80 – 3.69 (m, 4H), 3.67 – 3.41 (m, 4H), 3.27 – 2.98 (m, 6H), 2.88 – 2.54 (m, 6H), 2.27 – 1.86 (m, 8H), 1.44 (s, 27H). ^{13}C NMR (151 MHz, DMSO) δ 173.06, 172.97, 171.32, 145.87, 145.27, 145.18, 136.78, 121.99, 103.87, 81.48, 55.72, 55.67, 55.06, 49.05, 48.65, 42.87, 40.82, 28.09, 28.00. HRMS (ESI-TOF): m/z calcd. $[M+Na]^+$ = 826.4439, found 826.4474.

Synthesis of NBD[Gd]-L2:

Compound 3.4 was dissolved in trifluoroacetic acid and stirred at room temperature for 24 hours. The reaction mixture was evaporated to dryness under reduced pressure. The residue was dissolved in MeOH/H_2O (1:2), followed by the addition of gadolinium(III) chloride hydrate. The mixture was maintained at a pH range of 6 - 7 by adding NaOH solution and stirred at 50°C for 12 hours. When the metal coordination was complete, the crude product was purified by Semi-Preparative High-Performance Liquid Chromatography to yield yellow product NBD[Gd]-L2 with a yield of 86%. HRMS (ESI-TOF): m/z calcd. $[M+Na]^+$ = 813.1567, found 813.1739.

3.6 Reference

[1] C. Szabó, "Hydrogen sulphide and its therapeutic potential," *Nature Reviews Drug Discovery,* vol. 6, no. 11, pp. 917-935, 2007, doi: 10.1038/nrd2425.

[2] J. Jiang, A. Chan, S. Ali, A. Saha, K. J. Haushalter, W.-L. M. Lam, M. Glasheen, J. Parker, M. Brenner, S. B. Mahon, H. H. Patel, R. Ambasudhan, S. A. Lipton, R. B. Pilz, and G. R. Boss, "Hydrogen Sulfide—Mechanisms of Toxicity and Development of an Antidote," *Scientific Reports,* vol. 6, no. 1, p. 20831, 2016, doi: 10.1038/srep20831.

[3] K. R. Olson, Y. Gao, F. Arif, K. Arora, S. Patel, E. R. DeLeon, T. R. Sutton, M. Feelisch, M. M. Cortese-Krott, and K. D. Straub, "Metabolism of hydrogen sulfide (H_2S) and Production of Reactive Sulfur Species (RSS) by superoxide dismutase," *Redox Biology,* vol. 15, pp. 74-85, May 2018, doi: 10.1016/j.redox.2017.11.009.

[4] R. Wang, "Two's company, three's a crowd: can H_2S be the third endogenous gaseous transmitter?," *The FASEB Journal,* vol. 16, no. 13, pp. 1792-8, Nov 2002, doi: 10.1096/fj.02-0211hyp.

[5] G. Cirino, C. Szabo, and A. Papapetropoulos, "Physiological roles of hydrogen sulfide in mammalian cells, tissues, and organs," *Physiological Reviews,* vol. 103, no. 1, pp. 31-276, Jan 1 2023, doi: 10.1152/physrev.00028.2021.

[6] B. Renga, "Hydrogen Sulfide Generation in Mammals: The Molecular Biology of Cystathionine-β-Synthase (CBS) and Cystathionine-γ;-Lyase (CSE)," *Inflammation & Allergy - Drug Targets,* vol. 10, no. 2, pp. 85-91, 2011, doi: 10.2174/187152811794776286.

[7] O. Kabil, V. Vitvitsky, P. Xie, and R. Banerjee, "The Quantitative Significance of the Transsulfuration Enzymes for H_2S Production in Murine Tissues," *Antioxidants & Redox Signaling,* vol. 15, no. 2, pp. 363-372, 2011, doi: 10.1089/ars.2010.3781.

[8] M. Bhatia, "Hydrogen sulfide as a vasodilator," *IUBMB Life (International Union of Biochemistry and Molecular Biology: Life),* vol. 57, no. 9, pp. 603-606, 2005, doi: 10.1080/15216540500217875.

[9] C. Szabó and A. Papapetropoulos, "Hydrogen sulphide and angiogenesis: mechanisms and applications," *British Journal of Pharmacology,* vol. 164, no. 3, pp. 853-865, 2011, doi: 10.1111/j.1476-5381.2010.01191.x.

[10] M. Whiteman and P. G. Winyard, "Hydrogen sulfide and inflammation: the good, the bad, the ugly and the promising," *Expert Review of Clinical Pharmacology,* vol. 4, no. 1, pp. 13-32, 2011, doi: 10.1586/ecp.10.134.

[11] C. Munteanu, M. A. Turnea, and M. Rotariu, "Hydrogen Sulfide: An Emerging Regulator of Oxidative Stress and Cellular Homeostasis—A Comprehensive One-Year Review," *Antioxidants,* vol. 12, no. 9, p. 1737, 2023, doi: 10.3390/antiox12091737.

[12] E. Disbrow, K. Y. Stokes, C. Ledbetter, J. Patterson, R. Kelley, S. Pardue, T. Reekes, L. Larmeu, V. Batra, S. Yuan, U. Cvek, M. Trutschl, P. Kilgore, J. S. Alexander, and C. G. Kevil, "Plasma hydrogen sulfide: A biomarker of Alzheimer's disease and related dementias," *Alzheimer's & Dementia,* vol. 17, no. 8, pp. 1391-1402, 2021, doi: 10.1002/alz.12305.

[13] L. F. Hu, M. Lu, C. X. Tiong, G. S. Dawe, G. Hu, and J. S. Bian, "Neuroprotective effects of hydrogen sulfide on Parkinson’s disease rat models," *Aging Cell,* vol. 9, no. 2, pp. 135-146, 2010, doi: 10.1111/j.1474-9726.2009.00543.x.

[14] C. Szabo, C. Coletta, C. Chao, K. Módis, B. Szczesny, A. Papapetropoulos, and M. R. Hellmich, "Tumor-derived hydrogen sulfide, produced by cystathionine-β-synthase, stimulates bioenergetics, cell proliferation, and angiogenesis in colon cancer," *Proceedings*

of the National Academy of Sciences, vol. 110, no. 30, pp. 12474-12479, 2013, doi: 10.1073/pnas.1306241110.

[15] W. J. Cai, M. J. Wang, L. H. Ju, C. Wang, and Y. C. Zhu, "Hydrogen sulfide induces human colon cancer cell proliferation: role of Akt, ERK and p21," *Cell Biology International,* vol. 34, no. 6, pp. 565-72, Apr 14 2010, doi: 10.1042/CBI20090368.

[16] J. Li, Z. Su, C. Yu, Y. Yuan, Q. Wu, J. Liu, B. Peng, W. Hu, X. Lu, H. Yu, L. Li, and W. Huang, "Recent progress in the development of sensing systems for in vivo detection of biological hydrogen sulfide," *Dyes and Pigments,* vol. 192, 2021, doi: 10.1016/j.dyepig.2021.109451.

[17] W. Liu, J. Chen, and Z. Xu, "Fluorescent probes for biothiols based on metal complex," *Coordination Chemistry Reviews,* vol. 429, 2021, doi: 10.1016/j.ccr.2020.213638.

[18] J. Zhao, J. Chen, S. Ma, Q. Liu, L. Huang, X. Chen, K. Lou, and W. Wang, "Recent developments in multimodality fluorescence imaging probes," *Acta Pharmaceutica Sinica B,* vol. 8, no. 3, pp. 320-338, May 2018, doi: 10.1016/j.apsb.2018.03.010.

[19] V. Hartwig, G. Giovannetti, N. Vanello, M. Lombardi, L. Landini, and S. Simi, "Biological Effects and Safety in Magnetic Resonance Imaging: A Review," *International Journal of Environmental Research and Public Health,* vol. 6, no. 6, pp. 1778-1798, 2009, doi: 10.3390/ijerph6061778.

[20] Q. Meng, M. Wu, Z. Shang, Z. Zhang, and R. Zhang, "Responsive gadolinium(III) complex-based small molecule magnetic resonance imaging probes: Design, mechanism and application," *Coordination Chemistry Reviews,* vol. 457, 2022, doi: 10.1016/j.ccr.2021.214398.

[21] X. Xiao, H. Cai, Q. Huang, B. Wang, X. Wang, Q. Luo, Y. Li, H. Zhang, Q. Gong, X. Ma, Z. Gu, and K. Luo, "Polymeric dual-modal imaging nanoprobe with two-photon aggregation-induced emission for fluorescence imaging and gadolinium-chelation for magnetic resonance imaging," *Bioactive Materials,* vol. 19, pp. 538-549, Jan 2023, doi: 10.1016/j.bioactmat.2022.04.026.

[22] Z. Nie, N. Luo, J. Liu, X. Zeng, Y. Zhang, and D. Su, "Multi-mode biodegradable tumour-microenvironment sensitive nanoparticles for targeted breast cancer imaging," *Nanoscale Research Letters,* vol. 15, no. 1, 2020, doi: 10.1186/s11671-020-03309-w.

[23] K. G. Fosnacht and M. D. Pluth, "Activity-Based Fluorescent Probes for Hydrogen Sulfide and Related Reactive Sulfur Species," *Chemical Reviews,* vol. 124, no. 7, pp. 4124-4257, Apr 10 2024, doi: 10.1021/acs.chemrev.3c00683.

[24] L. Jiang, H.-N. Mak, E. R. H. Walter, W.-T. Wong, K.-L. Wong, and N. J. Long, "A fluorescent probe for the discrimination of oxidation states of palladium," *Chem. Sci.,* vol. 12, no. 29, pp. 9977-9982, 2021, doi: 10.1039/d1sc01616d.

[25] Y. Luo, C. Zhu, D. Du, and Y. Lin, "A review of optical probes based on nanomaterials for the detection of hydrogen sulfide in biosystems," *Analytica Chimica Acta,* vol. 1061, pp. 1-12, Jul 11 2019, doi: 10.1016/j.aca.2019.02.045.

[26] B. Chen, L. Liu, R. Yue, Z. Dong, C. Lu, C. Zhang, G. Guan, H. Liu, Q. Zhang, and G. Song, "Stimuli-responsive switchable MRI nanoprobe for tumor theranostics," *Nano Today,* vol. 51, 2023, doi: 10.1016/j.nantod.2023.101931.

[27] V. S. Lin, W. Chen, M. Xian, and C. J. Chang, "Chemical probes for molecular imaging and detection of hydrogen sulfide and reactive sulfur species in biological systems," *Chemical Society Reviews,* vol. 44, no. 14, pp. 4596-4618, 2015, doi: 10.1039/c4cs00298a.

[28] K. Sasakura, K. Hanaoka, N. Shibuya, Y. Mikami, Y. Kimura, T. Komatsu, T. Ueno, T. Terai, H. Kimura, and T. Nagano, "Development of a Highly Selective Fluorescence Probe for Hydrogen Sulfide," *Journal of the American Chemical Society,* vol. 133, no. 45, pp. 18003-18005, 2011, doi: 10.1021/ja207851s.

[29] H. Zhu, C. Liang, X. Cai, H. Zhang, C. Liu, P. Jia, Z. Li, Y. Yu, X. Zhang, W. Sheng, and B. Zhu, "Rational Design of a Targetable Fluorescent Probe for Visualizing H_2S Production under Golgi Stress Response Elicited by Monensin," *Analytical Chemistry,* vol. 92, no. 2, pp. 1883-1889, 2020, doi: 10.1021/acs.analchem.9b04009.

[30] J. Ou-Yang, W.-L. Jiang, K.-Y. Tan, H.-W. Liu, S.-J. Li, J. Liu, Y.-F. Li, and C.-Y. Li, "Two-photon fluorescence probe for precisely detecting endogenous H_2S in lysosome by employing a dual lock system," *Sensors and Actuators B: Chemical,* vol. 260, pp. 264-273, 2018, doi: 10.1016/j.snb.2017.12.205.

[31] Y. Ning, M. Zhu, and J.-L. Zhang, "Near-infrared (NIR) lanthanide molecular probes for bioimaging and biosensing," *Coordination Chemistry Reviews,* vol. 399, 2019, doi: 10.1016/j.ccr.2019.213028.

[32] W. Zeng, L. Wu, Y. Ishigaki, T. Harimoto, Y. Hu, Y. Sun, Y. Wang, T. Suzuki, H. Y. Chen, and D. Ye, "An Activatable Afterglow/MRI Bimodal Nanoprobe with Fast Response to H_2S for In Vivo Imaging of Acute Hepatitis," *Angewandte Chemie International Edition,* vol. 61, no. 4, p. e202111759, Jan 21 2022, doi: 10.1002/anie.202111759.

[33] C. Zhang, J. Li, C. Lu, T. Yang, Y. Zhao, L. Teng, Y. Yang, G. Song, and X.-B. Zhang, "H_2S-Activated “One-Key Triple-Lock” Bis-Metal Coordination Network for Visualizing Precise Therapy of Colon Cancer," *CCS Chemistry,* vol. 3, no. 8, pp. 2126-2142, 2021, doi: 10.31635/ccschem.020.202000369.

[34] F. Song, Z. Li, J. Li, S. Wu, X. Qiu, Z. Xi, and L. Yi, "Investigation of thiolysis of NBD amines for the development of H_2S probes and evaluating the stability of NBD dyes," *Organic & Biomolecular Chemistry,* vol. 14, no. 47, pp. 11117-11124, 2016, doi: 10.1039/c6ob02354a.

[35] C. Jiang, H. Huang, X. Kang, L. Yang, Z. Xi, H. Sun, M. D. Pluth, and L. Yi, "NBD-based synthetic probes for sensing small molecules and proteins: design, sensing mechanisms and biological applications," *Chemical Society Reviews,* vol. 50, no. 13, pp. 7436-7495, 2021, doi: 10.1039/d0cs01096k.

[36] H.-N. Mak, X. Lu, S. Pan, Y. Gu, L. Jiang, and W.-T. Wong, "A water-soluble Gd(III)-based fluorescence/T_1-MR dual-modality probe for H_2S sensing," *Chemical Communications,* vol. 60, pp. 14419-14422, 2024, doi: 10.1039/d4cc05042h.

[37] D. Parker, J. D. Fradgley, and K.-L. Wong, "The design of responsive luminescent lanthanide probes and sensors," *Chemical Society Reviews,* vol. 50, no. 14, pp. 8193-8213, 2021, doi: 10.1039/d1cs00310k.

[38] T. J. Clough, L. Jiang, K. L. Wong, and N. J. Long, "Ligand design strategies to increase stability of gadolinium-based magnetic resonance imaging contrast agents," *Nature Communications,* vol. 10, no. 1, p. 1420, Mar 29 2019, doi: 10.1038/s41467-019-09342-3.

[39] I. Ismail, Z. Chen, L. Sun, X. Ji, H. Ye, X. Kang, H. Huang, H. Song, S. G. Bolton, Z. Xi, M. D. Pluth, and L. Yi, "Highly efficient H_2S scavengers *via* thiolysis of positively-charged NBD amines," *Chemical Science,* vol. 11, no. 30, pp. 7823-7828, 2020, doi: 10.1039/d0sc01518k.

[40] J. Zhang, Y. Zhang, Q. Guo, G. Wen, H. Xiao, S. Qi, Y. Wang, H. Zhang, L. Wang, and H. Sun, "Photoacoustic/Fluorescence Dual-Modality Probe for Biothiol Discrimination and

Tumor Diagnosis in Cells and Mice," *ACS Sensors,* vol. 7, no. 4, pp. 1105-1112, Apr 22 2022, doi: 10.1021/acssensors.2c00058.

[41] Y. Li, W. Chen, Y. Qi, S. Wang, L. Li, W. Li, T. Xie, H. Zhu, Z. Tang, and M. Zhou, "H_2S-Scavenged and Activated Iron Oxide-Hydroxide Nanospindles for MRI-Guided Photothermal Therapy and Ferroptosis in Colon Cancer," *Small,* vol. 16, no. 37, p. e2001356, Sep 2020, doi: 10.1002/smll.202001356.

[42] S. Khattak, M. A. Rauf, N. H. Khan, Q.-Q. Zhang, H.-J. Chen, P. Muhammad, M. A. Ansari, M. N. Alomary, M. Jahangir, C.-Y. Zhang, X.-Y. Ji, and D.-D. Wu, "Hydrogen Sulfide Biology and Its Role in Cancer," *Molecules,* vol. 27, no. 11, p. 3389, 2022, doi: 10.3390/molecules27113389.

[43] E. J. Werner, A. Datta, C. J. Jocher, and K. N. Raymond, "High-Relaxivity MRI Contrast Agents: Where Coordination Chemistry Meets Medical Imaging," *Angewandte Chemie International Edition,* vol. 47, no. 45, pp. 8568-8580, 2008, doi: 10.1002/anie.200800212.

[44] L. Leone, G. Ferrauto, M. Cossi, M. Botta, and L. Tei, "Optimizing the Relaxivity of MRI Probes at High Magnetic Field Strengths With Binuclear GdIII Complexes," *Frontiers in Chemistry,* vol. 6, 2018, doi: 10.3389/fchem.2018.00158.

[45] P. Caravan, G. Parigi, J. M. Chasse, N. J. Cloutier, J. J. Ellison, R. B. Lauffer, C. Luchinat, S. A. McDermid, M. Spiller, and T. J. McMurry, "Albumin Binding, Relaxivity, and Water Exchange Kinetics of the Diastereoisomers of MS-325, a Gadolinium(III)-Based Magnetic Resonance Angiography Contrast Agent," *Inorganic Chemistry,* vol. 46, no. 16, pp. 6632-6639, 2007, doi: 10.1021/ic700686k.

[46] O. Florès, J. Pliquett, L. Abad Galan, R. Lescure, F. Denat, O. Maury, A. Pallier, P.-S. Bellaye, B. Collin, S. Même, C. S. Bonnet, E. Bodio, and C. Goze, "Aza-BODIPY Platform:

Toward an Efficient Water-Soluble Bimodal Imaging Probe for MRI and Near-Infrared Fluorescence," *Inorganic Chemistry,* vol. 59, no. 2, pp. 1306-1314, 2020, doi: 10.1021/acs.inorgchem.9b03017.

[47] E. M. Gale, J. Zhu, and P. Caravan, "Direct measurement of the Mn(II) hydration state in metal complexes and metalloproteins through 17O NMR line widths," *Journal of the American Chemical Society,* vol. 135, no. 49, pp. 18600-8, Dec 11 2013, doi: 10.1021/ja4094132.

3.7 Appendix

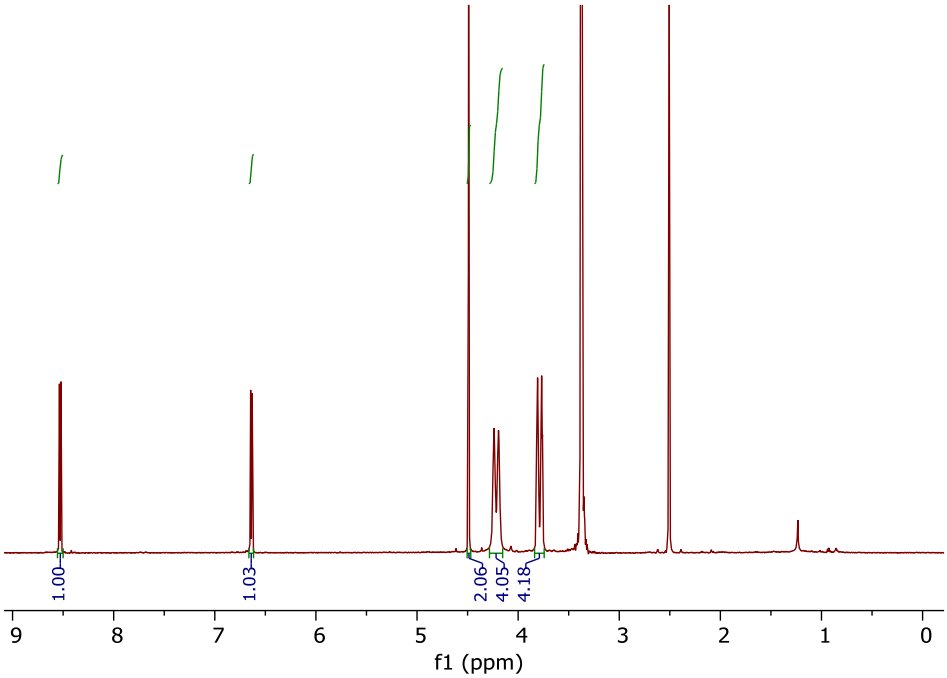

Figure 3.23: ^{1}H NMR spectrum of compound 3.3 (600 MHz, DMSO-d_6).

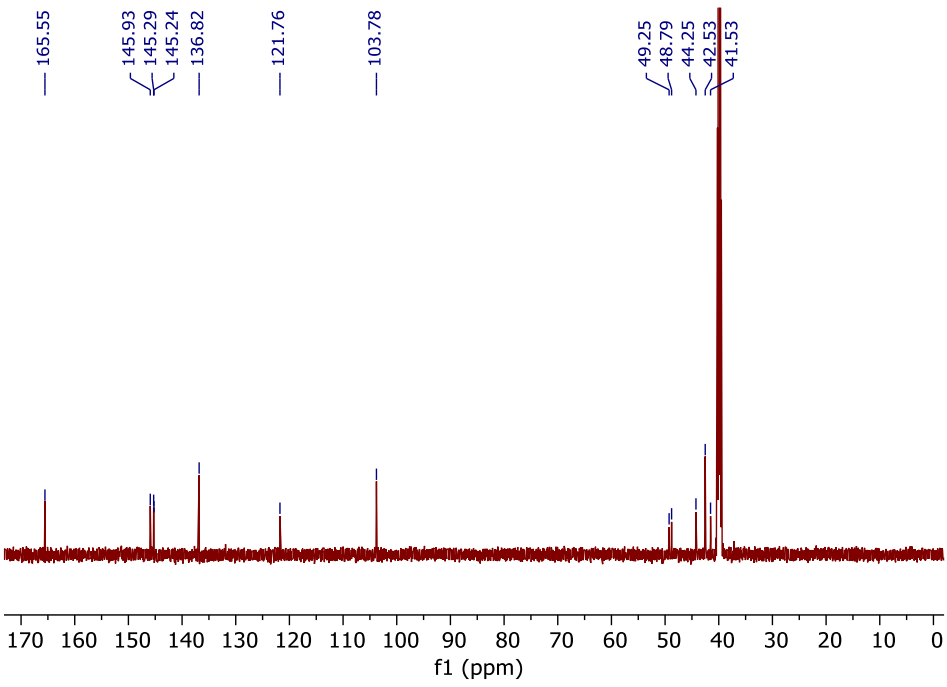

Figure 3.24: ^{13}C NMR spectrum of compound 3.3 (151 MHz, DMSO-d_6).

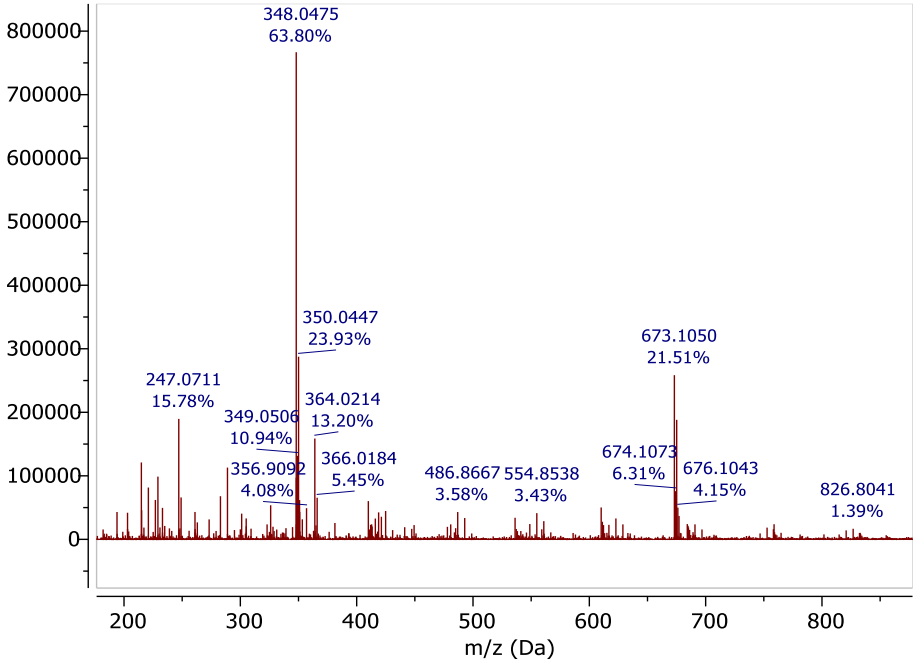

Figure 3.25: High-resolution mass spectrum of compound 3.3.

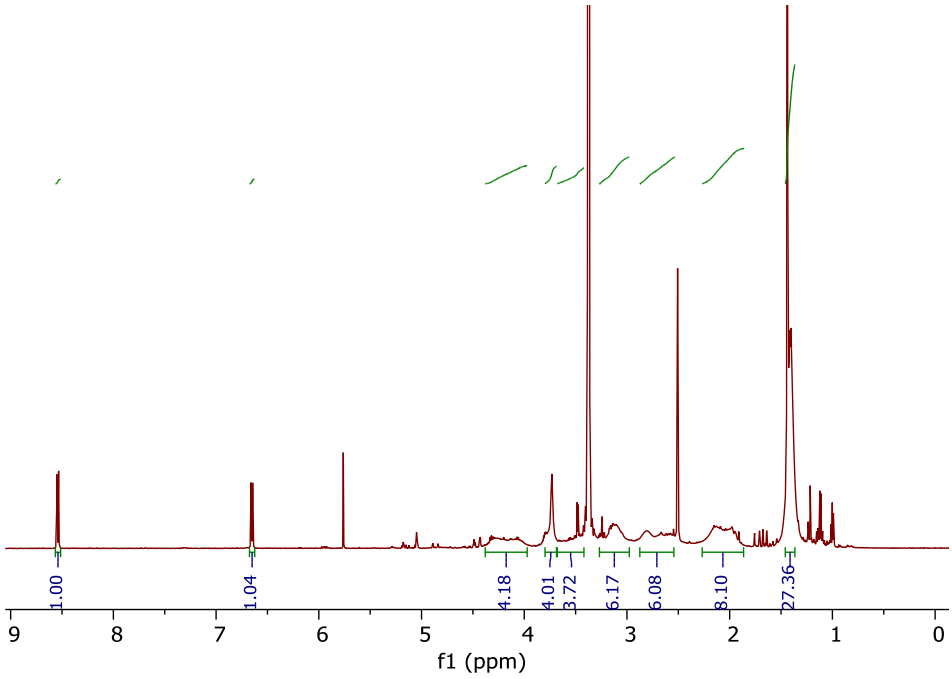

Figure 3.26: ^{1}H NMR spectrum of compound 3.4 (600 MHz, DMSO-d_6)

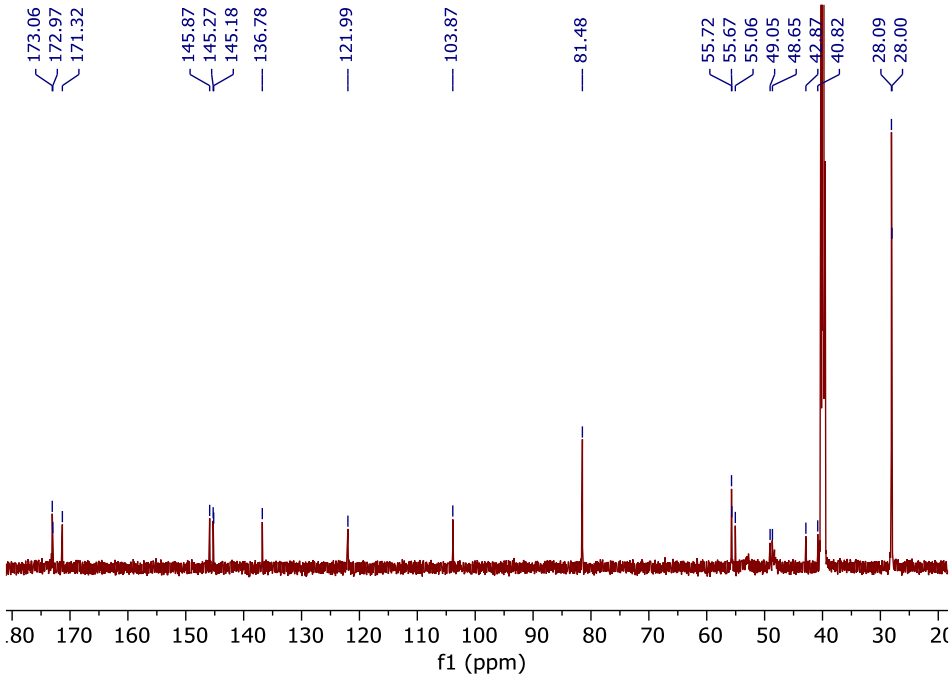

Figure 3.27: ^{13}C NMR spectrum of compound 3.4 (151 MHz, DMSO-d6).

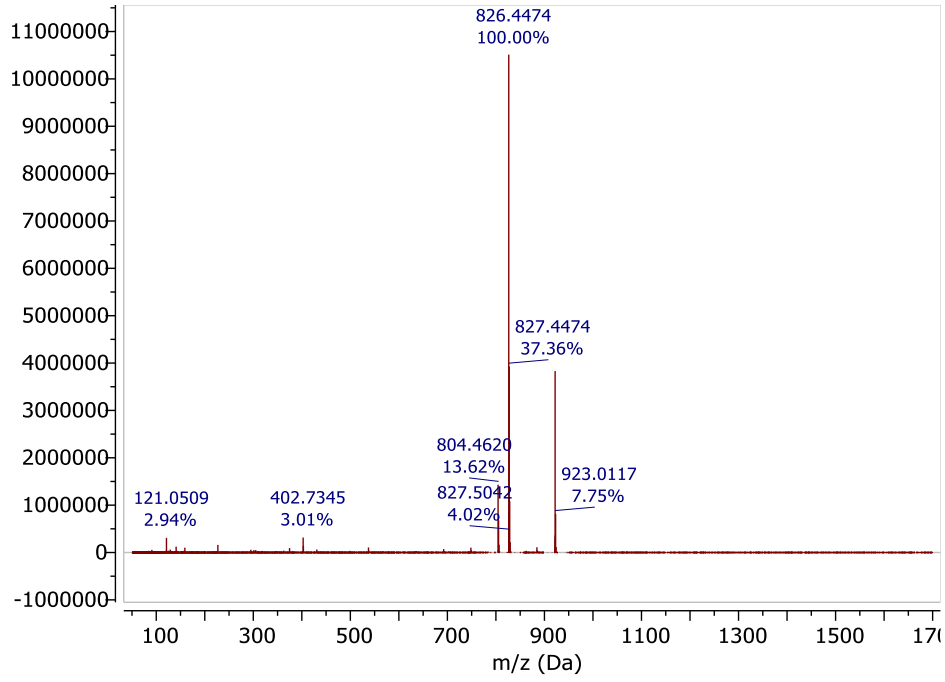

Figure 3.28: High-resolution mass spectrum of compound 3.4.

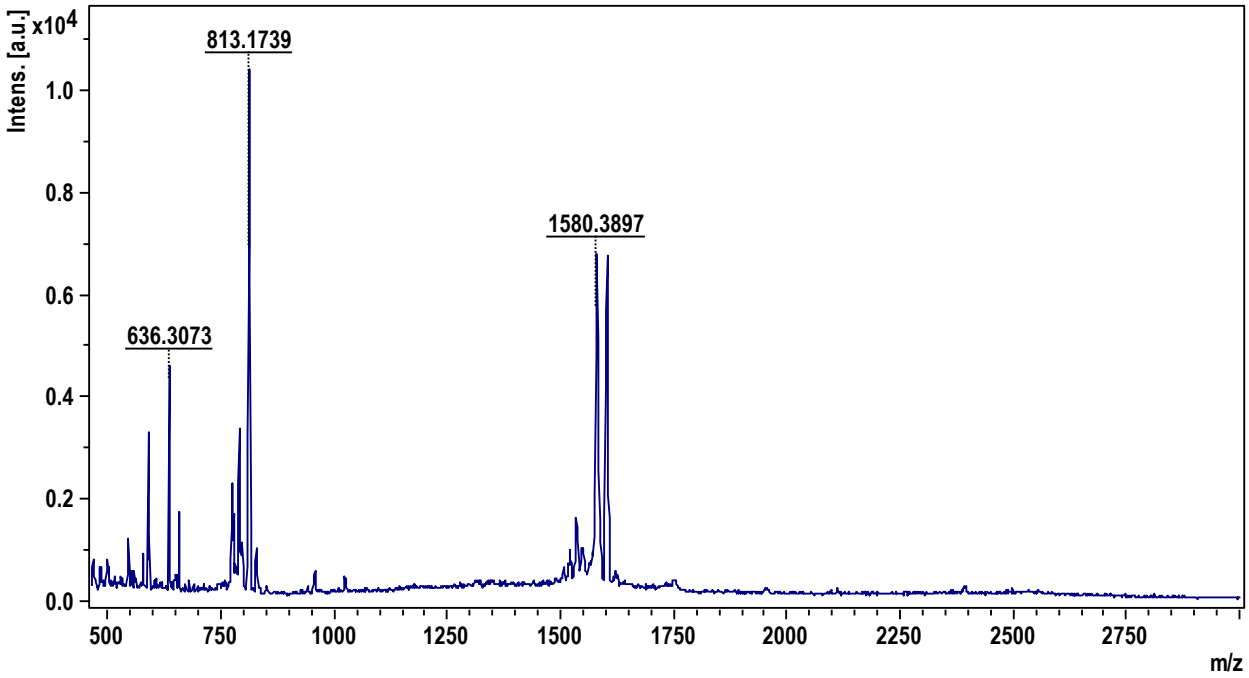

Figure 3.29: High-resolution mass spectrum of compound NBD[Gd]-L2.

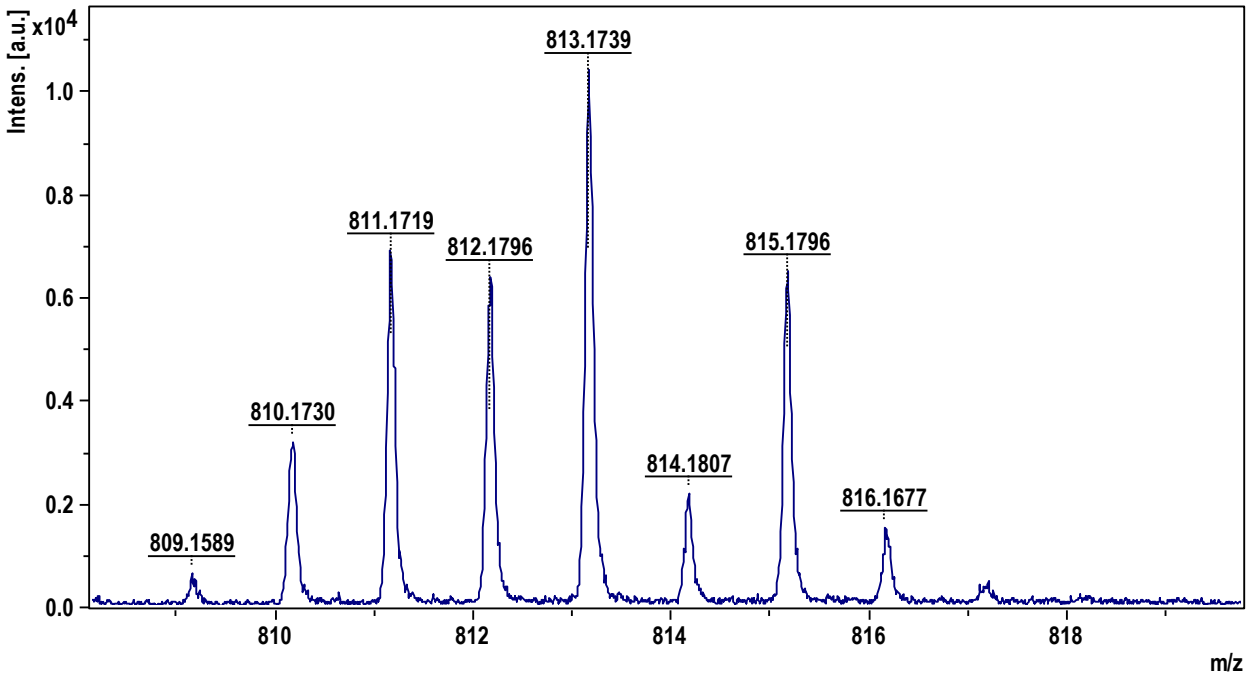

Figure 3.30: Zoom-in high-resolution mass spectrum (m/z: 802 – 820) of compound NBD[Gd]-L2.

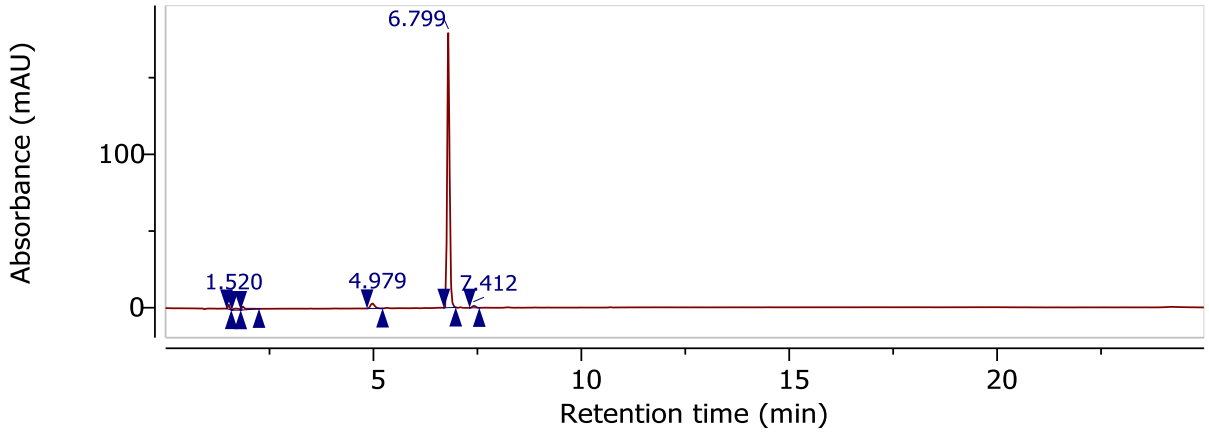

Figure 3.31: HPLC chromatogram of NBD[Gd]-L2.

Table 3.4: Solvent gradient used for analytical HPLC.

Time (min)	% H_2O (+ 0.05% TFA)	% ACN (+ 0.05% TFA)	Flow (ml/min)
0	95	5	1.2
20	5	95	1.2
22	95	5	1.2
25	95	5	1.2

Table 3.5: Solvent gradient used for semi-preparative HPLC.

Time (min)	% H_2O (+ 0.05% TFA)	% ACN (+ 0.05% TFA)	Flow (ml/min)
0	95	5	8
30	5	95	8
31	95	5	8
35	95	5	8

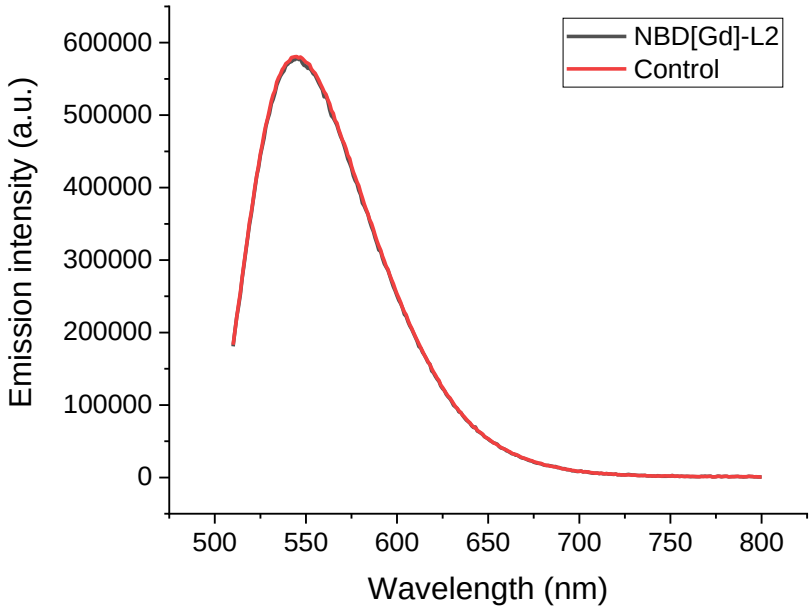

Figure 3.32: Fluorescence selectivity experiment of 10 μM NBD[Gd]-L2 in PBS control sample after one hour of incubation. λex: 490 nm, slit: 5-5 nm.

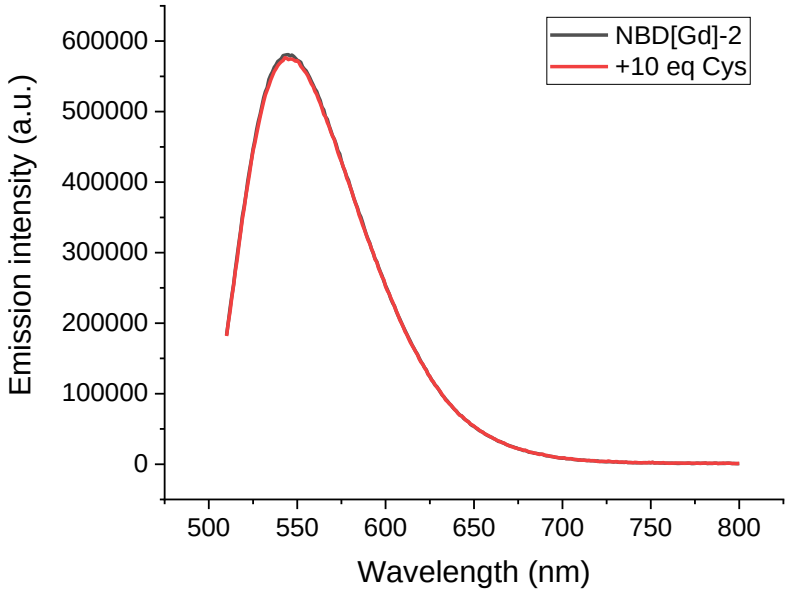

Figure 3.33: Fluorescence selectivity experiment of 10 μM NBD[Gd]-L2 in PBS to 100 μM Cys after one hour of incubation. λex: 490 nm, slit: 5-5 nm.

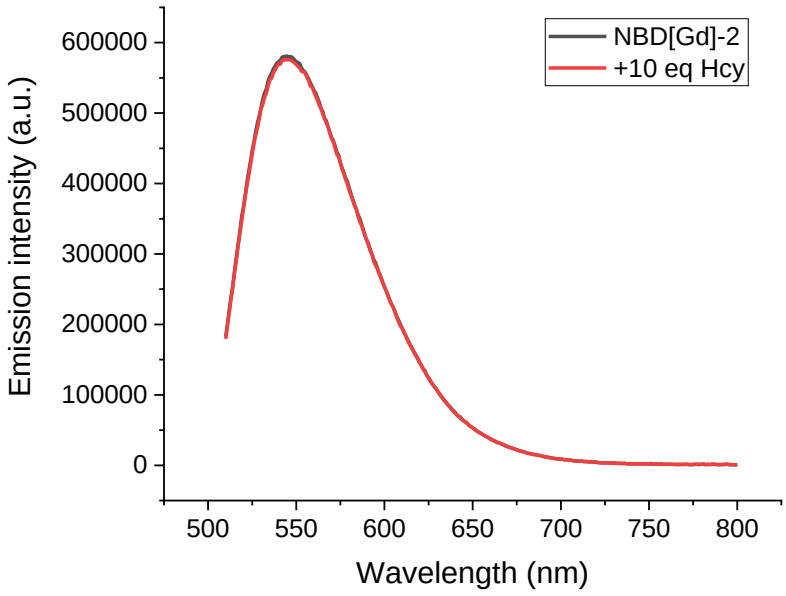

Figure 3.34: Fluorescence selectivity experiment of 10 µM NBD[Gd]-L2 in PBS to 100 µM Hcy after one hour of incubation. λex: 490 nm, slit: 5-5 nm.

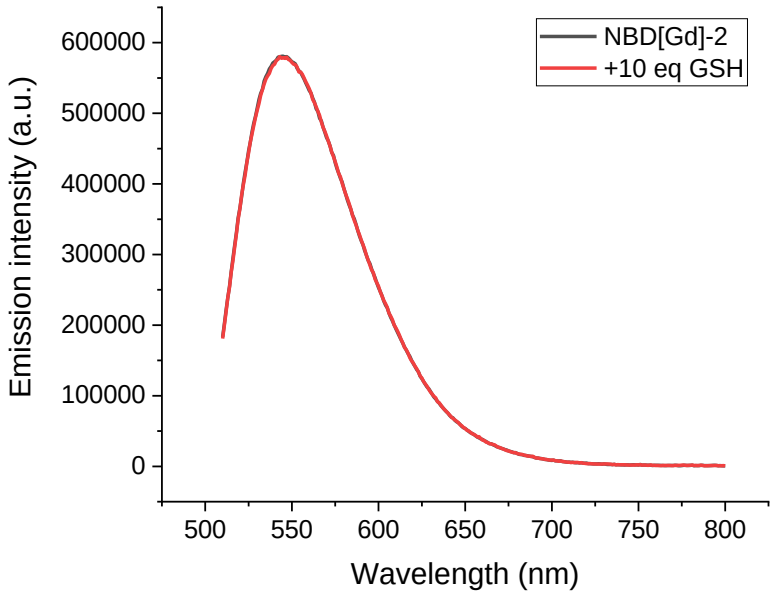

Figure 3.35: Fluorescence selectivity experiment of 10 µM NBD[Gd]-L2 in PBS to 100 µM GSH after one hour of incubation. λex: 490 nm, slit: 5-5 nm.

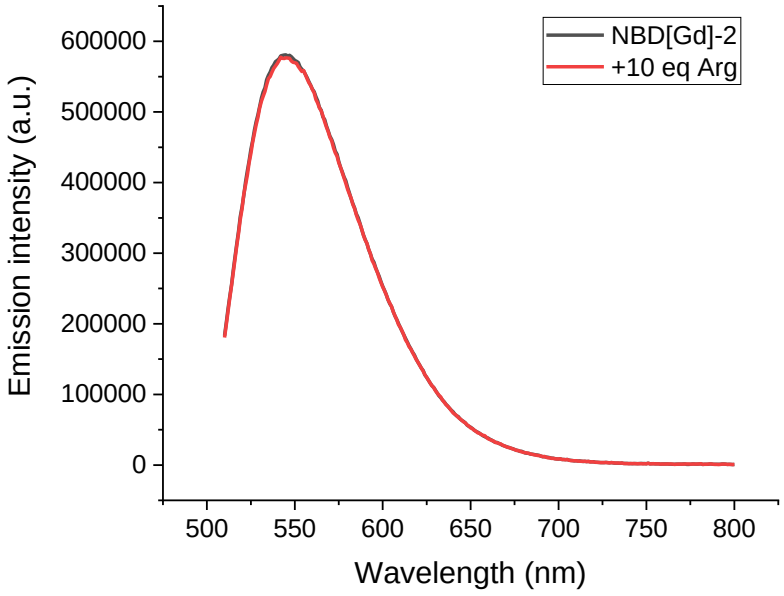

Figure 3.36: Fluorescence selectivity experiment of 10 µM NBD[Gd]-L2 in PBS to 100 µM Arg after one hour of incubation. λex: 490 nm, slit: 5-5 nm.

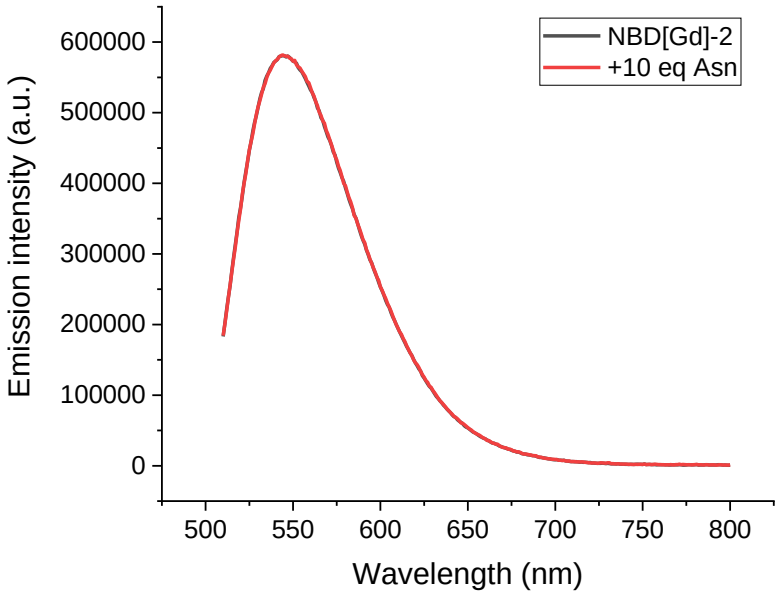

Figure 3.37: Fluorescence selectivity experiment of 10 µM NBD[Gd]-L2 in PBS to 100 µM Asn after one hour of incubation. λex: 490 nm, slit: 5-5 nm.

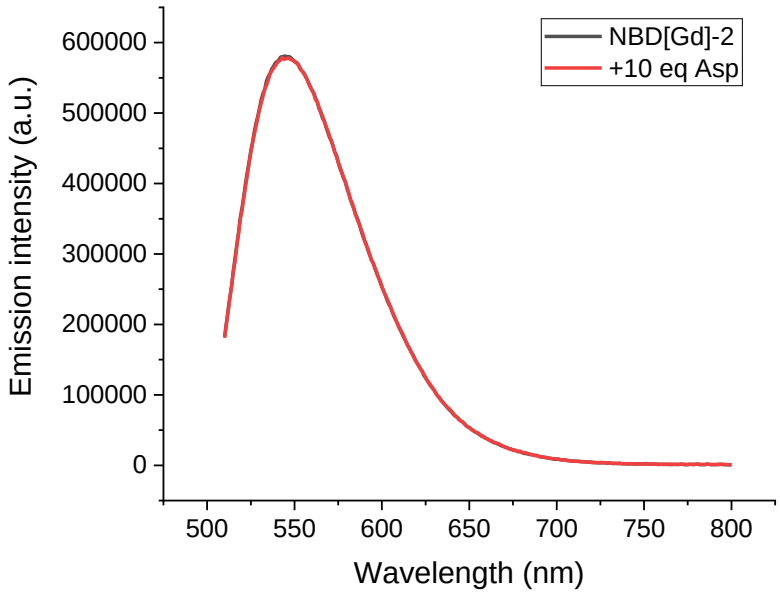

Figure 3.38: Fluorescence selectivity experiment of 10 µM NBD[Gd]-L2 in PBS to 100 µM Asp after one hour of incubation. λex: 490 nm, slit: 5-5 nm.

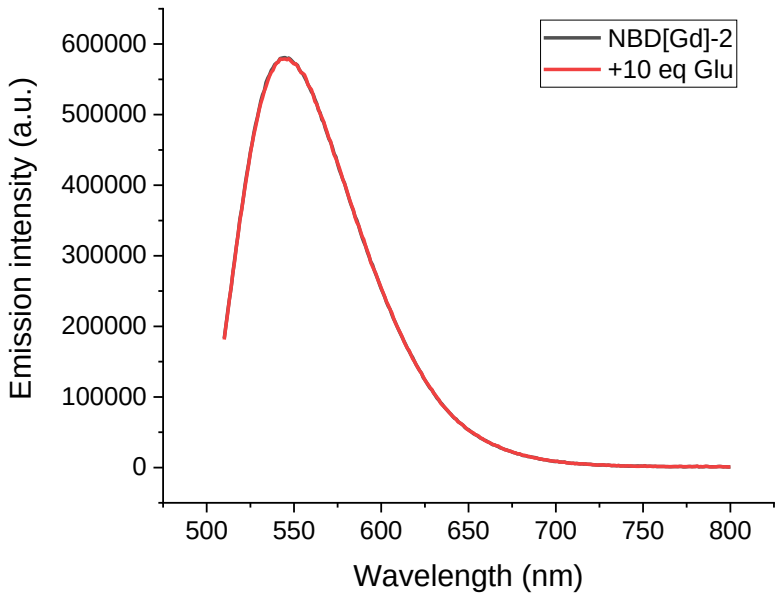

Figure 3.39: Fluorescence selectivity experiment of 10 µM NBD[Gd]-L2 in PBS to 100 µM Glu after one hour of incubation. λex: 490 nm, slit: 5-5 nm.

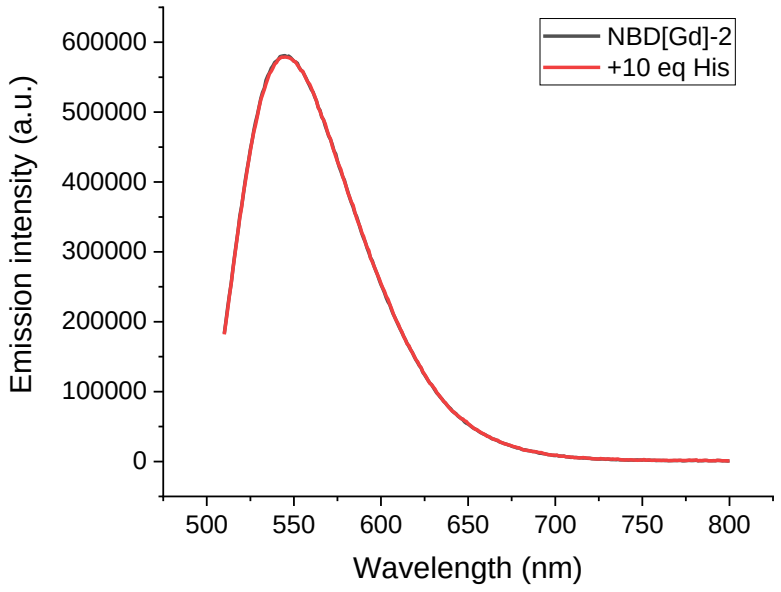

Figure 3.40: Fluorescence selectivity experiment of 10 μM NBD[Gd]-L2 in PBS to 100 μM His after one hour of incubation. λex: 490 nm, slit: 5-5 nm.

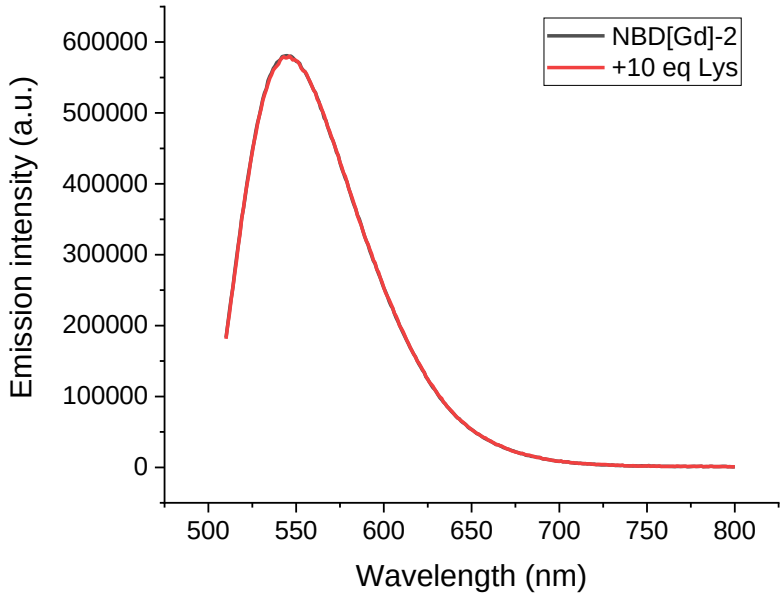

Figure 3.41: Fluorescence selectivity experiment of 10 μM NBD[Gd]-L2 in PBS to 100 μM Lys after one hour of incubation. λex: 490 nm, slit: 5-5 nm.

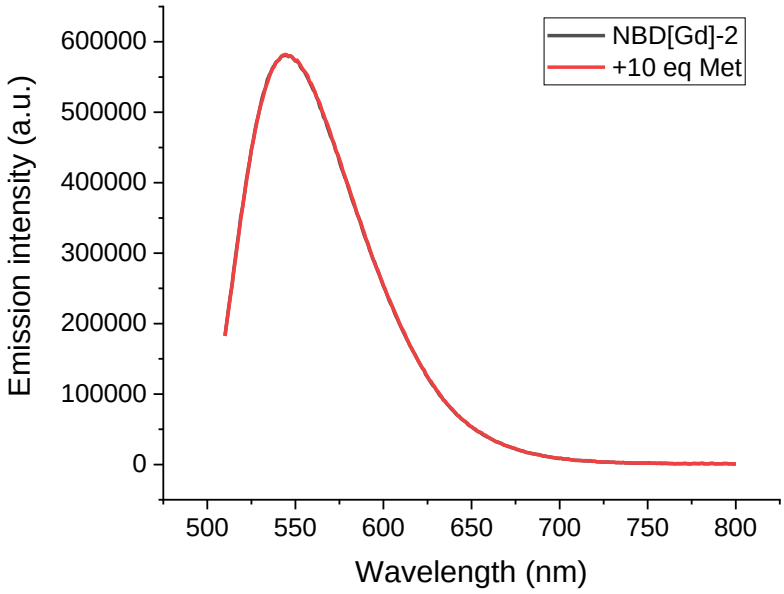

Figure 3.42: Fluorescence selectivity experiment of 10 μM NBD[Gd]-L2 in PBS to 100 μM Met after one hour of incubation. λex: 490 nm, slit: 5-5 nm.

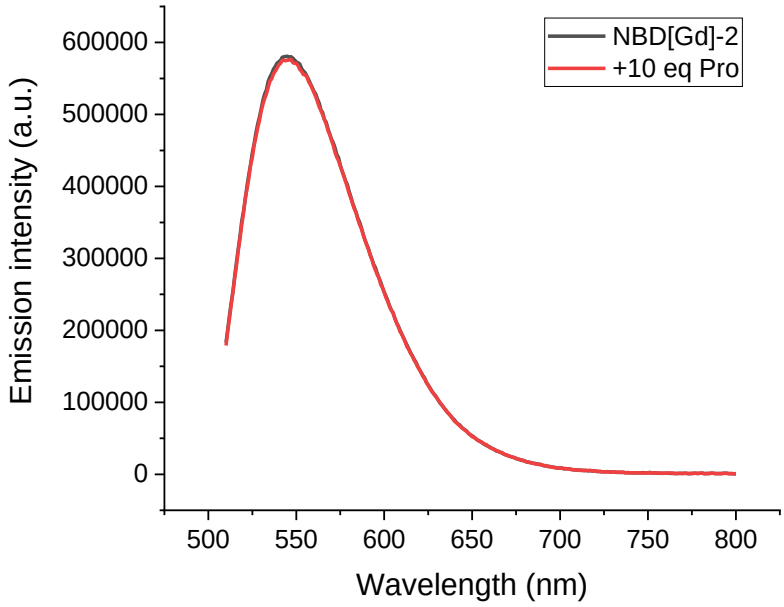

Figure 3.43: Fluorescence selectivity experiment of 10 μM NBD[Gd]-L2 in PBS to 100 μM Pro after one hour of incubation. λex: 490 nm, slit: 5-5 nm.

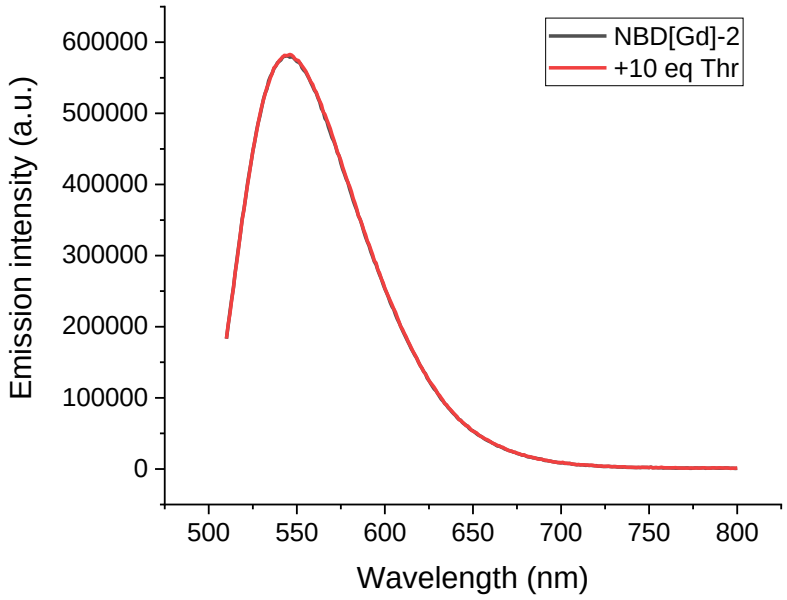

Figure 3.44: Fluorescence selectivity experiment of 10 μM NBD[Gd]-L2 in PBS to 100 μM Thr after one hour of incubation. λex: 490 nm, slit: 5-5 nm.

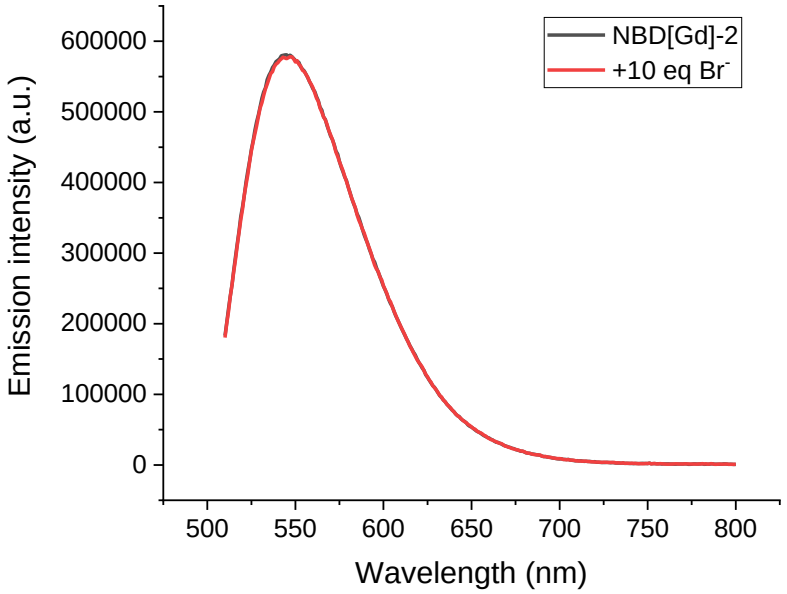

Figure 3.45: Fluorescence selectivity experiment of 10 μM NBD[Gd]-L2 in PBS to 100 μM Br^- after one hour of incubation. λex: 490 nm, slit: 5-5 nm.

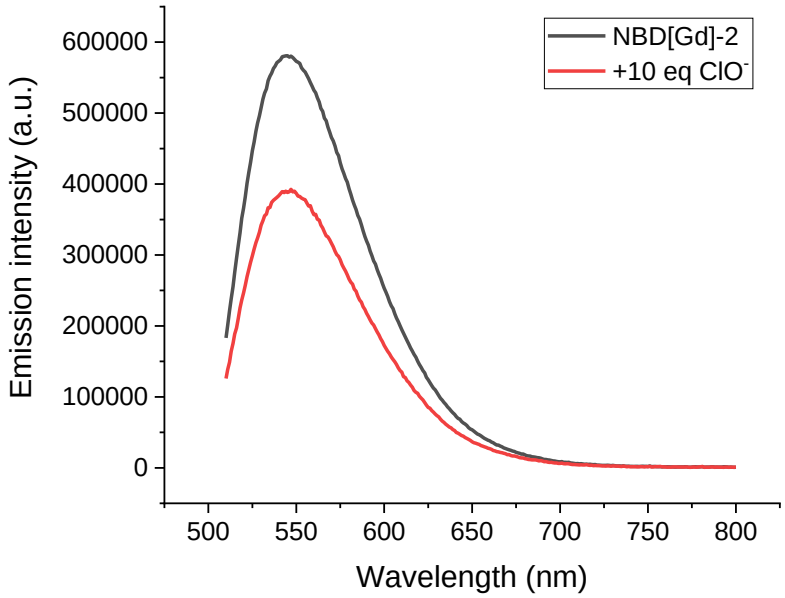

Figure 3.46: Fluorescence selectivity experiment of 10 µM NBD[Gd]-L2 in PBS to 100 µM ClO^- after one hour of incubation. λex: 490 nm, slit: 5-5 nm.

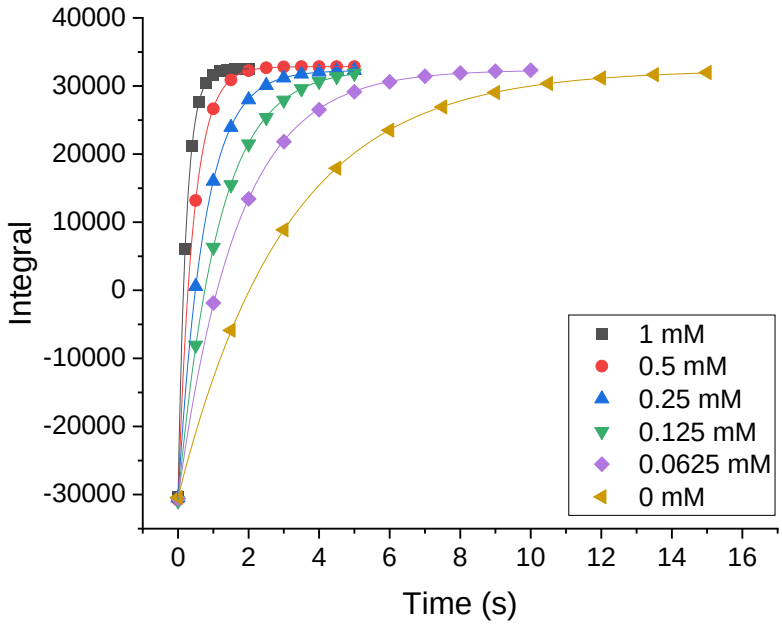

Figure 3.47: T_1 relaxation of 0 – 1 mM GdDOTA in PBS (10 mM, pH 7.4). The curves are fitted to the equation: $y = y_0(1-e^{-x/T1})$, where y_0 is the initial maximum value.

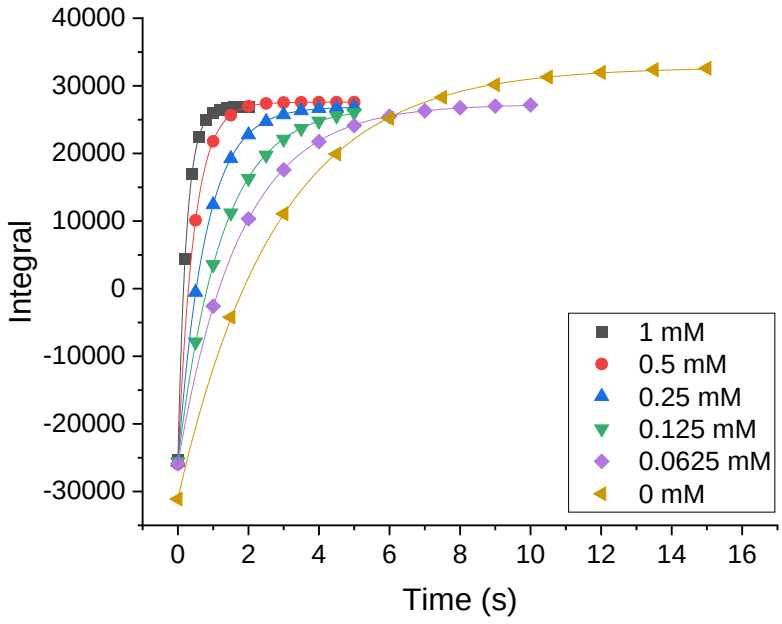

Figure 3. 48: T_1 relaxation of 0 – 1 mM GdDOTA + H_2S in PBS (10 mM, pH 7.4). The curves are fitted to the equation: $y = y_0(1\text{-}e^{-x/T1})$, where y_0 is the initial maximum value.

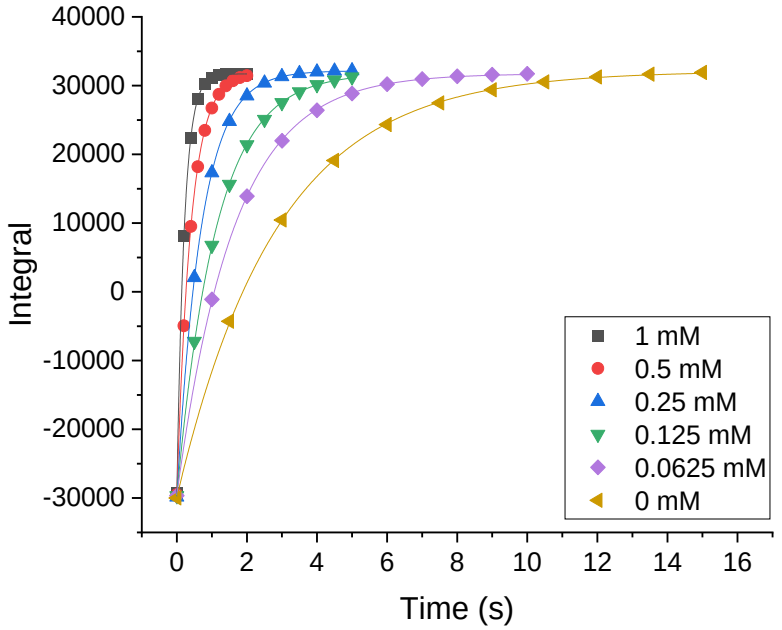

Figure 3.49: T_1 relaxation of 0 – 1 mM NBD[Gd]-L2 in PBS (10 mM, pH 7.4). The curves are fitted to the equation: $y = y_0(1\text{-}e^{-x/T1})$, where y_0 is the initial maximum value.

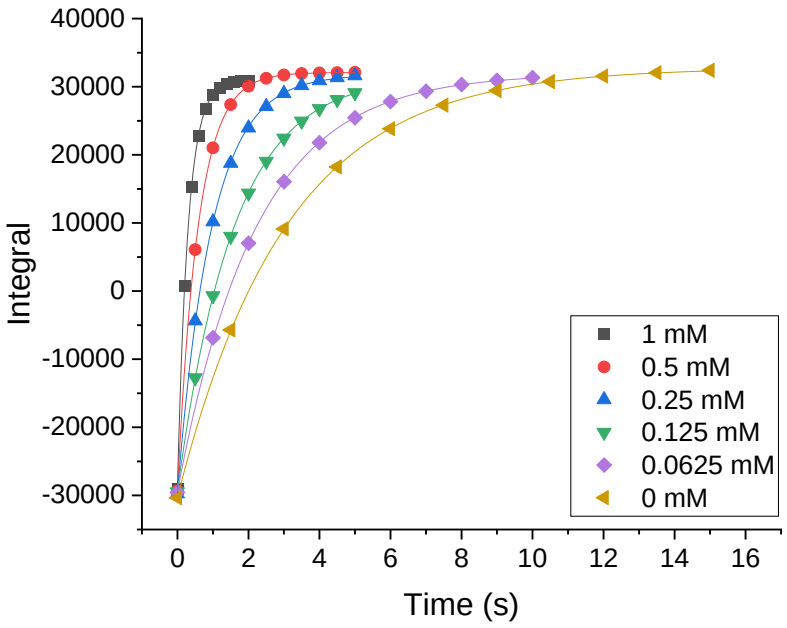

Figure 3.50: T_1 relaxation of 0 – 1 mM NBD[Gd]-L2 + H_2S in PBS (10 mM, pH 7.4). The curves are fitted to the equation: $y = y_0(1-e^{-x/T1})$, where y_0 is the initial maximum value.

Table 3.6: Relaxation rate, $1/\Delta T_1$ (s^{-1}) of 0 – 1 mM of GdDOTA, and GdDOTA + H_2S.

Concentration of Gd	**GdDOTA**	**σ**	**GdDOTA+ H_2S**	**σ**
1 mM	4.24948	0.02658	4.14952	0.029699
0.5 mM	2.28893	0.00381	2.227194	0.008572
0.25 mM	1.31092	0.01552	1.281527	0.006646
0.125 mM	0.81664	0.00789	0.804291	0.001348
0.0625 mM	0.57081	0.00177	0.569911	0.001228
0 mM	0.32265	2.28×10^{-04}	0.348221	0.009463

Table 3.7: Relaxation rate, $1/\Delta T_1$ (s^{-1}) of 0 – 1 mM of NBD[Gd]-L2 and NBD[Gd]-L2 + H_2S.

Concentration of Gd	**NBD[Gd]-L2**	**σ**	**NBD[Gd]-L2 + H_2S**	**σ**
1 mM	4.70794	0.02975	3.23913	0.08873
0.5 mM	2.52911	0.00337	1.74911	0.05064
0.25 mM	1.43941	0.00604	1.0088	0.02916
0.125 mM	0.89161	5.78×10^{-04}	0.65145	0.03371
0.0625 mM	0.61944	0.00296	0.4566	0.00521
0 mM	0.32265	2.28×10^{-04}	0.348221	0.009463

Chapter 4: Luminescence/T_1-MRI dual-modality probe for hydrazine imaging.

4.1 Introduction

Hydrazine (N_2H_4) is well-known as a highly reactive chemical compound and has been utilized into different scientific research and industrial fields.[1] Due to its excellent physical and chemical properties such as strong reducing power and high combustion heat, this simple diamine compound has been applied to space technology as liquid rocket fuel[2] and to organic synthesis for the production of pharmaceutical products such as isoniazid and hydralazine.[3, 4] Despite the benefits of hydrazine, utilization of hydrazine remains a challenge because of the high toxicity to human body[5, 6] and its potential to pollute the environment during water treatment, transportation and bulk storage processes.[7, 8] There are two major ways for hydrazine to enter the human body: through metabolism of drugs and intake from the environment such as drinking water and inhalation. When hydrazine reacts with alpha-keto acids to form hydrazone derivatives, some active molecules such as pyridoxine (vitamin B6) are consumed. The downstream reactions, including the amino acid transamination, decarboxylation and lipid metabolism that require pyridoxine as a cofactor can lead to anaemia and refractory seizures.[5, 9] Additionally, the hydrazine-generated organic free radicals can cause DNA damage in human body.[10, 11]

Since the development of fast and effective methods for hydrazine detection in the environment and biological systems has been an urgent need in the last decade, scientists have designed several types of reaction-based fluorescent probes. In general, the reaction-based fluorescent probes can be divided into four categories: the deprotection reactions, group transformations, cyclization and

ring opening.[7, 12] In the deprotection mechanism, the fluorescence of the probe is quenched by the protection groups such as acetyl group, 4-bromobutyrate group, phthalimide group, levulinate group and 2-thiophenecarbonyl group.[13-16] Through hydrazine-mediated deprotection reaction, the ICT quenching mechanism is removed, restoring the fluorescence of the probe (Figure 4.1).

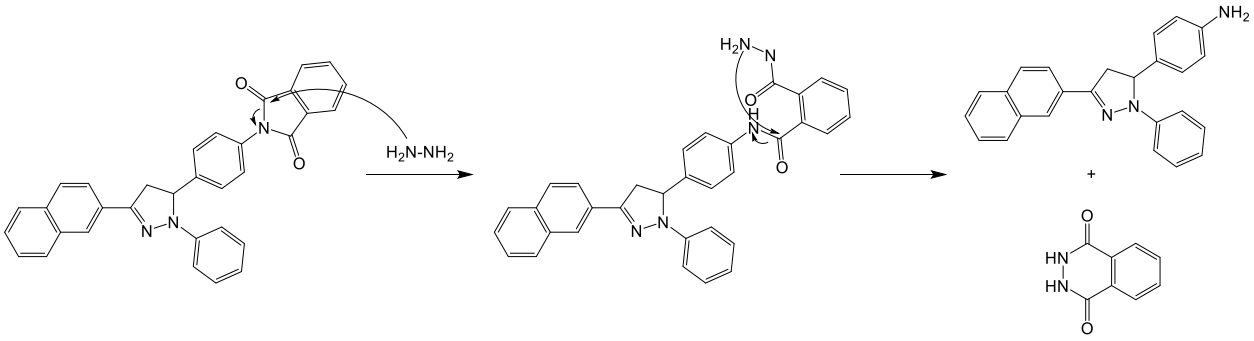

Figure 4.1: Example and sensing mechanism of phthalimide-based fluorescent probe.[17]

For the group transformation mechanism, the probes show weak initial fluorescence due to electron-withdrawing sensing groups such as aldehyde, malononitrile, and allyl group.[18-20] In the presence of hydrazine, the sensing group is converted into another moiety such as hydrazine, and hydrazone. In most of the examples, the fluorescence signal response occurs through the removal of PET or ICT, resulting in hypsochromic shifts (blue shifts in maximum emission wavelength) (Figure 4.2).[21]

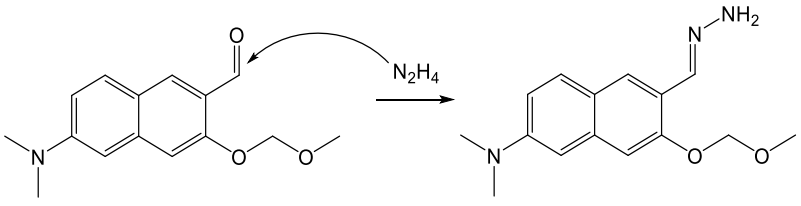

Figure 4.2: Example and sensing mechanism of aldehyde transformation-based fluorescent probe.

For the cyclization probes, 1,3-diketo, chalcone, and o-phthalaldehyde are commonly used as the sensing moieties.[22-24] A cyclization reaction occurs when hydrazine is added to the probe. The formation of pyrazole and phthalazine gives the fluorescent response signal by extending the π-conjugated structure. Conversely, in the ring-opening mechanism, the fluorescence of the probe is enhanced by opening of the spiro and lactonic rings (Figure 4.3, 4.4).[25, 26]

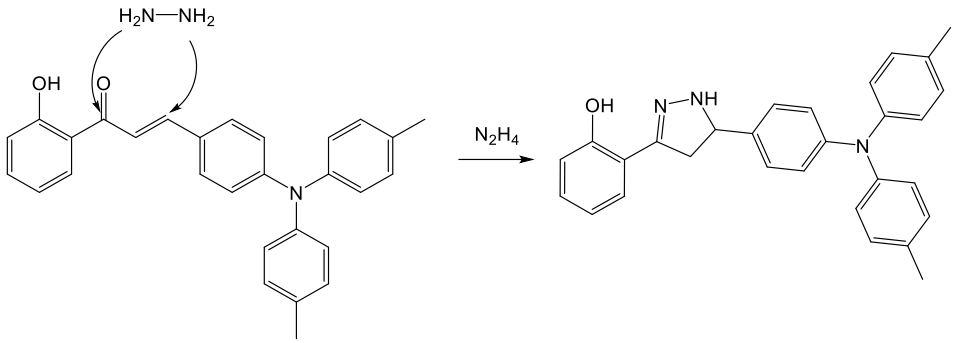

Figure 4.3: Example and sensing mechanism of chalcone cyclization based fluorescent probe.[23]

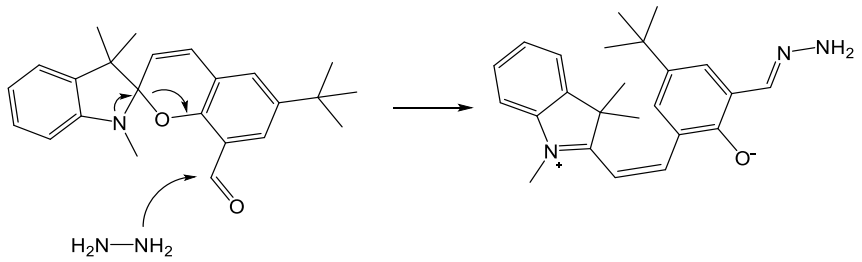

Figure 4.4: Example and sensing mechanism of hydrazine-induced spiro ring opening-based fluorescent probe.[25]

4.2 Scope of study

Although many examples of reaction-based luminescent probes for hydrazine detection exist, reaction-based MRI probes still lack sufficient development. Therefore, it is necessary to design and develop probes for magnetic resonance imaging and even multi-functional reaction-based chemical probes for hydrazine sensing. In this chapter, Hz[Ln]-L1 was designed and synthesized. In Hz[Ln]-L1, Tb^{3+} and Gd^{3+} were inserted into the ligand. The optical response properties and magnetic response properties of Hz[Tb]-L1 and Hz[Gd]-L1, respectively, were studied in the presence of hydrazine (Figure 4.5).

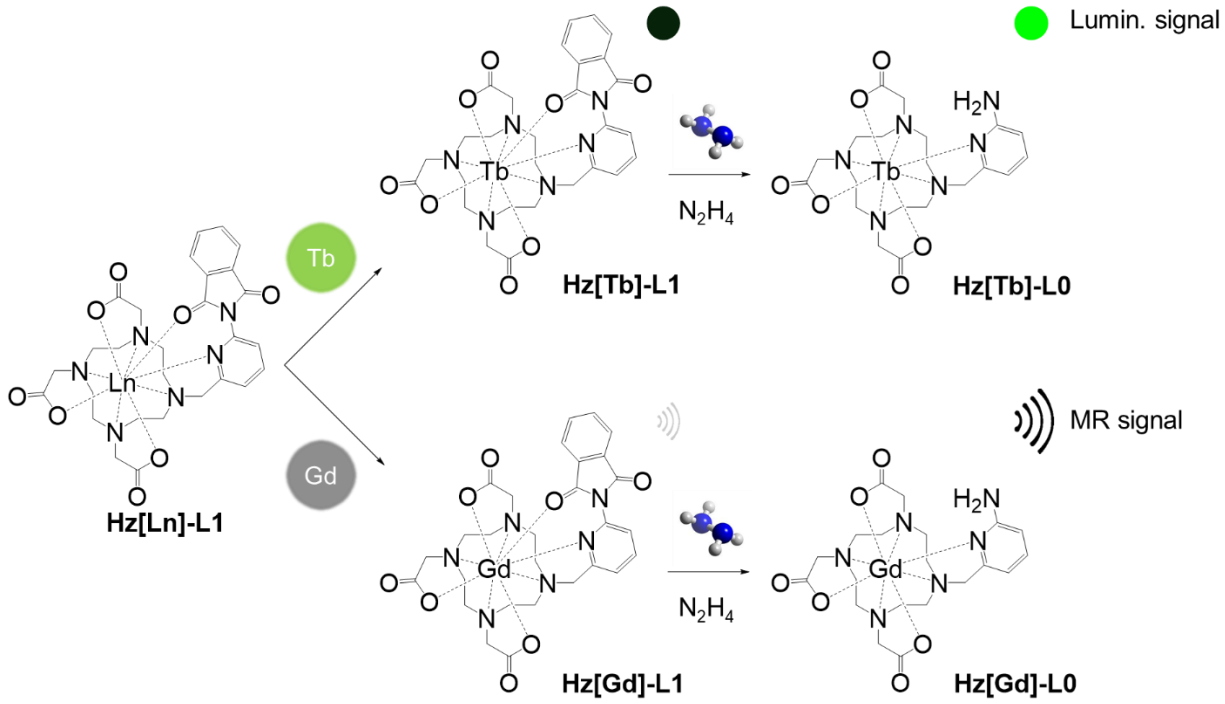

Figure 4.5: Design of the Hz[Ln]-L1, Hz[Tb]-L1 and Hz[Gd]-L1.

4.3 Result and discussion

4.3.1 Design and synthesis of Hz[Ln]-L1

In designing the dual-modality probe for hydrazine detection, 6-amino-2-pyridinemethanol was chosen as the starting material. 6-amino-2-pyridinemethanol served as an antenna to conduct energy transfer to the lanthanide metal centre for lanthanide luminescence. In the probe Hz[Ln]-L1, 6-amino-2-pyridinemethanol was allowed to react with phthalic anhydride to form a phthalimide group, masking the primary amine group of 6-amino-2-pyridinemethanol. Upon the protection of the amine group, the fluorescence of 6-amino-2-pyridinemethanol was quenched by ICT mechanism and the antenna effect was largely reduced, leading to weak luminescence from the lanthanide metal centre. Besides the luminescence property, the nitrogen atom in pyridine moiety can form a coordination bond with lanthanide metal, occupying one of the coordination sites. While the primary amine group is protected by phthalimide group, the carbonyl group on the phthalimide can form another coordination bond with lanthanide metal centre, occupying an additional coordination site. With more coordination bonds formed, the number of water molecules coordinated with lanthanide will be reduced, lowering the hydration number (q) (Figure 4.6 and 4.7). For Hz[Ln]-L1, Tb^{3+} and Gd^{3+} were inserted into the ligand to form Hz[Tb]-L1 and Hz[Gd]-L1, respectively, each serving different purposes. The luminescence properties of Hz[Tb]-L1 can be applied for environmental hydrazine detection, while the magnetic properties of Hz[Gd]-L1 can be applied to biomedical imaging in MRI-based hydrazine detection.

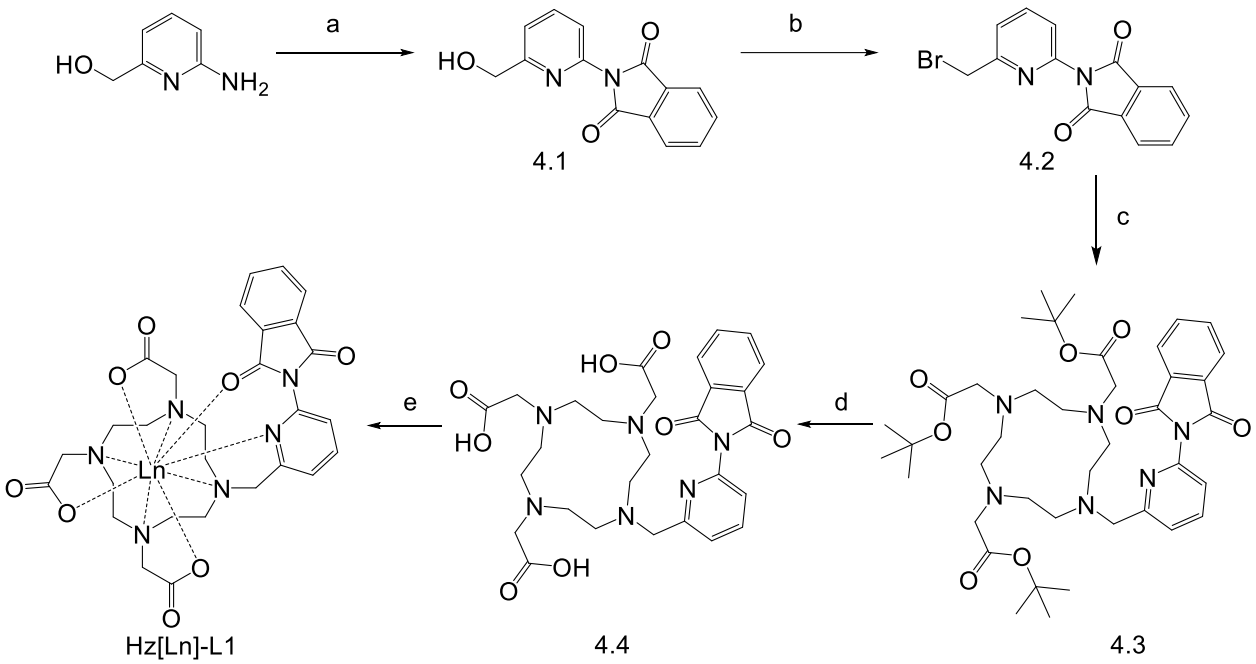

Figure 4.6: Synthetic route of Hz[Ln]-L1. Reagents and conditions: a. phthalic anhydride, toluene, N_2, reflux, 12 h; b. PBr_3, DCM, 0°C, 2 h; c. DO3A-tBu, K_2CO_3, ACN, N_2, 50°C, 12 h; d. TFA, RT, 12 h; e. $GdCl_3 \cdot 6H_2O$, H_2O/MeOH, pH 6-7, RT, 24 h.

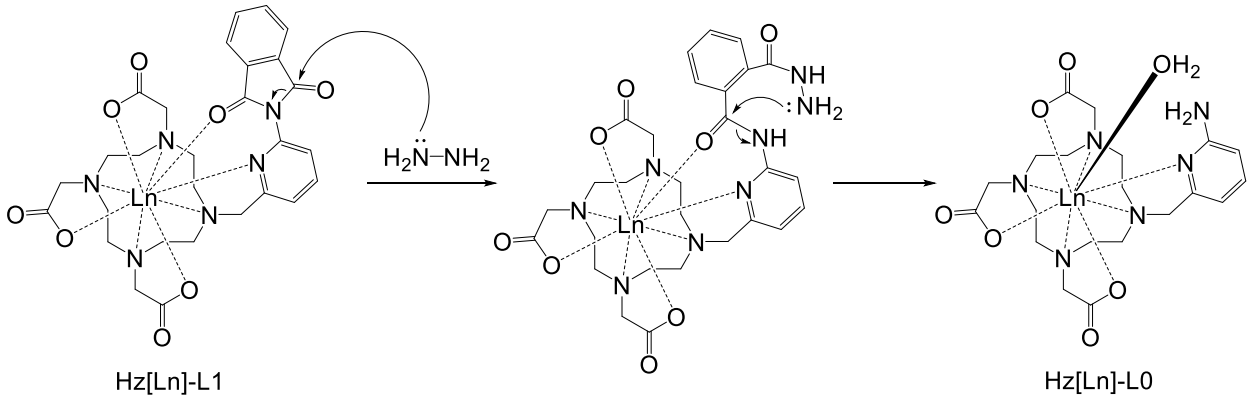

Figure 4.7: Proposed sensing mechanism for Hz[Ln]-L1.

To achieve the synthesis of Hz[Ln]-L1, a five steps synthetic route was designed to obtain the target molecules. In the first step of the synthetic route, the starting material, 6-amino-2-pyridinemethanol, was reacted with phthalic anhydride in order to form phthalimide, protecting the primary amine group and quenching the fluorescence from 6-amino-2-pyridinemethanol by ICT mechanism. According to the protocol, protecting the primary amine group with phthalic anhydride is commonly achieved by refluxing in acetic acid. However, when 6-amino-2-pyridinemethanol and phthalic anhydride were heated to reflux in acetic acid, a side product was obtained in a very high yield (> 80%) and no targeted compound 4.1 was produced. In ^{1}H NMR spectrum, the seven integrals in the range of δ 8.15 – 7.5 ppm indicated the presence of three protons on pyridine ring and four protons on the phthalimide moiety, indicating the primary amine group had reacted with phthalic anhydride to form phthalimide. The two integrals at δ 5.17 corresponded to the two protons on the methyl group next to the pyridine. However, there was an unknown peak appeared at δ 2.17 ppm with an integral of three. From the mass spectrum, a peak at m/z = 297.0912 was observed. The obtained mass was 42 units larger than the expected $[M+H]^{+}$ of compound 4.1 (calc m/z = 255.0770). Combined with the evidence from the ^{1}H NMR spectrum and mass spectrum, the side product was identified as the acetyl ester group from the reaction between the primary alcohol group on 6-amino-2-pyridinemethanol and acetic acid (compound 4.1a). To eliminate the formation of the side product, the solvent was changed from acetic acid to anhydrous toluene and the reaction was conducted under reflux in N_2 environment. With the modification of the solvent, the target molecule of compound 4.1 was obtained with good yield (Figure 4.8 – 4.10).

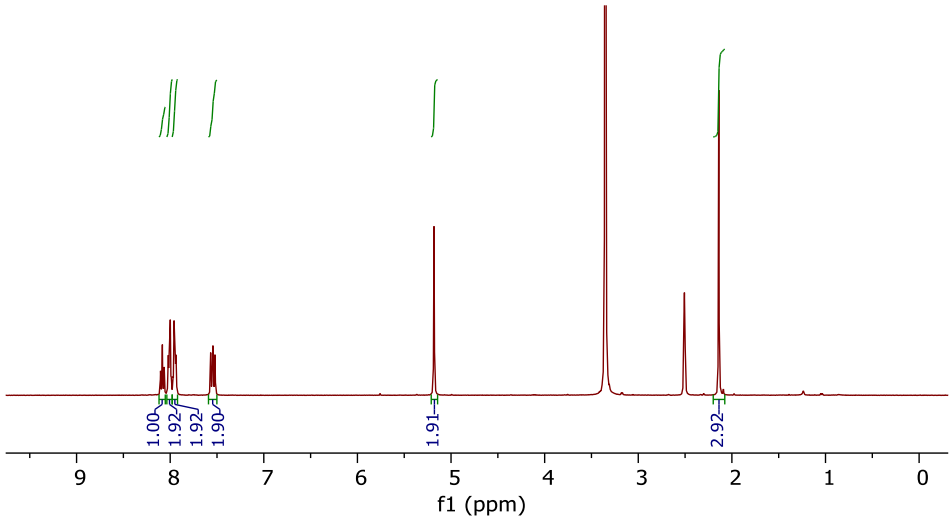

Figure 4.8: ^{1}H NMR spectrum of the side product in step 1.

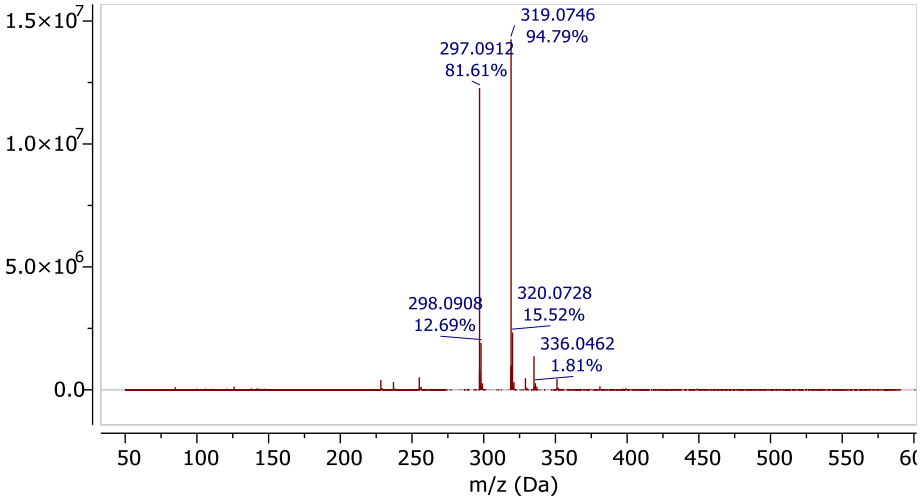

Figure 4.9: HRMS spectrum of the side product in step 1.

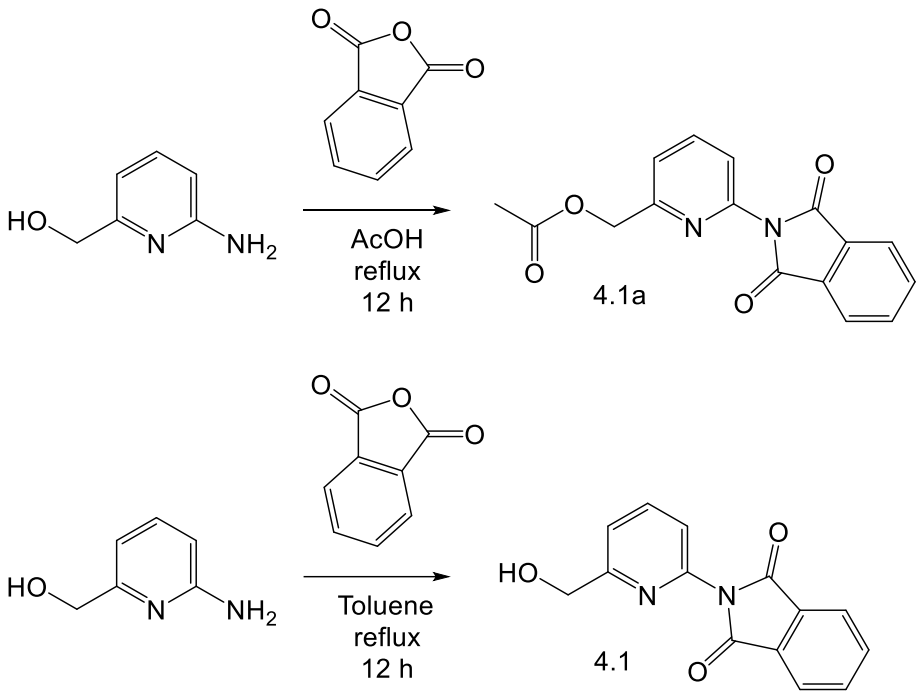

Figure 4.10: Synthesis of compound 4.1a and 4.1.

After purification of compound 4.1, a classic bromination reaction was conducted using phosphorus tribromide (PBr_3) to convert the alkyl alcohol group into an alkyl bromide to yield compound 4.2. Compound 4.2 was then allowed to react with lanthanide chelator, DO3A-tert-butyl ester, under mild heat, mildly basic condition and anhydrous conditions to produce compound 4.3. After deprotection of the three carboxylic acids on DO3A-tert-butyl ester using trifluoroacetic acid (TFA), enhancing the interaction between lanthanide ions and compound 4.4 due to the interaction between the cation and anion. In the lanthanide complexation part, terbium(III) chloride hexahydrate and gadolinium(III) chloride hexahydrate were employed to produce Hz[Tb]-L1 and Hz[Gd]-L1, respectively. In Hz[Tb]-L1, the responsive luminescence property of Tb^{3+} complex was utilized for optical sensing of hydrazine; while the responsive magnetic resonance property of Gd^{3+} complex was utilized for hydrazine sensing by magnetic resonance imaging (MRI).

4.3.2 Spectral measurements and response of Hz[Tb]-L1 towards hydrazine

In the preliminary testing of the hydrazine sensing ability, 10 μM of compound 4.1 was first dissolved in 0.1% DMSO in H_2O. Then, 100 μM of hydrazine were added to the testing solution and incubated stationary for three minutes. In the emission spectra, compound 4.1 displayed a strong emission peak centred at 359 nm with > 1000-fold of fluorescence enhancement after the addition of hydrazine. This result demonstrated a fast and sensitive reaction between the phthalimide sensing group and hydrazine (Figure 4.11).

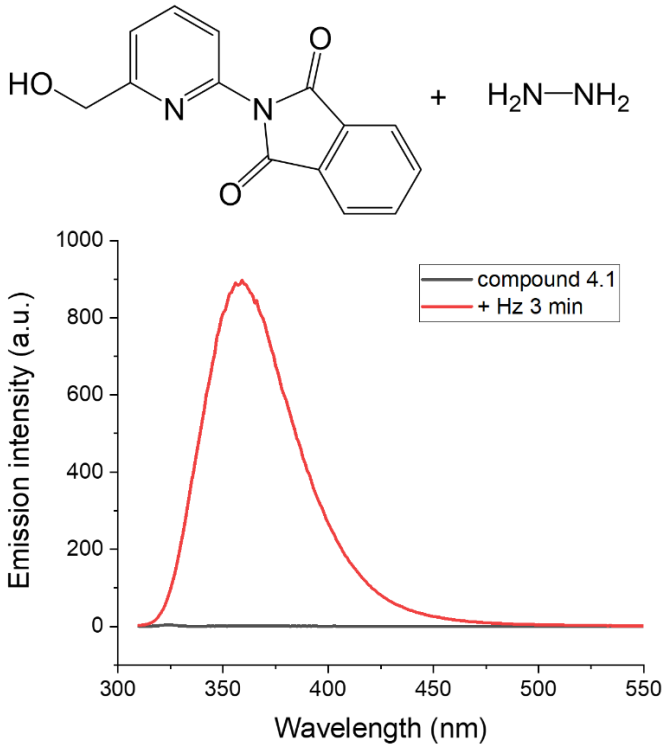

Figure 4.11: Preliminary testing of the hydrazine sensing ability of 10 μM compound 4.1 with 100 μM of hydrazine. λex: 290 nm, slit: 10-10 nm.

In the study of Hz[Tb]-L1 towards hydrazine, the testing conditions were similar to those of the preliminary study. 5 μM of Hz[Tb]-L1 in H_2O was allowed to react with 50 μM hydrazine. During

the titration with hydrazine, the probe Hz[Tb]-L1 displayed a set of emission peaks corresponding to the $^5D_4 \rightarrow {}^7F_J$ transition of the Tb(III) complex. Moreover, after adding 50 μM of hydrazine and incubating for three minutes, the sharp emission peak centred at 546 nm appeared, showing a 129-fold emission enhancement (Figure 4.12). The large emission response provides a good contrast in emission signals, demonstrating Hz[Tb]-L1's potential as an effective hydrazine luminescence sensor.

In the dose-dependent emission response titration, various concentrations of hydrazine (0, 0.625, 1.25, 5, 7.5, 10 μM) were added to the testing solution with 5 μM of Hz[Tb]-L1 in H_2O. The probe demonstrated a good linearity with ($r^2 = 0.9951$) in the range of 0 – 7.5 μM of hydrazine added (Figure 4.13). With the good linearity of emission intensity and concentration of hydrazine, limit of detection (LOD) was calculated to be 0.256 μM using three-sigma equation, $LOD = 3\sigma/k$, where σ is the standard deviation from 10 blank measurements and k is slope of the luminescence intensity vs hydrazine concentration. To confirm the sensing mechanism, HRMS analysis was conducted directly on the reaction mixture. The mass spectrum showed a target peak at m/z = 609.1482, confirming that phthalimide group was deprotected successfully, yielding the final product Hz[Tb]-L0 (Figure 4.14).

In the selectivity experiment, 50 μM of other analytes were added to the testing solution of Hz[Tb]-L1. The chosen analytes included the amine containing substance (ethylamine, ethylenediamine, hydroxylamine and lysine), amino acids (aspartic acid, cysteine, glutamic acid, histidine, proline and threonine), cations (Na^+, K^+, Fe^{3+}, Mn^{2+} and Zn^{2+}) and anions ($SO3^{2-}$, NO^{2-}, Cl^-, Br^-, I^- and

OAc^-). When most of the amino acids, cations, anions and single amine substances (ethylamine and hydroxylamine) were added to the testing solution, the probe Hz[Tb]-L1 demonstrated no significant luminescence response. However, when multiple amine substances were added to the testing solution, a significant luminescence response was observed. Although the luminescence response was not as high as that caused by hydrazine, it still caused a significant challenge in sensing hydrazine in the matrix with multiple amine substances. Therefore, structural modifications to the probe may be necessary to increase the selectivity of the probe towards multiple amine analytes in the future (Figure 4.15).

Nevertheless, the quantification ability of Hz[Tb]-L1 was then investigated. To simulate the water pollution problem, four tap water samples were prepared by spiking them with 0, 2, 4 and 6 μM hydrazine. Then, 5 μM of the probe, Hz[Tb]-L1, was added directly to the sample solutions and the luminescence intensity was measured. Each experiment for the four samples was repeated three times. The mean value of luminescence intensity was taken to calculate the concentration of hydrazine in the sample solutions. The linear equation obtained in Figure 4.13 was used as the calibration curve to calculate the hydrazine concentration. The calculated concentrations of the four sample solutions were “not detected”, 1.95 μM, 3.95 μM and 6.34 μM for 0, 2, 4 and 6 μM hydrazine spiked solutions, respectively. Comparing the calculated concentrations with the actual concentrations, the two values demonstrated an error of less than 10% which was within our acceptable range (Table 4.1).

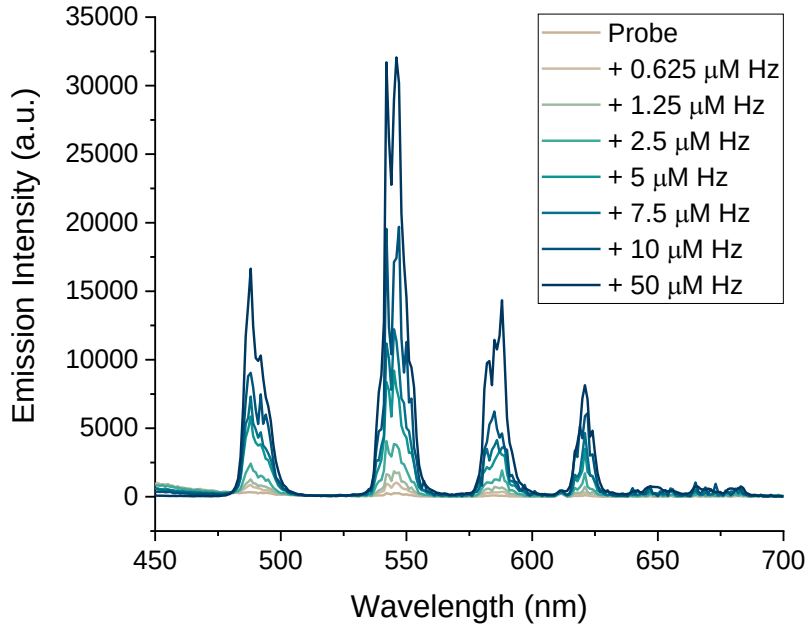

Figure 4.12: Dose-dependent luminescence titration of 5 μM Hz[Tb]-L1 in H_2O to 0 – 50 μM of hydrazine after three minutes of incubation. λex: 306 nm, slit: 1-1 nm.

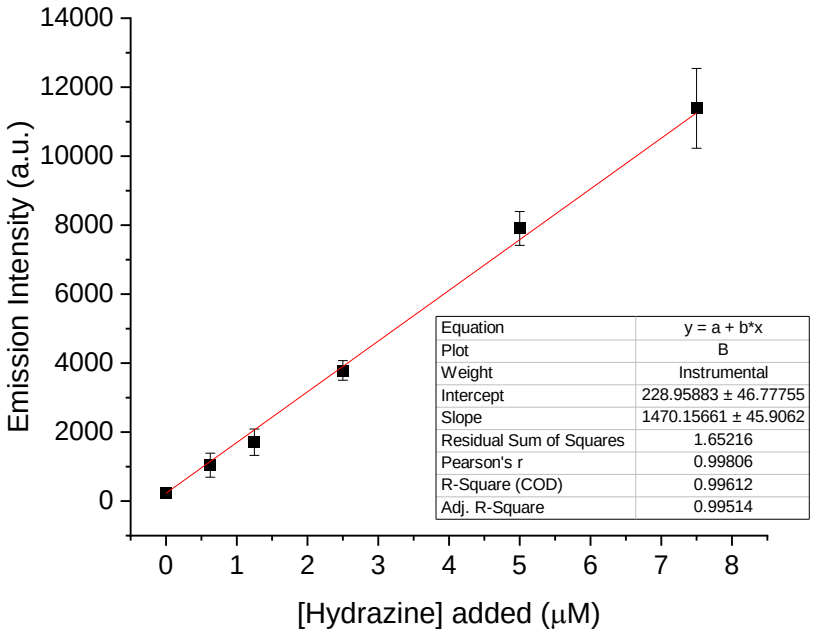

Figure 4.13: Dose-dependent luminescence titration of 5 μM Hz[Tb]-L1 after adding 0 – 7.5 μM of hydrazine with three minutes of incubation. λex: 306 nm, λem: 546 nm, slit: 1-1 nm.

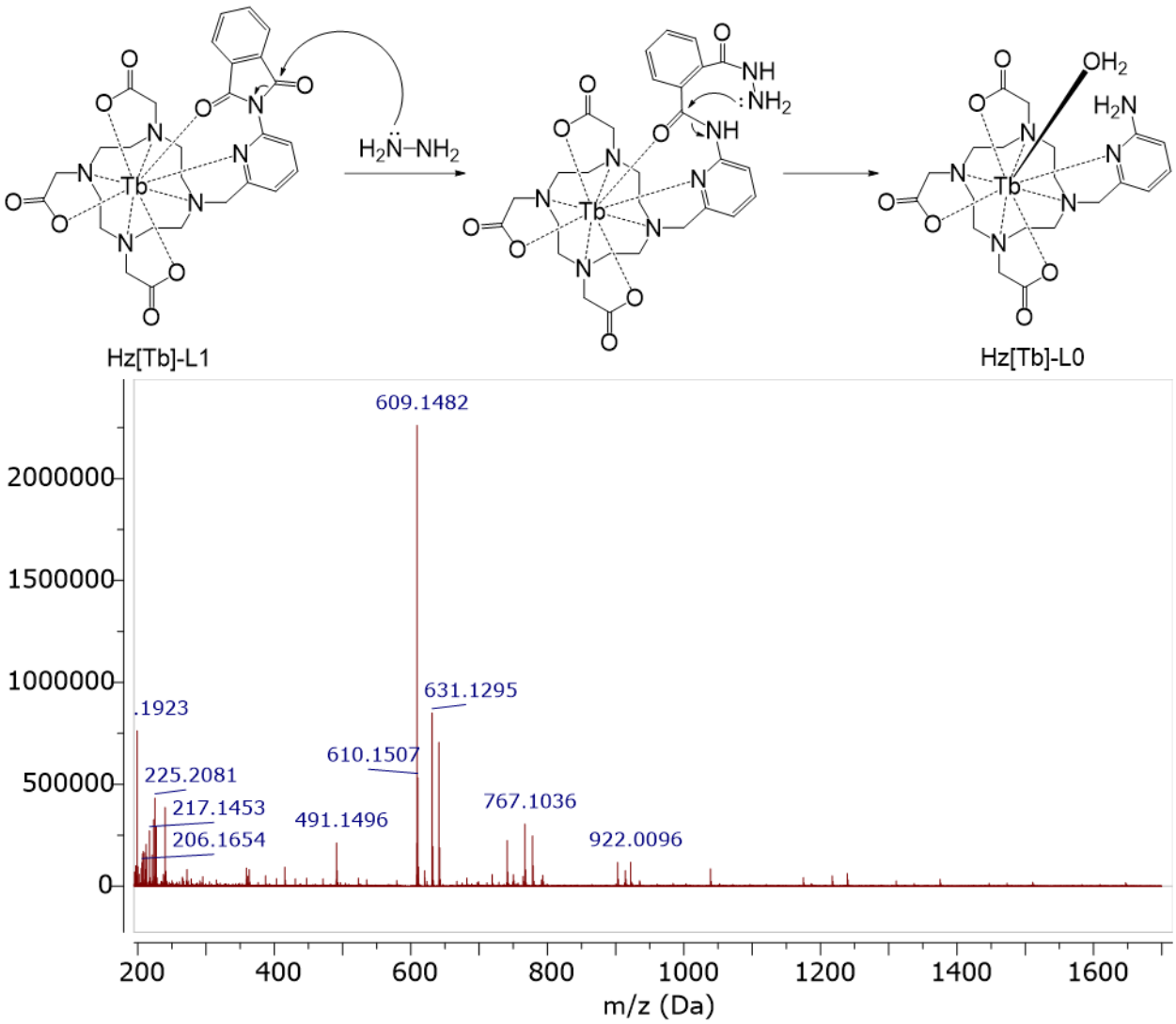

Figure 4.14: (top) Proposed sensing mechanism for Hz[Tb]-L1. (bottom) Mass spectrum of 50 µM hydrazine added to 5 µM Hz[Tb]-L1 (calc $[M+H]^+$ = 609.1480).

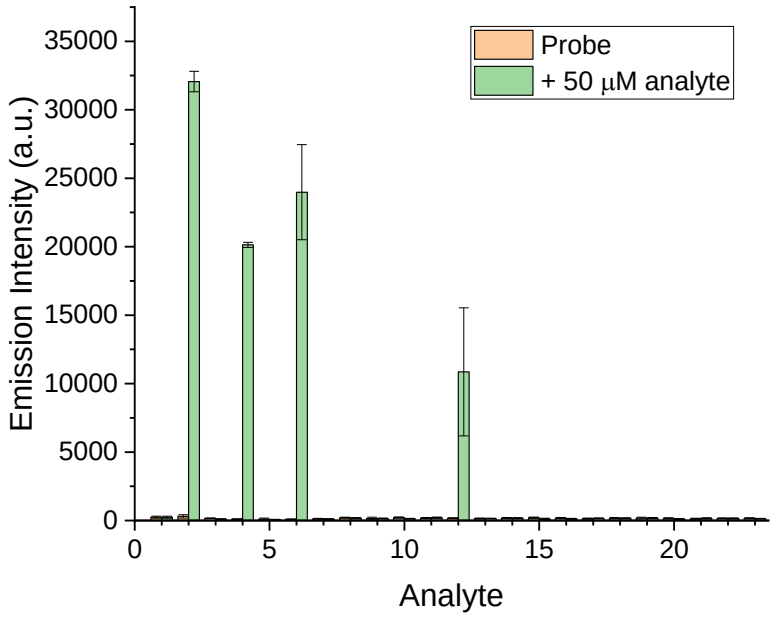

Figure 4.15: Luminescence selectivity experiment of 5 μM Hz[Tb]-L1 after adding 50 μM of analyte after three minutes of incubation. λex: 306 nm, λem: 546 nm slit: 1-1nm. 1: Control, 2: hydrazine, 3: ethylamine, 4: ethylenediamine, 5: hydroxylamine, 6: Lys, 7: Pro, 8: Thr, 9: Asp, 10: Glu, 11: Cys, 12: His, 13: Na^{+}, 14: K^{+}, 15: Fe^{3+}, 16: Mn^{2+}, 17: Zn^{2+}, 18: SO_3^{2-}, 19: NO_2^{-}, 20: Cl^{-}, 21: Br^{-}, 22: I^{-}, 23: OAc^{-}.

Table 4.1: Quantification of hydrazine by Hz[Tb]-L1 in a sample mixture. The luminescence measurements were conducted three times. The mean values were taken for calculation.

Analyte	**Intensity measured (a.u.)**	**Calculated concentration (μM)**	**Actual concentration (μM)**	**% Error**
Tap water	228.28 ± 30.61	Not detected	0	--
	3100.91 ± 56.13	1.95 ± 0.038	2	-2.5
	6028.99 ± 62.52	3.95 ± 0.043	4	-1.25
	8885.84± 194.31	6.34 ± 0.30	6	5.5

4.3.3 Magnetic resonance imaging (MRI) signal response of Hz[Gd]-L1 towards hydrazine

After studying the luminescence property of Hz[Tb]-L1, magnetic resonance property of Hz[Gd]-L1 was investigated for its potential application as an MRI contrast agent. Similar to the relaxivity measurements in Chapter 3, the clinical contrast agent Gadoteric acid (GdDOTA) was used as a reference. According to the equation $1/\Delta T_1 = r_1 \cdot [Gd]$, the longitudinal relaxivity (r_1) can be calculated as the slope from the $1/\Delta T_1$ vs [Gd] plot.[27] The relaxivity measurement was first conducted on GdDOTA. A series of concentrations (0 – 1 mM) of GdDOTA in H_2O was prepared and the T_1-weighted relaxivity was determined to be 3.7 $mM^{-1}s^{-1}$ (1.4T, 20°C). The same set of concentrations of Hz[Gd]-L1 and Hz[Gd]-L1 + Hz were prepared. For sample solution preparation of Hz[Gd]-L1 + Hz, Hz[Gd]-L1 was first dissolved in water to prepare the 1 mM stock solution of Hz[Gd]-L1. Then, 5 equivalents of hydrazine were added to the stock solution and stirred for one hour to prepare the 1 mM stock solution of Hz[Gd]-L1 + Hz. After the reaction was completed and confirmed with high-resolution mass spectrometry, the serial dilution method was used to prepare 1, 0.5, 0.25, 0.125, 0.0625 mM testing solutions of Hz[Gd]-L1 + Hz. The T_1-weighted r_1 value for Hz[Gd]-L1 was calculated as 1.5 $mM^{-1}s^{-1}$. In the presence of hydrazine, the phthalimide group was removed and T_1-weighted r_1 value was calculated to be 4.0 $mM^{-1}s^{-1}$ which shows a 2.7-fold enhancement (Figure 4.16 and Table 4.2). Similar to Hz[Tb]-L1, HRMS analysis was performed on the reaction mixture after hydrazine was added to Hz[Gd]-L1. From the mass spectrum, the major peak with m/z = 608.1476 with the pattern of isotopic mass of Gd atom was observed. This confirmed that Hz[Gd]-L0 was formed after the addition of hydrazine to Hz[Tb]-L1 (Figure 4.17).

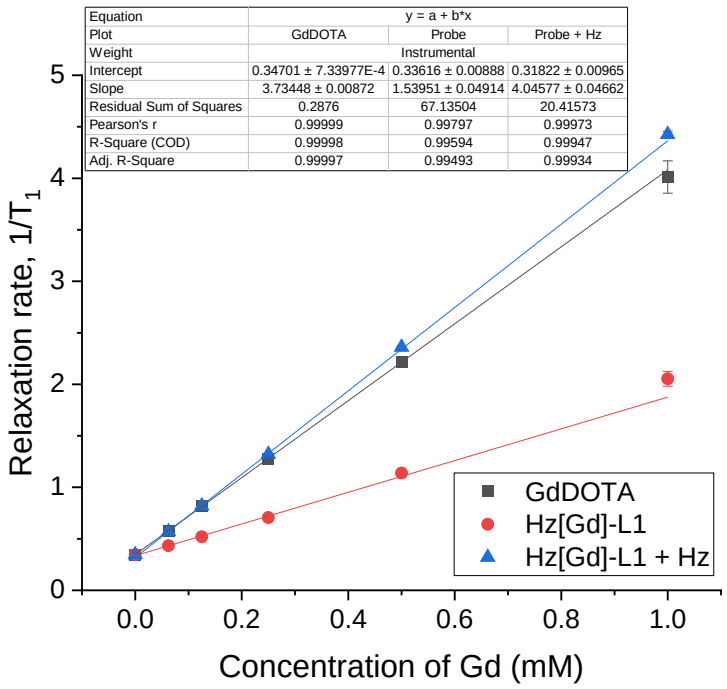

Figure 4.16: The T_1-weighted relaxivity (r_1) of GdDOTA, Hz[Gd]-L1 and [Gd]-L1 + hydrazine measured at 1.4 T and 20°C.

Table 4.2: T_1-weighted relaxivity (r_1) values of GdDOTA, Hz[Gd]-L1 and [Gd]-L1 + hydrazine.

At 1.4T, 25°C in H_2O:	**r_1, $mM^{-1}s^{-1}$**
GdDOTA (reference)	3.7 ± 0.0087
Hz[Gd]-L1	1.5 ± 0.049
Hz[Gd]-L1 + Hz	4.0 ± 0.047

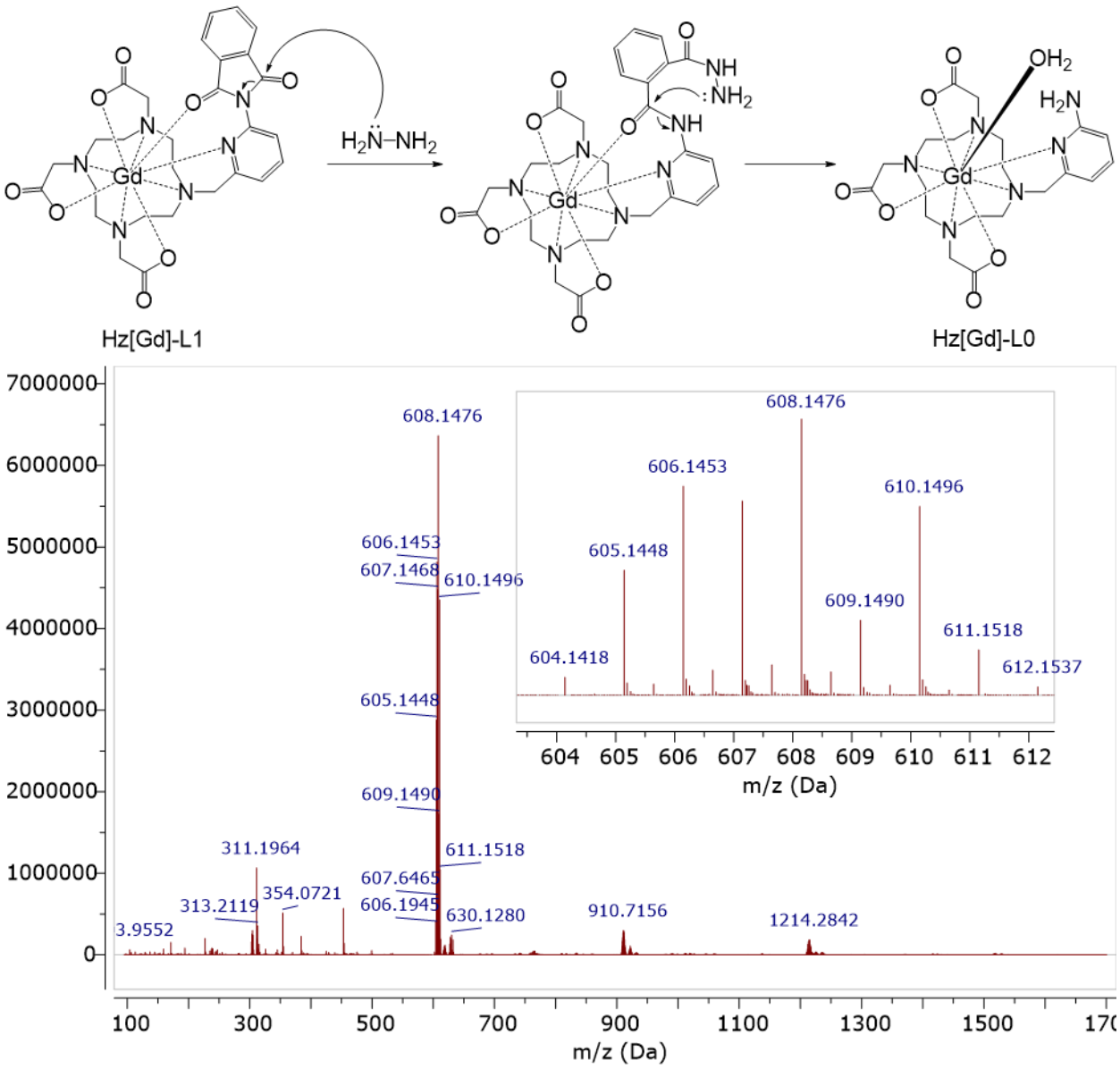

Figure 4.17: (top) Proposed sensing mechanism for Hz[Gd]-L1. (bottom) Mass spectrum of 50 μM hydrazine added to 5 μM Hz[Gd]-L1 (calc $[M+H]^+$ = 608.1468). Inlet: Zoom in mass spectrum for m/z = 604 – 612.

In the MR phantom experiment, five different concentrations of GdDOTA, Hz[Gd]-L1 and Hz[Gd]-L1 + Hz in water, together with blank solution (H_2O), were prepared and placed in glass

capillaries with a diameter of approximately 1 mm. In the MR phantom image, there was a distinct change between the Hz[Gd]-L1 and Hz[Gd]-L1 + Hz. The sample with hydrazine, Hz[Gd]-L1 + Hz, demonstrated a much "brighter" and higher signal intensity than the sample without hydrazine, Hz[Gd]-L1. Also, the image of Hz[Gd]-L1 + Hz was slightly "brighter" and the signal intensity was higher than that of GdDOTA. These results matched the r_1 measurement obtained in measurements at 1.4 T, showing that Hz[Gd]-L1 + Hz had slightly higher r_1 value than GdDOTA and significantly higher value than Hz[Gd]-L1 (Figure 4.18 and 4.19). The slight difference between Hz[Gd]-L1 + Hz and GdDOTA was attributed to the increased molecular weight and hindrance of water exchange by aminopyridine group in Hz[Gd]-L1 + Hz. The lower r_1 value in Hz[Gd]-L1 compared to Hz[Gd]-L1 + Hz and GdDOTA was due to the changes in the hydration number (q) of the Gd^{3+} complex. The hydration number of GdDOTA was determined to be q = 1 according to previous literature. The hydration number of Hz[Gd]-L1 and Hz[Gd]-L1 + Hz can be estimated from the luminescence lifetimes of Hz[Tb]-L1 and Hz[Tb]-L1 + Hz in H_2O and D_2O[28] by using the following equation:

$$q(Tb) = 5\left(\frac{1}{\tau_{H_2O}} - \frac{1}{\tau_{D_2O}} - 0.06\right) \qquad \text{Equation 4.1}$$

where τ_{H_2O} indicated the luminescence lifetime in H_2O and τ_{D_2O} indicated the luminescence lifetime in D_2O.

For Hz[Tb]-L1, the luminescence lifetimes in H_2O and D_2O were 2.61 and 2.91 ms respectively (Figure 4.20 and 4.21). The calculated q value was -0.1 which can be rounded off to q(Tb) = 0 (Table 4.3). For Hz[Tb]-L1 + Hz, the luminescence lifetimes in H_2O and D_2O were 1.95 and 3.36 ms respectively (Figure 4.22 and 4.23). The calculated q value was 0.8 which can be rounded off

to q(Tb) = 1 (Table 4.4). From the luminescence lifetime results, it can be concluded that the nine coordination sites of the lanthanide metal centre were fully occupied (q = 0) by the ligand in the absence of hydrazine. In the presence of hydrazine, the phthalimide protection group was removed. The carbonyl group on phthalimide no longer occupied the coordination site, allowing one H_2O molecule to coordinate with the lanthanide metal centre. The q value changed from 0 to 1, allowing the chemical exchange of the inner sphere water with the bulk (r_{1Is}) and enhancing the relaxation rate of the proton on water molecule attached to the lanthanide metal centre. Furthermore, the biological safety of Hz[Tb]-L1 was assessed. To examine the cell cytotoxicity, an MTT assay was conducted on the cervical cancer cells (HeLa). After incubating Hz[Tb]-L1 with HeLa cells for 24 hours, cell viability was determined. From the graph (Figure 4.24), the cell viability dropped to 80% at the probe concentration of 10 μM. However, the cell viability remained stable at around 80% with the probe concentrations up to 1000 μM. Therefore, Hz[Tb]-L1 is still considered safe for use in MRI.

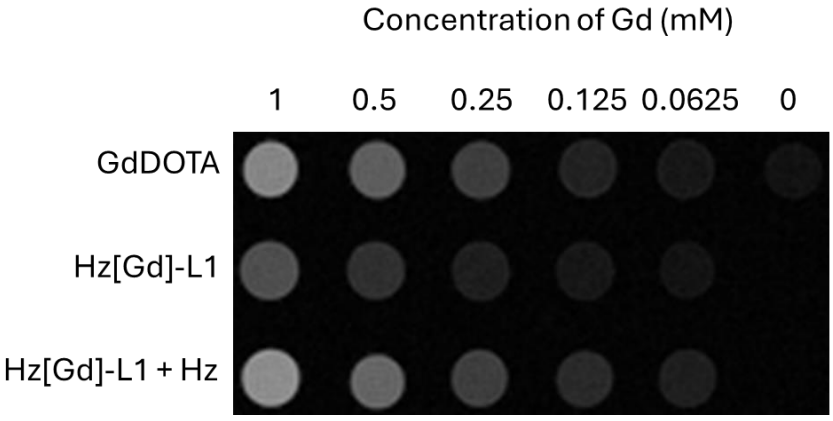

Figure 4.18: T_1-weighted MR phantom image of various concentrations of GdDOTA, Hz[Gd]-L1 and Hz[Gd]-L1 + hydrazine acquired at 7 T and 25°C.

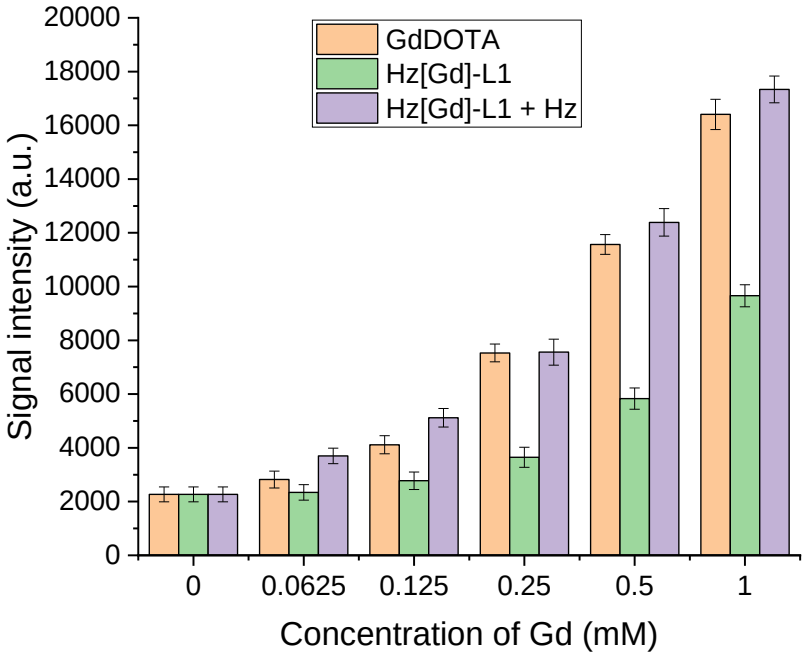

Figure 4.19: Signal intensity of the T_1-weighted MR phantom image of various concentrations of GdDOTA, Hz[Gd]-L1 and Hz[Gd]-L1 + hydrazine acquired at 7 T and 25°C.

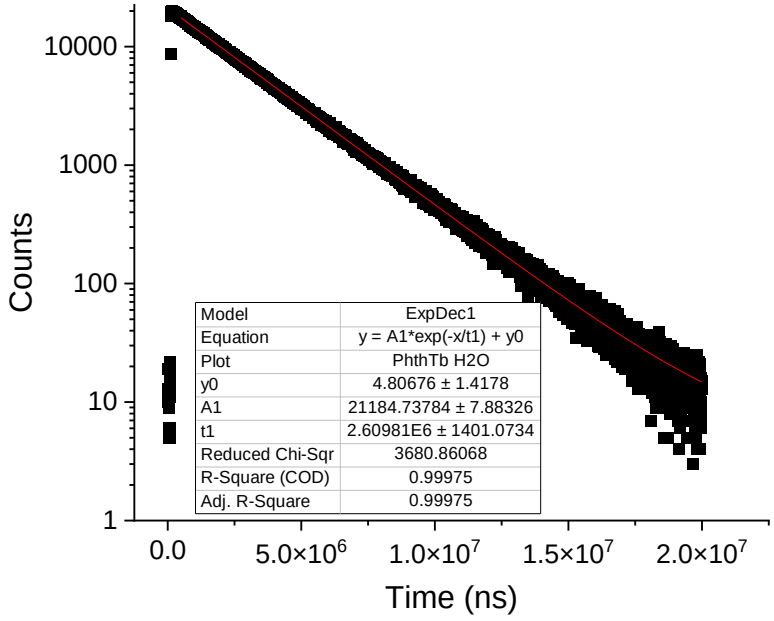

Figure 4.20: Decay curve of luminescence lifetime measurement of 5 μM Hz[Tb]-L1 in H_2O. λex: 306 nm, λem: 546 nm, slit: 5-5 nm.

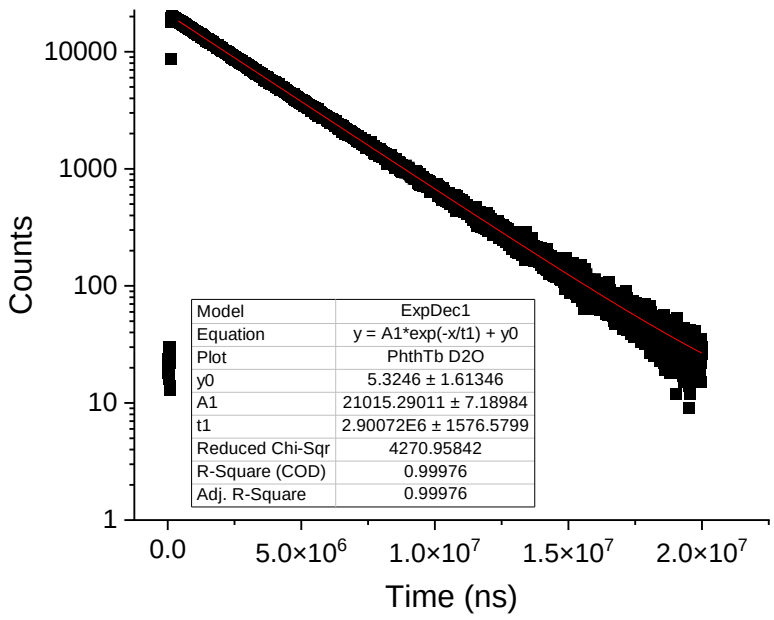

Figure 4.21: Decay curve of luminescence lifetime measurement of 5 μM Hz[Tb]-L1 in D_2O. λex: 306 nm, λem: 546 nm, slit: 5-5 nm.

Table 4.3: Hydration number calculation of Hz[Tb]-L1.

	Solvent	**τ_{obs}**	**q (Tb)**
Hz[Tb]-L1	H_2O	2.61 ms	-0.1 ≈ 0
	D_2O	2.91 ms	

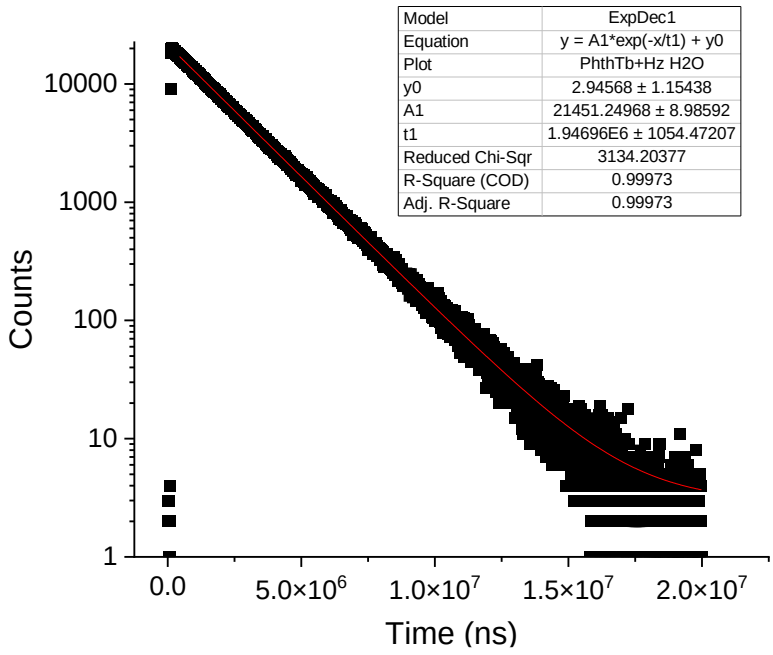

Figure 4.22: Decay curve of luminescence lifetime measurement of 5 μM Hz[Tb]-L1 + hydrazine in H_2O. λex: 306 nm, λem: 546 nm, slit: 5-5 nm.

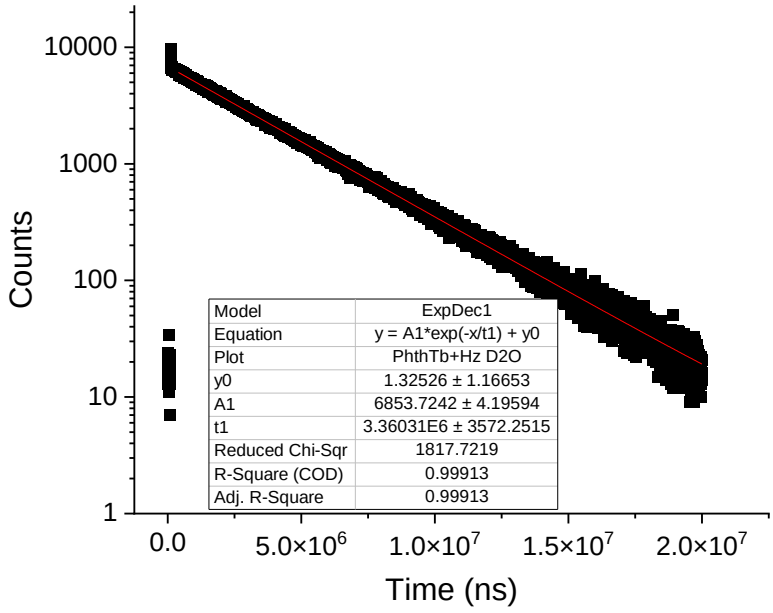

Figure 4.23: Decay curve of luminescence lifetime measurement of 5 μM Hz[Tb]-L1 + hydrazine in D_2O. λex: 306 nm, λem: 546 nm, slit: 5-5 nm.

Table 4.4: Hydration number calculation of Hz[Tb]-L1 + hydrazine.

	Solvent	τ_{obs}	q (Tb)
Hz[Tb]-L1 + Hz	H_2O	1.95 ms	0.8 ≈ 1
	D_2O	3.36 ms	

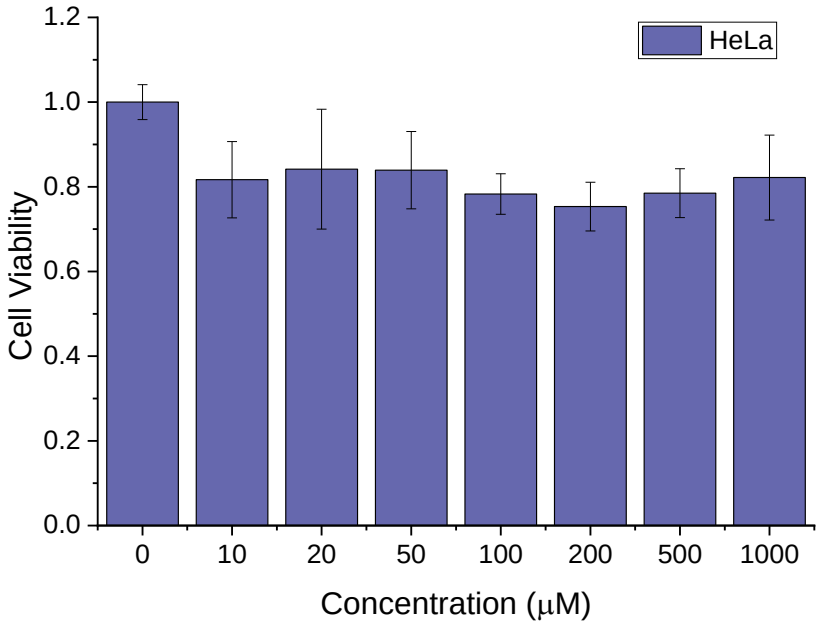

Figure 4.24: Cell viability of Hz[Gd]-L1 at 0 - 1000 μM for HeLa cells after 24 h incubation.

4.4 Conclusion and future works

In this chapter, reaction-based chemical probe, Hz[Ln]-L1, was designed and synthesized for hydrazine detection. For Hz[Ln]-L1, Tb^{3+} and Gd^{3+} ions were inserted into the ligand. Hz[Tb]-L1 and Hz[Gd]-L1 successfully demonstrated luminescence and magnetic responses, respectively, in the presence of hydrazine. In optical response experiments, Hz[Tb]-L1 demonstrated a good luminescent signal enhancement with 129-fold increase in three minutes after 10 equivalents of hydrazine were added, providing a good contrast in luminescence hydrazine sensing.

In the selectivity experiment, the probe showed good selectivity towards most of the amino acids, anions, cations and amine group-containing species. However, after adding some diamine-containing species such as ethylenediamine and lysine, Hz[Tb]-L1 also showed a responsive luminescence signal as the multiple amine group can undergo a similar deprotection mechanism as hydrazine. Although the selectivity of the probe was not optimal, it displayed a good linearity when reacting with 0 – 7.5 μM of hydrazine and had a good limit of detection of 0.256 μM.

In the magnetic response of Hz[Gd]-L1 toward hydrazine, the T_1-weighted relaxivity value for Hz[Gd]-L1 was determined to be 1.5 $mM^{-1}s^{-1}$. After the addition of hydrazine, the T_1-weighted relaxivity value showed a 2.7-fold enhancement, increasing to 4.0 $mM^{-1}s^{-1}$. The MR phantom experiment also showed that Hz[Gd]-L1 + Hz produced a much “brighter” image than Hz[Gd]-L1 alone. To confirm the reaction mechanism, HRMS was used to confirm that phthalimide protection was successfully removed.

From the luminescence lifetime experiment on Hz[Tb]-L1, the calculated hydration number of Hz[Tb]-L1 was 0 while that of Hz[Tb]-L1 + Hz was 1. This also confirms that the hydration number of Hz[Ln]-L1 increases from 0 to 1 in the presence of hydrazine. Moreover, the increase in hydration can also explain the increase in relaxivity in Hz[Gd]-L1. With the above luminescence and magnetic properties of Hz[Ln]-L1, it demonstrates potential for hydrazine detection in both environmental monitoring and biomedical MR imaging.

In the future work, there are a few improvements that can be made on Hz[Ln]-L1. In the optical imaging aspect, the antenna for Tb^{3+} can be modified to a larger π-conjugated chromophore. As the excitation wavelength is 306 nm for Hz[Tb]-L1, the short excitation wavelength is not ideal for biomedical imaging purpose because high excitation energy may damage to cells or tissues. In analyte selectivity aspect, the next generation of luminescence and MRI dual modality probe should enhance the selectivity toward hydrazine against over other multiple amine groups containing species by optimizing the sensing activities of the hydrazine sensing group. In MRI aspect, although the imaging contrast is good, there is still room for improvement. The future MRI probe could focus on enhancing the hydration number of the complex from 0 to 2 or even more to obtain a much “brighter” image and improve the image quality. However, when designing complexes with higher hydration number, it means that fewer coordination bonds are attached to the lanthanide centre. The lanthanide metal ions may be easily released to cause toxic effects to the biological system. Therefore, the thermodynamic stability of the complex must be carefully considered when designing high contrast gadolinium-based MRI probes.

4.5 Experimental section

General information

Deuterated solvents were purchased from Cambridge Isotope Laboratories. All other solvents and reagents were reagent grade and purchased from either Sigma-Aldrich Chemical Co. or Dieckmann and used without further purification. Thin-layer chromatography (TLC) was performed using pre-coated silica gel 60, F254 plates with a thickness of 0.2 mm. Column chromatography was conducted using silica gel and laboratory grade solvents. NMR spectra were recorded on Bruker Avance III 600 MHz spectrometers (^{1}H NMR on 600 MHz, ^{13}C NMR on 151 MHz) at 298 K. Chemical shifts δ were reported in parts per million (ppm) and referenced to the corresponding solvent peak (2.50 for DMSO-d6 and 7.26 for $CDCl_3$). Coupling constants *J* were reported in Hertz (Hz) and multiplicities were abbreviated as: s = singlet, d = doublet, t = triplet, dd = doublets of doublets, td = triplets of doublets and m = multiplet. High-resolution mass spectra, reported as m/z, were conducted by University Research Facility in Life Science, Hong Kong Polytechnic University from Agilent 6540 liquid chromatography – electrospray ionisation quadrupole-TOF mass. Low-resolution mass spectra were conducted by Waters Acquity H-Class UPLC with QDa mass detector for monitoring reaction and determining correct fraction during purification of product. Luminescence spectra were recorded on Edinburgh Instruments FLS920 Photoluminescence Spectrometer in a 1 cm quartz cuvette.

HPLC methods

Analytical HPLC was carried out using Agilent 1260 Infinity II LC system equipped with a 1260 Infinity II Quaternary Pump and an inline diode array UV-Vis detector. Semi-preparative HPLC was carried out with Waters semi-preparative HPLC system equipped with 2535 Quaternary Gradient Solvent Pump, 2707 Autosampler, Fraction Collector III and 2998 Photodiode Array Detector. Absorbance at 254 and 490 nm was monitored. The column used for analytical HPLC was an Atlantis T3 Column, 5 μm, 4.6 x 250 mm C18 reverse phase column. The column used for semi-preparative HPLC was an Atlantis T3 OBD Prep Column, 5 μm, 19 x 250 mm, C18 reverse phase column.

Relaxometry at 1.41 T

T_1-weighted relaxation times were measured on a Magritek Benchtop NMR Spinsolve 60 MHz equipped with MestReNova software. T_1 relaxation time was measured with the parameter: Scans: 2, Acquisition time: 6.4 s, Repetition time: 30 s, Maximum inversion time: 2, 5, 10, 15 s, Dummy Scans: 2, Number of steps: 11.

MR imaging of solution phantom at 7 T

MR phantom experiment at 7 Tesla were performed on Bruker Biospec 70/20 USR Magnetic Resonance Imaging System with a 20 cm bore running on a ParaVision® 360 software. Samples were prepared and placed in glass capillary tube with approximate diameter of 1 mm. The capillary tube was then secured to a 15 ml centrifuge tube which was placed in a volume radiofrequency

coil with 40 mm inner diameter and centred in the magnet bore. T_1 relaxation time was measured using variable repetition time accelerated spin echo sequence (RARE-VTR) with the parameter: variable TR = 150, 250, 500, 750, 1000, 2000, 4000, 8000, 10000 ms; TE = 11ms, fields of view = 25mm x 25 mm, matrix size = 384 x 384, number of axial slices = 5, slice thickness = 1 mm.

Cell culture and Cytotoxicity Test

HeLa cells were grown in Dulbecco's Modified Eagle Medium (DMEM). The medium was supplemented with 10% fetal bovine serum and 1% penicillin and streptomycin. The cell lines were incubated at 37°C in a humidified atmosphere containing 5% CO2. Cell viability was measured by the MTT assay. The cells were placed in a 96-well plate and maintained for twelve hours for adherence. The various concentrations of Hz[Gd]-L1 (0, 10, 50, 100, 200, 500, 1000 μM) in phosphate-buffered saline (PBS) were added and incubated for 24 hours. After discarding media from cell cultures, 50 μL of serum-free media and 50 μL of MTT solution were added to each well and the plate was incubated at 37°C for 3 hours. After the incubation finished 150 μL of MTT solvent was added into each well. The plate was wrapped in foil and shaken on an orbital shaker for 15 minutes. Optical absorbance was measured at 590 nm on a BioTek Synergy 2 plate reader. Relative cell viability was determined by the equation RV = (Ae – A0)/(Ac – A0) x 100%, where Ae is the absorbance of the experimental test; Ac is the absorbance of the control test (DMSO only); A0 is the absorbance of the blank test (no cells).

Synthesis work and characterization:

Synthesis of compound 4.1:

6-Amino-2-pyridinemethanol (1.61 mmol) and phthalic anhydride (3.22 mmol) were suspended in anhydrous toluene (15 mL) under a nitrogen atmosphere and the suspension was refluxed for 12 hours. When the reaction was confirmed complete by TLC, the reaction mixture was allowed to return to room temperature. It was then evaporated to dryness under reduced pressure. The residue was purified by flash column chromatography (ethyl acetate/ n-hexane = 1:1) on silica gel to give white compound 4.1 with a yield of 48.9%. ^{1}H NMR (600 MHz, Chloroform-*d*) δ 7.98 (dd, *J* = 5.8, 3.1 Hz, 2H), 7.90 (t, *J* = 7.8 Hz, 1H), 7.82 (dd, *J* = 5.7, 3.0 Hz, 2H), 7.36 (t, *J* = 8.2 Hz, 2H), 4.84 (s, 2H), 3.39 (s, 1H). ^{13}C NMR (151 MHz, $CDCl_3$) δ 166.62, 159.98, 145.33, 138.97, 134.67, 131.76, 124.02, 120.48, 120.23, 64.20. HRMS (ESI-TOF): m/z calcd. $[M+H]^+$ = 255.0770, $[M+Na]^+$ = 277.0589, $[M+H+MeOH]^+$ = 287.1032, $[M+Na+MeOH]^+$ = 309.0851, found: 255.0774, 277.0595, 287.1076, 309.0822.

Synthesis of compound 4.2:

Compound 4.1 (0.787 mmol) was first dissolved in anhydrous DCM (10 mL) at 0°C under a nitrogen atmosphere. Phosphorus tribromide (1.574 mmol) was slowly added to the solution and the resulting mixture was stirred for 2 hours at 0°C. When the reaction was confirmed complete by TLC, the reaction was quenched by the addition of saturated $NaHCO_3$ aqueous solution. The reaction mixture was then extracted with DCM (3 x 20 mL). The combined organic layers were dried over Na_2SO_4. After filtration of the inorganic salts, the combined organic solvent was evaporated to dryness under reduced pressure. The residue was purified by flash column

chromatography (ethyl acetate/ n-hexane = 1:3) on silica gel to give white compound 4.2 with a yield of 65%. ^{1}H NMR (600 MHz, Chloroform-*d*) δ 7.98 (dd, *J* = 5.6, 3.0 Hz, 2H), 7.91 (t, *J* = 8.0 Hz, 1H), 7.82 (dd, *J* = 5.6, 3.0 Hz, 2H), 7.55 (d, *J* = 7.7 Hz, 1H), 7.36 (d, *J* = 7.9 Hz, 1H), 4.60 (s, 2H). ^{13}C NMR (151 MHz, $CDCl_3$) δ 166.56, 157.23, 145.64, 139.36, 134.67, 131.77, 124.03, 123.38, 121.48, 32.93. HRMS (ESI-TOF): m/z calcd. $[M+H]^+$ = 316.9926, $[M+Na]^+$ = 338.9745, $[M+H+MeOH]^+$ = 349.0188, $[M+Na+MeOH]^+$ = 371.0007, found: 316.9925, 338.9747, 349.084, 371.0005.

Synthesis of compound 4.3:

Compound 4.2 (0.451 mmol), DO3A-tBu (0.451 mmol) and K_2CO_3 (1.353 mmol) were suspended in anhydrous ACN under a nitrogen atmosphere and the suspension was stirred at 50°C for 12 hours. When the reaction was confirmed complete by TLC, the reaction mixture was allowed to return to room temperature and inorganic salts were filtered off. The mixture was then evaporated to dryness under reduced pressure. The residue was purified by flash column chromatography (dichloromethane/methanol = 15:1 v/v) on silica gel to give white solid compound 4.3 with a yield of 82%. ^{1}H NMR (600 MHz, Chloroform-*d*) δ 7.97 (dd, *J* = 5.5, 3.0 Hz, 2H), 7.92 (t, *J* = 7.8 Hz, 1H), 7.88 (dd, *J* = 5.5, 3.1 Hz, 2H), 7.66 (dd, *J* = 7.8, 0.9 Hz, 1H), 7.39 (dd, *J* = 7.8, 0.9 Hz, 1H), 3.81 (d, *J* = 35.1 Hz, 2H), 3.16 (d, *J* = 26.5 Hz, 4H), 3.02 – 2.54 (m, 13H), 2.39 (d, *J* = 32.5 Hz, 4H), 1.43 (s, 10H), 1.36 (s, 17H). ^{13}C NMR (151 MHz, $CDCl_3$) δ 172.72, 172.09, 166.82, 158.33, 145.64, 139.23, 135.09, 131.49, 124.10, 123.80, 120.28, 82.31, 82.24, 59.10, 56.26, 55.78, 50.22, 28.15, 28.11, 27.98, 27.94, 27.90. HRMS (ESI-TOF): m/z calcd. $[M+H]^+$ = 751.4394, $[M+Na]^+$ = 773.4214, $[M+H+MeOH]^+$ = 783.4657, $[M+Na+MeOH]^+$ = 805.4476, found: 751.4419, 773.4229, 783.4620, 805.4607.

Synthesis of Hz[Tb]-L1:

Compound 4.3 (0.088 mmol) was dissolved in trifluoroacetic acid and stirred at room temperature for 12 hours. The reaction mixture was evaporated to dryness under reduced pressure. The residue was then dissolved in MeOH/H_2O (2:1, v/v), followed by the addition of terbium(III) chloride hydrate (0.088 mmol). The mixture was maintained in the pH range of 6-7 by adding NaOH solution and stirred at room temperature for 24 hours. When the metal coordination was complete, the crude product was purified by Semi-Preparative High-Performance Liquid Chromatography to yield yellow product Hz[Tb]-L1 with a yield of 33.1%. HRMS (ESI-TOF): m/z calcd. $[M+Na+MeOH]^+$ = 793.1617, found 793.1617.

Synthesis of Hz[Gd]-L1:

Compound 4.3 (0.102 mmol) was dissolved in trifluoroacetic acid and stirred at room temperature for 12 hours. The reaction mixture was evaporated to dryness under reduced pressure. The residue was then dissolved in MeOH/H_2O (2:1, v/v), followed by the addition of gadolinium(III) chloride hydrate (0.102 mmol). The mixture was maintained in the pH range of 6-7 by adding NaOH solution and stirred at room temperature for 24 hours. When the metal coordination was complete, the crude product was purified by Semi-Preparative High-Performance Liquid Chromatography to yield yellow product Hz[Gd]-L1 with a yield of 31.7%. HRMS (ESI-TOF): m/z calcd. $[M+H+MeOH]^+$ = 770.1785, found 770.1800.

4.6 Reference

[1] J. E. Troyan, "Properties, Production, and Uses of Hydrazine," *Industrial & Engineering Chemistry,* vol. 45, no. 12, pp. 2608-2612, 1953, doi: 10.1021/ie50528a020.

[2] S. M. Davis and N. Yilmaz, "Advances in Hypergolic Propellants: Ignition, Hydrazine, and Hydrogen Peroxide Research," *Advances in Aerospace Engineering,* vol. 2014, pp. 1-9, 2014, doi: 10.1155/2014/729313.

[3] C. T. Brewer, L. Yang, A. Edwards, Y. Lu, J. Low, J. Wu, R. E. Lee, and T. Chen, "The Isoniazid Metabolites Hydrazine and Pyridoxal Isonicotinoyl Hydrazone Modulate Heme Biosynthesis," *Toxicological Sciences,* vol. 168, no. 1, pp. 209-224, 2019, doi: 10.1093/toxsci/kfy294.

[4] S. Galvani, C. Coatrieux, M. Elbaz, M.-H. Grazide, J.-C. Thiers, A. Parini, K. Uchida, N. Kamar, L. Rostaing, M. Baltas, R. Salvayre, and A. Nègre-Salvayre, "Carbonyl scavenger and antiatherogenic effects of hydrazine derivatives," *Free Radical Biology and Medicine,* vol. 45, no. 10, pp. 1457-1467, 2008, doi: 10.1016/j.freeradbiomed.2008.08.026.

[5] H. N. Nguyen, J. A. Chenoweth, V. S. Bebarta, T. E. Albertson, and C. D. Nowadly, "The Toxicity, Pathophysiology, and Treatment of Acute Hydrazine Propellant Exposure: A Systematic Review," *Military Medicine,* vol. 186, no. 3-4, pp. e319-e326, 2021, doi: 10.1093/milmed/usaa429.

[6] G. Choudhary and H. Hansen, "Human health perspective of environmental exposure to hydrazines: A review," *Chemosphere,* vol. 37, no. 5, pp. 801-843, 1998, doi: 10.1016/s0045-6535(98)00088-5.

[7] X.-Y. Zhang, Y.-S. Yang, W. Wang, Q.-C. Jiao, and H.-L. Zhu, "Fluorescent sensors for the detection of hydrazine in environmental and biological systems: Recent advances and

future prospects," *Coordination Chemistry Reviews,* vol. 417, 2020, doi: 10.1016/j.ccr.2020.213367.

[8] J. K. Niemeier and D. P. Kjell, "Hydrazine and Aqueous Hydrazine Solutions: Evaluating Safety in Chemical Processes," *Organic Process Research & Development,* vol. 17, no. 12, pp. 1580-1590, 2013, doi: 10.1021/op400120g.

[9] U. S. A. f. T. Substances, D. Registry, I. Sciences International, and R. T. Institute, *Toxicological Profile for Hydrazines*. U.S. Department of Health and Human Services, Public Health Service, Agency for Toxic Substances and Disease Registry, 1997.

[10] M. Rungemorris, N. Wu, and R. F. Novak, "Hydrazine-Mediated DNA Damage: Role of Hemoprotein, Electron Transport, and Organic Free Radicals," *Toxicology and Applied Pharmacology,* vol. 125, no. 1, pp. 123-132, 1994, doi: 10.1006/taap.1994.1056.

[11] B. Kalyanaraman and B. K. Sinha, "Free radical-mediated activation of hydrazine derivatives," *Environmental Health Perspectives,* vol. 64, pp. 179-184, 1985, doi: 10.1289/ehp.8564179.

[12] L. Yan, S. Zhang, Y. Xie, X. Mu, and J. Zhu, "Recent Progress in the Development of Fluorescent Probes for the Detection of Hydrazine (N_2H_4)," *Critical Reviews in Analytical Chemistry,* vol. 52, no. 1, pp. 210-229, 2022, doi: 10.1080/10408347.2020.1797464.

[13] K. Li, H.-R. Xu, K.-K. Yu, J.-T. Hou, and X.-Q. Yu, "A coumarin-based chromogenic and ratiometric probe for hydrazine," *Analytical Methods,* vol. 5, no. 11, p. 2653, 2013, doi: 10.1039/c3ay40148k.

[14] S. Goswami, S. Das, K. Aich, B. Pakhira, S. Panja, S. K. Mukherjee, and S. Sarkar, "A Chemodosimeter for the Ratiometric Detection of Hydrazine Based on Return of ESIPT

and Its Application in Live-Cell Imaging," *Organic Letters,* vol. 15, no. 21, pp. 5412-5415, 2013, doi: 10.1021/ol4026759.

[15] L. Cui, Z. Peng, C. Ji, J. Huang, D. Huang, J. Ma, S. Zhang, X. Qian, and Y. Xu, "Hydrazine detection in the gas state and aqueous solution based on the Gabriel mechanism and its imaging in living cells," *Chemical Communications,* vol. 50, no. 12, pp. 1485-1487, 2014, doi: 10.1039/c3cc48304e.

[16] X. Jiang, Z. Lu, M. Shangguan, S. Yi, X. Zeng, Y. Zhang, and L. Hou, "A fluorescence "turn-on" sensor for detecting hydrazine in environment," *Microchemical Journal,* vol. 152, p. 104376, 2020, doi: 10.1016/j.microc.2019.104376.

[17] L. Wang, F.-Y. Liu, H.-Y. Liu, Y.-S. Dong, T.-Q. Liu, J.-F. Liu, Y.-W. Yao, and X.-J. Wan, "A novel pyrazoline-based fluorescent probe for detection of hydrazine in aqueous solution and gas state and its imaging in living cells," *Sensors and Actuators B: Chemical,* vol. 229, pp. 441-452, 2016, doi: 10.1016/j.snb.2016.02.001.

[18] J. Fan, W. Sun, M. Hu, J. Cao, G. Cheng, H. Dong, K. Song, Y. Liu, S. Sun, and X. Peng, "An ICT-based ratiometric probe for hydrazine and its application in live cells," *Chemical Communications,* vol. 48, no. 65, p. 8117, 2012, doi: 10.1039/c2cc34168a.

[19] L. Xiao, J. Tu, S. Sun, Z. Pei, Y. Pei, Y. Pang, and Y. Xu, "A fluorescent probe for hydrazine and its in vivo applications," *RSC Advances,* vol. 4, no. 79, pp. 41807-41811, 2014, doi: 10.1039/c4ra08101c.

[20] Y. He, Z. Li, B. Shi, Z. An, M. Yu, L. Wei, and Z. Ni, "A new near-infrared ratiometric fluorescent probe for hydrazine," *RSC Advances,* vol. 7, no. 41, pp. 25634-25639, 2017, doi: 10.1039/c7ra04270a.

[21] Y. Jung, I. G. Ju, Y. H. Choe, Y. Kim, S. Park, Y.-M. Hyun, M. S. Oh, and D. Kim, "Hydrazine Exposé: The Next-Generation Fluorescent Probe," *ACS Sensors,* vol. 4, no. 2, pp. 441-449, 2019, doi: 10.1021/acssensors.8b01429.

[22] B. Roy, S. Halder, A. Guha, and S. Bandyopadhyay, "Highly Selective Sub-ppm Naked-Eye Detection of Hydrazine with Conjugated-1,3-Diketo Probes: Imaging Hydrazine in *Drosophila* Larvae," *Analytical Chemistry,* vol. 89, no. 19, pp. 10625-10636, 2017, doi: 10.1021/acs.analchem.7b03503.

[23] Z. Luo, B. Liu, T. Qin, K. Zhu, C. Zhao, C. Pan, and L. Wang, "Cyclization of chalcone enables ratiometric fluorescence determination of hydrazine with a high selectivity," *Sensors and Actuators B: Chemical,* vol. 263, pp. 229-236, 2018, doi: 10.1016/j.snb.2018.02.120.

[24] Y. Zhang, Y. Huang, Y. Yue, J. Chao, F. Huo, and C. Yin, "A compact fluorescent probe based on o-phthalaldehyde for ultrasensitive detection of hydrazine in gas and solution phases," *Sensors and Actuators B: Chemical,* vol. 273, pp. 944-950, 2018, doi: 10.1016/j.snb.2018.06.112.

[25] G. Yu, Y. Cao, H. Liu, Q. Wu, Q. Hu, B. Jiang, and Z. Yuan, "A spirobenzopyran-based multifunctional chemosensor for the chromogenic sensing of Cu2+ and fluorescent sensing of hydrazine with practical applications," *Sensors and Actuators B: Chemical,* vol. 245, pp. 803-814, 2017, doi: 10.1016/j.snb.2017.02.020.

[26] X. Shi, C. Yin, Y. Zhang, Y. Wen, and F. Huo, "A novel ratiometric and colorimetric fluorescent probe for hydrazine based on ring-opening reaction and its applications," *Sensors and Actuators B: Chemical,* vol. 285, pp. 368-374, 2019, doi: 10.1016/j.snb.2019.01.075.

[27] E. J. Werner, A. Datta, C. J. Jocher, and K. N. Raymond, "High-Relaxivity MRI Contrast Agents: Where Coordination Chemistry Meets Medical Imaging," *Angewandte Chemie International Edition,* vol. 47, no. 45, pp. 8568-8580, 2008, doi: 10.1002/anie.200800212.

[28] A. Beeby, I. M. Clarkson, R. S. Dickins, S. Faulkner, D. Parker, L. Royle, A. S. De Sousa, J. A. G. Williams, and M. Woods, "Non-radiative deactivation of the excited states of europium, terbium and ytterbium complexes by proximate energy-matched OH, NH and CH oscillators: an improved luminescence method for establishing solution hydration states," *Journal of the Chemical Society, Perkin Transactions 2,* no. 3, pp. 493-504, 1999, doi: 10.1039/a808692c.

4.7 Appendix

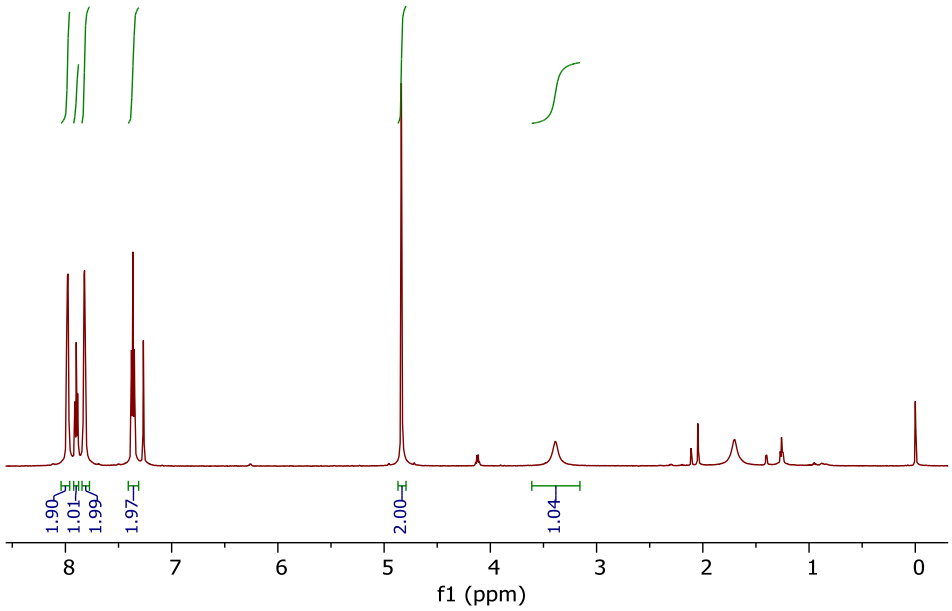

Figure 4.25: ^{1}H NMR spectrum of compound 4.1 (600 MHz, $CDCl_3$).

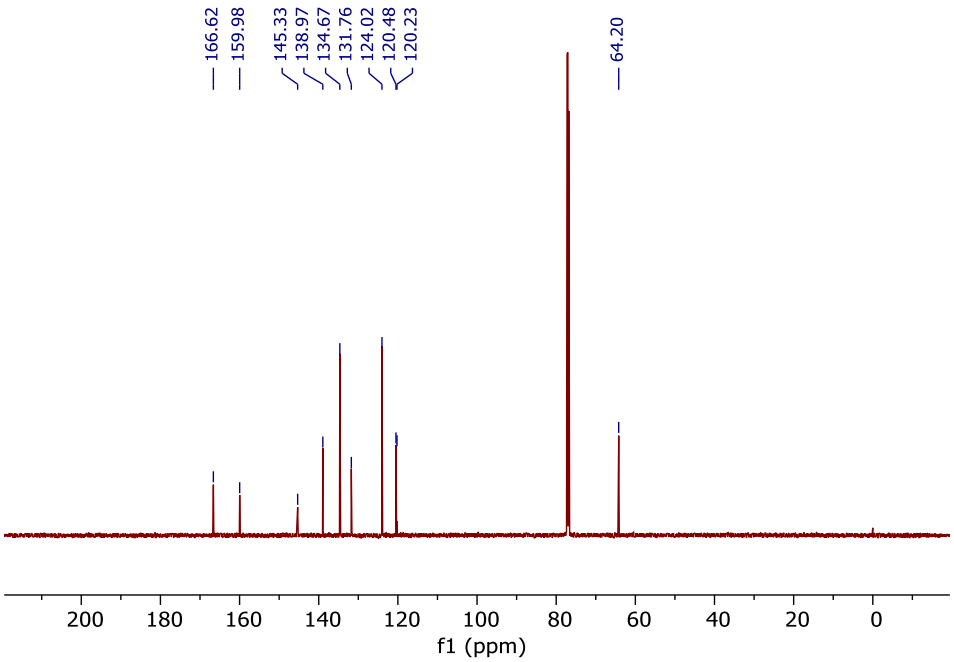

Figure 4.26: ^{13}C NMR spectrum of compound 4.1 (151 MHz, $CDCl_3$).

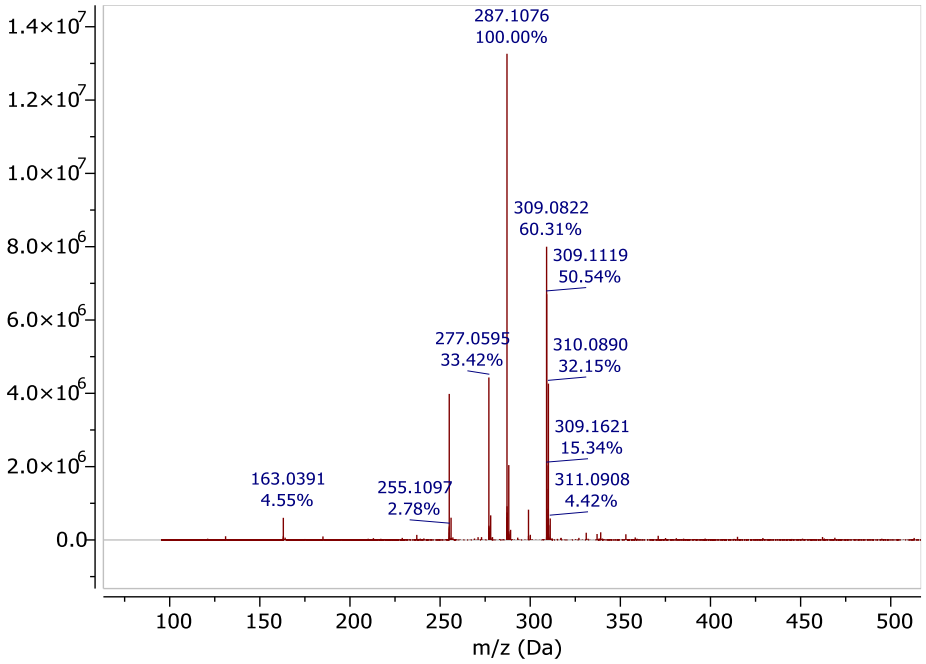

Figure 4.27: High-resolution mass spectrum of compound 4.1.

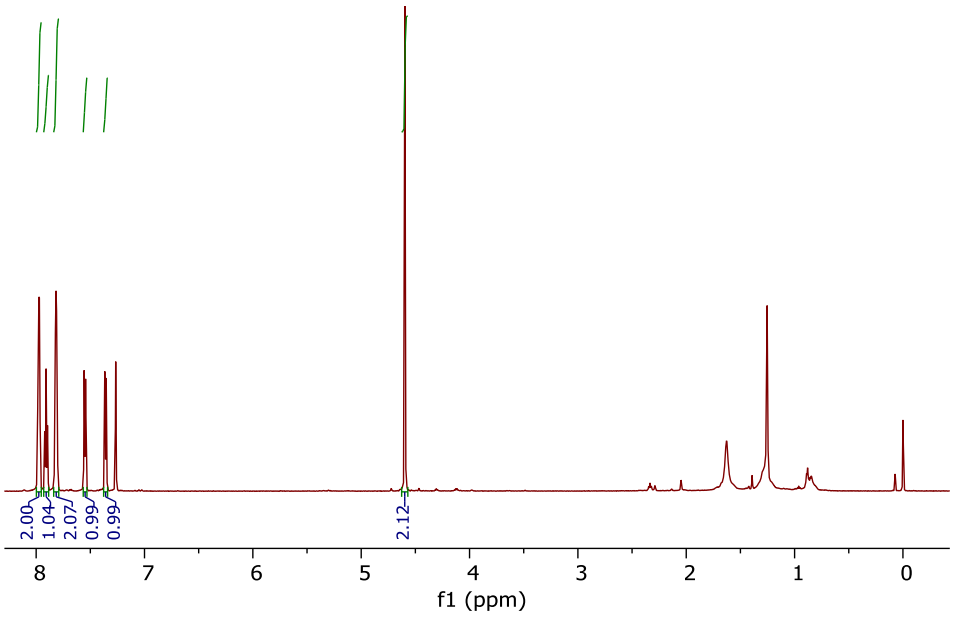

Figure 4.28: ^{1}H NMR spectrum of compound 4.2 (600 MHz, $CDCl_3$)

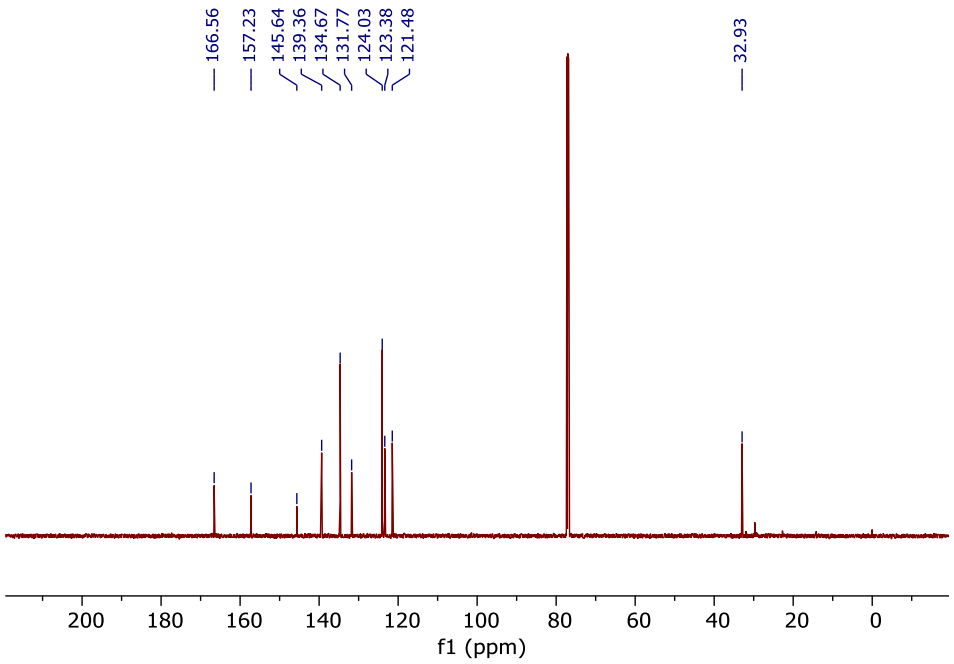

Figure 4.29: ^{13}C NMR spectrum of compound 4.2 (151 MHz, $CDCl_3$).

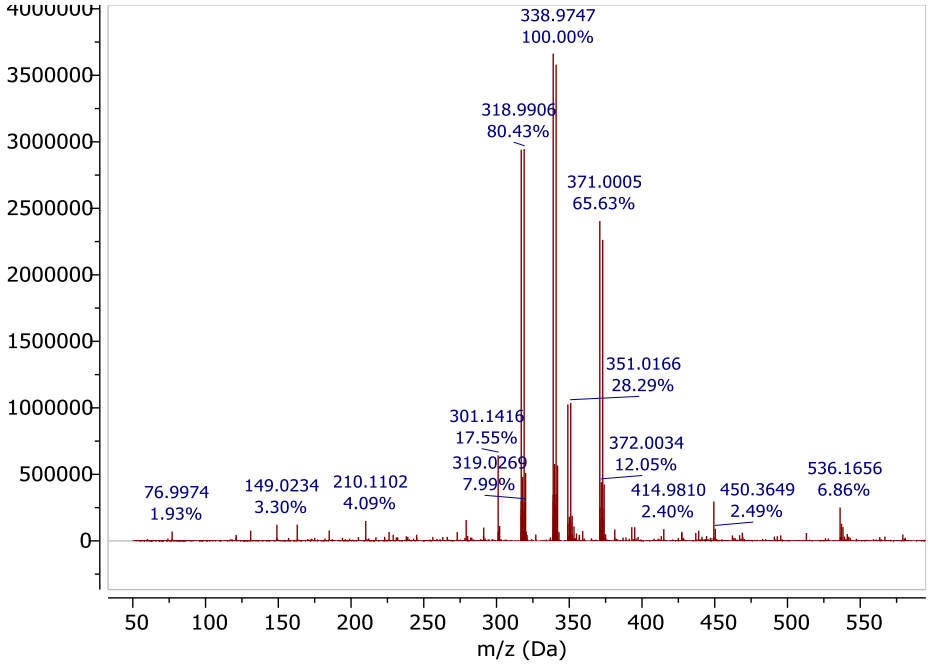

Figure 4.30: High-resolution mass spectrum of compound 4.2.

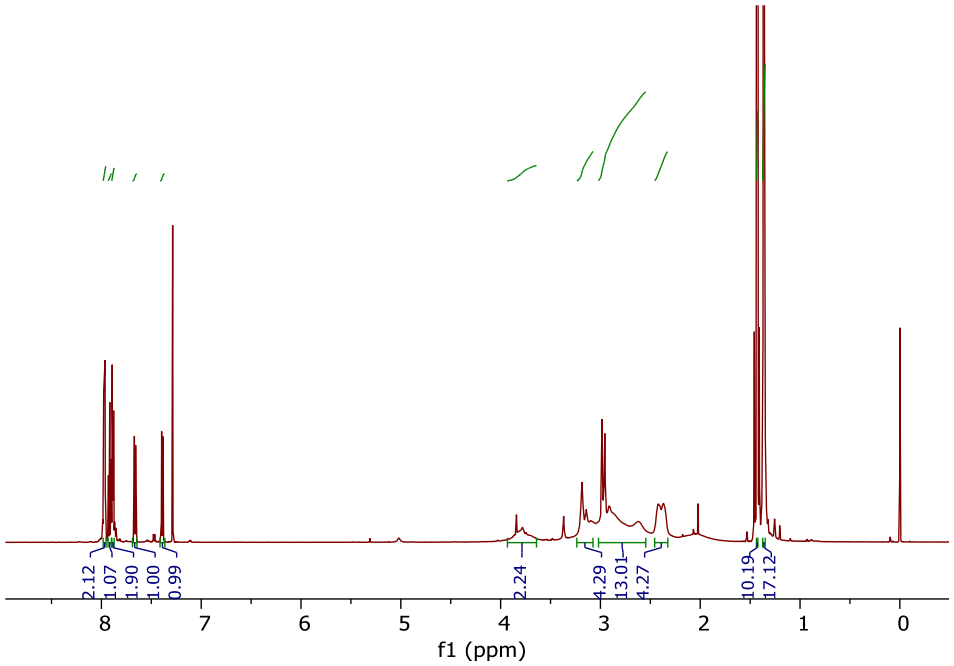

Figure 4.31: ^{1}H NMR spectrum of compound 4.3 (600 MHz, $CDCl_3$)

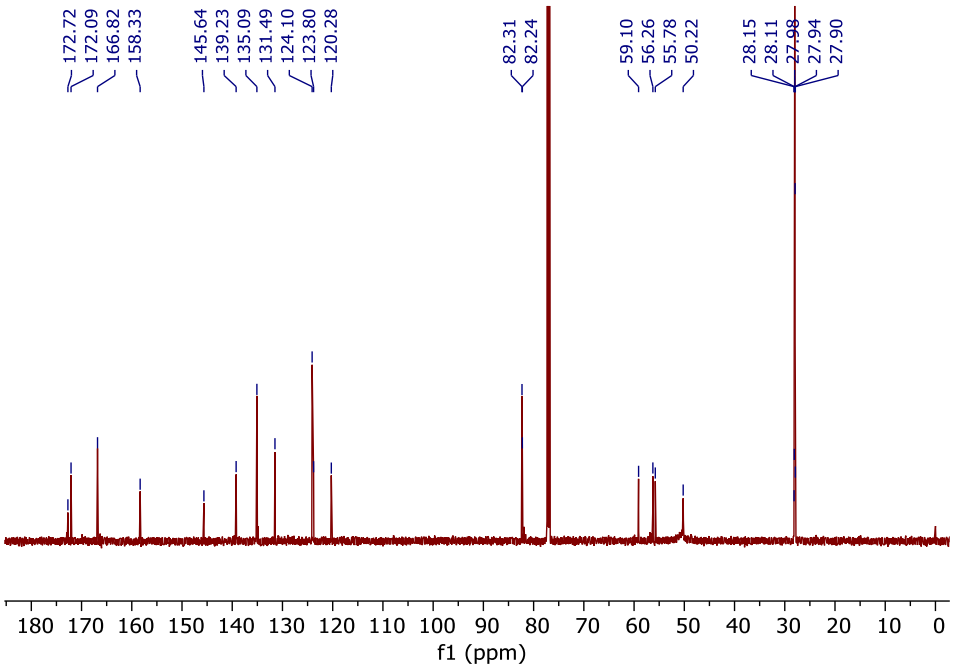

Figure 4.32: ^{13}C NMR spectrum of compound 4.3 (151 MHz, $CDCl_3$).

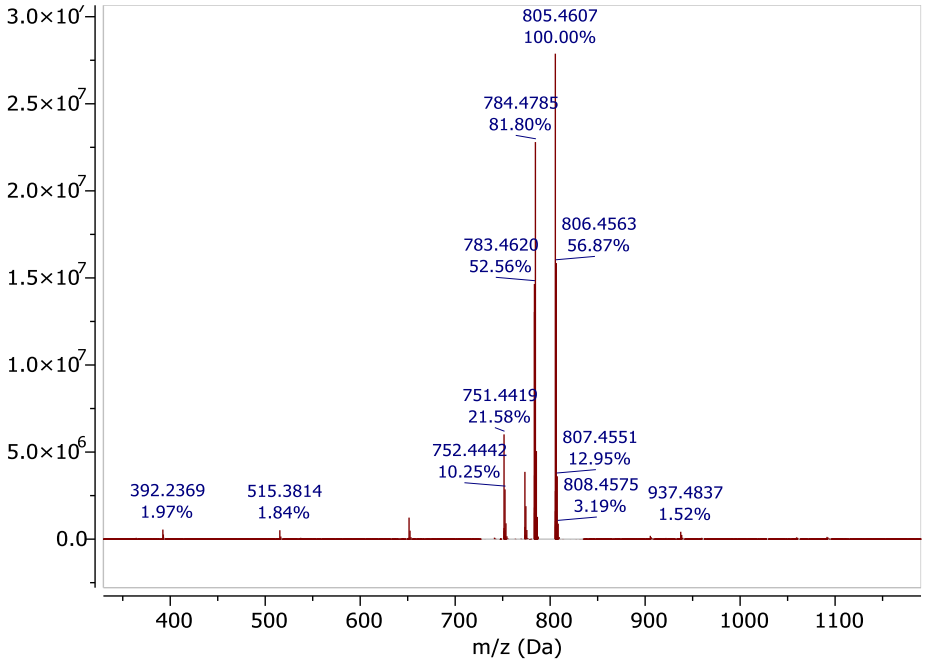

Figure 4.33: High-resolution mass spectrum of compound 4.3.

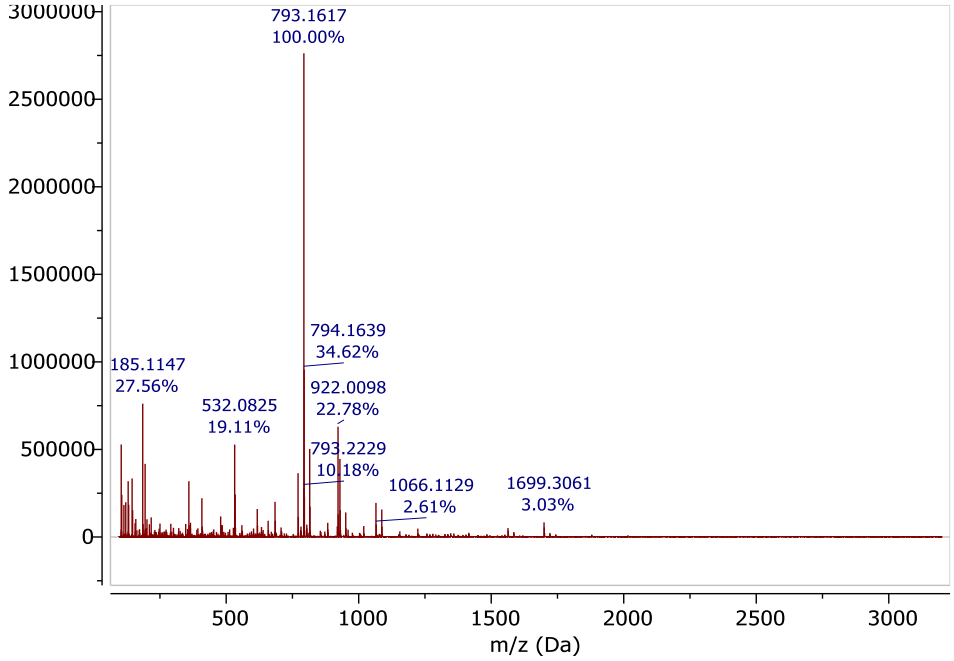

Figure 4.34: High-resolution mass spectrum of Hz[Tb]-L1.

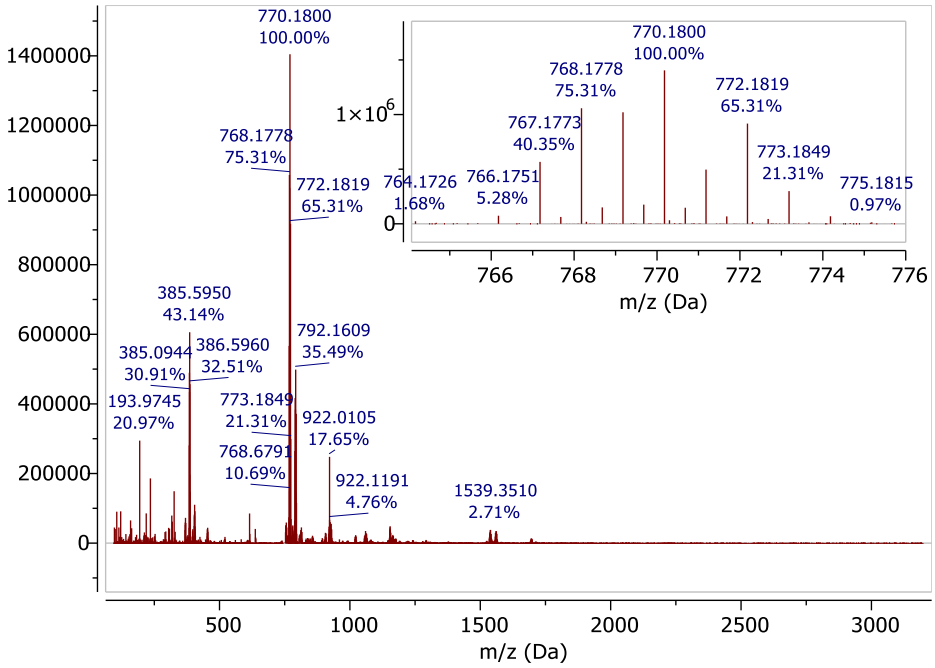

Figure 4.35: High-resolution mass spectrum of Hz[Gd]-L1. Inlet graph: Zoom in mass spectrum (m/z = 765 – 776).

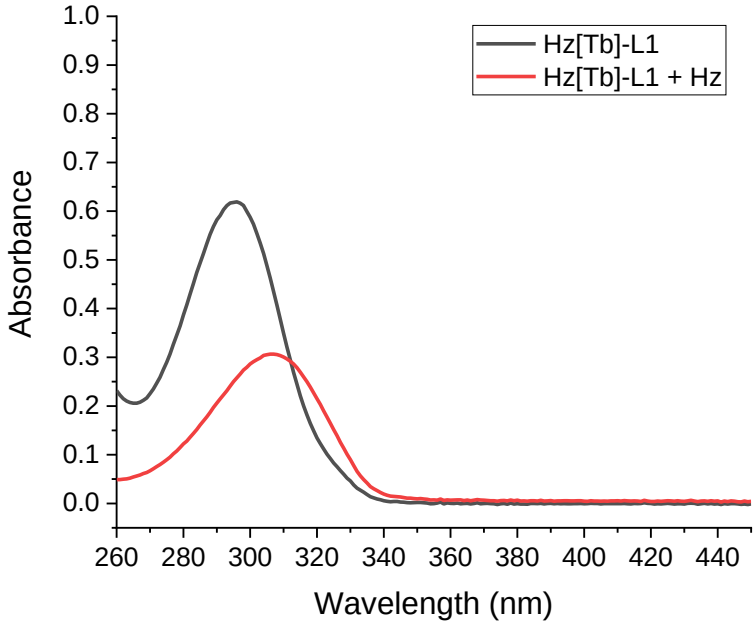

Figure 4.36: Absorption spectrum of 100 µM of Hz[Tb]-L1 in H_2O after incubation with 1000 µM hydrazine for three minutes.

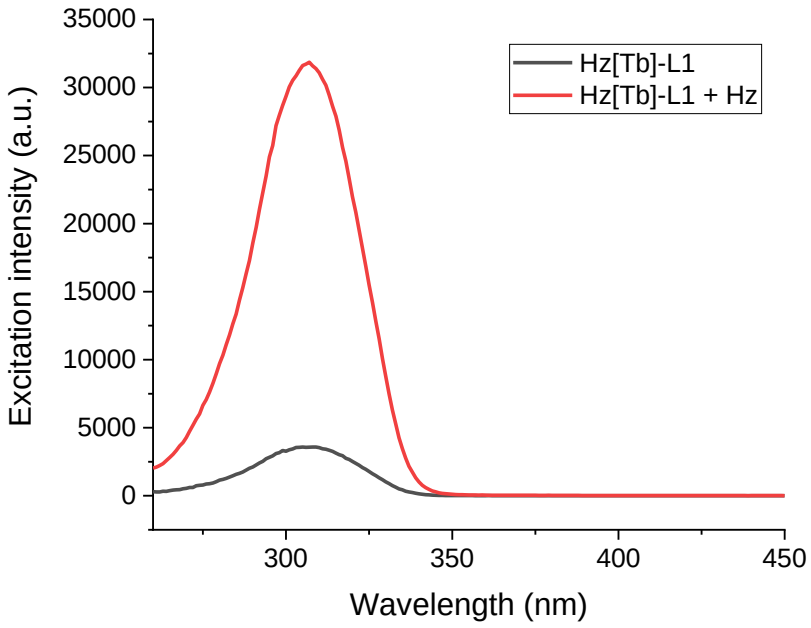

Figure 4.37: Excitation spectrum of 5 µM Hz[Tb]-L1 in H_2O after incubation with 50 µM hydrazine for three minutes. λem: 546 nm, slit: 1-1 nm

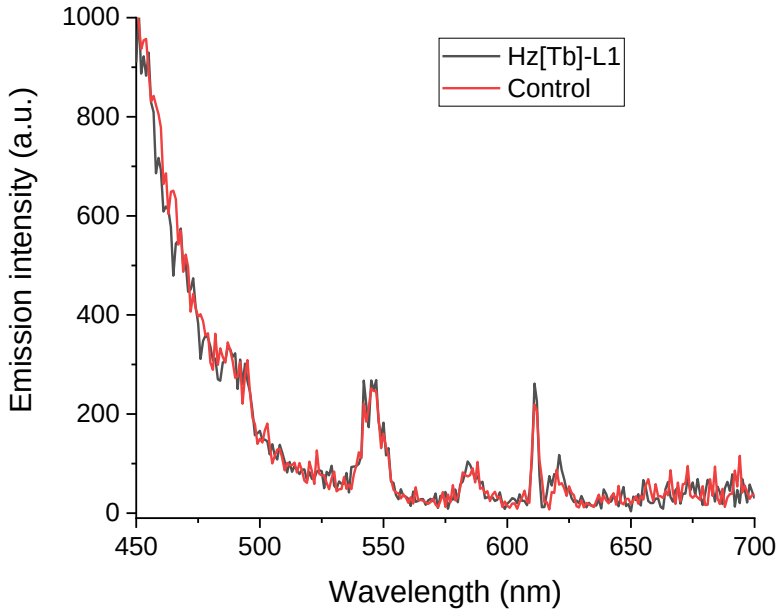

Figure 4.38: Luminescence selectivity experiment of 5 µM Hz[Tb]-L1 in H_2O control sample after three minutes of incubation. λex: 306 nm, slit: 1-1 nm.

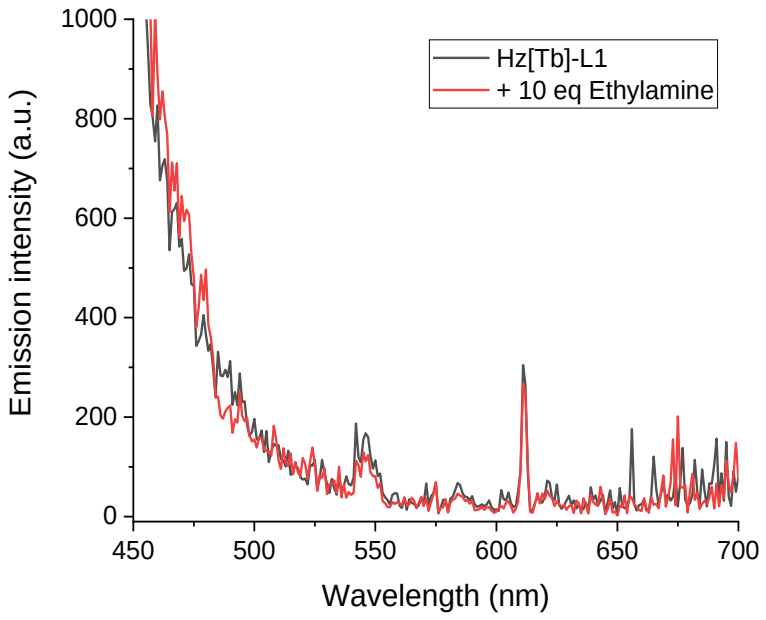

Figure 4.39: Luminescence selectivity experiment of 5 μM Hz[Tb]-L1 in H_2O to 50 μM ethylamine after three minutes of incubation. λex: 306 nm, slit: 1-1 nm.

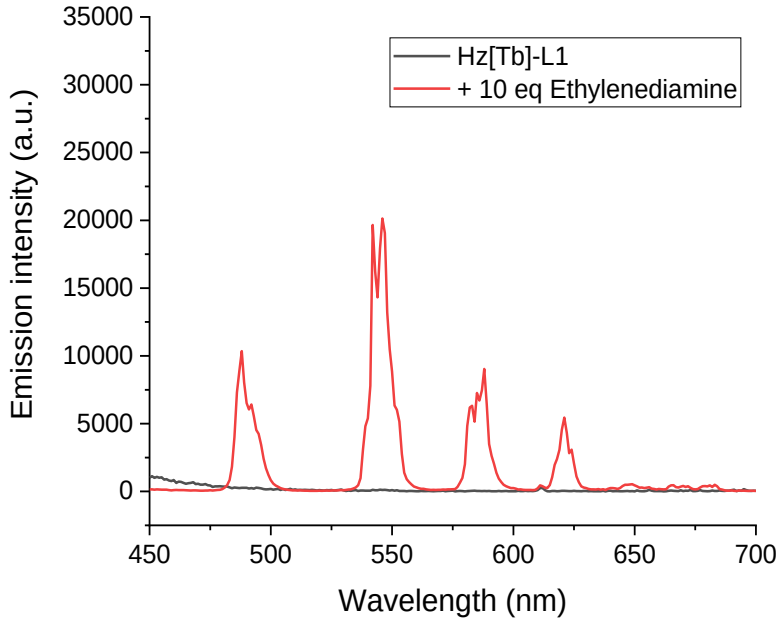

Figure 4.40: Luminescence selectivity experiment of 5 μM Hz[Tb]-L1 in H_2O to 50 μM ethylenediamine after three minutes of incubation. λex: 306 nm, slit: 1-1 nm.

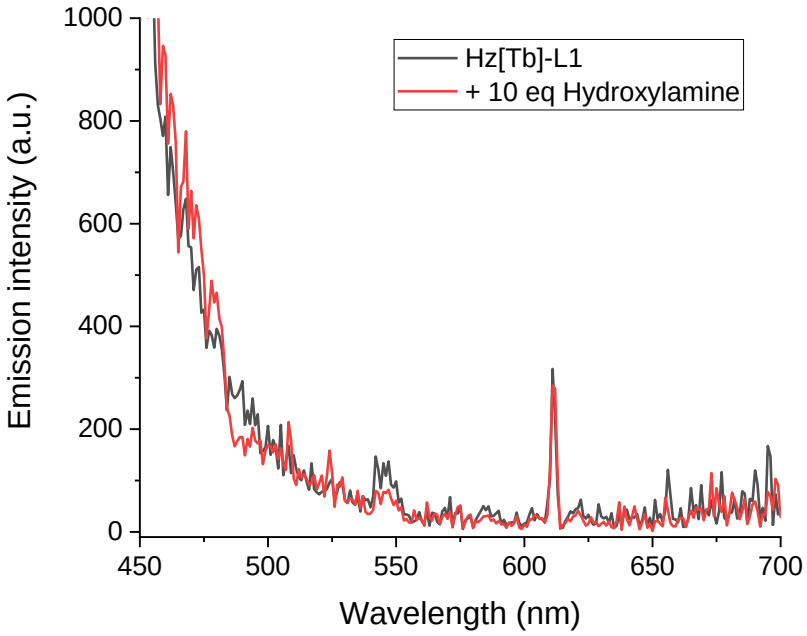

Figure 4.41: Luminescence selectivity experiment of 5 µM Hz[Tb]-L1 in H_2O to 50 µM hydroxylamine after three minutes of incubation. λex: 306 nm, slit: 1-1 nm.

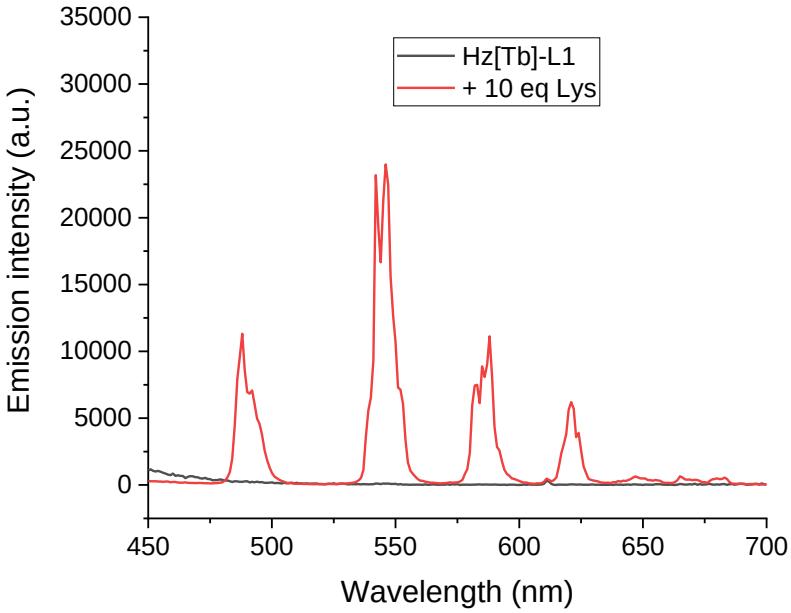

Figure 4.42: Luminescence selectivity experiment of 5 µM Hz[Tb]-L1 in H_2O to 50 µM Lys after three minutes of incubation. λex: 306 nm, slit: 1-1 nm.

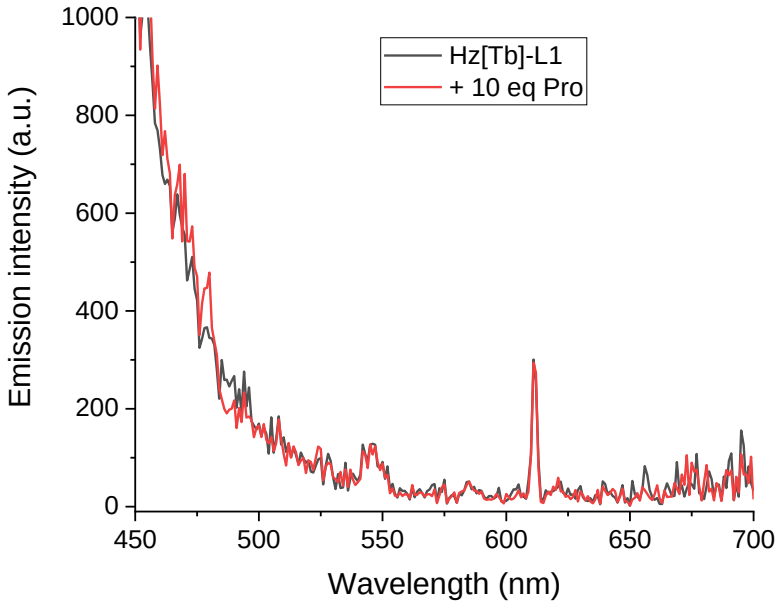

Figure 4.43: Luminescence selectivity experiment of 5 µM Hz[Tb]-L1 in H_2O to 50 µM Pro after three minutes of incubation. λex: 306 nm, slit: 1-1 nm.

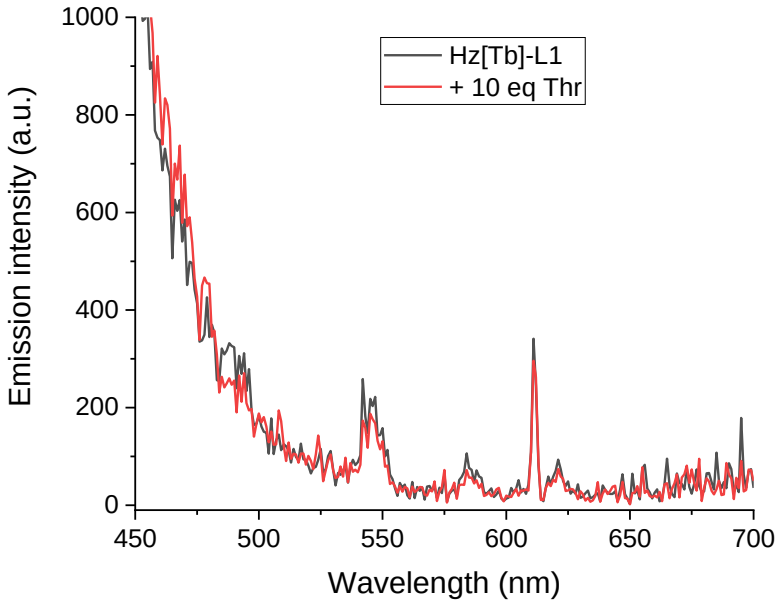

Figure 4.44: Luminescence selectivity experiment of 5 µM Hz[Tb]-L1 in H_2O to 50 µM Thr after three minutes of incubation. λex: 306 nm, slit: 1-1 nm.

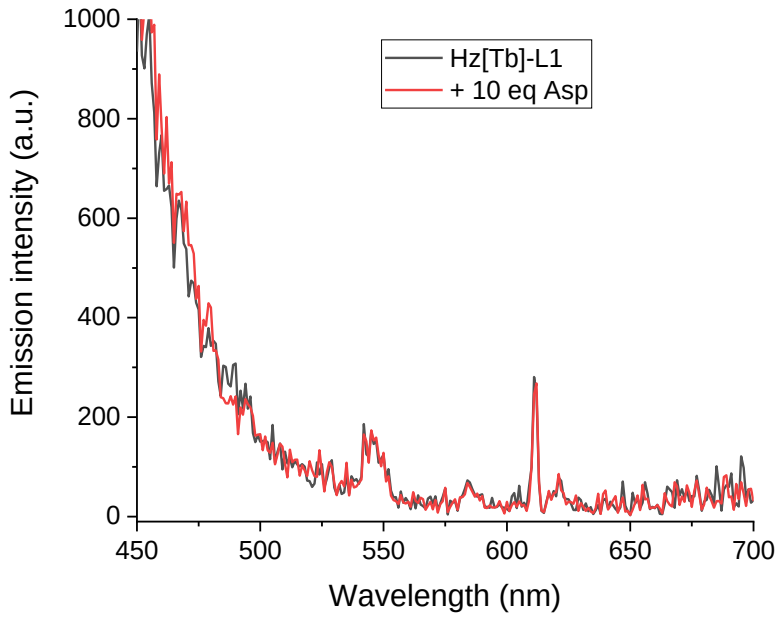

Figure 4.45: Luminescence selectivity experiment of 5 μM Hz[Tb]-L1 in H_2O to 50 μM Asp after three minutes of incubation. λex: 306 nm, slit: 1-1 nm.

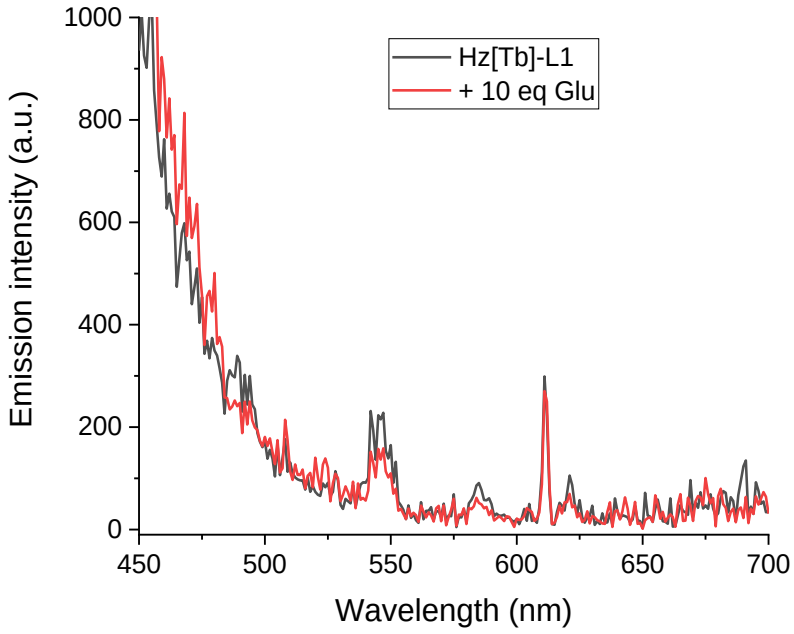

Figure 4.46: Luminescence selectivity experiment of 5 μM Hz[Tb]-L1 in H_2O to 50 μM Glu after three minutes of incubation. λex: 306 nm, slit: 1-1 nm.

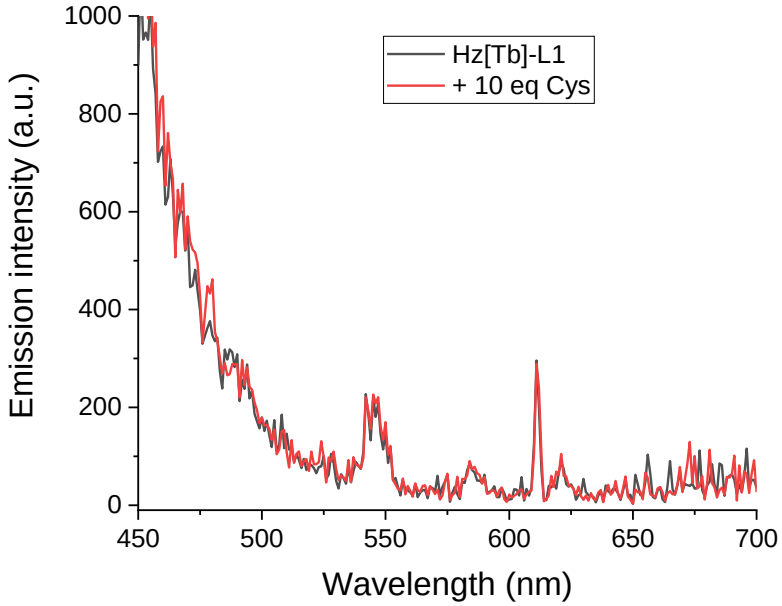

Figure 4.47: Luminescence selectivity experiment of 5 μM Hz[Tb]-L1 in H_2O to 50 μM Cys after three minutes of incubation. λex: 306 nm, slit: 1-1 nm.

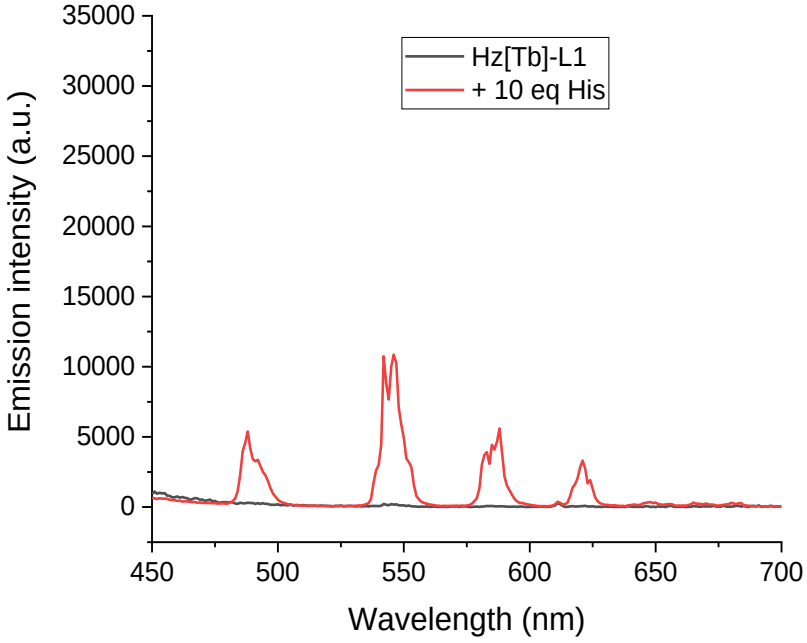

Figure 4.48: Luminescence selectivity experiment of 5 μM Hz[Tb]-L1 in H_2O to 50 μM His after three minutes of incubation. λex: 306 nm, slit: 1-1 nm.

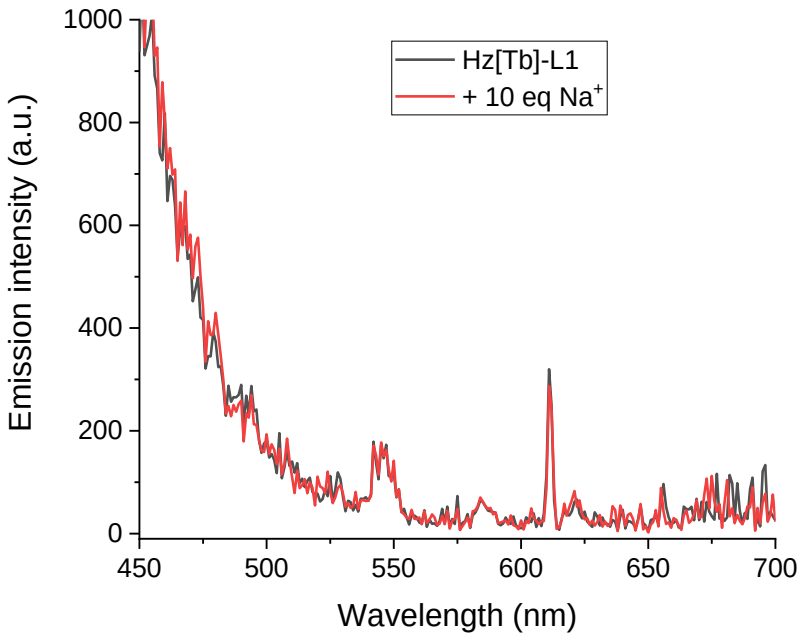

Figure 4.49: Luminescence selectivity experiment of 5 μM Hz[Tb]-L1 in H_2O to 50 μM Na^+ after three minutes of incubation. λex: 306 nm, slit: 1-1 nm.

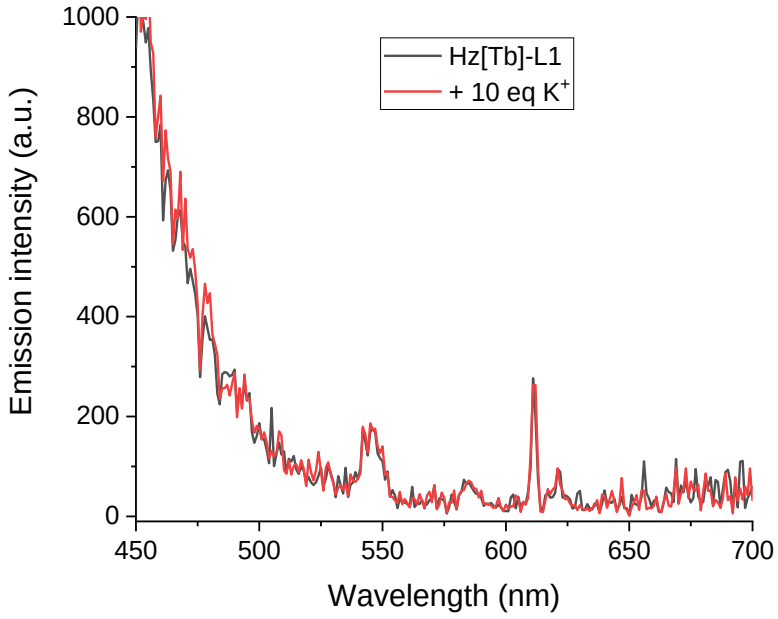

Figure 4.50: Luminescence selectivity experiment of 5 μM Hz[Tb]-L1 in H_2O to 50 μM K^+ after three minutes of incubation. λex: 306 nm, slit: 1-1 nm.

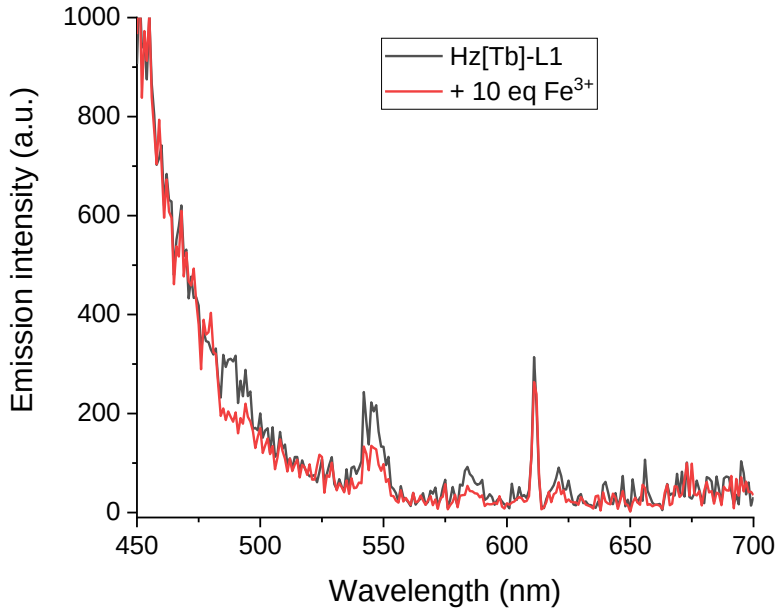

Figure 4.51: Luminescence selectivity experiment of 5 μM Hz[Tb]-L1 in H_2O to 50 μM Fe^{3+} after three minutes of incubation. λex: 306 nm, slit: 1-1 nm.

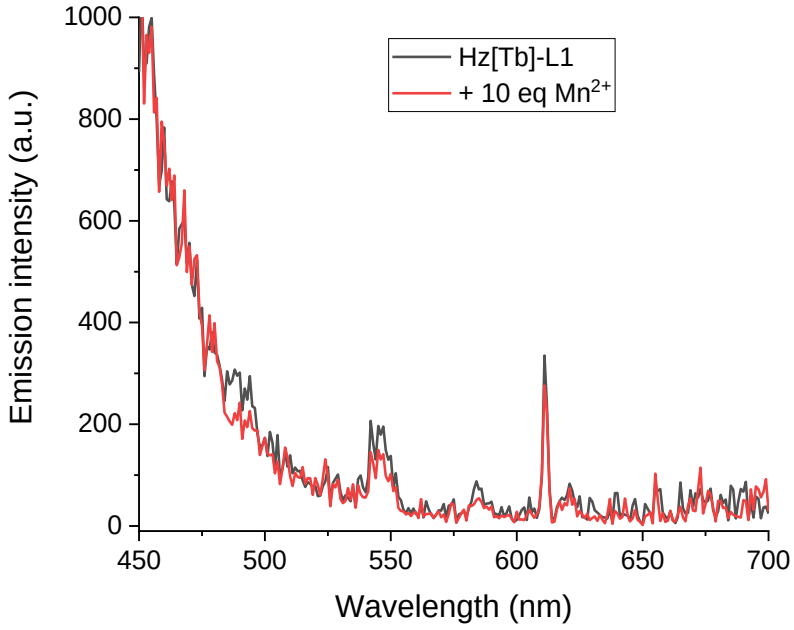

Figure 4.52: Luminescence selectivity experiment of 5 μM Hz[Tb]-L1 in H_2O to 50 μM Mn^{2+} after three minutes of incubation. λex: 306 nm, slit: 1-1 nm.

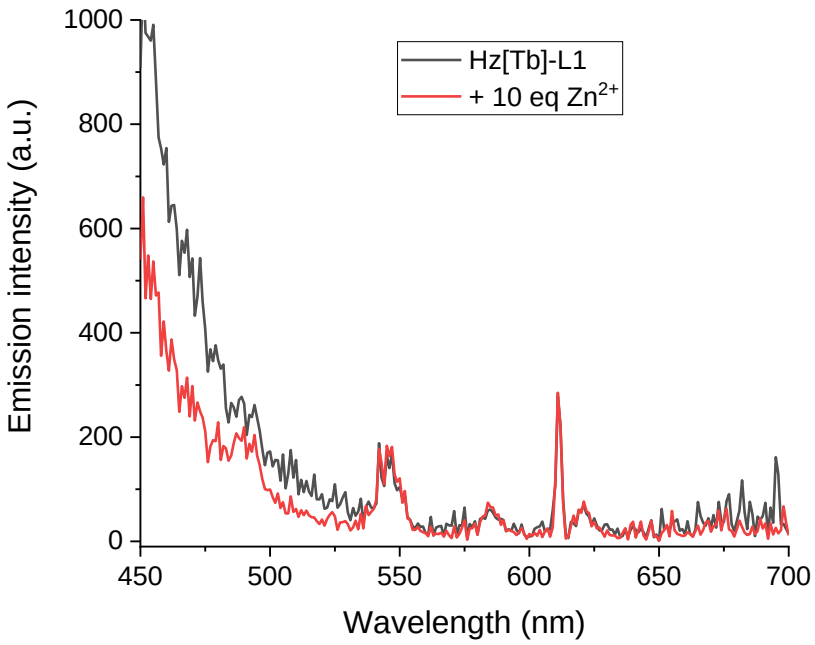

Figure 4.53: Luminescence selectivity experiment of 5 μM Hz[Tb]-L1 in H_2O to 50 μM Zn^{2+} after three minutes of incubation. λex: 306 nm, slit: 1-1 nm.

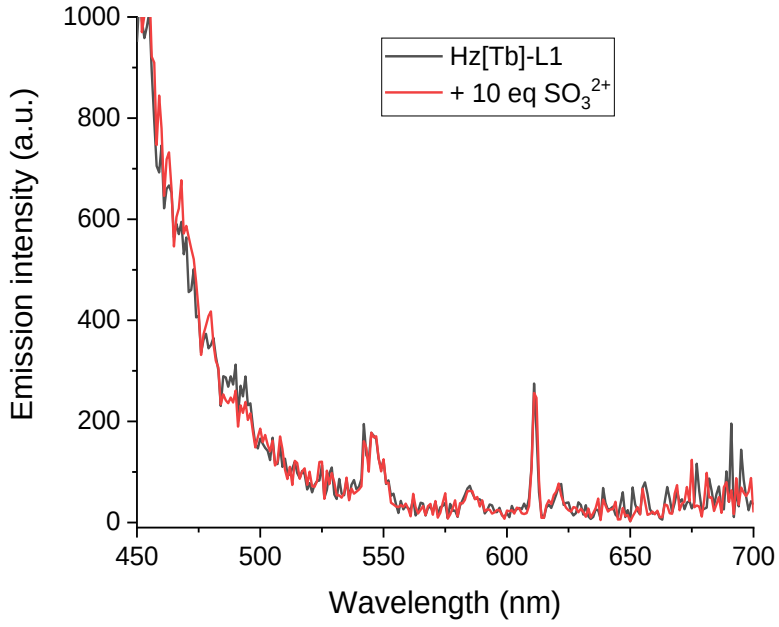

Figure 4.54: Luminescence selectivity experiment of 5 μM Hz[Tb]-L1 in H_2O to 50 μM SO_3^{2-} after three minutes of incubation. λex: 306 nm, slit: 1-1 nm.

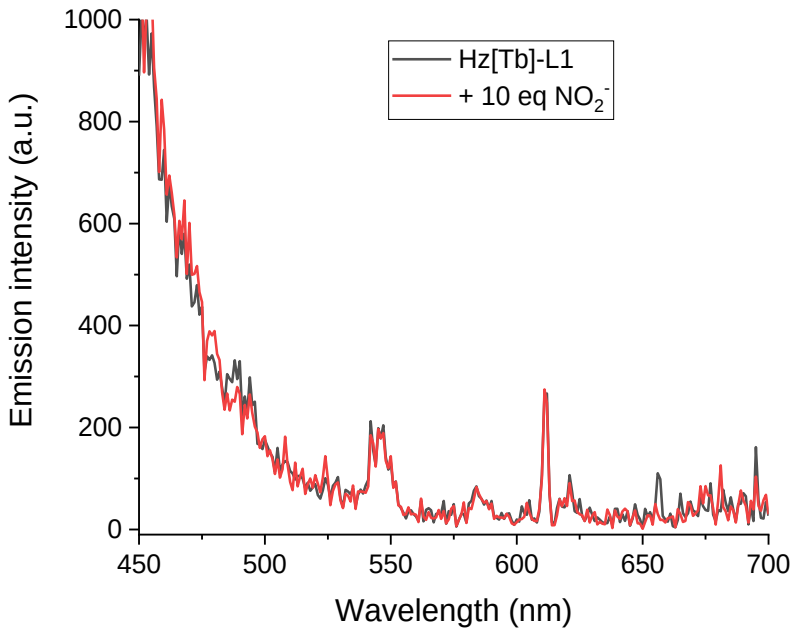

Figure 4.55: Luminescence selectivity experiment of 5 μM Hz[Tb]-L1 in H_2O to 50 μM NO_2^- after three minutes of incubation. λex: 306 nm, slit: 1-1 nm.

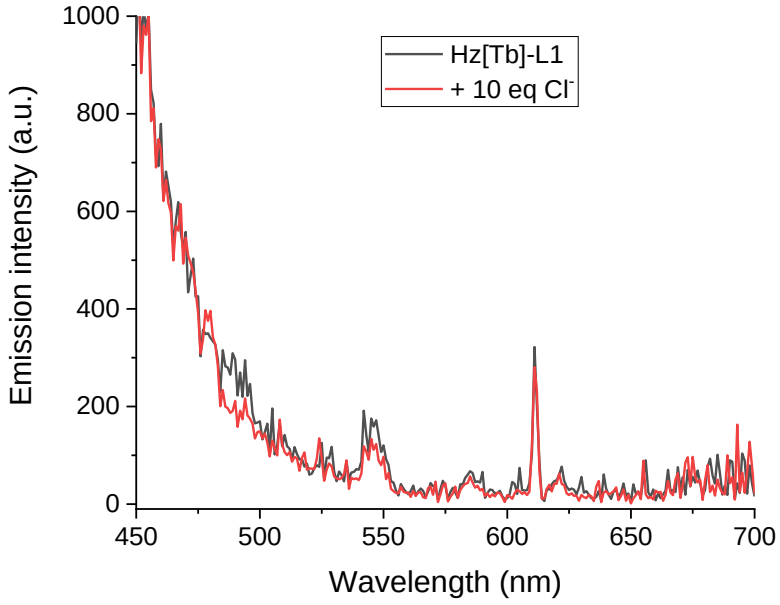

Figure 4.56: Luminescence selectivity experiment of 5 μM Hz[Tb]-L1 in H_2O to 50 μM Cl^- after three minutes of incubation. λex: 306 nm, slit: 1-1 nm.

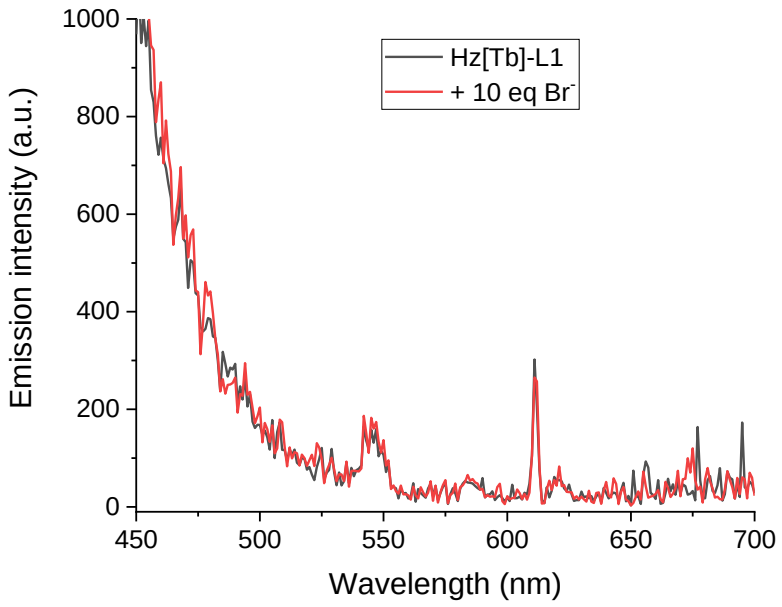

Figure 4.57: Luminescence selectivity experiment of 5 µM Hz[Tb]-L1 in H_2O to 50 µM Br^- after three minutes of incubation. λex: 306 nm, slit: 1-1 nm.

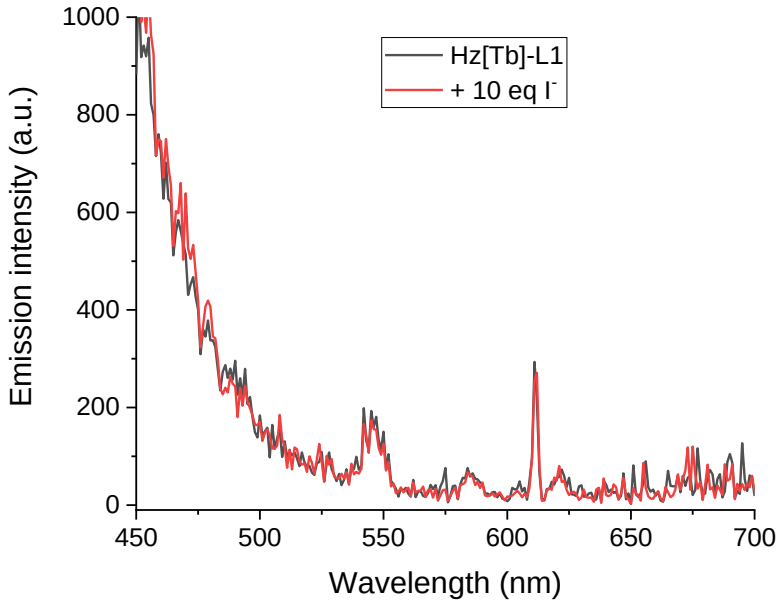

Figure 4.58: Luminescence selectivity experiment of 5 µM Hz[Tb]-L1 in H_2O to 50 µM I^- after three minutes of incubation. λex: 306 nm, slit: 1-1 nm.

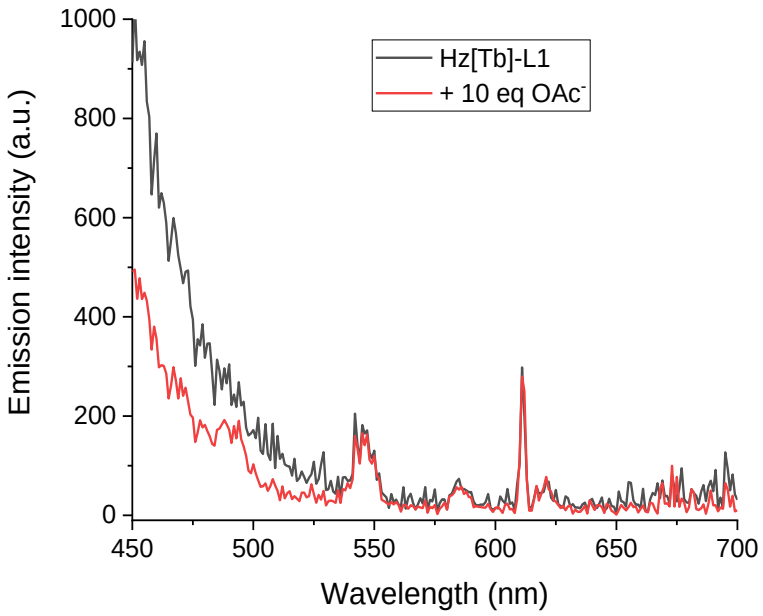

Figure 4.59: Luminescence selectivity experiment of 5 µM Hz[Tb]-L1 in H_2O to 50 µM OAc^- after three minutes of incubation. λex: 306 nm, slit: 1-1 nm.

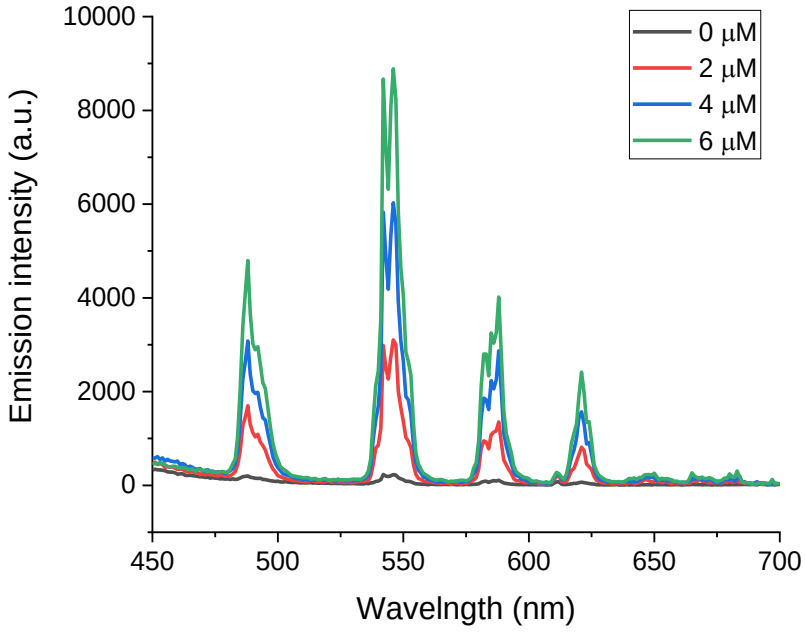

Figure 4.60: Quantification of 0, 2, 4 and 6 µM hydrazine by 5 µM of Hz[Tb]-L1 in H_2O. λex: 306 nm, slit: 1-1 nm.

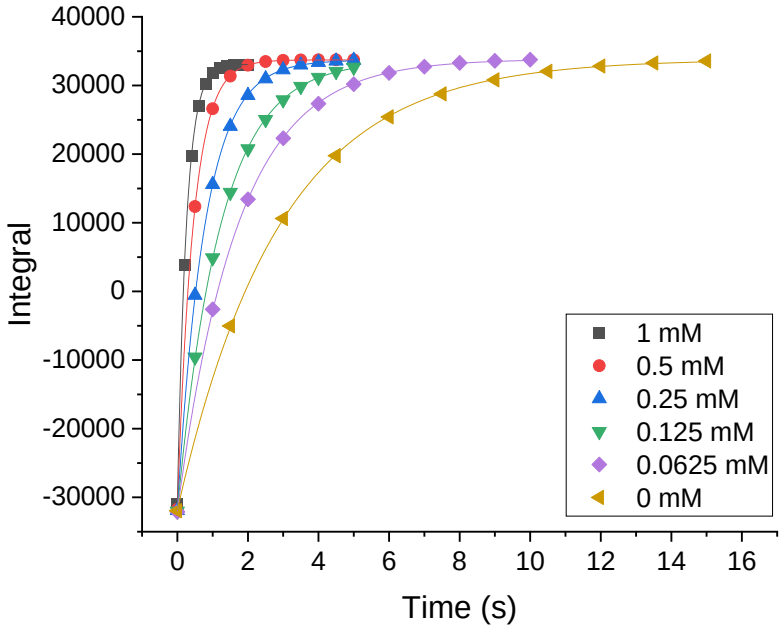

Figure 4.61: T_1 relaxation of 0 – 1 mM GdDOTA in H_2O. The curves are fitted to the equation: $y = y_0(1-e^{-x/T1})$, where y_0 is the initial maximum value.

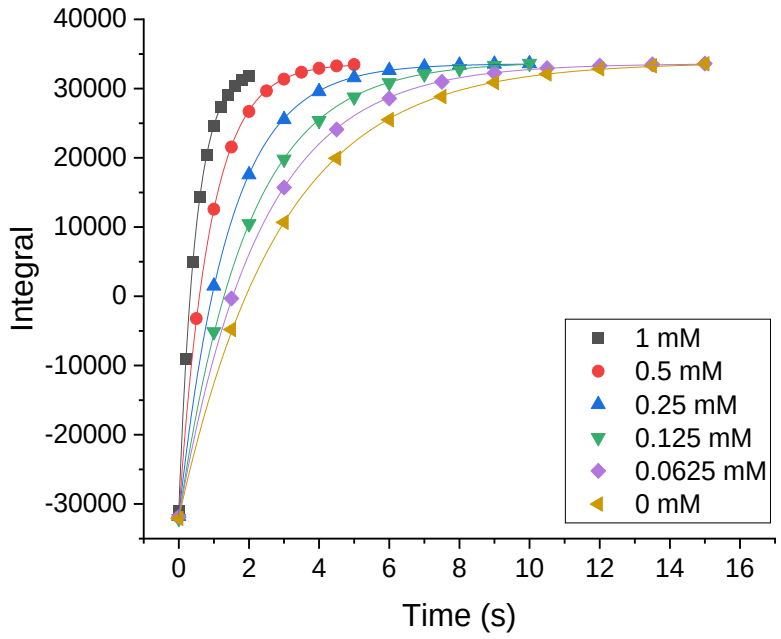

Figure 4.62: T_1 relaxation of 0 – 1 mM Hz[Gd]-L1 in H_2O. The curves are fitted to the equation: $y = y_0(1-e^{-x/T1})$, where y_0 is the initial maximum value.

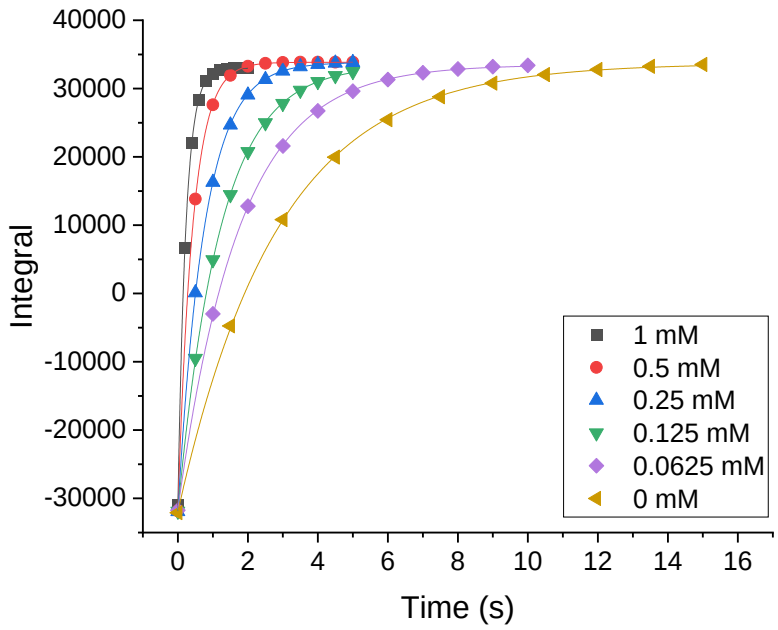

Figure 4.63: T_1 relaxation of 0 – 1 mM Hz[Gd]-L1 + hydrazine in H_2O. The curves are fitted to the equation: $y = y_0(1-e^{-x/T1})$, where y_0 is the initial maximum value.

Table 4.5: Relaxation rate, $1/\Delta T_1$ (s^{-1}) of 0 – 1 mM GdDOTA, Hz[Gd]-L1 and Hz[Gd]-L1 + Hz.

Concentration of Gd	**GdDOTA**	**σ**	**Hz[Gd]-L1**	**σ**	**Hz[Gd]-L1 + Hz**	**σ**
1 mM	4.01173	0.15703	2.05382	0.0723	4.42482	0.03197
0.5 mM	2.21739	0.03535	1.13809	0.00652	2.3599	0.01404
0.25 mM	1.27988	0.00948	0.70555	0.0032	1.3197	0.00523
0.125 mM	0.81612	0.00859	0.51895	0.00514	0.81935	0.00782
0.0625 mM	0.58039	0.00293	0.43353	0.00245	0.56859	0.00486
0 mM	0.34679	0.00344	0.34679	0.00344	0.34578	0.0084

Chapter 5 Study of analyte regenerating strategy for formaldehyde sensing

5.1 Introduction

Formaldehyde (methanal) is the simplest aldehyde and a reactive carbonyl species. It is well known that formaldehyde is an environmental toxin and a carcinogen. It poses a threat to human health if inhaling or injecting excess amounts exogenous formaldehyde. Overloading of formaldehyde can damage the central nervous system and cause adverse effects on memory, cognitive abilities, learning abilities and behaviour. Moreover, it has been reported that the increased formaldehyde levels and increased the activity of formaldehyde generating enzymes cause some disease such as Alzheimer's disease.[1, 2] However, formaldehyde is produced endogenously and released during biological processes, including one carbon metabolism.[3] For example, the demethylation of the N-methylated amino acid, such as histidine, arginine, and lysine produce formaldehyde by some demethylase enzymes. Jumonji domain-containing proteins and lysine-specific demethylase, KDM1-6, are responsible for generating formaldehyde.[4] Additionally, formaldehyde is produced during DNA and RNA demethylation by AlkB homologues (ABH) family enzymes within the nucleus.[5] Furthermore, semicarbazide-sensitive amine oxidases release formaldehyde during the metabolism of methylated amines.[6] For a healthy human, the concentration of formaldehyde in the brain ranges from 200 to 400 μM.[7] It has been suggested that formaldehyde helps in preserving, storing and retrieving long-term memory by DNA and RNA demethylation. It is also found that the concentration of formaldehyde in the brain tissue is over 500 μM in Alzheimer's disease animal models.[8] To understand the detailed biological functions of formaldehyde, it is important to develop tools to monitor the dynamics of formaldehyde in biological systems.

To detect the formaldehyde level, several traditional methods have been developed by using precise instruments such as gas chromatography,[9] reversed phased high-performance liquid chromatography,[10] and mass spectrometry.[11] Although these methods provide fast, effective, and sensitive ways to detect formaldehyde level, it remains challenging to detect the formaldehyde level in living cells or complex biological specimens. Without spatiotemporal resolution imaging, it is difficult to study the role of formaldehyde in physiology and pathology.

To address this issue, reaction-based fluorescent probes can effectively be developed and applied to live biological systems to provide formaldehyde detection and three-dimensional imaging. Over the last decade, several different formaldehyde sensing mechanisms have been reported, including formimine, 2-aza-Cope and methylenehydrazine reactions.[12-14] However, these sensing methods function in an irreversible manner, consuming formaldehyde in the system and may disrupt formaldehyde homeostasis. The analyte regenerating/replacing strategy is a method that enables the detection of analyte without consuming it, so it has been applied to detection of various analytes such as H_2S,[15, 16] CO,[17] and hypochlorite.[18] To date, there are only three examples have been reported in analyte regenerating formaldehyde detection. The first two examples utilized amino-succinimide as the sensing part.[19, 20] By using the amine group to capture formaldehyde, the generated alkyl hydroxyl group could nucleophilic attack the imide moiety, resulting fluorescence enhancement. After the hydrolysis of the probe, formaldehyde is released to reach the analyte-regenerating property. In the third example, it utilized a similar formaldehyde capture method but intramolecular nucleophilic attack on an ester group to produce fluorescence enhancement. After the hydrolysis of the probe, formaldehyde is also released to create analyte-regenerating property (Figure 5.1, 5.2).

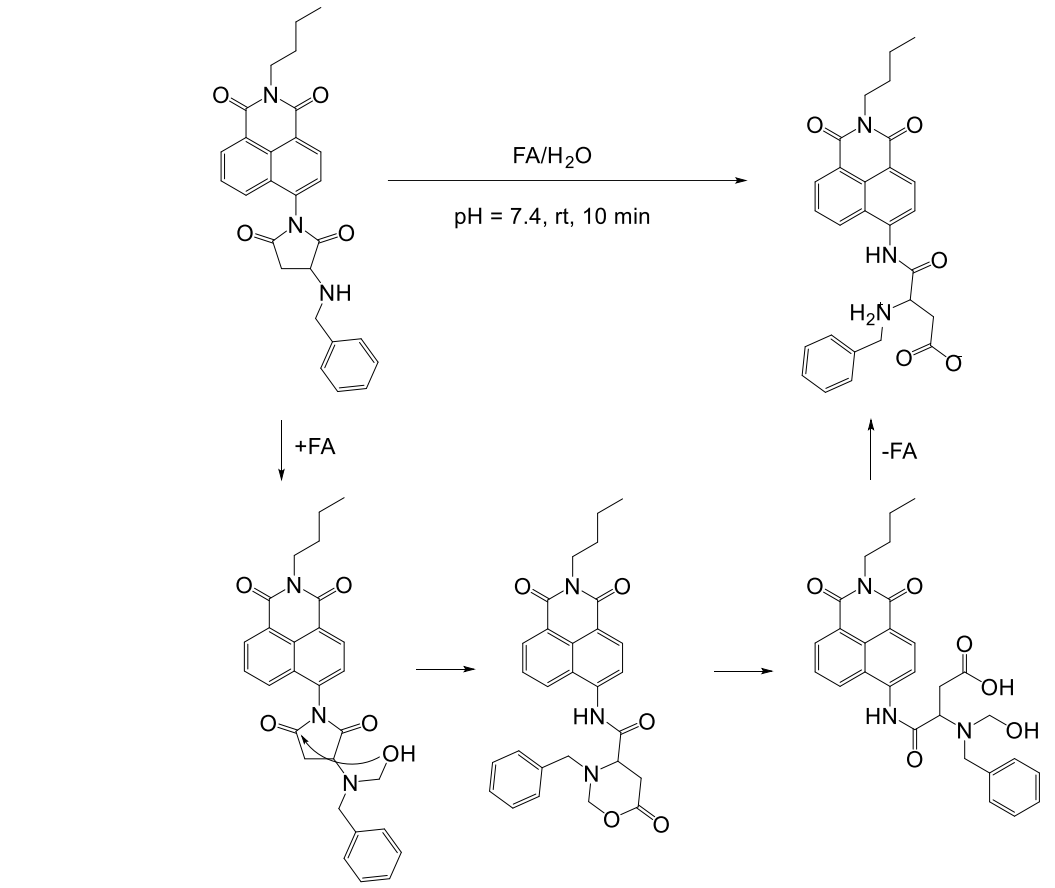

Figure 5.1: Mechanism of analyte regenerating formaldehyde detection using amino-succinimide group.

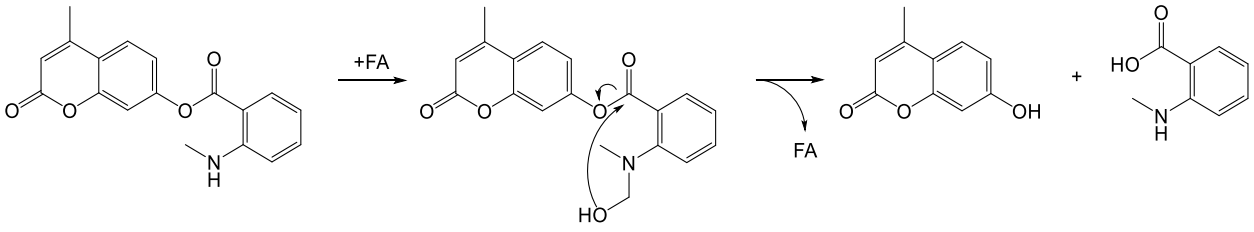

Figure 5.2: Mechanism of analyte regenerating formaldehyde detection using ester group.

5.2 Scope of study

As an analyte regenerating/replacing strategy capable of providing analyte detection without affecting homeostasis, it is then planned to extend this strategy to develop the next generation of reaction-based chemical probes. In this chapter, an analyte-regenerating fluorescence probe, Cou-NSu, is designed to study the amino-succinimide sensing mechanism on 7-amino-4-methylcoumarin.

5.3 Result and discussion

5.3.1 Design and synthesis of Cou-NSu

As 7-amino-4-methylcoumarin is a commonly used fluorescent dye for analyte sensing and was also used in Chapter 2 with good results, we employed the 7-amino-4-methylcoumarin again as the starting material for the analyte-regenerating fluorescence probe. A simple and efficient synthetic route to our target molecule, Cou-NSu, is shown in Figure 5.3. In the first reaction, 7-amino-4-methylcoumarin was allowed to react with maleic anhydride. Under acidic conditions, the primary amine group of 7-amino-4-methylcoumarin reacted with maleic anhydride to form the maleimide compound 5.1. As N-aryl maleimides are well known as the Michael acceptors, they can undergo Michael addition with benzylamine to yield the final product Cou-NSu. By adding the 3-(benzylamine)-succinimide group to 7-amino-4-methylcoumarin, the fluorescence of the coumarin moiety was successfully quenched by photoinduced electron transfer and intramolecular charge transfer pathways through the nitrogen atom on the 3-(benzylamine)-succinimide group and the maleimide group (Figure 5.3).

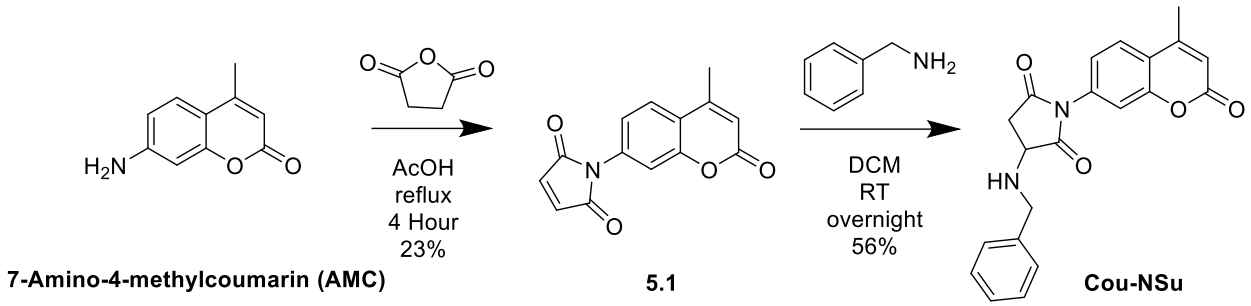

Figure 5.3: Synthetic route of Cou-NSu.

5.3.2 Cou-NSu responds to formaldehyde

To study the fluorescence response of Cou-NSu towards formaldehyde, fluorescence titration experiments were conducted. It was expected that the probe, Cou-NSu, would undergo a mechanism similar to that of Wang's[19] and Zeng's[20] probes and exhibit imide bond hydrolysis in the presence of formaldehyde (Figure 5.4a, b). Cou-NSu was dissolved in a 10 mM PBS buffer solution (pH 7.4)/ 1% DMSO. After the addition of 50 μM formaldehyde solution to Cou-NSu, the probe exhibited a quick and obvious fluorescence turn-on effect. The coumarin demonstrated a good Stoke's shift (65 nm) and the fluorescence signal centred at 394 nm increased (Figure 5.5). From the bar chart (Figure 5.10), Cou-NSu demonstrated a time-dependent response and showed a quick response to formaldehyde. There was a rapid increase in fluorescence signal in the first 10 minutes with the fluorescence intensity increasing by approximately 2.4-fold.

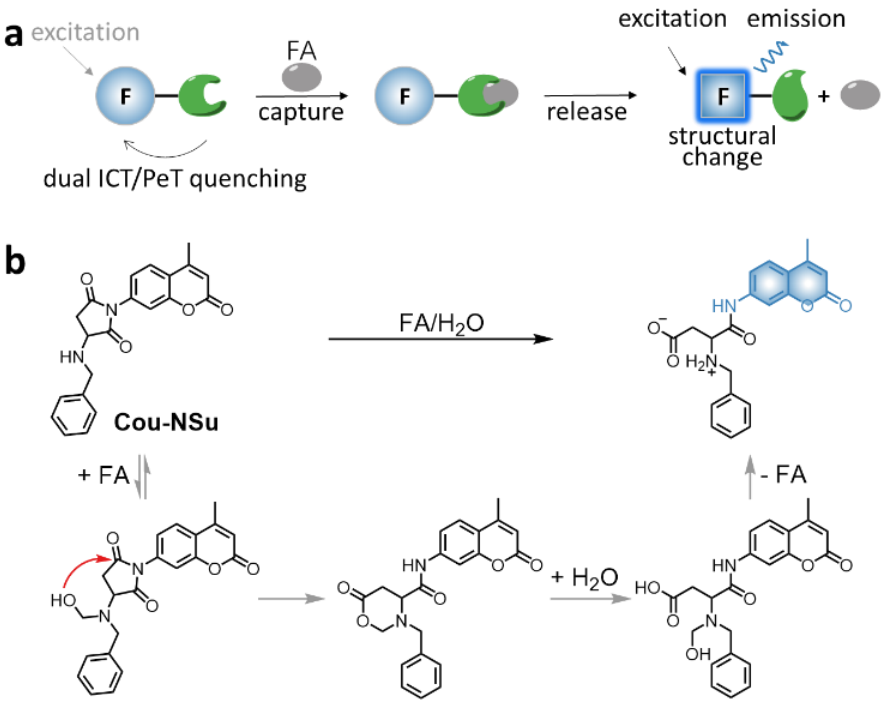

Figure 5.4: (a) Schematic illustration (b) Proposed mechanism of the designed analyte regenerating probe (Cou-NSu) towards formaldehyde.

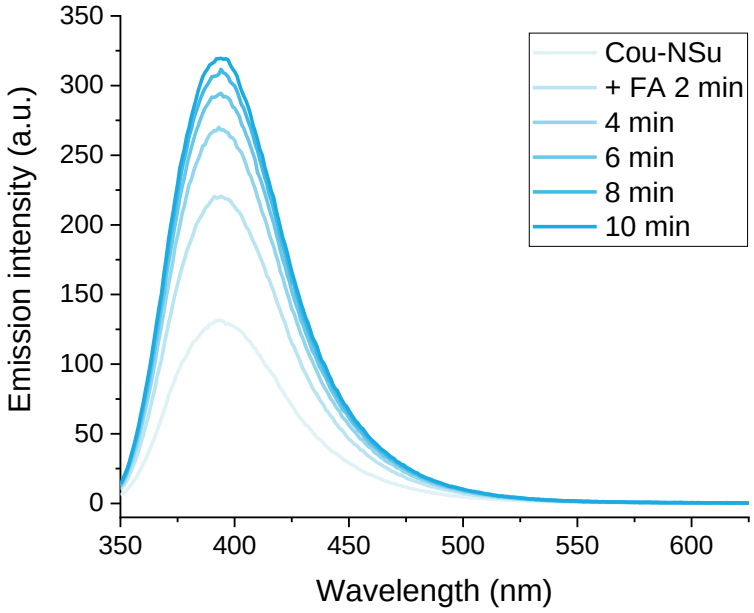

Figure 5.5: Time-dependent fluorescence titration of 5 µM Cou-NSu in PBS/ 1% DMSO to 50 µM of formaldehyde (FA). λex: 329 nm, slit: 5-5 nm.

Next, a preliminary selectivity experiment was conducted by titrating 50 µM of formaldehyde and 50 µM of other aldehyde analytes, including acetaldehyde, benzaldehyde, glyoxal, and methylglyoxal, into Cou-NSu (Figure 5.6 – 5.10). It was clearly observed that time-dependent fluorescence enhancement occurred after the addition of formaldehyde compared to other aldehyde analytes. From these data, it is suggested that Cou-NSu is selective for formaldehyde. However, in all other samples, including the control sample, the peak centred at 394 nm also gradually increased over time which attracted our attention. The uncontrollable enhancement of the signal can negatively impact the accuracy of qualitative or quantitative research on formaldehyde. To determine the cause of unexpected peak enhancement, the blank solution of Cou-NSu was tested. To eliminate the possibility of buffer factors, Cou-NSu was dissolved in H_2O/ 1% DMSO and incubated for 24 hours at room temperature. It was observed that the fluorescence intensity still increased by approximately 2.5-fold (Figure 5.11).

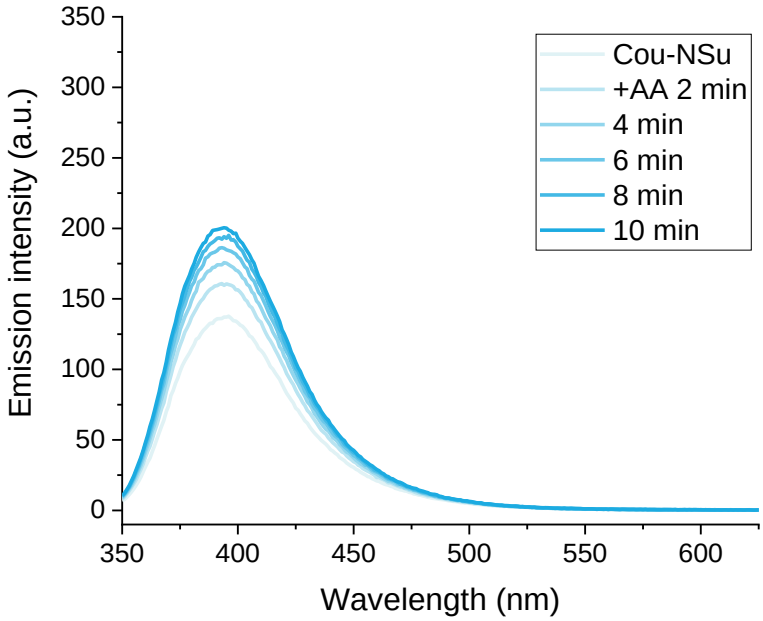

Figure 5.6: Time-dependent fluorescence titration of 5 µM Cou-NSu in PBS/ 1% DMSO to 50 µM of acetaldehyde (AA). λex: 329 nm, slit: 5-5 nm.

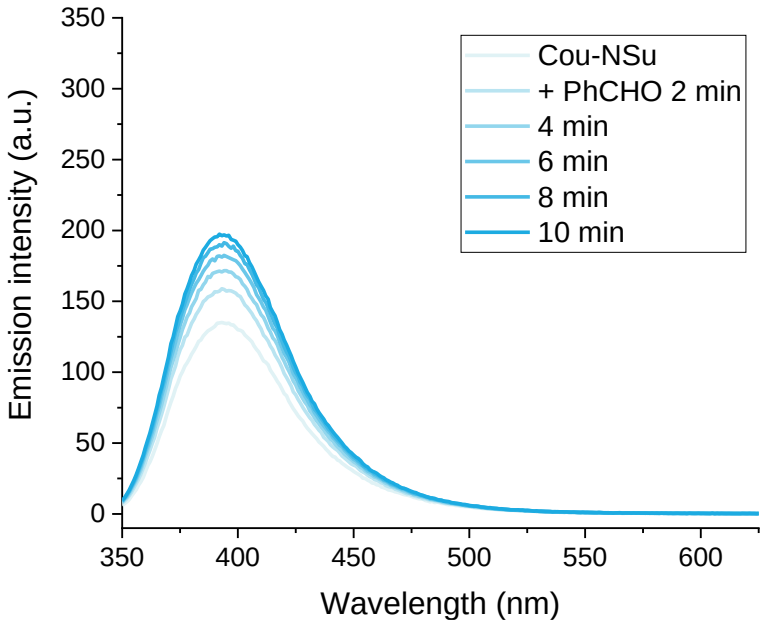

Figure 5.7: Time-dependent fluorescence titration of 5 µM Cou-NSu in PBS/ 1% DMSO to 50 µM of benzaldehyde (PhCHO). λex: 329 nm, slit: 5-5 nm.

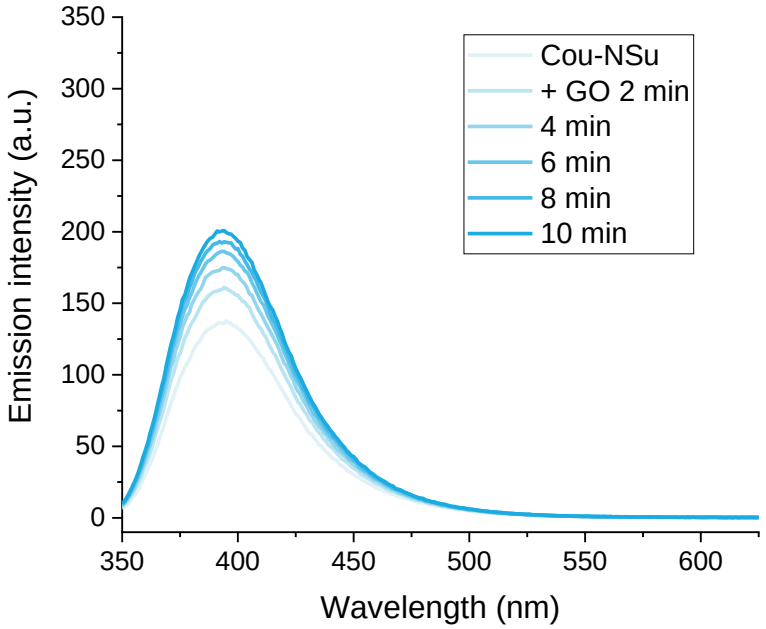

Figure 5.8: Time-dependent fluorescence titration of 5 µM Cou-NSu in PBS/ 1% DMSO to 50 µM of glyoxal (GO). λex: 329 nm, slit: 5-5 nm.

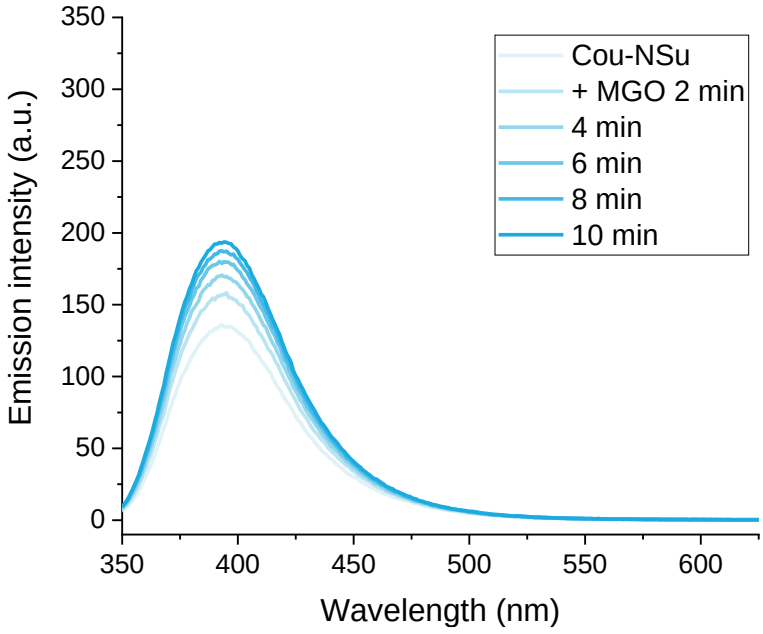

Figure 5.9: Time-dependent fluorescence titration of 5 µM Cou-NSu in PBS/ 1% DMSO to 50 µM of methylglyoxal (MGO). λex: 329 nm, slit: 5-5 nm.

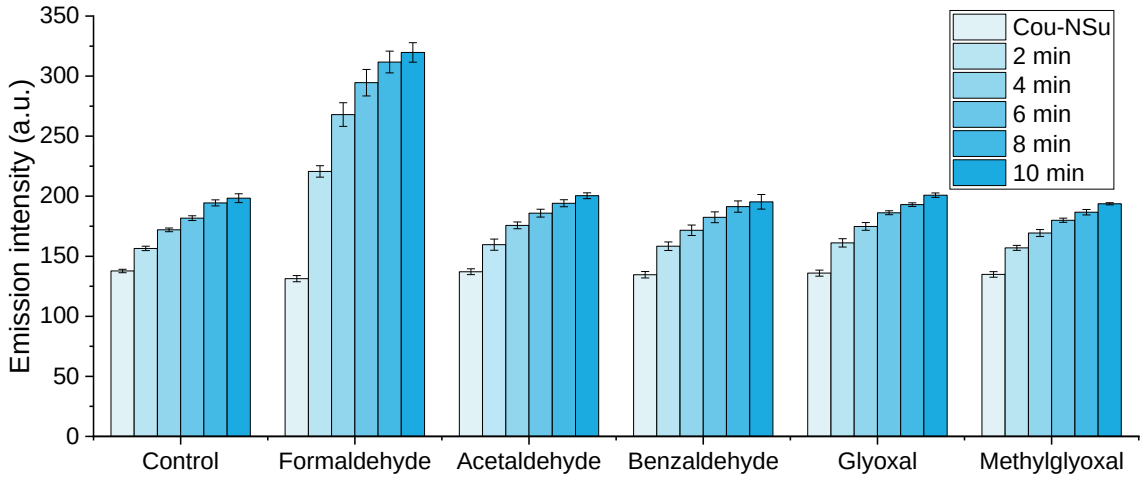

Figure 5.10: Fluorescence selectivity experiment of 5 µM Cou-NSu in M PBS/ 1% DMSO to 50 µM of different aldehydes. The y-axis represents the Cou-NSu fluorescence intensity at 394 nm. λex: 329 nm, slit: 5-5 nm.

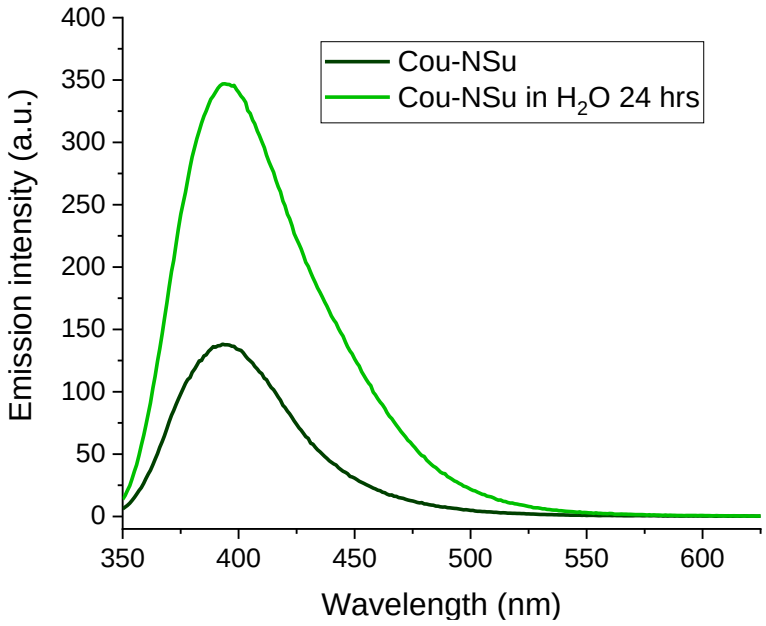

Figure 5.11: Time-dependent fluorescence titration of 5 μM Cou-NSu in H_2O/ 1% DMSO after 24 hours of incubation without adding analyte. λex: 329 nm, slit: 5-5 nm.

5.3.3 Assumption and proof

It is important to find out the underlying reason for the unexpected peak enhancement which can help in developing the second-generation analyte-regenerating formaldehyde sensing probe. In reviewing the literature, several reports demonstrated that the succinimide group can undergo self-hydrolysis at neutral pH and room temperature.[21] Therefore, it is assumed that the water content in the PBS buffer solution may be the main cause for the hydrolysis of the 3-amino-succinimide group on Cou-NSu. Through the nucleophilic attack by water molecules on either the C2 or C5 position of imide bond, a metastable gem-diol structure intermediate may formed.[22] Then, a proton is transferred to the nearby nitrogen atom, promoting the cleavage of the C-N bond. The formation of the ring-opened structure may explain the fluorescence unexpected peak enhancement (Figure 5.12).

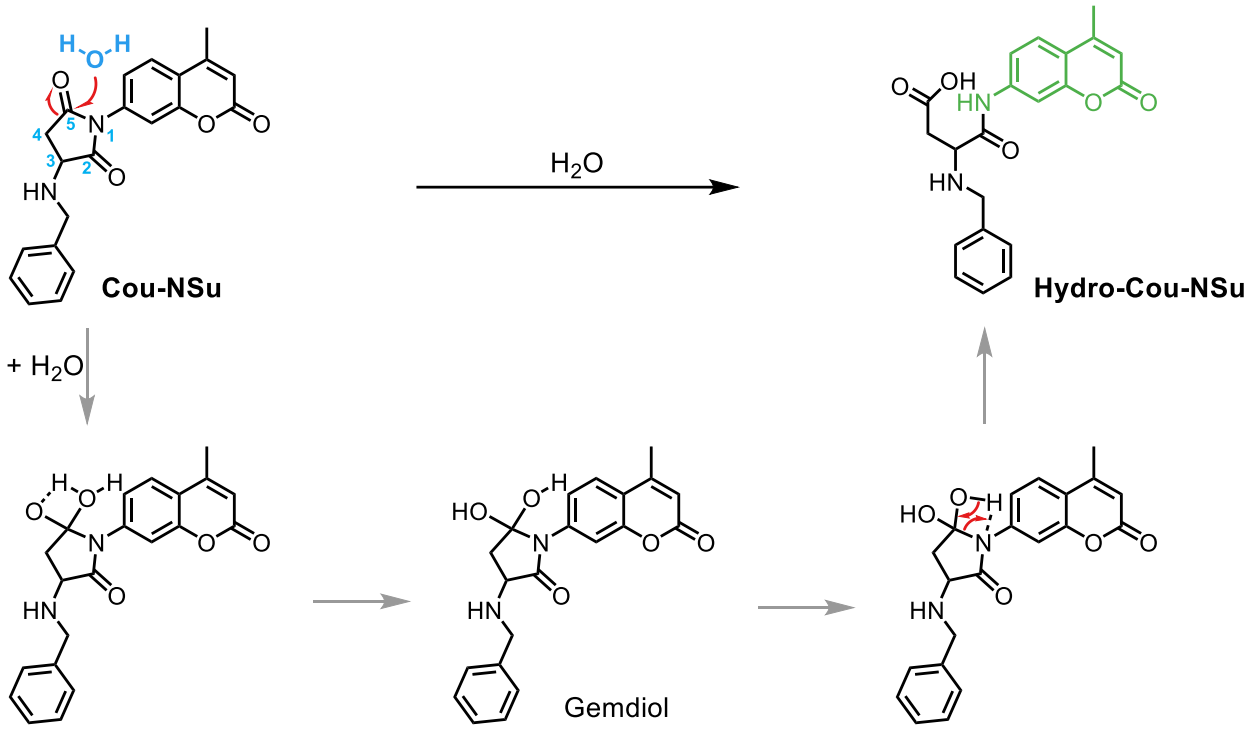

Figure 5.12: Proposed hydrolysis mechanism of Cou-NSu.

To test the assumption of the solvent effect that causes the hydrolysis of the probe, NMR and UPLC-MS were used to check the stability of the probe. The solvent effect of DMSO was first checked. The stability of Cou-NSu in DMSO was tested using NMR spectroscopy. Cou-NSu was dissolved in deuterated DMSO to obtain the first NMR spectrum. It was allowed to incubate for 24 hours at room temperature and a second NMR spectrum of Cou-NSu was then obtained. When comparing the first and second NMR spectra of Cou-NSu, there was no shift in the peaks or appearance of new peaks in the spectra. It was believed that Cou-NSu was stable in DMSO, and no solvent effect was observed (Figure 5.13).

In studying the stability of Cou-NSu in H_2O/DMSO, Cou-NSu was first dissolved in the solvent mixture and incubated for 24 hours to ensure enough time for the interaction between the probe and water molecules. Then, the resulting solution was analysed by UPLC-MS. Cou-NSu displayed a chromatographic retention time of 4.003 minutes with an expected mass for $[M+MeOH+H]^+$ at 395.161 (calculated: 395.161). After overnight stirring, the resulting solution showed a left-shifted peak at 3.852 minutes with $[M+H]^+$ found at 381.1499, which was assigned as Hydro-Cou-NSu. Hydro-Cou-NSu was shown to have a shorter retention time. This matched our expectation, as the hydrolysis of imide bond would form a new carboxylic acid and a secondary amine functional group, the increased polarity of the hydrolysate would make it easier to elute. As the hydrolysis of the succinimide group may occur at either C2 or C5 position of the imide bond, a DFT calculation was performed to calculate the hydrolysis position. As the Mulliken charge of C5 was more positive than that of C2, it was suggested that hydrolysis may preferentially occur at C5, which is more electrophilic. These results confirmed the formation of the Cou-NSu hydrolysate due to the action of water molecules, and hydrolysate formation is responsible for the uncontrollable fluorescence intensity enhancement at 394 nm (Figure 5.14 – 5.16 and Table 5.1).

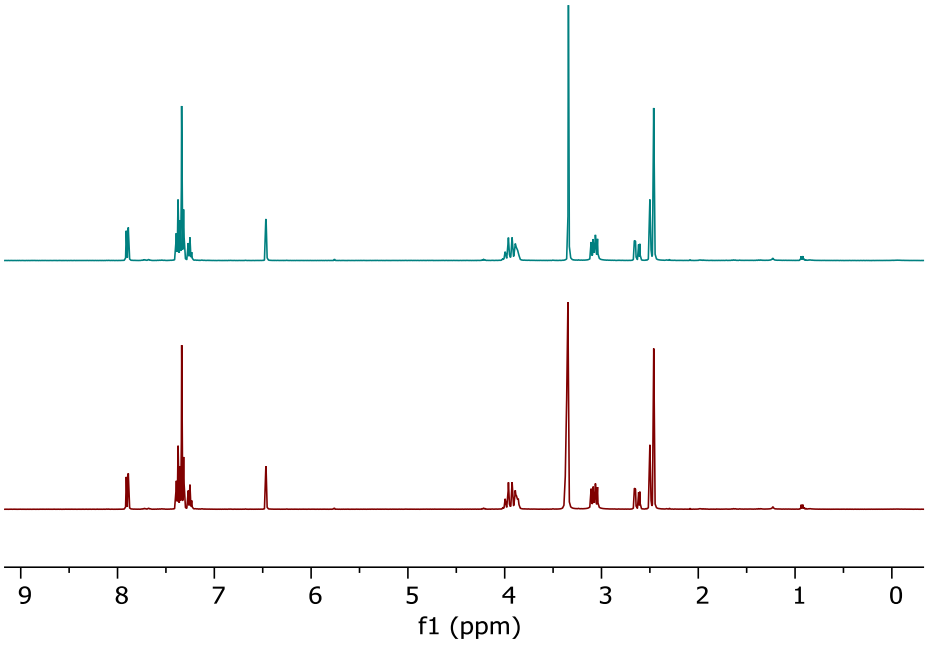

Figure 5.13: DMSO solvent effect test on Cou-NSu. (top) ^{1}H NMR spectrum of Cou-NSu obtained on the first day. (bottom) 1H NMR spectrum of Cou-NSu obtained on the second day.

Table 5.1: Solvent gradient used for UPLC-MS.

Time (minutes)	H_2O + 0.1% FA (%)	ACN + 0.1% FA (%)	Flow (mL/min)
0.00	95.00	5.00	0.4
1.00	95.00	5.00	0.4
10.00	5.00	95.00	0.4
12.00	95.00	5.00	0.4
15.00	95.00	5.00	0.4

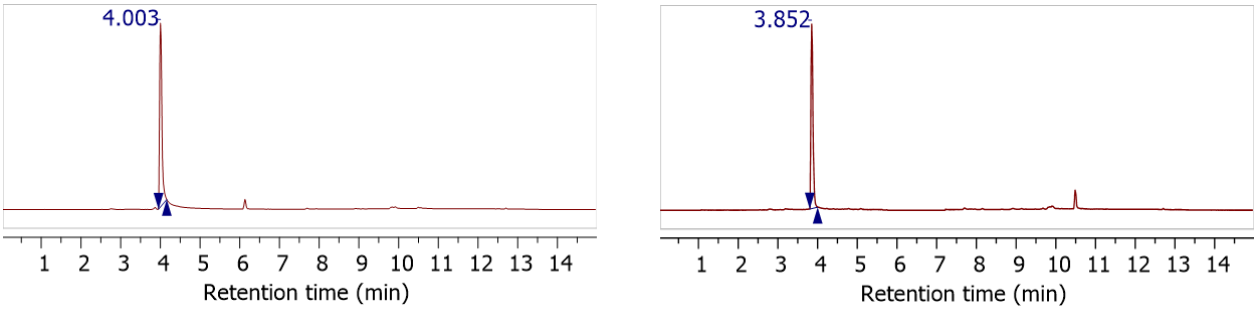

Figure 5.14: (left) UPLC chromatogram of Cou-NSu. (right) UPLC chromatogram of Cou-NSu after overnight stirring in H_2O/ DMSO.

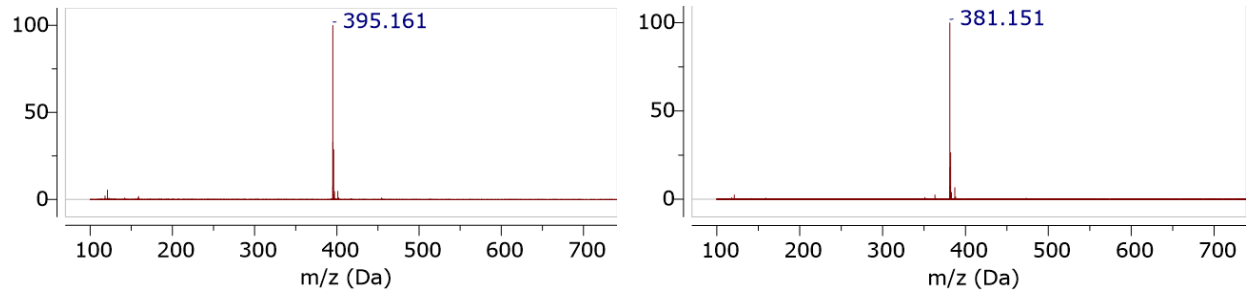

Figure 5.15: (left) ESI-TOF mass spectrum of Cou-NSu. (right) ESI-TOF mass spectrum of Cou-NSu after overnight stirring in H_2O/ DMSO.

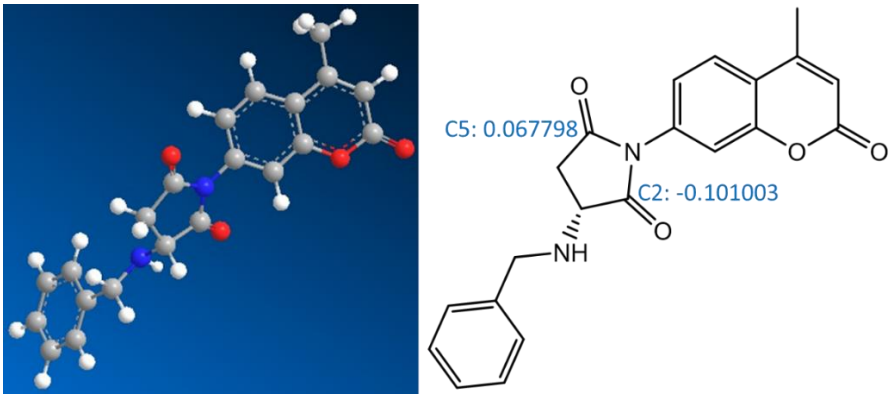

Figure 5.16: (left) Optimized 3D structure of Cou-NSu. DFT calculations were done by using Orca 4.2.1.[23, 24] Geometry optimization and frequency calculation were performed at B3LYP/6-311++G(d,p) level of theory. (right) Mulliken charges (shown in blue) were calculated on the optimized structure of Cou-NSu.

5.4 Conclusion and future works

To conclude, a coumarin amino-succinimide fluorescent probe (Cou-NSu) was synthesized. Preliminary fluorescence response titrations towards formaldehyde, acetaldehyde, benzaldehyde, glyoxal, and methylglyoxal were performed. The probe showed good selectivity with emission 2.4-fold increasing in the presence of formaldehyde and no obvious emission change after the addition of acetaldehyde, benzaldehyde, glyoxal, and methylglyoxal. However, there was a self-enhancing peak at 394 nm in the emission spectra. This peak can significantly affect the accuracy and reproducibility of the sensing results. To identify the cause of the self-enhancing peak, a stability study of Cou-NSu was conducted in DMSO and H_2O/DMSO without adding any analyte. In DMSO, the probe did not show any structural changes. However, when Cou-NSu was dissolved in H_2O/DMSO, a hydrolysate of Cou-NSu was found. This result suggests that water molecules play a role in inducing the self-enhancing peak and causing hydrolysis of Cou-NSu. Therefore, there is a risk of hydrolysis when utilizing 3-amino-succinimide as the sensing component to construct formaldehyde-regenerating fluorescent probes, which would negatively impact the accuracy and reproducibility of the detection. Future research on formaldehyde-regenerating fluorescent probes could focus on optimizing the structure of the sensing part to strengthen its stability in water. Moreover, the ability of the probe to pass through the blood-brain barrier remains a challenge. Further research can be conducted on the probe delivery methods in order to effectively deliver the probes to the brain for brain-related disease detection.

5.5 Experimental section:

Deuterated solvents were purchased from Cambridge Isotope Laboratories. All other solvents and reagents were of reagent grade and purchased from either Sigma-Aldrich Chemical Co. or

Dieckmann and were used without further purification. Thin-layer chromatography (TLC) was performed using pre-coated silica gel 60, F254 plates with a thickness of 0.2 mm. Column chromatography was conducted using silica gel and laboratory grade solvents. NMR spectra were recorded on Bruker Avance III 400 MHz spectrometers (^{1}H NMR on 400 MHz, ^{13}C NMR on 101 MHz) at 298 K. Chemical shifts δ were reported in parts per million (ppm) and referenced to corresponding solvent peak (2.50 for DMSO-d6 and 7.26 for $CDCl_3$). Coupling constants *J* were reported in Hertz (Hz) and multiplicities were abbreviated as: s = singlet, d = doublet, t = triplet, dd = doublets of doublets, td = triplets of doublets and m = multiplet. High-resolution mass spectra, reported as *m/z*, were conducted by University Research Facility in Life Science, Hong Kong Polytechnic University from Agilent 6540 liquid chromatography – electrospray ionisation quadrupole-TOF mass. Low-resolution mass spectra were conducted by Waters Acquity H-Class UPLC with QDa mass detector for monitoring reaction and determining correct fraction during purification of product. LC-MS chromatogram and spectra were obtained from Agilent 6540 liquid chromatography – electrospray ionisation quadrupole-TOF mass spectrometer with Acquity UPLC BEH C18 1.7 μm column. Fluorescence spectra were recorded on Horiba FluoroMax 4 Spectrofluorometer in a 1 cm quartz cuvette.

Synthesis work and characterization:

Synthesis of compound 5.1:

To a stirred solution of 7-amino-4-methylcoumarin (1.14 mmol) in acetic acid (10 mL) at room temperature, maleic anhydride (1.71 mmol) was added. The resulting mixture was refluxed for 4 hours. The progress of the reaction was monitored by TLC. When the starting material, 7-amino-

4-methyl coumarin, was consumed, the mixture was allowed to cool to room temperature. The reaction mixture was evaporated to dryness under reduced pressure. The residue was purified by flash column chromatography (dichloromethane/methanol = 100:1, v/v) on silica gel to give a pale-yellow solid compound 5.1 (Yield: 23%). ^{1}H NMR (400 MHz, DMSO-d_6) δ 7.89 (d, J = 8.4 Hz, 1H), 7.47 – 7.38 (m, 2H), 7.26 (s, 2H), 6.45 (d, J = 1.5 Hz, 1H), 2.47 (d, J = 1.3 Hz, 3H). ^{13}C NMR (101 MHz, DMSO) δ 169.89, 160.01, 153.28, 135.41, 134.96, 126.26, 122.57, 119.10, 115.00, 114.43, 18.56. HRMS (ESI TOF): m/z calcd $[M+MeOH+Na]^+$ = 310.0691, found 310.0743.

Synthesis of Cou-NSu:

Compound 5.1 (0.078 mmol) and benzylamine (0.0858 mmol) were dissolved in anhydrous DCM (3 mL) under a nitrogen atmosphere and the solution was stirred overnight at room temperature. The reaction mixture was evaporated to dryness under reduced pressure. The residue was purified by flash column chromatography (hexane/ethyl acetate = 1:1, v/v) on silica gel to give a pale-yellow solid Cou-NSu (Yield: 56%). ^{1}H NMR (400 MHz, Chloroform-d) δ 7.68 (d, J = 8.6 Hz, 1H), 7.40 – 7.34 (m, 5H), 7.30 (dd, J = 8.5, 2.1 Hz, 2H), 6.32 (s, 1H), 4.00 – 3.89 (m, 3H), 3.07 (dd, J = 18.1, 8.5 Hz, 1H), 2.75 (dd, J = 18.1, 5.4 Hz, 1H). ^{13}C NMR (101 MHz, $CDCl_3$) δ 176.36, 173.54, 160.14, 153.57, 151.62, 138.45, 134.33, 128.79, 128.36, 127.75, 125.17, 121.84, 119.93, 115.82, 114.96, 55.55, 51.96, 36.62, 18.67. HRMS (ESI TOF): m/z calcd. $[M+MeOH+H]^+$ = 395.1602, found 395.1629.

5.6 Reference

[1] A. Songur, O. A. Ozen, and M. Sarsilmaz, "The toxic effects of formaldehyde on the nervous system," *Reviews of Environmental Contamination and Toxicology,* vol. 203, pp. 105-18, 2010, doi: 10.1007/978-1-4419-1352-4_3.

[2] K. Tulpule and R. Dringen, "Formaldehyde in brain: an overlooked player in neurodegeneration?," *J. Neurochem.,* vol. 127, no. 1, pp. 7-21, Oct 2013, doi: 10.1111/jnc.12356.

[3] R. He, J. Lu, and J. Miao, "Formaldehyde stress," *Sci. China Life Sci.,* vol. 53, no. 12, pp. 1399-404, Dec 2010, doi: 10.1007/s11427-010-4112-3.

[4] Y. Tsukada, J. Fang, H. Erdjument-Bromage, M. E. Warren, C. H. Borchers, P. Tempst, and Y. Zhang, "Histone demethylation by a family of JmjC domain-containing proteins," *Nature,* vol. 439, no. 7078, pp. 811-6, Feb 16 2006, doi: 10.1038/nature04433.

[5] K. Tsujikawa, K. Koike, K. Kitae, A. Shinkawa, H. Arima, T. Suzuki, M. Tsuchiya, Y. Makino, T. Furukawa, N. Konishi, and H. Yamamoto, "Expression and sub-cellular localization of human ABH family molecules," *Journal of Cellular and Molecular Medicine,* vol. 11, no. 5, pp. 1105-1116, 2007, doi: 10.1111/j.1582-4934.2007.00094.x.

[6] J. O'Sullivan, M. Unzeta, J. Healy, M. I. O'Sullivan, G. Davey, and K. F. Tipton, "Semicarbazide-Sensitive Amine Oxidases: Enzymes with Quite a Lot to Do," *NeuroToxicology,* vol. 25, no. 1-2, pp. 303-315, 2004, doi: 10.1016/s0161-813x(03)00117-7.

[7] Z. Tong, C. Han, W. Luo, X. Wang, H. Li, H. Luo, J. Zhou, J. Qi, and R. He, "Accumulated hippocampal formaldehyde induces age-dependent memory decline," *Age (Dordr),* vol. 35, no. 3, pp. 583-96, Jun 2013, doi: 10.1007/s11357-012-9388-8.

[8] Z. Tong, J. Zhang, W. Luo, W. Wang, F. Li, H. Li, H. Luo, J. Lu, J. Zhou, Y. Wan, and R. He, "Urine formaldehyde level is inversely correlated to mini mental state examination scores in senile dementia," *Neurobiol Aging,* vol. 32, no. 1, pp. 31-41, Jan 2011, doi: 10.1016/j.neurobiolaging.2009.07.013.

[9] A. Takeuchi, T. Takigawa, M. Abe, T. Kawai, Y. Endo, T. Yasugi, G. Endo, and K. Ogino, "Determination of formaldehyde in urine by headspace gas chromatography," *Bull. Environ. Contam. Toxicol.,* vol. 79, no. 1, pp. 1-4, Jul 2007, doi: 10.1007/s00128-007-9172-0.

[10] A. Soman, Y. Qiu, and Q. Chan Li, "HPLC-UV Method Development and Validation for the Determination of Low Level Formaldehyde in a Drug Substance," *J. Chromatogr. Sci.,* vol. 46, no. 6, pp. 461-465, 2008, doi: 10.1093/chromsci/46.6.461.

[11] S. Kato, P. J. Burke, T. H. Koch, and V. M. Bierbaum, "Formaldehyde in Human Cancer Cells: Detection by Preconcentration-Chemical Ionization Mass Spectrometry," *Anal. Chem.,* vol. 73, no. 13, pp. 2992-2997, 2001, doi: 10.1021/ac001498q.

[12] T. F. Brewer and C. J. Chang, "An Aza-Cope Reactivity-Based Fluorescent Probe for Imaging Formaldehyde in Living Cells," *J. Am. Chem. Soc.,* vol. 137, no. 34, pp. 10886-9, Sep 2 2015, doi: 10.1021/jacs.5b05340.

[13] Y. Tang, X. Kong, A. Xu, B. Dong, and W. Lin, "Development of a Two-Photon Fluorescent Probe for Imaging of Endogenous Formaldehyde in Living Tissues," *Angew. Chem., Int. Ed.,* vol. 55, no. 10, pp. 3356-9, Mar 1 2016, doi: 10.1002/anie.201510373.

[14] W. Zhou, H. Dong, H. Yan, C. Shi, M. Yu, L. Wei, and Z. Li, "HCHO-reactive molecule with dual-emission-enhancement property for quantitatively detecting HCHO in near 100% water solution," *Sensors and Actuators B: Chemical,* vol. 209, pp. 664-669, 2015, doi: 10.1016/j.snb.2014.12.043.

[15] A. K. Steiger, S. Pardue, C. G. Kevil, and M. D. Pluth, "Self-Immolative Thiocarbamates Provide Access to Triggered H2S Donors and Analyte Replacement Fluorescent Probes," *J. Am. Chem. Soc.,* vol. 138, no. 23, pp. 7256-9, Jun 15 2016, doi: 10.1021/jacs.6b03780.

[16] J. Zhang, S. Mu, W. Wang, H. Sun, S. Li, X. Shi, Y. Liu, X. Liu, and H. Zhang, "Design strategy for an analyte-compensated fluorescent probe to reduce its toxicity," *Chem. Commun.,* 2022, doi: 10.1039/d2cc02789e.

[17] M. Popova, T. Soboleva, A. D. Benninghoff, and L. M. Berreau, "CO Sense and Release Flavonols: Progress toward the Development of an Analyte Replacement PhotoCORM for Use in Living Cells," *ACS Omega,* vol. 5, no. 17, pp. 10021-10033, May 5 2020, doi: 10.1021/acsomega.0c00409.

[18] X. L. Liu, X. Yang, L. Li, T. Xie, X. Zhang, T. Yang, D. Jiang, J. Chen, Y. Chen, L. Cai, Y. Wang, and P. Zhang, "An analyte-replacement near-infrared fluorogenic probe for ultrafast detection of hypochlorite in rheumatoid arthritis," *Bioorg. Chem.,* vol. 139, p. 106757, Oct 2023, doi: 10.1016/j.bioorg.2023.106757.

[19] H. Xu, H. Xu, S. Ma, X. Chen, L. Huang, J. Chen, F. Gao, R. Wang, K. Lou, and W. Wang, "Analyte Regeneration Fluorescent Probes for Formaldehyde Enabled by Regiospecific Formaldehyde-Induced Intramolecularity," *J. Am. Chem. Soc.,* vol. 140, no. 48, pp. 16408-16412, 2018, doi: 10.1021/jacs.8b09794.

[20] A. Bi, M. Liu, S. Huang, F. Zheng, J. Ding, J. Wu, G. Tang, and W. Zeng, "Construction and theoretical insights into the ESIPT fluorescent probe for imaging formaldehyde in vitro and in vivo," *Chem. Commun.,* vol. 57, no. 28, pp. 3496-3499, 2021, doi: 10.1039/d1cc00429h.

[21] R. P. Lyon, J. R. Setter, T. D. Bovee, S. O. Doronina, J. H. Hunter, M. E. Anderson, C. L. Balasubramanian, S. M. Duniho, C. I. Leiske, F. Li, and P. D. Senter, "Self-hydrolyzing maleimides improve the stability and pharmacological properties of antibody-drug conjugates," *Nat. Biotechnol.,* vol. 32, no. 10, pp. 1059-1062, 2014, doi: 10.1038/nbt.2968.

[22] S. Catak, G. Monard, V. Aviyente, and M. F. Ruiz-López, "Deamidation of Asparagine Residues: Direct Hydrolysis versus Succinimide-Mediated Deamidation Mechanisms," *J. Phys. Chem. A,* vol. 113, no. 6, pp. 1111-1120, 2009, doi: 10.1021/jp808597v.

[23] F. Neese, "The ORCA program system," *WIREs Computational Molecular Science,* vol. 2, no. 1, pp. 73-78, 2012, doi: 10.1002/wcms.81.

[24] F. Neese, "Software update: the ORCA program system, version 4.0," *WIREs Computational Molecular Science,* vol. 8, no. 1, p. e1327, 2018, doi: 10.1002/wcms.1327.

5.7 Appendix

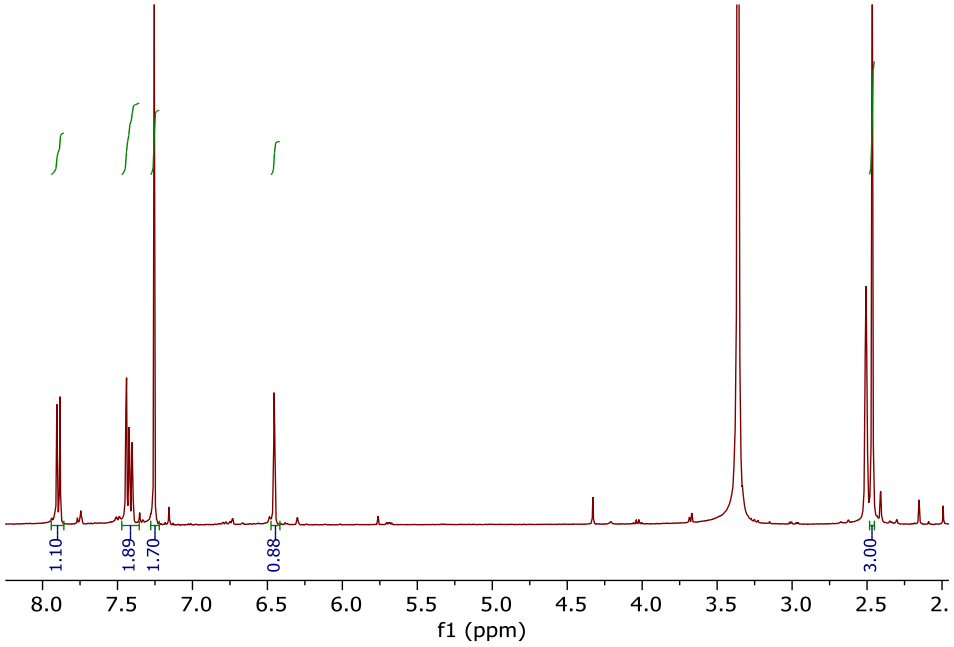

Figure 5.17: ^{1}H NMR spectrum of compound 5.1 (600 MHz, DMSO-d_6).

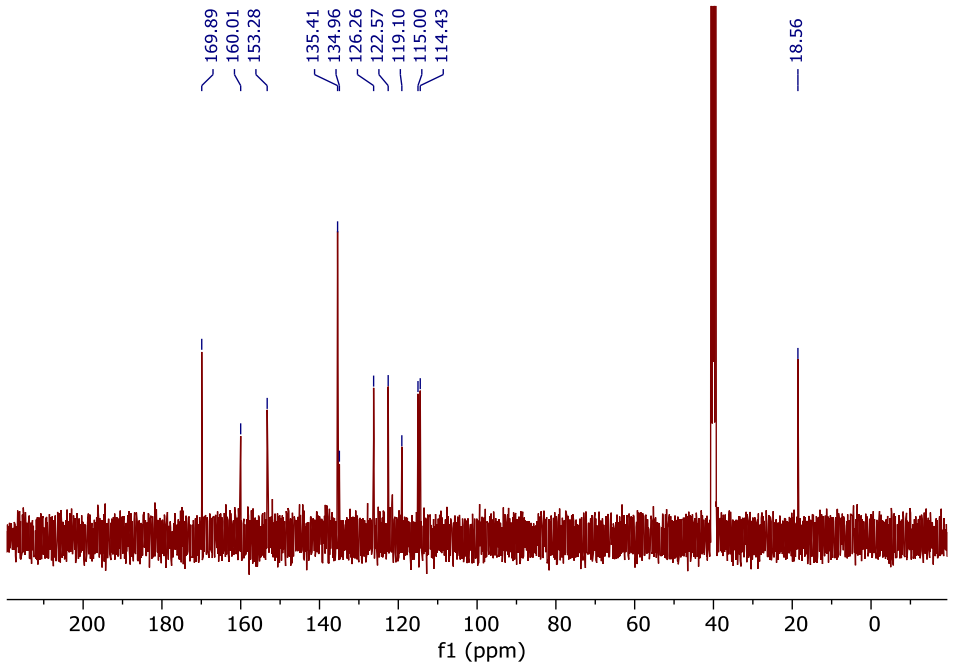

Figure 5.18: ^{13}C NMR spectrum of compound 5.1 (151 MHz, DMSO-d_6).

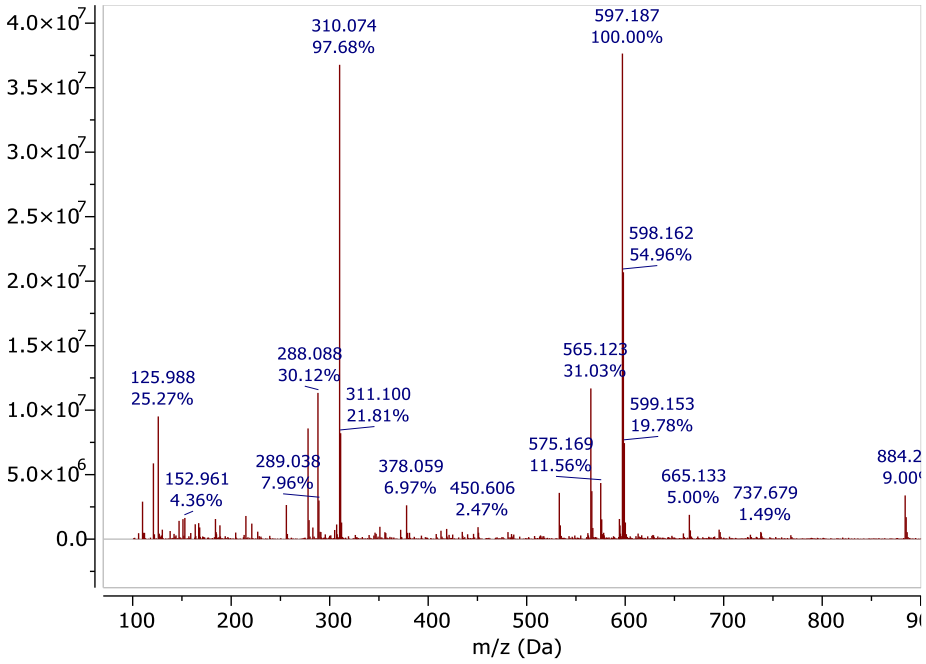

Figure 5.19: High-resolution mass spectrum of compound 5.1.

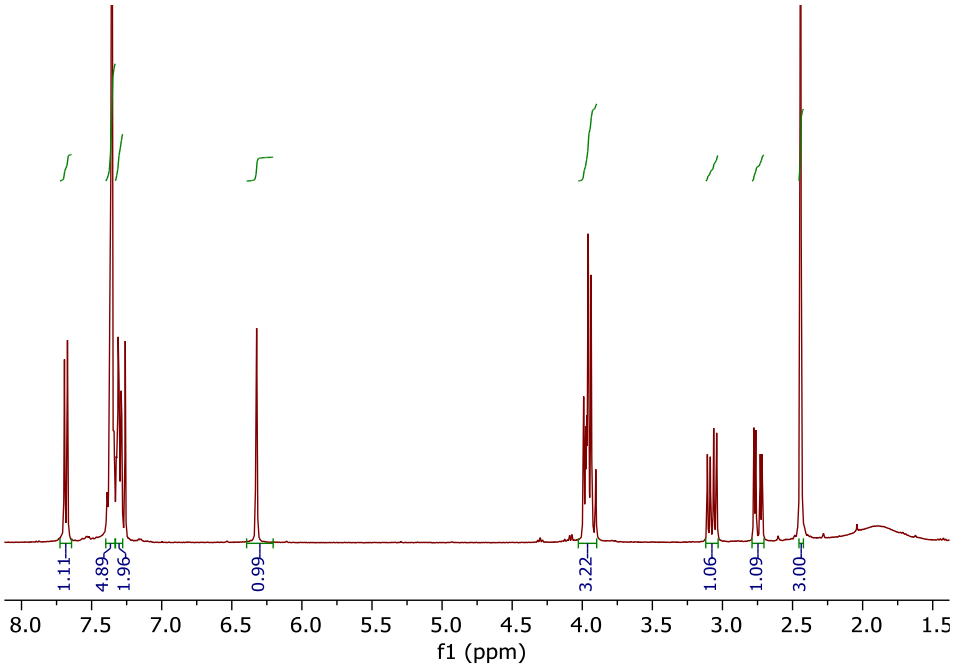

Figure 5.20: ^{1}H NMR spectrum of Cou-NSu (600 MHz, $CDCl_3$).

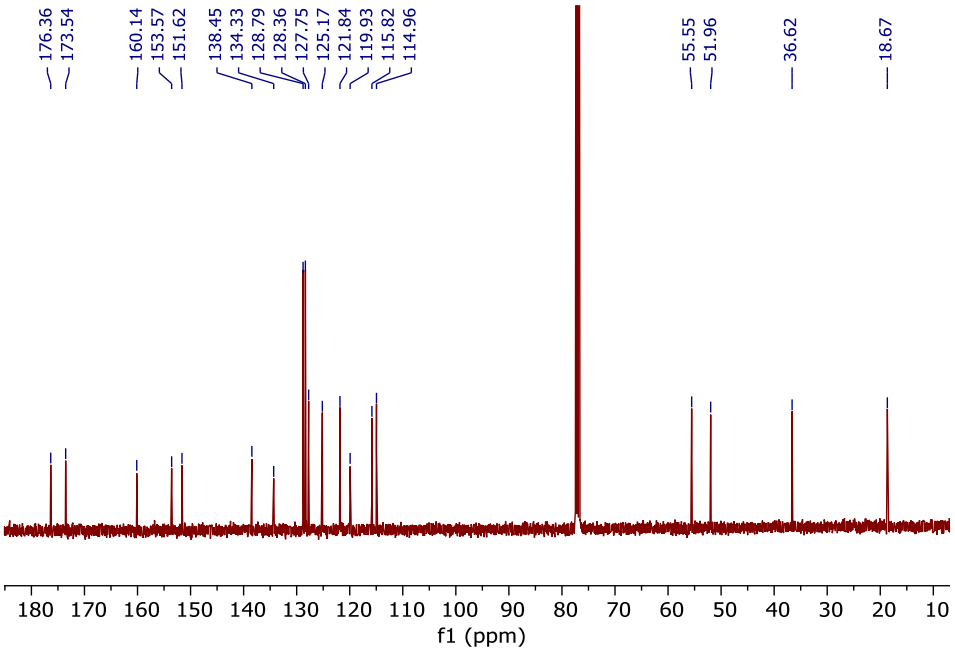

Figure 5.21: ^{13}C NMR spectrum of Cou-NSu (151 MHz, $CDCl_3$).

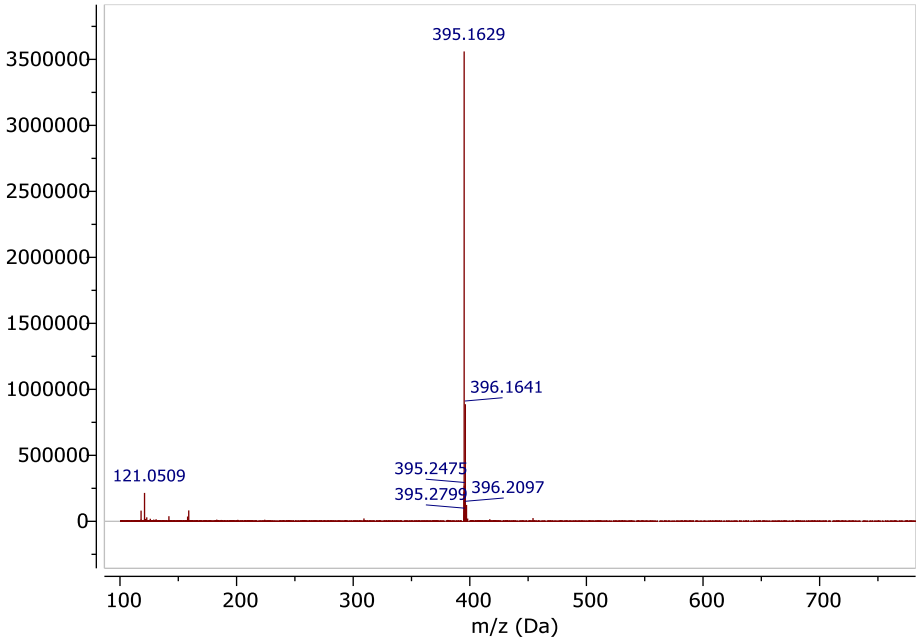

Figure 5.22: High-resolution mass spectrum of Cou-NSu.